# Temperature and dissipation in finite quantum systems

**Phillip Cussen Burke**

**B.Sc.**


Thesis presented for the degree of

Doctor of Philosophy

to the

National University of Ireland Maynooth

Department of Theoretical Physics

February 2023

Department Head

Dr. Joost Slingerland

Research advisors

Dr. Masudul Haque & Dr. Jon-Ivar Skullerud

To my parents.

# Contents

# Declaration

This thesis has not been submitted in whole, or in part, to this or any other university for any other degree and is, except where otherwise stated, the original work of the author.

Phillip Cussen Burke, June 9, 2023

# Acknowledgments

First, I would like to thank my supervisor Masud Haque for his guidance throughout my (many) years at Maynooth University. He has always offered his advice and knowledge when it was needed. I am also ever grateful to Jonivar Skullerud, whom I have perhaps known for the longest time at Maynooth, for taking on the role of my supervisor when Masud was no longer able to. I must also thank Goran for the countless discussions and collaboration over the last four years, and of course, for the BBQs.

There are many past and present members of the department I'd like to thank; I'll start with Stephen and Paul for many insightful conversations, research related and otherwise. I should thank Ken, Adam, Shane, Babatunde, Ian, and Jesuel, with whom I had the pleasure of sharing an office. When it comes to offices, I have probably spent far too many hours talking about anything other than physics in the front office, which I must thank Darragh, Aonghus, John, Goran (again), Stephen (again), and of course, Dale for.

Before the pandemic, which feels like a lifetime ago, I would look forward to our weekly 'Jackie cans' event, something I especially missed once it was no longer possible. During the pandemic, when I could no longer procrastinate in person amongst the many lockdowns, our weekly Friday coffee mornings (which usually ran on to late afternoons) provided a great escape, for which I must again thank many of those whom I have already mentioned, but also Aoibhinn, Nathan, and Hannah. Those same people are also responsible for many lunches which went on for far too long, along with Suzie, Joe, and Saoirse. I must thank Aaron, Kevin, and Domenico, who have gone before me and offered me their advice, and also Eddie, Kay, Rachel, Jasmin, Gert, and Thomas, who have made the department

a friendly environment. I am also grateful to the various heads of departments and, most importantly, Suzie for keeping the department running.

I am especially grateful for my friends of many years, Daragh, Jack, Gerry, Rob, Anto, and Daragh, who have always been there for me and offered distraction when it was needed most.

I would like to thank my family: my parents, my sisters, and my grandmother Máire, for their love and support over the years. My mother and father have always encouraged and supported me in every aspect of my life, for which I am eternally grateful.

Finally, I must thank my partner Rebecca, who has given me love, fun, and companionship over the last six years. I am not sure my sanity would have made it to the other side of the pandemic intact without her, and I will be forever grateful for her support throughout my Ph.D.

I acknowledge the financial support from Maynooth University via the John & Pat Hume Scholarship program and the COVID-19 costed extension.

# Abstract

The ideas in this thesis are placed broadly within the context of many-body quantum dynamics, an area of research that has gained significant interest in recent years due to developments in cold atom experiments that enable the realization of isolated many-body quantum systems.

In this thesis, we first focus on the concept of connecting quantum mechanical systems to statistical mechanics, which often arises in the study of 'thermalization' in isolated many-body systems. An inescapable issue in the endeavor to connect the two is the definition of temperature. The first core definition of temperature we consider is inspired by the eigenstate thermalization hypothesis, which posits that the eigenstates of a generic thermalizing system have information regarding thermalization encoded within them. We consider temperatures based on comparing the structure of (full or reduced) eigenstate density matrices to thermal density matrices. The second temperature definition invokes the standard temperature-entropy relation from statistical mechanics relating temperature and microcanonical entropy. We explore various ways to define the microcanonical entropy in finite isolated quantum systems and numerically compute the corresponding temperature.

Following this, we study the diametrical opposite of isolated quantum systems — open quantum systems. We study a quantum particle on a tight-binding lattice with a non-Hermitian (purely imaginary) local potential. Non-Hermitian Hamiltonians are effective models for describing open quantum systems. We analyze the scattering dynamics and spectrum, identifying an exceptional point where the entire spectrum pairs up into mutually coalescing eigenstate pairs. At large potential strengths, the absorption coefficient decreases, and the effect of

the imaginary potential is similar to that of a real potential, which we quantify by utilizing the properties of a localized eigenstate. We demonstrate the existence of many exceptional points in a similar $\mathcal{PT}$-symmetric system and non-interacting many-particle model. This investigation contributes to a many-body understanding of this non-Hermitian setup.

# Chapter 1

# Introduction

In recent years, there has been an ever-growing interest in many-body quantum systems. This growth was stimulated in the last two decades by newly emerging cold atom experiments, providing a platform to simulate such systems. The collective behavior of many quantum particles can be deeply complex, and as a result, the study of many-body quantum dynamics has bloomed into an extensive field of fundamental research in theoretical physics.

Within the field of many-body quantum dynamics, an area of considerable interest in recent years is understanding the emergence of statistical mechanics from the dynamics of isolated many-body systems. A primary question is how observables in such isolated quantum systems can relax to statistical mechanical predictions despite the absence of an external bath, a process dubbed *thermalization*. Endeavors made to reconcile statistical mechanics with quantum mechanical systems invariably require a correspondence between energy, a quantity well-defined in quantum mechanics, and temperature, which is necessary for a statistical mechanical description. In finite isolated quantum systems, the assignment of temperature to energy is generally a non-trivial task. In this thesis, we critically examine various ways to define temperature in isolated quantum systems. In the following Section 1.1, we introduce two core definitions of temperature that we will investigate. The first is based on insight from the eigenstate thermalization hypothesis (ETH), which posits that each eigenstate contains information relevant to thermalization if it occurs. We outline ideas of thermalization and the ETH

in Section 1.2 of this introduction. The second definition utilizes a standard definition from statistical mechanics that relates (microcanonical) entropy to temperature. We outline various ways to compute the microcanonical entropy in isolated quantum systems and calculate the corresponding temperature.

The antithesis of an isolated quantum system is an open quantum system, which is a system that interacts with an external environment (or bath). The interaction between the system and the environment has a significant effect on the dynamics of the system. Particular open quantum systems can be effectively described by non-Hermitian Hamiltonians despite Hermiticity being regarded as a postulate of standard quantum mechanics. In this thesis, we investigate the dynamics and spectrum of a quantum particle in a non-Hermitian quantum system, a tight-binding lattice subject to a purely imaginary local potential. While much of our non-Hermitian investigation focuses on the context of a single particle, we build toward understanding many-body systems by establishing a detailed description of the single particle and non-interacting many-body systems.

In the following Section 1.1, we define the various temperatures to be investigated in this thesis and discuss their motivation. In Section 1.2, we provide context for thermalization, particularly the eigenstate thermalization hypothesis, which underlies a core temperature definition. Moving to Section 1.3, we detail some of the phenomena unique to non-Hermitian systems and outline our investigation. Following this, in Section 1.4, we describe the various many-body quantum systems to be utilized in this thesis, along with the proposed non-Hermitian system. In addition, we provide a brief description of level spacing statistics, a tool oft-used to characterize many-body systems as thermalizing. Finally, in Section 1.5, we provide an overview of the chapters in this thesis.

## 1.1 Temperature in isolated quantum systems

In this section, we motivate and outline the various ways we shall consider defining temperature in isolated many-body quantum systems.

Within the field of thermalization in isolated many-body quantum systems,

the eigenstate thermalization hypothesis (ETH) [1–10] is considered a cornerstone in understanding how thermalization can occur.

While it is generally accepted that a pure state of an isolated quantum system will never thermalize, it has been observed that a subsystem of such a state can, in fact, thermalize. This subsystem thermalization can occur due to the remainder of the system, i.e., the complement subsystem, acting as a bath to the primary subsystem under consideration. The principal constraint on this reasoning is that the 'bath' subsystem should be larger than the primary subsystem [11]. The concept of thermalization in quantum systems and the ETH are discussed in detail in Section 1.2.

Ideas regarding thermalization in isolated quantum systems, such as the eigenstate thermalization hypothesis, and its extensions or variants, are often tested or verified using numerical "exact diagonalization" calculations [8–48]. As a result, quantum systems with Hilbert space dimensions between $\sim 10^3$ and $\sim 10^5$ have acquired particular relevance. Therefore, it is necessary to ask how meaningful the various definitions of thermodynamic quantities like temperature or entropy are for finite systems, particularly systems of sizes typically treated by full numerical diagonalization. In Chapter 3 of this thesis, we critically examine different ways of calculating entropy from the energy eigenvalues of finite systems and derive a temperature from the entropy as outlined below.

The ETH posits that each eigenstate of a thermalizing isolated quantum system contains information relevant to thermalization, particularly the temperature associated with the equilibrium 'thermal' state (see Section 1.2). Thus, a natural question is how to assign temperatures to each eigenstate based on information encoded in the eigenstates. In Chapter 2 of this thesis, we examine possible ways of doing so.

Before delving into the temperature definitions in isolated quantum systems under investigation in this thesis, we first discuss an energy-temperature correspondence regularly used in the study of quantum thermalization. The most common definition of temperature for finite isolated quantum systems is the 'canonical

temperature'. For a system described by the Hamiltonian $H$, the canonical temperature is obtained for any energy $E$ by inverting the canonical equation

$$E = \langle H \rangle_C = \frac{\mathrm{tr}\left(e^{-H/k_B T} H\right)}{\mathrm{tr}(e^{-H/k_B T})} = \frac{\sum_j e^{-\beta E_j} E_j}{\sum_j e^{-\beta E_j}}, \tag{1.1}$$

where $E_j$ are the eigenvalues of $H$. This relationship provides a map between energy and the canonical temperature $T_C = (k_B \beta_C)^{-1}$, where $k_B$ is the Boltzmann constant. We denote this temperature as the 'canonical temperature' as $\langle H \rangle_C$ is the expectation value of $H$ in the canonical ensemble.

Curiously, this definition relies only on the energy eigenvalues, disregarding the physics of the eigenstates. The relationship in Eq. (1.1) originates in statistical mechanics from the context of a system coupled with a bath, although it is widely used in the study of thermalization of isolated, i.e., bath-less, quantum systems [8–13, 15, 17–20, 25, 27, 29, 43, 49–53].

In Chapters 2 and 3 this thesis, our focus is on two core ideas of temperature assignment in isolated quantum systems. The first idea, inspired by the ETH, is based on the structure of the eigenstates and the information encoded within them. The second idea is to use another standard definition of temperature from statistical mechanics relating temperature and entropy. Entropy, unlike temperature, is defined in a quantum mechanical system, although, as we will see, choosing the most appropriate definition in finite isolated systems is a non-trivial task. We explore possible ways to define entropy in an isolated system of a size accessible to exact diagonalization and derive a temperature for each case. In every case, we compare the resulting temperature obtained with the canonical temperature $\beta_C$ obtained directly by inverting Eq. (1.1).

### 1.1.1 Eigenstate-temperature relations

Consider an eigenstate $|E_n\rangle$ of a many-body system; if the temperature corresponding to the equilibrium thermal state is encoded within the structure of this eigenstate, then we could naïvely expect that the eigenstate density matrix, $\rho = |E_n\rangle\langle E_n|$, should be closest to the canonical ('Gibbs' or 'thermal') density

matrix

$$\rho_C = \frac{e^{-\beta H}}{Z} \tag{1.2}$$

at the value of the inverse temperature $\beta$. Here, $Z = \mathrm{tr}\big(e^{-\beta H}\big)$ is the partition function. Thus, one could propose minimizing the distance $d(\rho, \rho_C)$ between these two density matrices as a function of $\beta$, as a possible way to assign a temperature to $E_n$. We refer to this optimal $\beta$ as the *eigenstate temperature* $\beta_E$. As $|E_n\rangle\langle E_n|$ is the limit of the microcanonical density matrix for an ultra-narrow energy window, this idea is also related to the equivalence of statistical ensembles [54, 55].

It is admittedly over-ambitious to expect the complete eigenstate density matrix, $\rho$, to resemble a Gibbs thermal state $\rho_C$, as the former is a pure state while the latter is a mixed state. The two density matrices cannot be expected to be 'close', as we will illustrate in Chapter 2. In real-time dynamics, the typical inquiry is whether a local sub-region, rather than the whole system, approaches a thermal state [21, 51, 53, 56–65]. The intuition is that the rest of the system acts as an effective bath, even if the textbook properties of a bath (weak coupling, no memory) are not satisfied. Accordingly, ETH is often formulated in terms of local observables or a spatial fraction of the system [11, 24, 28, 34, 35, 51, 63, 64, 66, 67], and similar ideas appear in the approach known as canonical typicality [7, 20, 57, 59, 66, 68–71], both of which are discussed in Section 1.2.

Thus, in thermalizing systems, one expects that if the system is partitioned spatially into $A$ and $B$, with $A$ smaller than $B$, then the reduced density matrix of subsystem $A$ for an eigenstate, $\rho^A = \mathrm{tr}_B\, \rho$, should approximate the reduced canonical density matrix, $\rho_C^A = \mathrm{tr}_B\, \rho_C$ [11, 35, 66]. Inverting this expectation, we obtain another way to assign a temperature to eigenstates — using the value of $\beta$ that minimizes the distance $d(\rho^A, \rho_C^A)$. We refer to this optimal $\beta$ as the *subsystem temperature* $\beta_S$.

In Chapter 2, we shall investigate these temperature definitions, particularly in isolated chaotic systems, expected to obey the ETH.

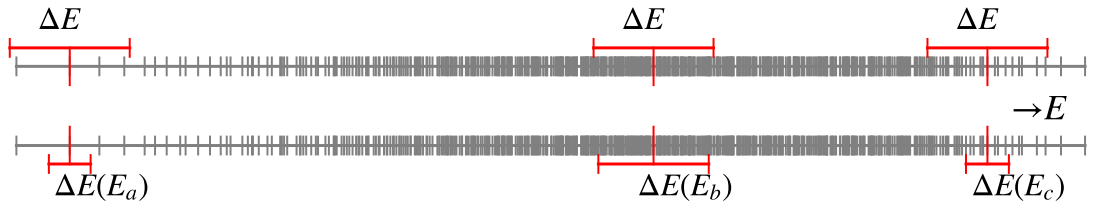


Figure 1.1: Illustration of two ways of choosing the energy window $\Delta E$ used to define the microcanonical entropy. The top figure shows the obvious choice: the width $\Delta E$ is the same at all energies. The lower schematic illustrates an energy-dependent width: $\Delta E(E) \propto \sqrt{T_c^2 C_c}$, where the temperature $T_c$ is the canonical temperature corresponding to energy $E$ and $C_c$ is the heat capacity at $T = T_c$. The window is shown at three energy values: $E_a$, $E_b$, and $E_c$, which are in the regime of low temperature, infinite temperature, and low negative temperature, respectively. Each vertical tick marks an eigenvalue.

### 1.1.2 Entropy-temperature relations

In statistical mechanics, a fundamental definition of temperature arises from the thermodynamic relation [72–77]

$$T = \left(\frac{\partial E}{\partial S}\right)_{X_i} = \left(\frac{\partial S}{\partial E}\right)^{-1}_{X_i}. \tag{1.3}$$

Here, $S$ is the (thermal) entropy, and the subscript $X_i$ denotes the system parameters that should be held constant. For an isolated (i.e., microcanonical) quantum system, defining the entropy $S(E)$ at a particular energy $E$ involves counting the number of eigenstates ('microstates') within an energy window $\Delta E$ around that energy $E$. This leads to the question of how to choose the energy width $\Delta E$ or possibly how to avoid counting eigenstates altogether (and perhaps explicitly choosing $\Delta E$) and approximate the density of states. In the large system size (thermodynamic) limit, these choices can be shown to be inconsequential.

In Chapter 3 of this thesis, we will explore the consequences of these choices for finite-sized systems, focusing on those with Hilbert space dimensions $\sim 10^4$ typical for full numerical diagonalization studies. Motivated by the analysis of Ref. [54], we consider four choices for defining the entropy.

First, we consider counting eigenstates in an arbitrarily chosen but constant (energy-independent) window, as illustrated in Figure 1.1 (top). This is the most

obvious choice but turns out to be far from optimal — the resulting temperature deviates strongly at finite sizes from the canonical temperature.

Second, noting that the leading correction to the large-size limit can be negated by choosing $\Delta E \propto \sqrt{T_c^2 C_c}$ [54], we examine the result of counting eigenstates in such an energy-dependent window width. (Here, $C_c$ is the heat capacity.) An example of an energy-dependent window is illustrated in Figure 1.1 (bottom). We show that this choice works remarkably well for the sizes of interest, modulo some caveats regarding constants of proportionality.

Finally, instead of counting eigenstates in a particular window around $E$, we can instead compute the microcanonical entropy using standard numerical approximation procedures for the density of states via approximations to the integrated density of states (cumulative spectral function). We first formulate this entropy definition without reference to a specific energy window $\Delta E$ and show that this choice is sub-optimal at reproducing the canonical temperature. We analyze the reason for the strong finite-size mismatch in this case. Lastly, we use the energy-dependent $\Delta E \propto \sqrt{T_c^2 C_c}$, designed to account for finite-size deviations, in conjunction with the integrated density of states formulation. This final method results in excellent agreement between the temperatures even at the small system sizes under investigation, without any fine-tuning of proportionality constants.

## 1.2 Thermalization and the ETH

In Chapters 2 and 3 of this thesis, we explore various definitions of temperature in isolated many-body quantum systems. The concept of temperature in such systems is usually defined in the context of thermalization. In particular, one of our core temperature definitions has its basis in the eigenstate thermalization hypothesis. Therefore, we provide the context needed for a thorough understanding.

There has been a lot of significant work done investigating the emergence of equilibrium (or thermal) ensembles from statistical mechanics in isolated quantum systems [10, 69, 70]. In this section, we outline the meaning of 'thermalization' in

isolated quantum systems and the eigenstate thermalization hypothesis. We also discuss some further ideas investigated in the field of thermalization.

### 1.2.1 Thermalization in isolated quantum systems

Consider an isolated quantum system in some non-equilibrium initial state $|\psi(0)\rangle$. This system is described by the Hamiltonian $H$ and evolves in time via the Schrödinger equation. This implies that at a time $t > 0$, the time evolved state is obtained via $|\psi(t)\rangle = e^{-iHt}|\psi(0)\rangle$ ($\hbar = 1$). Taking $H$ as Hermitian, the time evolution is unitary; this implies the state $|\psi(t)\rangle$ can never reach a stationary state unless $|\psi(0)\rangle$ is an eigenstate of $H$.

Now, suppose we measure some local (or few-body) observable $\hat{O}$ in the state $|\psi(t)\rangle$, at time $t$, i.e., $\langle\psi(t)|\hat{O}|\psi(t)\rangle$. After some long time, the system can relax to an equilibrium state, whereby the observable $\hat{O}$ measured in the long-time evolved state is essentially constant. Equilibration is generally considered to have occurred when the temporal fluctuations of the expectation value have essentially vanished.

If a system has undergone equilibration, i.e., $\langle\psi(t)|\hat{O}|\psi(t)\rangle$ is on average constant for all subsequent times, and the expectation value of the observable in the equilibrium state coincides with the 'thermal' expectation value predicted by statistical mechanics, then thermalization is said to have occurred. This predicted value is the expectation value of the observable in the relevant statistical ensemble. The ensemble is taken to be either the microcanonical or canonical ensemble, which generally are equivalent in the thermodynamic limit. For example, in a system with only energy conservation, one would use the canonical ensemble (also called the Gibbs ensemble) at the canonical temperature associated with the initial state energy $E_0 = \langle\psi(0)|H|\psi(0)\rangle$ via Eq. (1.1). An illustration of thermalization for a local operator in a chaotic spin system is shown in Figure 1.2. In this figure, we plot the canonical and microcanonical expectation values,

$$\langle O\rangle_C = \mathrm{tr}(\rho_C O)\ , \quad \langle O\rangle_{MC} = \mathrm{tr}(\rho_{MC} O), \tag{1.4}$$

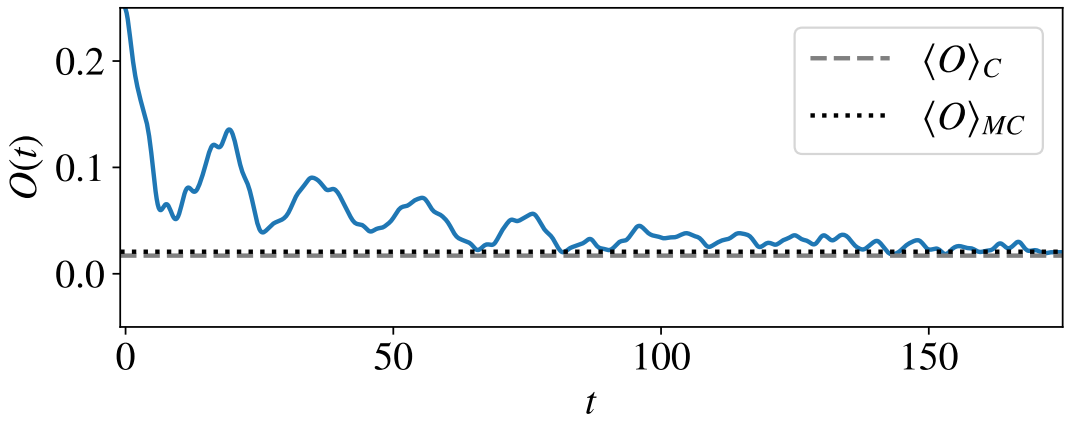


Figure 1.2: Illustration of thermalization: Eigenstate expectation values of a local operator $O = S_4^z S_5^z$ for the staggered field model, Eq. (1.15), with $J = 1$, $\Delta = 0.95$ and $h_x = h_z = 0.5$ for $L = 12$ spins. Also shown is the canonical expectation value $\langle O \rangle_C$ and the microcanonical expectation value $\langle O \rangle_{MC}$.

with $\rho_C$ the canonical density matrix, Eq. (1.2), and

$$\rho_{MC} = \frac{1}{\mathcal{N}} \sum_{E_j \in \{E_n \pm \Delta E/2\}} |E_j\rangle\langle E_j| \tag{1.5}$$

the microcanonical density matrix. Here, $\Delta E$ is the width of an energy window around $E_n$ from which the state is constructed, and $\mathcal{N}$ is the number of states in this window. It has been experimentally demonstrated that isolated many-body quantum systems can indeed thermalize, such as in quantum simulators consisting of ultra-cold atoms on an optical lattice [51, 78], trapped ions [79, 80], and a small number of qubits [81].

Not every system equilibrates such that observables relax to the predicted thermal (Gibbs) value, i.e., they do not thermalize as described above. In integrable systems, e.g., those exactly solvable via the Bethe ansatz, observables measured following a quantum quench are expected to equilibrate to predictions of the generalized Gibbs ensemble (GGE) [10, 82, 83]. The GGE is given by $\rho_{GGE} = Z_{GGE}^{-1} e^{-\sum_n \lambda_n I_n}$ ($Z_{GGE} = \mathrm{tr}\big(e^{-\sum_n \lambda_n I_n}\big)$), with $I_n$ the conserved quantities of the integrable system, and $\lambda_n$ the Lagrange multipliers, fixed by the initial state, analogous to setting the temperature in the Gibbs ensemble via the initial state energy. These conserved quantities are precisely what prevent standard relaxation to a thermal state from occurring. The relaxation to non-Gibbs states is often

denoted generalized thermalization [84, 85].

Localized systems have emerged as another possible example of systems that fail to thermalize as described above [86]. Systems exhibiting many-body localization (MBL) are considered the quintessential non-thermalizing models [87]. MBL is the extension of disorder-induced localization, introduced by Anderson in free systems [88], to many-body interacting systems. It is debated whether MBL is a genuine phase, in that it persists in the thermodynamic limit, or whether it is simply a finite size regime [89, 90]. Nevertheless, in sufficiently disordered finite 1D quantum chains, localization is observed, and thermalization does not occur.

In weakly non-integrable systems, i.e., systems with a small integrability breaking perturbation, observables can initially equilibrate to a non-thermal value corresponding to the integrable system equilibrium value. After a long time, the observable can eventually relax to the actual thermal value. This notion of equilibration followed by further relaxation to the thermal state has been coined prethermalization [91, 92].

Chaotic systems, i.e., non-integrable and non-localized, are expected to thermalize in the infinite size limit up to their integrable point. However, the time for the system to reach thermalization should diverge as one approaches the integrable limit. For finite systems, the required strength of any integrability breaking term to induce chaos is dependent on the size of the system [93].

### 1.2.2 Eigenstate thermalization hypothesis

We have thus far discussed the meaning of thermalization but not the mechanism behind it. The eigenstate thermalization hypothesis (ETH) is widely thought to encapsulate the mechanism by which thermalization occurs in isolated quantum systems [1–10]. It conjectures that thermalization is permitted in isolated quantum systems due to information regarding thermalization being encoded into the system eigenstates themselves. Formally, the ETH is a statement about the matrix elements of 'typical' observables, usually taken as local operators, in the eigenstate basis of the Hamiltonian for large isolated quantum systems. It states

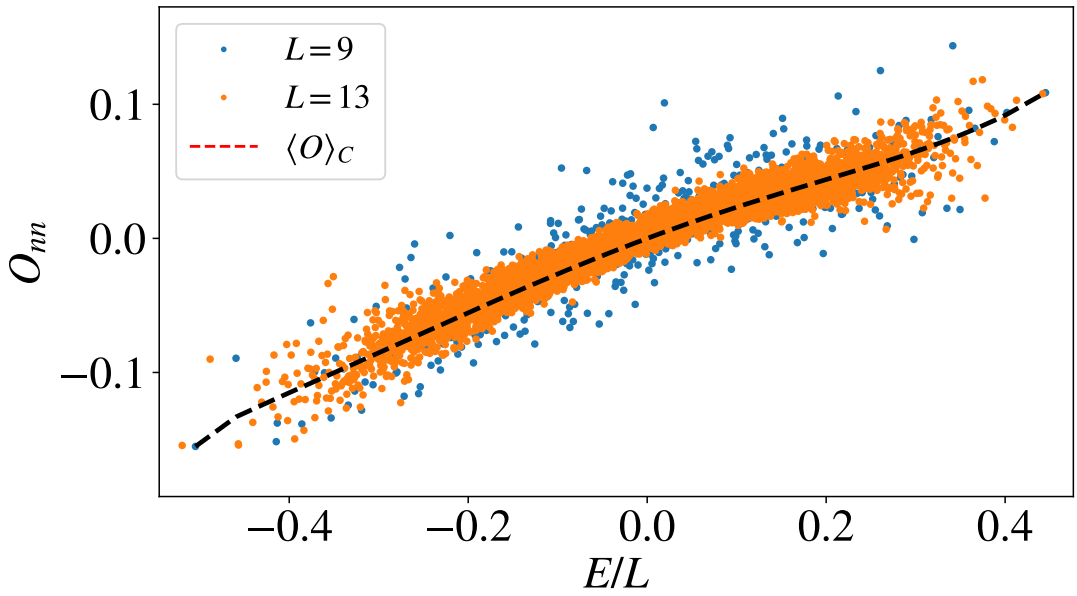


Figure 1.3: Illustration of the ETH: Eigenstate expectation values of a local operator $O$ for the staggered field model (Eq. (1.15)) with $J = 1$, $\Delta = 0.95$ and $h_x = h_z = 0.5$. Data is shown for $L = 9$ ($O = S^z_4 S^z_5$) and $L = 13$ ($O = S^z_6 S^z_7$) spins. Also shown is the canonical expectation value $\langle O\rangle_C$ calculated at the canonical temperature.

that diagonal matrix elements, i.e., the eigenstate expectation values (EEVs), of a typical observable $\hat{O}$ are smooth functions of (eigen-) energy, with fluctuations that are exponentially small in the system size. The off-diagonal elements are also exponentially suppressed in the system size. This statement can be written quantitatively for a Hamiltonian system with eigenstates $H\,|E_n\rangle = E_n\,|E_n\rangle$, via the ansatz put forward by Srednicki [4]:

$$\langle E_m|\,\hat{O}\,|E_n\rangle = O_{mn} = O(\bar{E})\delta_{mn} + e^{-S(\bar{E})/2} f_O(\bar{E},\omega) R_{mn}. \tag{1.6}$$

Here, $\bar{E} = \frac{1}{2}(E_m + E_n)$ is the average energy, $\omega = E_m - E_n$ is the energy difference, and $S(\bar{E})$ is the thermal entropy as defined in Section 1.1.2. $O(\bar{E})$ and $f_O(\bar{E},\omega)$ are smooth functions of energy, and $R_{mn}$ is a random variable with mean zero and variance one. $O(E)$ is the expectation value of $O$ in the diagonal ensemble.

The ETH is believed to be valid in generic chaotic systems [10], as has been numerically verified in many investigations, e.g., [8–48]. To date, there is no analytical proof of the ETH. Particular systems are known to violate the ETH, such as integrable systems [13], which undergo 'generalized thermalization' to

a GGE. Localized systems, such as those in an MBL regime, fail to thermalize and violate the ETH [87]. Finite systems with long-range interactions have only recently been investigated in the context of the ETH and thermalization. In such systems, it appears possible for a system to present as chaotic while violating the ETH [48, 94]. This has been related to the in-equivalence between the canonical and microcanonical ensembles, often accompanied by non-convex microcanonical entropy in such long-range systems [94].

If the ETH is valid in a system, then in the thermodynamic limit, the EEV of an operator concerning a finite energy density eigenstate, i.e., a bulk eigenstate far from the spectral edges, is equal to the expectation value in the thermal ensemble predicted by statistical mechanics. For example, in a system with only energy conservation, the canonical ensemble prediction $\langle O \rangle_C$ for the operator $O$ in an eigenstate with energy $E_n$ is given by

$$\langle E_n | \, O \, | E_n \rangle = \mathrm{tr}(O\rho_C) = \frac{\mathrm{tr}\big(Oe^{-\beta H}\big)}{\mathrm{tr}\big(e^{-\beta H}\big)}, \tag{1.7}$$

with $\beta$ the canonical temperature associated with $E_n$ via Eq. (1.1). It is often said that in systems where Eq. (1.7) holds, it does so only for 'few-body' or 'local' operators. An illustration of the diagonal statement of ETH is provided in Figure 1.3, wherein we plot the EEVs of a chaotic spin system for two different system lengths. One can observe the fluctuations decreasing with growing system size $L$. In the infinite system size limit, the EEVs should be a smooth function of energy, corresponding to the thermal expectation value ($\langle O \rangle_C$ in Figure 1.3).

If a system obeys the ETH, in that it follows the ansatz Eq. (1.6), then it should thermalize, as one can observe from the long-time average of an observable. To demonstrate, we first denote the time evolution of an observable $O$ as $O(t)$. Expanding in the eigenstate basis

$$O(t) = \langle \psi(t) | \, O \, | \psi(t) \rangle = \sum_n |C_n|^2 O_{nn} + \sum_{m,n} C_m^* C_n O_{mn} e^{i(E_m - E_n)t}. \tag{1.8}$$

Then, assuming a non-degenerate spectrum in a large system, we obtain the

long-time average as

$$\overline{O} = \lim_{T\to\infty} \frac{1}{T} \int_0^T dt O(t) = \sum_n |C_n|^2 O_{nn}. \tag{1.9}$$

We point out that it might take an exceptionally long time for the second term on the right-hand side of Eq. (1.8) to cancel out. Now, assuming the validity of the ETH, Eq. (1.6), and that $|C_n|$ are narrowly distributed for a generic initial state $|\psi_0\rangle$, i.e., $O_{mn} \approx O(E_0)\delta_{mn}$ for states with energy near $E_0 = \langle\psi(0)| H |\psi(0)\rangle$, we can take $O_{nn}$ out of the sum, and obtain

$$\overline{O} \approx O(E_0) \sum_n |C_n|^2 = O(E_0). \tag{1.10}$$

Under the same assumptions on $O_{nn}$, the microcanonical (and hence canonical) ensemble expectation value at $E_0$ is precisely Eq. (1.10). Thus if a system obeys the ETH, it should thermalize. It should be noted that this tells us nothing about the timescale on which thermalization occurs.

It is often considered that if a system thermalizes, it obeys the ETH. This assumes that *all* eigenstates of the system follow the ETH ansatz. It has been conjectured that thermalization is possible, even if there are a small number of exceptional eigenstates that do not obey the ETH [95], however this can restrict certain initial states from thermalizing. This is related to the concept of many-body quantum scars, the name given to a small collection of eigenstates in an otherwise chaotic quantum system that violate the ETH. They are an increasingly studied phenomenon in the field of thermalization [96, 97].

Consider the system Hamiltonian $H$, we can arbitrarily separate the Hamiltonian into (local) spatial regions $A$ and $B$ such that

$$H = H_A + H_B + H_{AB}. \tag{1.11}$$

Here, $H_A$ and $H_B$ are the local Hamiltonians describing $A$ and $B$, and $H_{AB}$ describes the interaction between the two regions. It has been conjectured that

the ETH, particularly Eq. (1.7), holds for the majority of operators within a subsystem $A$, once $V_A \ll V$ [11], i.e., the 'size' of $A$ is much less than the total system. Eq. (1.7) holding for most operators in a subsystem $A$, when the total system size is significantly larger than that of $A$, is equivalent to the statement that the reduced density matrix of an eigenstate should become equivalent to the reduced canonical density matrix in the large size limit,

$$\rho_n^A = \mathrm{tr}_B(|E_n\rangle\langle E_n|) = \rho_C^A = \mathrm{tr}_B(\rho_C). \tag{1.12}$$

Again, $\rho_C$ is the canonical density matrix, and $\beta$ is the canonical temperature associated with $E_n$. Thus, in a sufficiently large system where the ETH is expected to be valid, one could expect the reduced eigenstate density matrix to equal the reduced canonical density matrix. This interpretation is the inspiration behind our eigenstate-based temperatures investigated in Chapter 2.

*Canonical typicality* - An idea closely related to the ETH is that of 'canonical typicality' [69, 70]. Instead of eigenstates, as in the ETH, consider a random pure state $|\psi\rangle$ made up of a superposition of eigenstates from within an energy window $[E \pm \Delta E]$, i.e., $|\psi\rangle = \sum_j c_j |E_j\rangle$, with $E_j \in [E \pm \Delta E]$. Canonical typicality states that for sufficiently large systems, provided the interaction between subsystems $A$ and $B$ can be neglected, i.e., $H \approx H_A + H_B$, the reduced density matrix corresponding to this state, $\rho_\psi^A = \mathrm{tr}_B |\psi\rangle\langle\psi|$, is approximately equal to a reduced microcanonical density matrix. Due to the equivalence of ensembles in the thermodynamic limit, this implies that $\rho_\psi^A$ is equivalent to a reduced canonical density matrix. In essence, the subsystem of a 'typical' pure state can be accurately approximated by a reduced canonical state provided the complement subsystem is sufficiently large (so that it can play the role of the bath).

Unlike the ETH, canonical typicality applies to all (isolated) quantum systems; however, it is a weaker statement. The ETH describes the emergence of thermal ensembles for not just random states but even single eigenstates. As previously discussed, the ETH is generally expected only to hold in chaotic quantum systems. From canonical typicality, one can interpret this restriction as an implication on

the eigenstates of chaotic systems — that they are sufficiently uncorrelated such that they resemble 'typical' states. This interpretation has led to investigations of properties of reduced eigenstate density matrices in chaotic systems [11, 35, 63], including the work in this thesis.

## 1.3 Non-Hermitian phenomena

Stepping away from isolated quantum systems, we move on to open quantum systems. In this section, we first describe phenomena of interest in non-Hermitian quantum systems, including a detailed description of so-called exceptional points, a phenomenon unique to non-Hermitian systems. Following this, we outline our investigation to be carried out in Chapter 4 concerning a particular lattice system under the influence of an imaginary potential.

### 1.3.1 Non-Hermitian physics

In recent years there has been a surge of interest in quantum systems that are described by non-Hermitian Hamiltonians. Although Hermiticity is regarded as a postulate of standard quantum mechanics, non-Hermitian Hamiltonians are useful as effective descriptions of systems where loss or gain plays an important role, such as open quantum systems [98] and optical systems described by wave equations formally analogous to a Schrödinger equation [99–101]. By now, several experimental platforms for the study of non-Hermitian quantum mechanics are available. These include lasers or optical resonators [102–105], coupled optical waveguides [106–110], microwave resonators [111–114] and arrays thereof [115], optical microcavities [99,116,117], optomechanical systems [118], photonic crystals [119, 120], acoustics [121–124] atom-cavity composites [125], exciton-polariton systems in semiconductor microcavities [126,127], and various other arrangements [128–133].

Phenomena of interest in non-Hermitian systems include; localization [134,135] including that induced by the so-called non-Hermitian skin effect (NHSE) [136] producible via asymmetric hopping amplitudes such as in the Hatano-Nelson

model [137], non-Hermitian topological phases [138], and level spacing statistics in complex spectra [139].

### 1.3.2 Exceptional points

Non-Hermitian Hamiltonians lead to various phenomena not present in Hermitian systems. In general, the eigenvalues of non-Hermitian Hamiltonians are complex. In addition, the left and right eigenstates of a non-Hermitian Hamiltonian are generally not equal, but together they form a biorthogonal basis. In this thesis, we shall confine our discussion to the right eigenstates of non-Hermitian Hamiltonians. The eigenstates are generally not mutually orthogonal, in contrast to those of a Hermitian matrix. This non-orthogonality becomes extreme at points in the parameter space referred to as *exceptional points* [140–144].

At an exceptional point, a collection of (or all) eigenvalues appears to be degenerate. However, it is not a genuine degeneracy as the corresponding eigenvectors coalesce as well, in that they become linearly dependent. This results in the eigenstates no longer providing a basis spanning the entire Hilbert space. Therefore, the Hamiltonian matrix is non-diagonalizable and is denoted a defective matrix [145, 146] at these exceptional points. We note that a Hermitian matrix cannot have an exceptional point, as Hermitian matrices are always diagonalizable. The spectrum of a non-Hermitian Hamiltonian exhibiting an exceptional point will have a so-called 'square-root branch point' bridging the coalescing eigenvalues. This is due to the characteristic polynomial of the Hamiltonian containing terms of the form $\sqrt{\gamma - \gamma_c}$, with $\gamma$ some tunable (complex) parameter of the Hamiltonian, and $\gamma_c$ the parameter corresponding to the exceptional point. For a second-order exceptional point, one can consider having two connected Riemann sheets representing the two coalescing levels in the $\gamma$ plane. The two sheets are connected at the value $\gamma_c$ (branch point) [144].

The surviving eigenstate, following the coalescence of two (or more) eigenstates, at an exceptional point is always chiral [147]; this chirality has been observed experimentally [104, 105, 113, 127, 148]. Other phenomena associated with

exceptional points include loss-induced transparency [106], unidirectional transmission [123, 129, 130], lasers with non-monotonic pump-dependence [102], and enhanced sensing [149–151]. Exceptional points are also associated with the real-to-complex spectral transition for parity-time ($\mathcal{PT}$) symmetric Hamiltonians [144] (See Section 4.4).

### 1.3.3 Non-Hermitian scattering

In Chapter 4 of this thesis, we are primarily concerned with the non-Hermitian physics of a quantum particle on a tight-binding lattice. Previous studies of non-Hermitian effects for a lattice particle include Anderson localization [137, 152–154] and localization in quasiperiodic potentials [155, 156], invisibility (reflectionless scattering) due to non-Hermitian hopping [157] or an oscillating imaginary scatterer [158], flat-band physics [159], Bloch oscillations [160], and $\mathcal{PT}$-symmetry obtained by combining an absorbing potential on one site with an emitting potential on another [161–167], which we shall also consider in Chapter 4. In addition, non-Hermitian tight-binding lattices form the basis of the study of non-Hermitian topological many-body systems, a topic of rapidly growing interest [168–170]. A few studies have also addressed *interacting* many-body systems in non-Hermitian lattice systems [171, 172].

We will consider an imaginary potential on a single lattice site, acting as an absorbing (or dissipative) scattering potential. This can be regarded as a lattice analog of a purely imaginary delta-function scattering potential in the continuum. An imaginary scattering potential is linked to measurement [173–175], and is thus related to quantum first-passage time problems and the quantum Zeno effect [176–183]. The quantum Zeno effect is essentially the cessation of dynamics of a quantum state due to the measurement being performed too frequently [176]. In analogy to the quantum Zeno effect, it is then expected that an imaginary potential will have suppressed absorption when the strength of the potential is large. This suggests that the absorption might be non-monotonic as a function of the strength of the dissipative potential. In Chapter 4, we explicitly show the

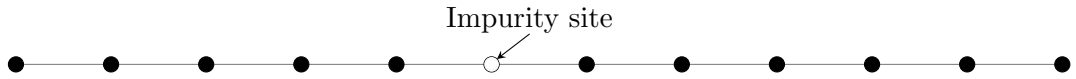


Figure 1.4: Illustration of a lattice: The impurity is placed at one of the center lattice sites, as shown here for $L = 12$. In this case, it could equivalently be placed on the seventh instead of the sixth site. For odd $L$, there is a definite central site.

non-monotonic dependence of the amount of absorption on the potential strength, in the context of a simple lattice model.

The model we shall investigate is the tight-binding lattice model (Eq. (1.22) in the following section), which describes particles hopping along an open boundary 1D chain with $L$ sites. We introduce a purely imaginary negative potential on a single site $q$ with strength $\gamma$, rendering the system non-Hermitian. As the potential is negative and purely imaginary, it can be considered an absorbing potential, i.e., dissipative. As we want to study reflection and transmission, it is convenient to place the potential at the center of the lattice at either site $\left\lfloor \frac{L}{2} \right\rfloor$ or $\left\lfloor \frac{L}{2} \right\rfloor + 1$. An example of such a setup is illustrated in Figure 1.4.

In Chapter 4, we present a study of the dynamics and eigenspectrum of the system described (Eq. (1.25) below). By scattering wavepackets numerically off the dissipative impurity, we show how the reflection, transmission, and absorption fractions depend on the strength $\gamma$ of the impurity. These results are compared with the continuum problem, a variant of the standard textbook problem of quantum scattering off a Hermitian delta-function potential. In both cases, the absorption coefficient is found to be a non-monotonic function of $\gamma$, having a maximum at a point that depends on the momentum of the incident particle or wavepacket. In addition, we present the spectrum of the Hamiltonian, which shows a peculiar exceptional point at $\gamma = 2$ at which all (or nearly all, depending on $L$) of the eigenvalues pair up. We can analytically prove the existence of this exceptional point. The absorption coefficient is non-monotonic and has a maximum near, but not necessarily at, the exceptional point.

At large $\gamma$, the absorption is vanishingly small, exhibiting the quantum Zeno effect, and the system behaves as if the impurity were a real potential $V$. In particular, the system has an (anti-)bound eigenstate, which allows us to draw a

correspondence between values of $\gamma$ and $V$. The localized eigenstate is purely a lattice phenomenon with no analog in the continuum.

We also consider the spectrum of a $\mathcal{PT}$-symmetric version of our system. Using the same analytical methodology, we can prove the existence of exceptional points similar to those found in the purely dissipative model. To build towards a many-body understanding, we consider many quantum particles in the purely dissipative system described. From our knowledge of exceptional points in the single particle model, we can argue the existence of exceptional points in the non-interacting case.

## 1.4 Quantum systems under investigation

Throughout this thesis, we investigate various quantum spin-1/2 lattice systems consisting of $L$ spins, of which $N$ are up. In this section, we outline the specific systems used in these investigations. We first introduce the many-body quantum systems used to explore various temperature definitions in Chapters 2 and 3. Following this, we introduce the tight-binding lattice, and the non-Hermitian models that are used in Chapter 4. Additionally, we describe level-spacing statistics, often used to characterize a many-body quantum system as thermalizing.

### 1.4.1 Many-body systems

Chapters 2 and 3 focus on temperature definitions in thermalizing systems. In this subsection, we present the various quantum systems used to explore these temperature definitions, constructed such that they should generally thermalize. We start by introducing the well-known anisotropic Heisenberg chain, often referred to as the $XXZ$ chain. While we only utilize the unaltered $XXZ$ chain once in this thesis, we study multiple chaotic models based on the $XXZ$ chain. In what follows, we describe the various chaotic systems obtained by introducing magnetic fields to the $XXZ$ model or by changing the geometry from a simple chain. Following this, we briefly introduce the quantum Ising chain and include magnetic fields to produce a chaotic quantum system.

### The XXZ chain

The open-boundary $XXZ$ chain Hamiltonian is given by

$$H_H \;=\; J\sum_{j=1}^{L-1}(S_j^x S_{j+1}^x + S_j^y S_{j+1}^y) + \Delta\sum_{j=1}^{L-1} S_j^z S_{j+1}^z, \tag{1.13}$$

with $J$ the site-to-site 'hopping' strength, and $\Delta$ the spin-spin interaction strength (anisotropy). $S_j^{(x,y,z)} = \hbar\sigma_j^{(x,y,z)}/2$ are the spin operators on site $j$ in three directions, with $\sigma_j^{(x,y,z)}$ being the Pauli matrices. We shall set $\hbar = 1$ throughout this thesis. $\Delta = J$ is the isotropic point, which also separates the $\Delta < J$ gapless and $\Delta > J$ gapped regimes. The ground state of the system is dependent on the value of $\Delta$; it can be anti-ferromagnetic ($\Delta > 1$), ferromagnetic ($\Delta \leq -1$), or paramagnetic ($-1 < \Delta \leq 1$)). The $XXZ$ chain is exactly solvable via the Bethe ansatz [184] and is thus known to be an integrable model. The $XXZ$ chain describes the couplings between nearest-neighboring spins. When we refer to $XXZ$-like couplings, we mean that the terms are of the form of those in Eq. (1.13), but need not be nearest-neighbor, i.e., they may be between any two spins on sites $j, k$.

Using the spin raising and lowering operators $S_j^{\pm} = S_j^x \pm iS_j^y$, we can rewrite the $XXZ$ chain as

$$H_H \;=\; \frac{J}{2}\sum_{j=1}^{L-1}(S_j^+ S_{j+1}^- + S_j^- S_{j+1}^+) + \Delta\sum_{j=1}^{L-1} S_j^z S_{j+1}^z. \tag{1.14}$$

In this notation, it is clear that the $XXZ$ chain describes spin excitations moving along a lattice by exchanging the neighboring spins of opposite orientation, with strength $J/2$. In addition, the spins interact via an Ising interaction with strength $\Delta$. The $XXZ$ chain has a $U(1)$ symmetry, conserving $N$, or equivalently total spin $S^z = \sum_{j=1}^{L} S_j^z$. Thus the Hilbert space dimension is $D = \binom{L}{N}$ when $N$ is conserved. If $N$ is not conserved, e.g., when $S^x$ (or $S^y$) fields are introduced, the Hilbert space dimension is instead $D = 2^L$. The $XXZ$ chain harbors various symmetries depending on the chosen parameters and boundary conditions, but generally it possesses reflection symmetry (parity), translational symmetry, spin

rotation symmetry, and a $U(1)$ symmetry characterized by the total spin in the $z$-direction.

Below, we outline the various non-integrable models to be used in the temperature investigations in Chapters 2 and 3 of this thesis.

### Staggered field model

Starting with the $XXZ$ chain, Eq. (1.13), we introduce transverse ($S^x$) and longitudinal ($S^z$) magnetic fields staggered along the even and odd sites of the chain, respectively. In addition, we break the staggered pattern at the start of the chain by inserting $x$ and $z$ fields on the first and second sites respectively to remove any symmetries. We refer to this model as the staggered field model, whose Hamiltonian is given by

$$\begin{aligned} H_S = &\sum_{j=1}^{L-1} \left( S_j^x S_{j+1}^x + S_j^y S_{j+1}^y + \Delta S_j^z S_{j+1}^z \right) \\ &+ \sum_{\text{even}} h_x S_j^x + \sum_{\text{odd}} h_z S_j^z + h_x S_1^x + h_z S_2^z. \end{aligned} \tag{1.15}$$

We use the values $h_z = h_x = 0.5$, unless otherwise stated, to ensure chaotic level spacing statistics such that the system should generally thermalize. We note that the total $S^z$ spin is not conserved in this model.

### Disordered field model

Again, starting with the $XXZ$ chain, Eq. (1.13), we introduce 'disordered' transverse and longitudinal magnetic fields on every site. Here, rather than uniform $h_z$ and $h_x$ values across the chain, the on-site strengths $h_j$, $h'_j$, are chosen from a uniform distribution $[-W, W]$. This model with only longitudinal fields is the archetypal model for many-body localization [87]. For non-zero $W$, below some critical value in finite systems, the model is known to exhibit chaotic behavior. We will refer to this model as the disordered field model, whose Hamiltonian is

given by

$$H_D = \sum_{j=1}^{L-1} \left( S_j^x S_{j+1}^x + S_j^y S_{j+1}^y + \Delta S_j^z S_{j+1}^z \right) + \sum_{j=1}^{L} (h_j S_j^z + h'_j S_j^x). \tag{1.16}$$

We use the value $W = 0.25$ to ensure chaotic level spacing statistics and to stay far from any possible localized regime in the finite systems under investigation. We again note that the total $S^z$ spin is not conserved in this model.

**Square lattice**

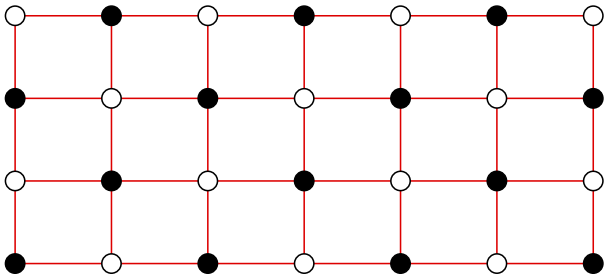

Figure 1.5: $7 \times 4$ Square Lattice geometry.

Moving away from 1D chains, we introduce a two-dimensional square lattice with open boundary conditions and $XXZ$-like couplings between neighboring spins on the lattice. The lattice geometry is illustrated by Figure 1.5. We refer to this model simply as the square lattice model, whose Hamiltonian is given by

$$H_{\text{SQ}} = \sum_{\langle j,k \rangle} J_{jk}(S_j^x S_k^x + S_j^y S_k^y) + \Delta_{jk} S_j^z S_k^z. \tag{1.17}$$

Here, $\langle j, k \rangle$ means that we restrict the summation to nearest-neighbor pairs. We take $J_{jk}, \Delta_{jk}$ to be real to ensure Hermiticity, and for simplicity we set $J_{jk} = J_{kj}$ and $\Delta_{jk} = \Delta_{kj}$. To remove any symmetries and ensure chaotic level spacing statistics, we draw the values $J_{jk}$, $\Delta_{jk}$ from the uniform distributions $[0, 2]$ and $[0, 1]$ respectively. Due to the absence of $S^x$ fields, the total $S^z$ spin is conserved.

In Chapter 2, to break total $S^z$ conservation, we introduce transverse magnetic fields ($S^x$) to the sites $j_a$ in one of the sub-lattices available within the bipartite lattice, i.e., to either the white or black lattice sites in Figure 1.5. We observed

that chaotic level spacing statistics were only obtained with the addition of longitudinal magnetic fields; hence, we include $S^z$ fields on the remaining $j_b$ sites in the alternate sub-lattice. The Hamiltonian for the non-spin conserving square lattice with $S^z$ and $S^x$ fields staggered on the sub-lattices is given by

$$H_{NS} = \sum_{\langle j,k \rangle} \left[ J_{jk} \left( S_j^x S_k^x + S_j^y S_k^y \right) + \Delta_{jk} S_j^z S_k^z \right] + \sum_{j_a} h_x S_{j_a}^x + \sum_{j_b} h_z S_{j_b}^z. \quad (1.18)$$

For the non-spin conserving model, we choose: $J_{jk}$, $\Delta_{jk}$ from the uniform distributions $[0, 1]$ and $[0, .9]$ respectively, and the magnetic field strength to be $h_z = h_x = 0.1$, unless otherwise stated.

### Fully connected lattice

Going beyond nearest-neighbor interactions, we consider a fully connected network of spins akin to a complete graph. In this setup, each spin $j$ is connected to every other spin $k$ via $XXZ$-like couplings, so the Hamiltonian is constructed of terms of an arbitrary range . We will refer to this model as the fully connected lattice, whose Hamiltonian is given by

$$H_{\text{FC}} = \sum_j \sum_{k \neq j} J_{jk} (S_j^x S_k^x + S_j^y S_k^y) + \Delta_{jk} S_j^z S_k^z. \quad (1.19)$$

Again, $J_{jk} = J_{kj}$ and $\Delta_{jk} = \Delta_{kj}$. To remove any symmetries and ensure chaotic level spacing statistics, we draw the values $J_{jk}$, $\Delta_{jk}$ from the uniform distributions $[-0.4, 0.4]$ and $[-0.1, 0.1]$, respectively. We note again that the total $S^z$ spin is conserved.

### Chaotic Ising model

The open-boundary 1D quantum Ising chain in the absence of magnetic fields is given by

$$H_I = \Delta \sum_{j=1}^{L-1} S_j^z S_{j+1}^z. \quad (1.20)$$

One can interpret this Hamiltonian as the $J/\Delta \to 0$ limit of the $XXZ$ chain in Eq. (1.13). This model is exactly solvable and is symmetric under a flip of every spin. The model also posses reflection and translation symmetries, in addition to a $U(1)$ symmetry characterized by its total $S^z$ spin. For $\Delta < 0$ ($\Delta > 0$), the model is classified as (anti-)ferromagnetic. To obtain a non-integrable model, we shall introduce magnetic fields along the entire chain in both the longitudinal ($S^z$) and transverse ($S^x$) directions, with strengths $h_z$ and $h_x$, respectively. These fields also break the spin-flip symmetry. The model with only a transverse field is commonly investigated; an exact solution is also known in this case. This case exhibits a quantum phase transition (at zero temperature), with critical point $\Delta = h_x$. The model with magnetic fields in both directions does not have an exact solution. To remove any possible remaining symmetries of the model, we swap the $x$ and $z$ field strength between the first two sites. We will refer to this model as the chaotic Ising model, whose Hamiltonian is given by

$$H_{CI} = \sum_{j=1}^{L-1} S_j^z S_{j+1}^z + \sum_{j=1}^{L} (h_x(1-\delta_{j,1})S_j^x + h_z(1-\delta_{j,2})S_j^z) + h_z S_1^x + h_x S_2^z. \tag{1.21}$$

Here, we have chosen $\Delta = 1$, as will be assumed for all uses of the Ising model in this thesis. In addition, we will generally use the values $h_z = 0.5$, $h_x = 0.75$, unless otherwise stated, to ensure chaotic level spacing statistics. We note that the total $S^z$ spin is not conserved in this model.

### 1.4.2 Non-Hermitian models

Here, we first introduce the standard tight-binding model. Following this, we present the non-Hermitian system that is the primary focus of our investigation in Chapter 4 — a tight-binding lattice under the influence of a purely imaginary local potential.

### Tight-binding model

The tight-binding lattice model is used to describe particles hopping along a lattice. Many models have tight-binding terms within them, such as the $XXZ$ chain (Eq. (1.14)), or the Hubbard model [185], and the many variants based on these models. In the second quantization language, the tight-binding Hamiltonian for spinless fermions with open boundaries is given as

$$H_T \;=\; t\sum_{j}^{L-1}(c_j^\dagger c_{j+1} + c_j c_{j+1}^\dagger). \tag{1.22}$$

Here, $c_j^\dagger$ and $c_j$ create and annihilate a particle on-site $j$ respectively, and $t$ is the site-to-site hopping strength. This open boundary chain of free-fermions (free from interactions) can be diagonalized by transforming the operators $c_j^\dagger$, $c_j$. A similar process can be carried out for the periodic chain.

This model can be mapped to a spin system via a Jordan-Wigner transformation [186], resulting in the Hamiltonian in spin language (with $t = J/2$)

$$H_T = \frac{J}{2}\sum_{j}^{L-1}(S_j^+ S_{j+1}^- + S_j^- S_{j+1}^+). \tag{1.23}$$

This is precisely the non-interacting ($\Delta \to 0$) limit of the $XXZ$ chain (Eq. (1.14)), i.e., the $XX$ chain (or $XY$ model with equal coefficients in the $x$ and $y$ directions). In this language, the analog of a particle excitation is a spin-up.

### Imaginary potential

In Chapter 4, we use the tight-binding lattice as the basis for our non-Hermitian system. Hermiticity is broken by introducing a purely imaginary potential to the lattice. In general, the Hamiltonian for such a system with an imaginary potential of strength $\gamma$ on-site $q$ is given in spin language via

$$H_{MB} = \frac{J}{2}\sum_{j}^{L-1}(S_j^+ S_{j+1}^- + S_j^- S_{j+1}^+) \pm i\gamma(S_q^z + \frac{1}{2}). \tag{1.24}$$

The sign in front of $\gamma$ (taking $\gamma > 0$) determines if the potential is absorbing or enhancing. The magnetic field term is shifted by 1/2, stemming from the Jordan-Wigner transformation of the on-site potential $n_j = c_j^\dagger c_j = S_j^z + 1/2$.

Our primary focus in Chapter 4 is a single quantum particle (i.e., single spin-up) in such a system. Thus is it helpful to write the Hamiltonian with an absorbing potential in terms of site occupations

$$H \;=\; -J\sum_{j=1}^{L-1}\Big(\,|j\rangle\,\langle j+1| + |j+1\rangle\,\langle j|\,\Big) - i\gamma\,|q\rangle\,\langle q|\,, \tag{1.25}$$

with $1 \le q \le L$. Here we shall focus on the case $\gamma > 0$ so that the imaginary potential is absorbing. The labels for the bras and kets here are site labels: The particle lives on an $L$-site chain with open boundary conditions. In Chapter 4, we provide an in-depth investigation of this non-Hermitian model, exploring features of its complex spectrum and analyzing the scattering dynamics of a wavepacket.

### Interacting model

In Chapter 4, we shall also consider an interacting version of Eq. (1.24). We allow nearest neighboring particles to interact via $n_j n_{j+1} = (c_j^\dagger c_j)(c_{j+1}^\dagger c_{j+1})$. Mapping this to a spin system, we obtain the interacting non-Hermitian Hamiltonian

$$\begin{aligned} H_q = \frac{J}{2}\sum_{j}^{L-1}(S_j^+ S_{j+1}^- + S_j^- S_{j+1}^+) - i\gamma(S_q^z + \frac{1}{2}) \\ +\Delta\sum_{j}^{L-1}(S_j^z + 1/2)(S_{j+1}^z + 1/2). \end{aligned} \tag{1.26}$$

Without the impurity, this spin model appears almost identical to the $XXZ$ chain (Eq. (1.14)); the Jordan-Wigner mapping $n_j = S_j^z + 1/2$ introduces additional 1/2 terms. In Section 4.5.2, we explore the fate of certain spectral phenomena, observed in the single particle and non-interacting many-body systems, in this interacting system.

### 1.4.3 Level spacing statistics

In Chapters 2 and 3 we explore temperature definitions in the context of thermalization in many-body quantum systems. Thermalization, as discussed in Section 1.2, is expected in chaotic many-body systems; thus, we need to ensure the models we have outlined above are chaotic.

Quantum chaos is often characterized by investigating the distribution of energy level spacings of the Hamiltonian. The energy levels in an integrable system are uncorrelated and can cross each other. This is in contrast to a chaotic system, where energy levels experience level repulsion and thus are highly correlated. This level repulsion, or lack of it, is an indicator of quantum chaos, and as such, exact measures based on this phenomenon have been developed [187].

Consider a system with an ordered set of energy levels $E_n$; one can define the consecutive level spacings as

$$s_n = E_{n+1} - E_n. \tag{1.27}$$

The probability distribution of this quantity, $P(s)$, can be used to classify a system as chaotic. It has been conjectured that level spacings of integrable systems follow a Poisson distribution [188], i.e., $P(s) \propto e^{-s}$. In contrast, the level spacings of a chaotic system are expected to follow a so-called Wigner-Dyson distribution, $P(s) \propto s^{\alpha} e^{-b_\alpha s^2}$, with $b_\alpha$ a constant. Depending on whether the Hamiltonian of the system is real symmetric, complex Hermitian, or quaternionic Hermitian, $\alpha$ is either 1,2, or 4, respectively. This classification of Hamiltonians corresponds to the three classical ensembles of random matrix theory (RMT). The three ensembles, the Gaussian Orthogonal Ensemble (GOE), Gaussian Unitary Ensemble (GUE), and Gaussian Symplectic Ensemble (GSE), are composed of Hermitian matrices whose entries are independently distributed as real, complex, or quaternionic random variables, respectively [189, 190].

The universality of RMT means that these random matrix ensembles describe the energy levels of physical systems at the statistical level. However, direct

comparison with the distributions of the random matrix ensembles is only possible in a local energy window with the mean level spacing set to unity.

The level spacing distribution $P(s)$ is an effective measure of chaos, but it does have its downfalls. Many systems have a non-uniform energy density, resulting in the spectrum needing to be 'unfolded'. Here, unfolding is a transformation that ensures the mean level density is indeed unity [15, 38, 187, 191–194]. In addition, one needs to be careful to account for any symmetries present in the Hamiltonian of the system. For example, the $XXZ$ chain, Eq. (1.13), conserves total $S^z$. This means the Hilbert space of the Hamiltonian can be broken into sectors with different $S^z$ values. One should thus take statistics in a particular sector. If we took statistics from across sectors, the statistics could appear to be those of an integrable system, as there is no level repulsion between levels in different symmetry sectors [10].

While the unfolding procedure can circumvent issues in analyzing $P(s)$, it can be a non-trivial task to execute and often require approximations. In order to avoid these issues, Oganesyan and Huse [195] proposed another quantity, the consecutive level spacing ratio,

$$r_n = \frac{\min(s_{n+1}, s_n)}{\max(s_{n+1}, s_n)}. \tag{1.28}$$

The benefit of $r_n$ is that it does not require the use of unfolding, as the ratio of consecutive level spacings is independent of the local density of states. Thus the distribution $P(r)$ can be preferential to study over $P(s)$.

Analytical predictions for the three RMT ensembles have been derived for the distribution $P(r)$ [196]. From these predictions, the simple indicator of the mean value of the ratio, $\langle r \rangle$, has become a prevalent indicator of chaos. In integrable systems with Poisson-like level spacing distributions, $\langle r \rangle = 2 \ln 2 \approx 0.38629$. In contrast, for chaotic systems with level spacing statistics expected to follow GOE-like level spacing statistics (i.e., the Hamiltonian is real symmetric), $\langle r \rangle = 4 - 2\sqrt{3} \approx 0.53590$. Throughout this thesis, when we require that a system be chaotic such that we expect it to thermalize, we will ensure its level spacing

statistics align with these predictions. In Figure 1.6, we present both the level spacing distribution $P(s)$ and the mean ratio $\langle r \rangle$, for each many-body quantum system detailed in Section 1.4, except for the non-Hermitian model, on account of its complex spectrum. We note that complex level spacing statistics are also used in non-Hermitian settings, where similar RMT predictions have been derived [139].

There are other indicators used to characterize quantum chaos (or lack thereof),

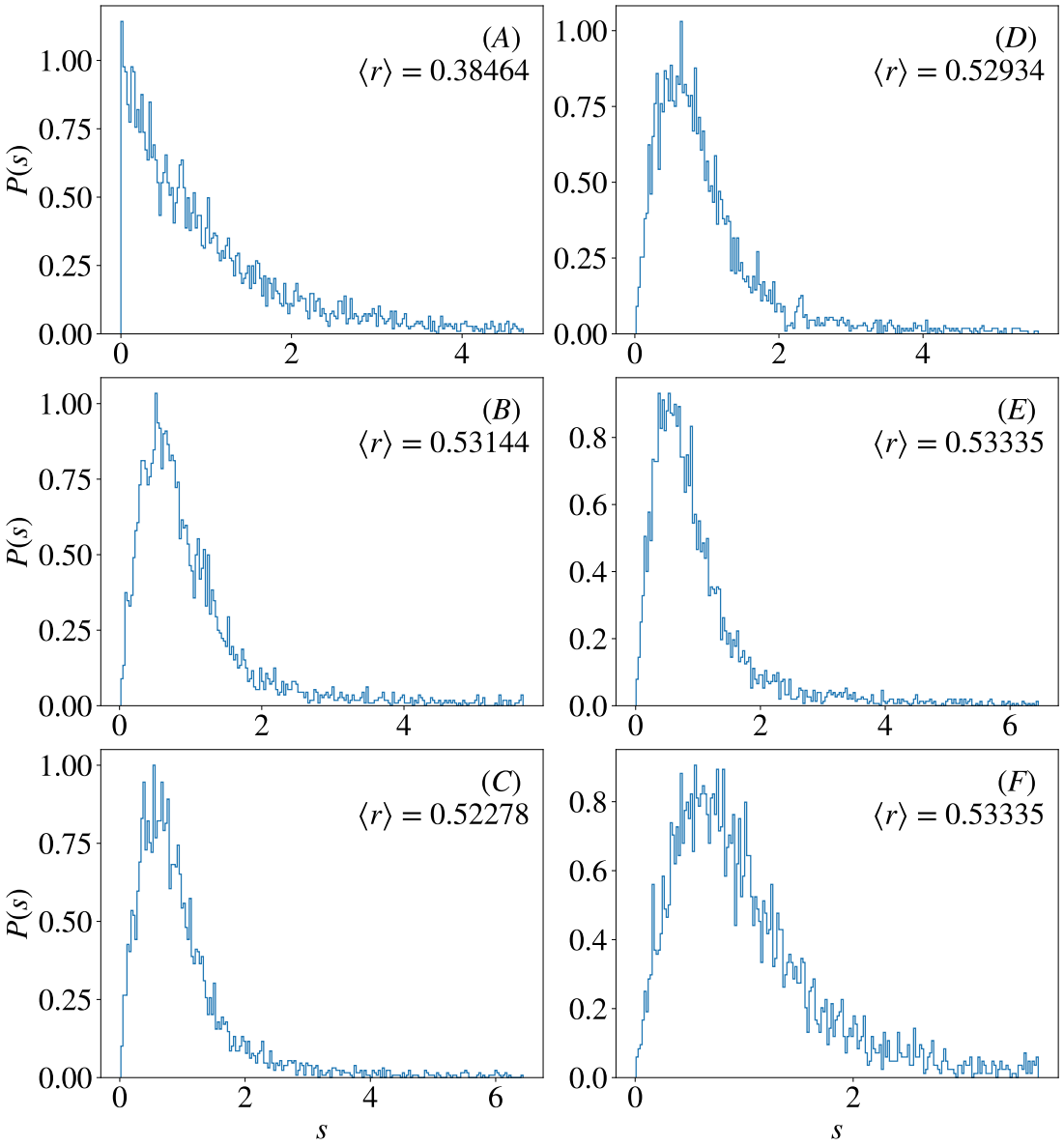


Figure 1.6: Normalized level spacing statistics ($s = s/\langle s \rangle$) for models: **(A)** $XXZ$ chain with $L = 20$ and $N = 4$, $J = 1$, $\Delta = 0.95$, Eq. (1.14). **(B)** Staggered field model with $L = 12$ and $h_z = h_x = 0.5$, $J = 1$, $\Delta = 0.95$, Eq. (1.15). **(C)** Disordered field model with $J = 1$, $\Delta = 0.95$, $L = 12$ and $W = 0.25$, Eq. (1.16). **(D)** Chaotic Ising model with $L = 12$, $h_z = 0.5$ and $h_x = 0.5$, Eq. (1.21). **(E)** Square lattice model with $J_{jk} \in [0, 2]$, $\Delta_{jk} \in [0, 1]$, $4 \times 5$ lattice ($L = 20$) and $N = 4$, Eq. (1.17). **(F)** Fully connected lattice model with $J_{jk} \in [-.4, .4]$, $\Delta_{jk} \in [-.1, .1]$, $L = 16$ and $N = 5$, Eq. (1.19).

such as spectral form factors [197], the fidelity susceptibility [93], and the adiabatic gauge potential norm [198].

The entanglement entropy of bulk eigenstates, i.e., those that are highly excited, is also emerging as an indicator of quantum chaos. The eigenstate entanglement entropy is the Von Neumann entropy of the eigenstate density matrix reduced to a local subsystem.

In ergodic systems (chaotic), bulk eigenstates are all strongly entangled and result in an entanglement entropy that scales with the volume of the subsystem (volume law). In contrast, bulk eigenstates of non-ergodic systems do not *all* follow this volume law; a large number of the states generally scale with the size of the boundary of the subsystem (area law) [199].

## 1.5 Overview

This thesis is organized as follows:

In Chapter 2, we investigate the eigenstate-based definitions of temperature, introduced in Section 1.1.1, in the context of chaotic many-body quantum systems. We start by providing some preliminary information necessary for the investigation. We then present our results for the eigenstate and subsystem temperatures in Sections 2.2 and 2.3 respectively. In each case, we compare the resultant temperature to the canonical temperature. Following this, we outline some alternative choices that could have been made in the formulation of the temperature definitions (Section 2.4) and examine the subsystem temperature in a system approaching the integrable limit (Section 2.5).

In Chapter 3, we explore various ways to calculate the microcanonical entropy in isolated quantum systems. We describe, in detail, the four procedures to calculate entropy introduced in Section 1.1.2 and derive a temperature in each case. First, Section 3.2.1 describes counting eigenstates in a constant-width energy window $\Delta E$. Second, Section 3.2.2 describes counting eigenstates in an energy-dependent $\Delta E$ designed to cancel out the explicit $\Delta E$-dependence of the resultant temperature, following/extending the suggestion of Ref. [54]. Section

3.3 outlines using a smoothed cumulative density of states, $\Omega(E)$, to calculate the density of states, $g(E)$. We first choose to avoid explicitly selecting an energy width $\Delta E$. Finally, we use the energy-dependent $\Delta E$ alongside the integrated density of states formulation. In each case, numerical results are presented for various many-body quantum systems and we compare the derived temperature to the canonical temperature.

In Chapter 4, we investigate the scattering dynamics and spectrum of a quantum particle on a tight-binding lattice subject to a non-Hermitian local potential. We first present the scattering results and make comparisons to the continuum case in Section 4.1. Following this we discuss the spectrum and the appearance of exceptional points in Section 4.2. Then we investigate the system at large potential strengths, and draw a comparison between real and imaginary potentials via their bound states. We present an alternative setup that is $\mathcal{PT}$-symmetric, and discuss its spectrum in Section 4.4. Finally, in Section 4.5 we begin building a many-body description of the system, by constructing an understanding of the non-interacting many-body system out of the single particle case.

Finally, in Chapter 5, we summarize the results of each chapter.

The contents of this thesis are largely based on the following publications by the author of this thesis:

> [200] P. C. Burke, G. Nakerst, and M. Haque, "Assigning temperatures to eigenstates," *Physical Review E*, 107:024102, February 2023.
>
> [201] P. C. Burke and M. Haque, "Entropy and temperature in finite isolated quantum systems," *Physical Review E*, 107:034125, March 2023.
>
> [202] P. C. Burke, J. Wiersig, and M. Haque, "Non-Hermitian scattering on a tight-binding lattice," *Physical Review A*, 102:012212, July 2020.

Chapters 2 and 3 are largely based on [200, 201] respectively — some changes to the presentation have been made. Chapter 4 is largely based on [202]. Sections 4.4 and 4.5 are new results that compliment those of the published work.

# Chapter 2

# Temperature from eigenstate information

In this chapter, we investigate temperature definitions based on the idea that information relating to thermalization is encoded in the eigenstates of chaotic quantum systems, as posited by the ETH. In particular, we will investigate the eigenstate and subsystem temperatures defined in the introduction (Section 1.1). We first provide some preliminary details in Section 2.1, starting with defining an appropriate distance measure for density matrices, as will be necessary for our distance-based temperatures. Then we discuss the chaotic many-body systems we will investigate, outlining how we spatially divide the system into subsystems when required. Following this, we then present our results for the eigenstate and subsystem temperatures in Sections 2.2 and 2.3 respectively. In Section 2.4 we outline alternative choices that could have been made in our investigations. Then, in Section 2.5 we investigate the deviation of the subsystem temperature from the canonical temperature, as a system approaches integrability. Finally, in Section 2.6 we summarize the chapter and discuss the relation of our findings to existing work. The majority of the results in this chapter are published in Ref. [200]. Some additional figures and discussions have been added.

## 2.1 Preliminaries

In this section, we first define an appropriate distance measure between density matrices. This distance measure is to be used in our temperature definitions. Following this, we outline the many-body quantum systems used in our numerical calculations; in particular, we discuss the geometry of the lattice subsystems.

### 2.1.1 Distance measures

To quantify the distance between two density matrices, we use the Schatten $p$-distance, the $p$-norm of the difference between the two normalized matrices:

$$d_p(\rho,\sigma) = \left\| \frac{\rho}{\|\rho\|_p} - \frac{\sigma}{\|\sigma\|_p} \right\|_p, \tag{2.1}$$

with the Schatten $p$-norm given by

$$\|A\|_p = \mathrm{tr}(|A|^p)^{1/p} = (\sum_n |s_n|^p)^{1/p}, \tag{2.2}$$

for a Hermitian matrix $A$ and $1 \leq p < \infty$. Here $s_n$ are the singular values of $A$, and $|A| = \sqrt{A^\dagger A}$. This class of distances includes commonly used measures of distance between density matrices, such as the trace distance ($p = 1$) [203, 204] and the Hilbert-Schmidt (or Frobenius) distance ($p = 2$) [205–219]. The range of $d_p$ is $[0, 2]$.

The main results in this chapter are based on the Schatten $p$-distances. In Section 2.4.1 we will examine briefly how our results are affected if the Bures distance [203, 204] is used instead.

### 2.1.2 Many-body systems

To confirm that the results we present here hold in general for chaotic (thermalizing) many-body Hamiltonians with local interactions, we will provide numerical results for three different 1D and one 2D, non-spin-conserving, chaotic models. These models are the staggered field model (Eq. (1.15)), the chaotic Ising model

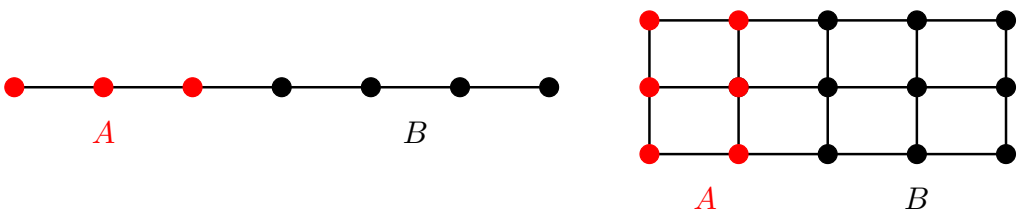


Figure 2.1: Illustration of subsystems for a spin chain and a square lattice. For the square lattice, we show the choice of taking $L_A$ sites column-wise.

(Eq. (1.21)), the disordered field model (Eq. (1.16)), and the square lattice with the addition of transverse and longitudinal magnetic fields (Eq. (1.18)), all of which are detailed in Section 1.4 of the introduction. For all systems, we consider a lattice consisting of $L$ spin-$\frac{1}{2}$ objects with open boundary conditions.

For 1D systems, the subsystem $A$ is taken to be the leftmost $L_A$ sites of the $L$-site chain, with $B$ being the remaining $L_B = L - L_A$ sites. In the 2D square lattice, the subsystem $A$ is taken to be the first $L_A$ consecutive sites, starting from a corner of the lattice and following either a row or column. $B$ again consists of the remaining $L_B$ sites. When this 2D model is used, illustrations of the lattice geometry are provided in order to avoid confusion. In Figure 2.1 we illustrate examples of subsystems in a chain and square lattice. For simplicity, we choose systems whose underlying Hilbert space $\mathcal{H}$ has a tensor product structure $\mathcal{H} = \mathcal{H}_A \otimes \mathcal{H}_B$. This is the case for spin and fermionic systems, where total spin and particle number respectively are not conserved. Then the full Hamiltonian can be written as $H = H_A \otimes \mathbb{1}_{D_B} + \mathbb{1}_{D_A} \otimes H_B + H_{AB}$, where $H_A$ and $H_B$ only act on $A$ and $B$ respectively, and $H_{AB}$ is the interaction between the two. The Hilbert space dimensions of $A$, $B$ and the total system are $D_A$, $D_B$ and $D = D_A D_B$ respectively.

## 2.2 Eigenstate temperature

In this section, we discuss the eigenstate temperature, which we have defined as the temperature that minimizes the distance between the eigenstate density

matrix $\rho$, and the canonical density matrix $\rho_C$,

$$\beta_E = \underset{\beta}{\operatorname{argmin}}\, d_p\left(\rho, \rho_C\right). \tag{2.3}$$

We first present analytical results that are general to all Hermitian systems. In addition, we provide numerical results that illustrate these analytical findings. Following this, we consider a variation of the eigenstate temperature. In particular, we consider a density matrix consisting of an equally weighted sum of eigenstates from a finite energy window, i.e., a microcanonical density matrix. Finally, we provide the full derivation of the analytical results presented.

### 2.2.1 Main results

In order to determine the value of $\beta_E$, Eq. (2.3), analytically, we express the two density matrices in the basis for which they are simultaneously diagonalized, namely the eigenstate basis, and set to zero the derivative of $d_p(\rho, \rho_C)$ with respect to $\beta$. The full derivation of the minimum can be found in subsection 2.2.3, the main result of which is that the minimum is precisely when

$$E_n = \frac{\operatorname{tr}\left(He^{-p\beta H}\right)}{\operatorname{tr}(e^{-p\beta H})}. \tag{2.4}$$

Thus, comparing this result with the definition of the canonical temperature, Eq.(1.1), we determine

$$\beta_E = \frac{\beta_C}{p}. \tag{2.5}$$

Thus, the eigenstate and canonical temperatures coincide for $p = 1$, while they differ by a factor of $p$ for $p > 1$. This result is purely mathematical and holds for an arbitrary Hermitian matrix $H$, irrespective of whether $H$ has the interpretation of a many-body Hamiltonian, e.g., even for a random matrix — see results in subsection 2.2.4.

Figure 2.2 illustrates the relation $\beta_C = p\beta_E$ in (A), and the behavior of the distance $d_p$ in (B,C), for the staggered field $XXZ$ chain.

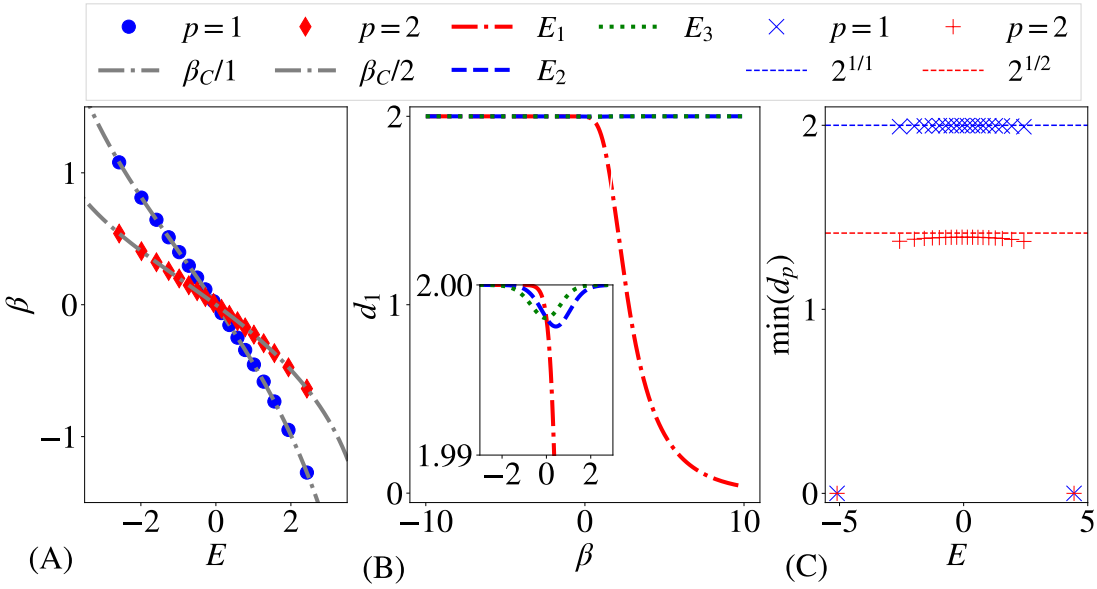


Figure 2.2: Eigenstate temperature results for staggered field model, Eq. (1.15): $h_x = h_z = 0.5$, $\Delta = 0.95$, $L = 10$. **(A)** $\beta_E$ against energy, for 20 eigenstates which are equally spaced in energy across the spectrum, with curves showing $\beta_C/p$. (Highest/lowest state not visible.) **(B)** $d_1(\rho, \rho_C)$ vs $\beta$ curve for ground state ($E_1$), mid-spectrum state ($E_3$), and $E_2$ in between the two. **(C)** The minimum of $d_p(\rho, \rho_C)$ plotted against eigenenergy, for the same eigenstates used in (A).

The result $\beta_E = \beta_C$ (for $p = 1$) does not imply that eigenstate density matrices $\rho = |E_n\rangle\langle E_n|$ closely resemble canonical states $\rho_C = Z^{-1}e^{-\beta H}$. We are comparing a pure state to a highly mixed state, i.e., a projection operator (a rank-1 operator) $\rho$ to a full-rank operator $\rho_C$. So, even the smallest distance between them (at $\beta = \beta_C$) is close to the maximum. The smallest $p$-distance is generally close to $2^{1/p}$, an analytical result derived in the following subsection 2.2.3. The minimum is thus very close to the maximum for most eigenstates, as shown in Figure 2.2(B,C). The highest and lowest eigenstates are exceptions to this behavior; clearly $\rho_C \to |E_0\rangle\langle E_0|$ for $\beta \to \infty$, and similarly, $\rho_C \to |E_D\rangle\langle E_D|$ for $\beta \to -\infty$.

### 2.2.2 Finite window eigenstate temperature

Instead of the eigenstate density matrix, $\rho = |E_n\rangle\langle E_n|$, we could use the micro-canonical density matrix,

$$\rho_{MC} = \frac{1}{\mathcal{N}} \sum_{E_j \in \{E_n \pm \Delta E/2\}} |E_j\rangle\langle E_j|, \tag{2.6}$$

as introduced in Eq. (1.5). This formalism might be considered more physical, as we are now comparing two mixed states.

Here, we fix the energy window width and allow each window to contain a different number of eigenstates. We want to compute the value of $\beta$ such that the distance $d_p(\rho_{MC}, \rho_C)$ is minimized. We label this minimizing value the finite window eigenstate temperature $\beta_{\Delta E}$. One can follow the same analytical procedure as is detailed in subsection 2.2.3 for the eigenstate temperature, and by making the assumption that the energy $E_{MC} = \mathrm{tr}(H\rho_{MC}) = 1/\mathcal{N}\sum_{E_j\in\Delta E} E_j$ of the

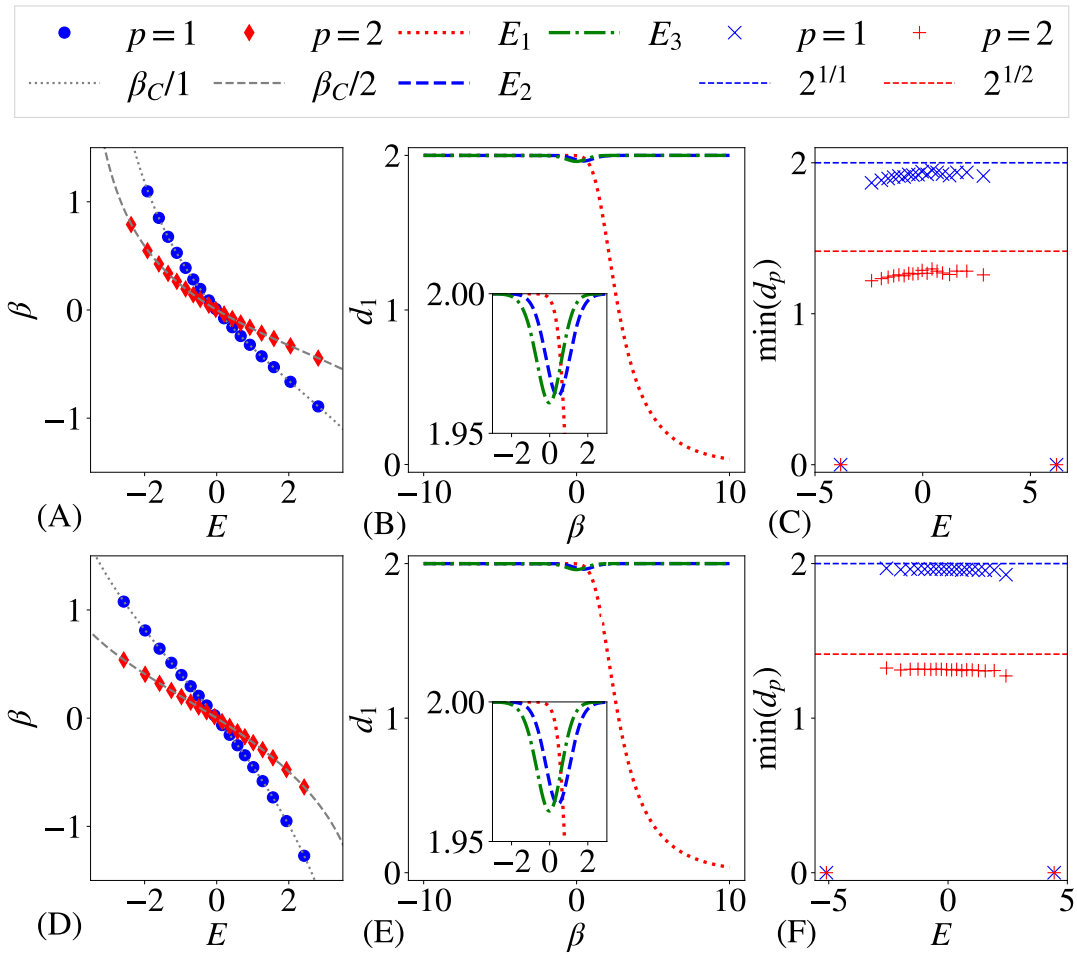


Figure 2.3: Finite window eigenstate temperature results for spin chains with $L = 10$, namely: **(A)-(C)** Chaotic Ising Model with $h_z = 0.5$, $h_x = 0.75$, Eq. (1.21),w and $\Delta E \sim 0.059$. **(D)-(F)** Staggered field $XXZ$ chain with $\Delta = 0.95$, $J = 1$, $h_x = h_z = 0.5$ Eq. (1.15), and $\Delta E \sim 0.0757$. **(A,D)** $\beta_{MC}$ against energy, for 20 energy windows which are equally spaced in energy across the spectrum, with curves showing $\beta_C/p$. (Highest/lowest state not visible.) **(B,E)** $d_1(\rho_{MC}, \rho_C)$ vs $\beta$ curve for energy windows: $E_1$ near the ground state, $E_2$ in the middle of spectrum, and $E_2$ in between the two. **(C,F)** The minimum of $d_p(\rho_{MC}, \rho_C)$ plotted against energy, for the same energy windows used in (A,D).

microcanonical state $\rho_{MC}$ is roughly $E_{MC} \approx E_j \in \Delta E$, which is valid if the energy interval is sufficiently small, we obtain the similar relation that $\beta_C \approx p\beta_{\Delta E}$.

This result is illustrated numerically in Figure 2.3, in which we present results for the chaotic Ising model (A-C) and the staggered field $XXZ$ chain (D-F). In (A,D), we plot $\beta_{\Delta E}$ that minimizes the Schatten $p$-distance for the given $p$, along with two canonical $\beta_C$ curves, versus energy. In (C,F), we plot the value of the minimum distance for the same energy slices as taken in the left figure. Finally, in (B,E), we plot the $d_1$ distance versus $\beta$ for three particular energy slices $E_1$, $E_2$, and $E_3$. The numerical results again illustrate the derived relation of $\beta_C = p\beta_{\Delta E}$ for the $p$-distance $d_p$ when taken between a microcanonical and canonical density matrix.

### 2.2.3 Derivation of analytical results

In this subsection, we present the derivations of our analytical results presented above. To start, we wish to minimize the Schatten $p$-distance, Eq. (2.1), between the canonical and eigenstate density matrices, i.e., $d_p(\rho, \rho_C)$ with respect to $\beta$. In particular, we want to determine the value of $\beta_E$, Eq. (2.3), and the value of $d_p$ at this minimum. All Schatten $p$-norms of a matrix $\rho$ can be expressed in terms of the singular values $s_n$ of $\rho$

$$\|\rho\|_p = \left( \sum_n s_n^p \right)^{1/p}. \tag{2.7}$$

In other words, the Schatten $p$-norm is the $l_p$ norm of the singular values. The singular values of a Hermitian matrix $\rho$ are the absolute values of the eigenvalues of $\rho$. The eigenstate density matrix $\rho$ and the canonical density matrix $\rho_C$ are jointly diagonalizable with respect to the eigenstate basis of $H$. The eigenvalues of the former are 1 and 0, while the eigenvalues of the latter are given by $e^{-\beta E_j}$, where $E_j$ are the eigenvalues of the Hamiltonian $H$. The Schatten norms are invariant under a basis transformation by definition, so the normed Schatten

$p$-distance can be written as

$$d_p^p(\rho, e^{-\beta H}) = \left| \frac{1}{\|\rho\|_p} - \frac{e^{-\beta E_n}}{\|e^{-\beta H}\|_p} \right|^p + \sum_{E_j \neq E_n} \frac{e^{-p\beta E_j}}{\|e^{-\beta H}\|_p^p}. \tag{2.8}$$

Here, we have normed the distance for convenience in the calculation. Now there are two results we wish to obtain, the value of $\beta$ for which Eq. (2.8) is minimized, and the value of that minimum. In the following, we first obtain the surprising result of $\beta_E = \beta_C/p$, and then we determine how the value of the minimum scales.

**Minimization**

To find the minimum of Eq. (2.8), we differentiate the $p$-normed Schatten $p$-distance of $\rho$ and $\exp(-\beta H)$ and obtain

$$\begin{aligned} \frac{\partial}{\partial\beta} d_p^p(\rho, e^{-\beta H}) = &- p \left( \frac{1}{\|\rho\|_p} - \frac{e^{-\beta E_n}}{\|e^{-\beta H}\|_p} \right)^{p-1} \\ &\times \frac{\partial}{\partial\beta} \frac{e^{-\beta E_n}}{\|e^{-\beta H}\|_p} + \sum_{E_j \neq E_n} \frac{\partial}{\partial\beta} \frac{e^{-p\beta E_j}}{\|e^{-\beta H}\|_p^p}. \end{aligned} \tag{2.9}$$

Here, we have assumed $||e^{-\beta H}||_p \geq ||\rho||_p e^{-\beta E_j}$ to ensure the sign of the first term is correct, which is true for a single eigenstate. Noting that

$$\|e^{-\beta H}\|_p \;=\; \Big( \sum_n |s_n|^p \Big)^{1/p} \;=\; \Big( \sum_n e^{-p\beta E_n} \Big)^{1/p} \;=\; \big( \mathrm{tr}\big(e^{-p\beta H}\big) \big)^{1/p}, \tag{2.10}$$

we can derive

$$\begin{aligned} \frac{\partial}{\partial\beta} \frac{e^{-\beta E_n}}{\|e^{-\beta H}\|_p} &= \frac{\partial_\beta \big(e^{-\beta E_n}\big)}{\|e^{-\beta H}\|_p} + e^{-\beta E_n} \frac{\partial}{\partial_\beta} \left( \frac{1}{\|e^{-\beta H}\|_p} \right) \\ &= -E_n \frac{e^{-\beta E_n}}{\|e^{-\beta H}\|_p} - \frac{e^{-\beta E_n}}{p} \Big( \mathrm{tr}\big(e^{-p\beta H}\big) \Big)^{-1-\frac{1}{p}} \cdot \mathrm{tr}\left( -pHe^{-p\beta H} \right) \\ &= -E_n \frac{e^{-\beta E_n}}{\|e^{-\beta H}\|_p} + \frac{e^{-\beta E_n}}{(\mathrm{tr}(e^{-p\beta H}))^{1/p}} \cdot \frac{\mathrm{tr}\big(He^{-p\beta H}\big)}{\mathrm{tr}(e^{-p\beta H})} \\ &= \frac{e^{-\beta E_n}}{\|e^{-\beta H}\|_p} \left( -E_n + \frac{\mathrm{tr}\big(He^{-p\beta H}\big)}{\mathrm{tr}(e^{-p\beta H})} \right). \end{aligned} \tag{2.11}$$

Similarly,

$$\frac{\partial}{\partial\beta}\frac{e^{-p\beta E_j}}{\|e^{-\beta H}\|_p^p} \;=\; \frac{pe^{-p\beta E_j}}{\|e^{-\beta H}\|_p^p}\left(-E_j \;+\; \frac{\mathrm{tr}\big(He^{-p\beta H}\big)}{\mathrm{tr}(e^{-p\beta H})}\right). \tag{2.12}$$

Now, Eq. (2.8) is minimal if and only if Eq. (2.9) is 0, which holds true if, and only if

$$\begin{aligned}0 = &-p\left(\frac{1}{\|\rho\|_p} - \frac{e^{-\beta E_n}}{\|e^{-\beta H}\|_p}\right)^{p-1}\frac{e^{-\beta E_n}}{\|e^{-\beta H}\|_p}\cdot\left[-E_n + \frac{\mathrm{tr}\big(He^{-p\beta H}\big)}{\mathrm{tr}(e^{-p\beta H})}\right]\\ &- p\frac{e^{-p\beta E_n}}{\mathrm{tr}(e^{-p\beta H})}\left[-E_n + \frac{\mathrm{tr}\big(He^{-p\beta H}\big)}{\mathrm{tr}(e^{-p\beta H})}\right]\\ &- p\frac{\mathrm{tr}\big(He^{-p\beta H}\big)}{\mathrm{tr}(e^{-p\beta H})} \;+\; p\frac{\mathrm{tr}\big(e^{-p\beta H}\big)}{\mathrm{tr}(e^{-p\beta H})}\frac{\mathrm{tr}\big(He^{-p\beta H}\big)}{\mathrm{tr}(e^{-p\beta H})}.\end{aligned} \tag{2.13}$$

The last two terms cancel, and we group the remaining terms together and divide by $p$ to obtain

$$\begin{aligned}0 = &\left[E_n - \frac{\mathrm{tr}\big(He^{-p\beta H}\big)}{\mathrm{tr}(e^{-p\beta H})}\right]\\ &\times\left(\left(\frac{1}{\|\rho\|_p} - \frac{e^{-\beta E_n}}{\|e^{-\beta H}\|_p}\right)^{p-1}\frac{e^{-\beta E_n}}{\|e^{-\beta H}\|_p} + \frac{e^{-p\beta E_n}}{\mathrm{tr}(e^{-p\beta H})}\right).\end{aligned} \tag{2.14}$$

This is zero if and only if

$$E_n = \frac{\mathrm{tr}\big(He^{-p\beta H}\big)}{\mathrm{tr}(e^{-p\beta H})}. \tag{2.15}$$

By the one-to-one correspondence of energies and canonical inverse temperatures there exists exactly one $\beta$ for a given $E_n$ which obeys Eq. (2.15). This $\beta$ minimizes Eq. (2.8) and we call it $\beta_E$. It is related to the canonical inverse temperature $\beta_C$, which is defined as the unique solution to Eq. (1.1), via $\beta_C = p \times \beta_E$.

### Value of the minimum

To allow for the case of using a microcanonical density matrix in place of the eigenstate density matrix (subsection 2.2.2), we consider the distance Eq. (2.8) with $\rho$ now of the form of Eq. (2.6) ($\mathcal{N} = 1$ gives eigenstate temperature), i.e.,

the finite window eigenstate temperature. We assume that $||e^{-\beta H}||_p \geq ||\rho||_p e^{-\beta E_j}$, which again is true for $\mathcal{N} \ll D$, and we separate the final sum into the difference of two sums.

$$d_p^p(\rho, e^{-\beta H}) = \sum_{E_j \in \Delta E} \left( \frac{1}{\mathcal{N}^{1/p}} - \frac{e^{-\beta E_j}}{\|e^{-\beta H}\|_p} \right)^p + \sum_{E_j} \frac{e^{-p\beta E_j}}{\|e^{-\beta H}\|_p^p} - \sum_{E_j \in \Delta E} \frac{e^{-p\beta E_j}}{\|e^{-\beta H}\|_p^p}. \tag{2.16}$$

Now, we assume $\rho$ to be constructed from states in the middle of the spectrum, hence we take $\beta$ close to zero. Provided the bandwidth of the energy is not too large, i.e., $|E_{\min}|, |E_{\max}| \ll \beta^{-1}$, we can approximate $e^{-\beta E_j} \approx 1$ for all $E_j$, and $\|e_p^{-\beta H}\| \approx D^{1/p}$, leading to

$$\begin{aligned} d_p^p(\rho, e^{-\beta H}) &= \frac{1}{\mathcal{N}} \sum_{E_j \in \Delta E} \left(1 - (\mathcal{N}/D)^{1/p}\right)^p + 1 - \sum_{E_j \in \Delta E} \frac{1}{D} \\ &= \left(1 - (\mathcal{N}/D)^{1/p}\right)^p + 1 - \frac{\mathcal{N}}{D}. \end{aligned} \tag{2.17}$$

If $p = 1$, and we assume $\mathcal{N} \ll D$, it is clear from Eq. (2.17) that $d_1 \approx 2$. For $p \geq 2$ we use the binomial expansion on Eq. (2.17), and let $D_E = \mathcal{N}/D$,

$$\left(1 - D_E^{1/p}\right)^p = \sum_{n=0}^{\infty} \binom{p}{n} (-1)^n D_E^{n/p}, \tag{2.18}$$

resulting in

$$d_p^p(\rho, e^{-\beta H}) = 2 - p D_E^{1/p} + O\left(D_E^{\ell}\right). \tag{2.19}$$

Here, $\ell = \min(1, 2/p)$. Then finally to obtain $d_p$, we raise both sides to $1/p$, and use the binomial expansion again,

$$d_p(\rho, e^{-\beta H}) = 2^{1/p} - 2^{1/p-1} D_E^{1/p} + O\left(D_E^{\ell}\right) \tag{2.20}$$

Thus the leading perturbation is $D_E^{1/p} = (\mathcal{N}/D)^{1/p}$. So when $\mathcal{N} \ll D$, $d_p$ is close to $2^{1/p}$ for bulk eigenstates.

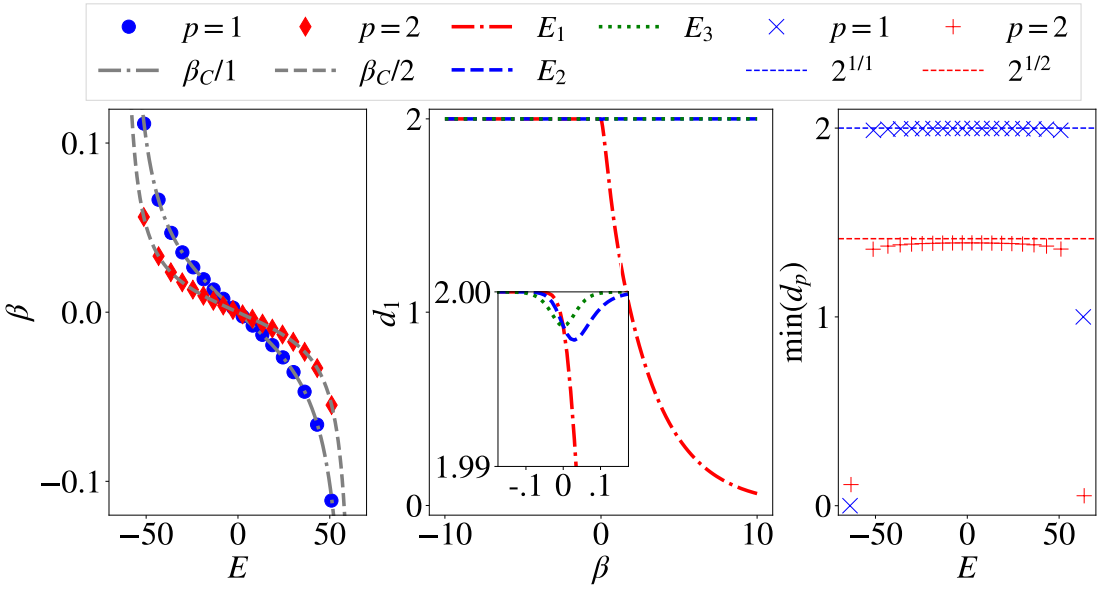


Figure 2.4: Eigenstate temperature results for random symmetric matrix with $D = 2^{10}$. **Left:** $\beta_E$ against energy, for 20 eigenstates which are equally spaced in energy across the spectrum, with curves showing $\beta_C/p$. (Highest/lowest state not visible.) **Mid:** $d_1(\rho, \rho_C)$ vs $\beta$ curve for ground state ($E_1$), mid-spectrum state ($E_3$), and $E_2$ in between the two. **Right:** The minimum of $d_p(\rho, \rho_C)$ plotted against eigenenergy, for the same eigenstates used in (A).

### 2.2.4 Random matrix results

We have demonstrated analytically that $\beta_E = \beta_C/p$ is a general mathematical result that will hold for any Hermitian matrix $H$. We now illustrate this result by computing the eigenstate temperature $\beta_E$ for a random matrix. In Figure 2.4, we present the results for a symmetric $D \times D$ matrix with elements drawn randomly from a normal distribution with mean 0 and variance 1. The figure clearly illustrates almost identical results to the physical models presented in subsection 2.2.1.

## 2.3 Subsystem temperature

In this section, we discuss the subsystem temperature, which we have defined as the temperature that minimizes the distance between the reduced eigenstate density matrix $\rho^A = \mathrm{tr}_B(\rho)$ and the reduced canonical density matrix $\rho_C^A = \mathrm{tr}_B(\rho_C)$,

$$\beta_S = \underset{\beta}{\mathrm{argmin}}\, d_p\left(\rho^A, \rho_C^A\right). \tag{2.21}$$

The partial trace prevents a calculation similar to that used to derive $\beta_E = \beta_C/p$; we thus do not have analytical predictions for the relationship between $\beta_S$ and $\beta_C$. On physical grounds, one expects $\beta_S$ to match $\beta_C$ for $L_A \ll L$ and large $L$, via the eigenstate thermalization hypothesis. We present our numerical findings for $\beta_S$ in various quantum systems, exploring this expected correspondence.

### 2.3.1 Main results

The values of $\beta_S$ are found in general to be scattered around $\beta_C$, as shown in Figure 2.5(A) for the chaotic Ising model. The width of this scatter generally decreases with system size (both $L_A$ and $L$), as quantified further below. In stark contrast to $\beta_E$, there is no obvious dependence on the distance measure used — the qualitative behavior is the same for all $p$ except $p = \infty$, see subsection 2.3.2 for scaling data using $p = 2$ and 3 and an example of the result of using $p = \infty$. We therefore present numerical results for the trace distance, $p = 1$.

The qualitative results of Figure 2.5 are not specific to 1D chains. This is clear from the strikingly similar results we obtain for the 2D square lattice model as shown in Figure 2.6. In Figure 2.6, we illustrate the geometry of the square lattice for each given system/subsystem parameters, alongside the respective $\beta_S$ and $\min(d_1)$ versus $E$ plots. In the geometry illustrations, the red and black points represent the subsystems $A$ and $B$ respectively. We observe similar results to that of a chaotic 1D spin chain such as those in Figure 2.5.

When increasing $L_A$ with fixed total system size $L$, the variance of $\beta_S$ and the distance between $\beta_S$ and $\beta_C$ decrease, up to $L_A = L/2$. These effects are visible in Figure 2.5 (A) and Figure 2.6 (A), and are also illustrated quantitatively in Appendix A.1. For $L_A > L/2$, the distribution of $\beta_S$ values changes shape and shows additional features, perhaps resulting from $\rho^A$ no longer having full rank. See Appendix A.1 for examples of results from systems with $L_A > L/2$.

Although $|\beta_S - \beta_C|$ and the variance of $\beta_S$ improve with increasing $L_A$, the minimum distance between $\rho^A$ and $\rho^A_C$ does not, as is visible from Figures 2.5(B) and 2.6(B). The average $\min(d_1)$ increases markedly with $L_A$. The reduced

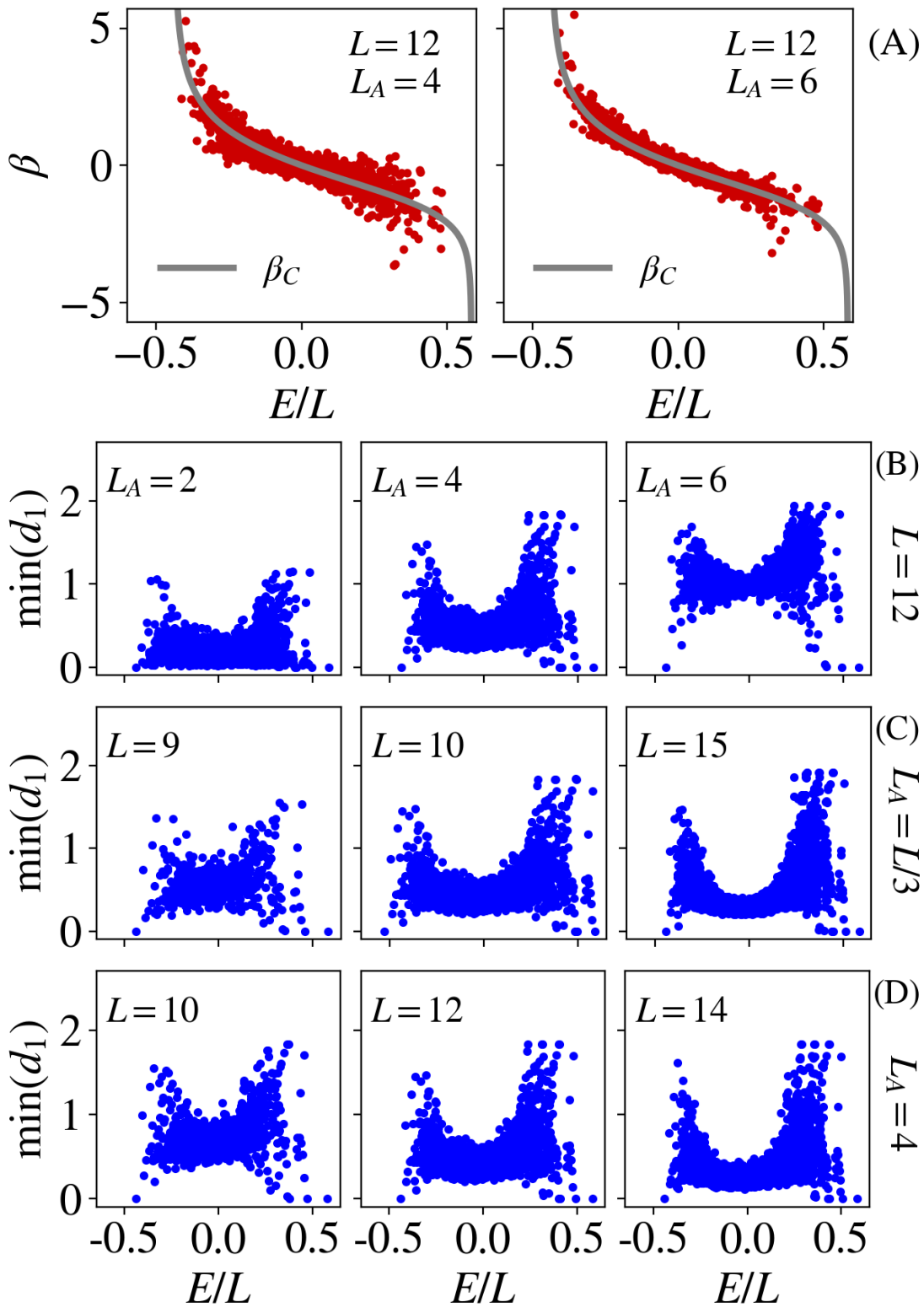


Figure 2.5: Subsystem temperature results for the chaotic Ising model, Eq. (1.21), with $h_z = 0.5$ and $h_x = 0.75$. **(A)** $\beta$ that minimizes $d_1(\rho^A, \rho_C^A)$ ($\beta_S$) versus energy, plotted along side the canonical $\beta_C$ curve, for the given $L$ and $L_A$. **(B)-(D)** $\min(d_1(\rho^A, \rho_C^A))$ plotted versus energy, each row illustrating a different scaling of system/subsystem size.

density matrix has decreasing resemblance to the reduced canonical density matrix, presumably because of the decreasing size of the complement $B$, which

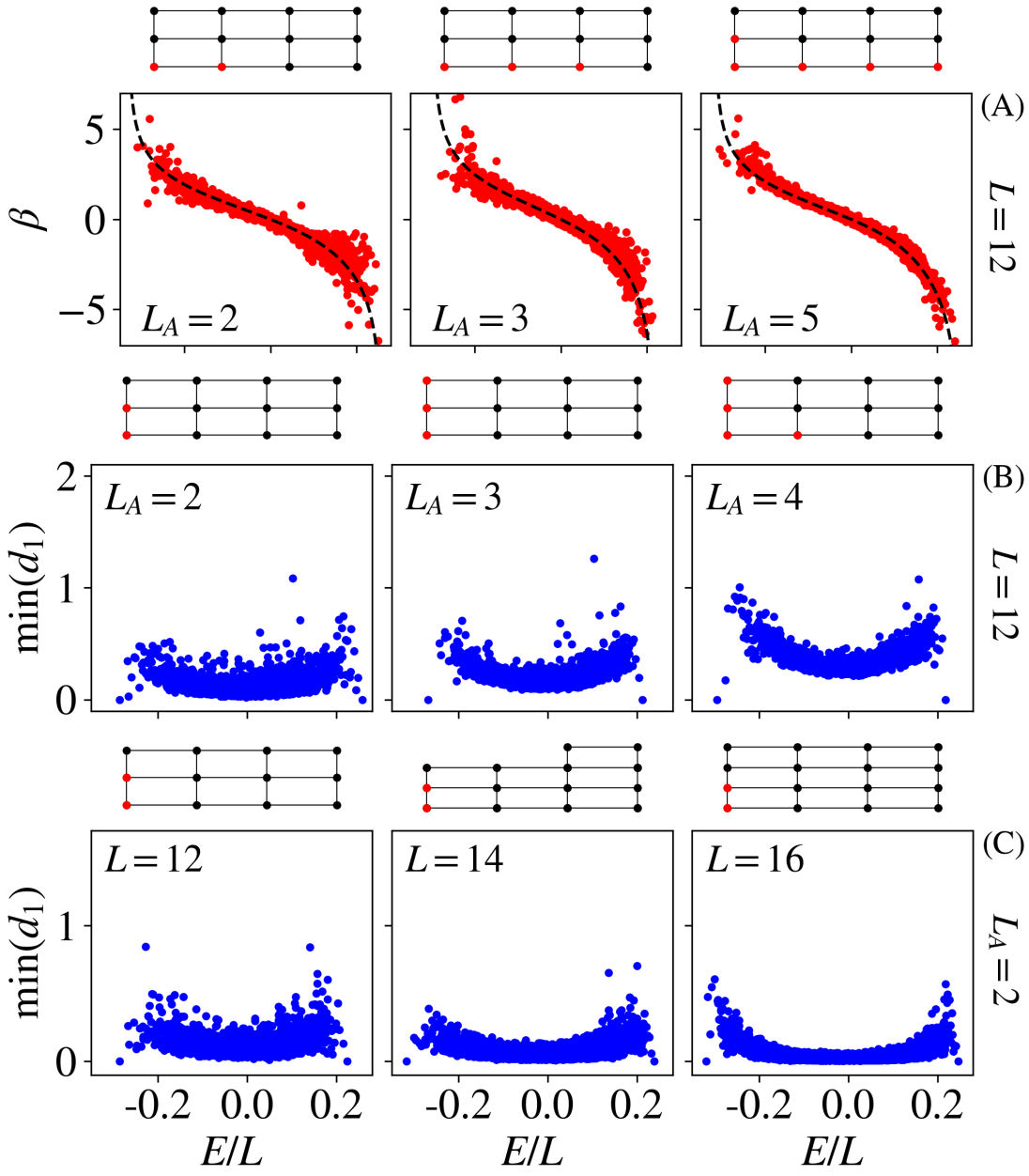


Figure 2.6: Subsystem temperature results for the non-number conserving square lattice model, Eq. (1.18), with $S^x$ and $S^z$ fields in alternate sub-lattices, with $h_x = h_z = 0.1$. The geometry of each system is illustrated above each plot, in which red and black sites correspond to the subsystems $A$ and $B$, respectively. - **(A):** $\beta$ that minimizes $d_1(\rho^A, \rho_C^A)$ ($\beta_S$) versus energy, plotted alongside the canonical $\beta_C$ curve, for the given $L$ and $L_A$. **(B-C):** $\min(d_1(\rho^A, \rho_C^A))$ plotted versus energy, each row illustrates a different scaling of system/subsystem size.

plays the role of a bath.

Increasing $L$ while keeping the fraction $L_A/L$ fixed, we again find the variance of $\beta_S$ to decrease. In this limit, $\min(d_1)$ on average decreases when the fraction $L_A/L$ is $< 1/2$ (see Figure 2.5(C)), and is remarkably stable as a function of $L$ when the fraction is $L_A/L = \frac{1}{2}$, see Appendix A.1.

We now consider fixed $L_A$ and increasing $L$ (or increasing $L_B = L - L_A$). The reduced density matrices become increasingly similar in this limit, as shown in Figures 2.5(D) and 2.6(C). In Figure 2.7 we show scaling behaviors in this limit computed using the central 20% of the spectrum. Figure 2.7 (A)-(C) shows results for the disordered-field $XXZ$ chain, while Figure 2.7 (D)-(F) shows those for the chaotic Ising model, both with $L_A = 2$.

The minimum distance between density matrices $\rho_C^A$ and $\rho^A$ decreases appar-

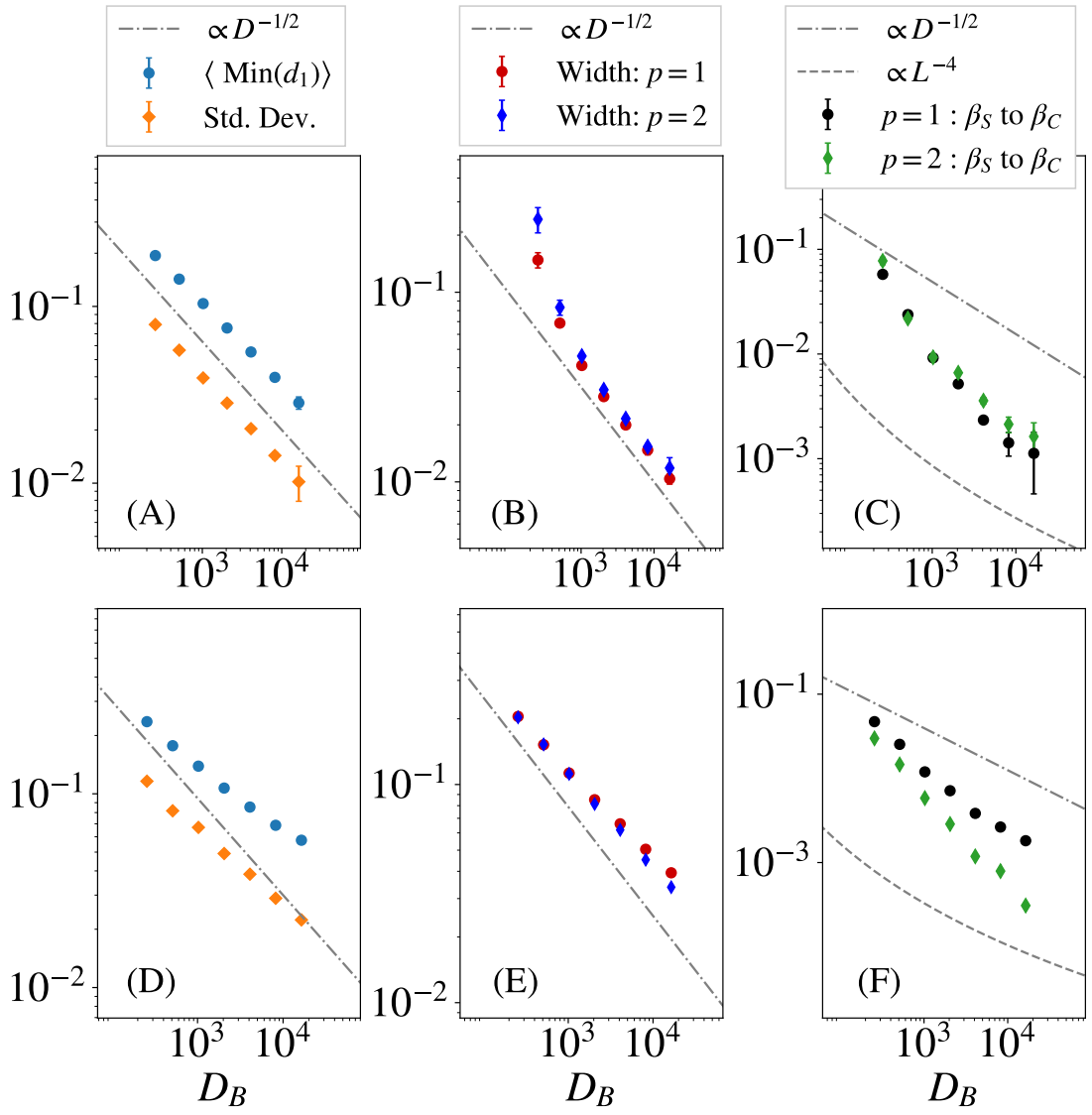


Figure 2.7: Subsystem temperature scaling for: **(A)-(C)** Disordered field model, Eq. (1.16), with $W = 0.25$ and $L_A = 2$, over many disorder realizations. **(D)-(F)** Chaotic Ising model, Eq.(1.21), with $h_x = 0.75$, $h_z = 0.5$, and $L_A = 2$. For both models, statistics are taken from the central 20% of the spectrum. **(A),(D)** Mean of $\min(d_1(\rho^A, \rho_C^A))$ and its standard deviation, vs. $D_B$ for $p = 1$. **(B),(E)** Width of $\beta_S$ vs. $D_B$ for $p = 1, 2$. **(C),(F)** RMS-distance from the linear fit of $\beta_S$, to $\beta_C$ curve versus $D_B$, for $p = 1, 2$.

ently exponentially with system size, consistent with a maximum exponent of 1/2, i.e., an upper bound of $\sim D_B^{-1/2}$ (equivalently $\sim D^{-1/2}$), see Figure 2.7(A)/(D). While this scaling is difficult to prove for a general Hamiltonian, one can argue for this dependence based on assuming the eigenstates to be effectively random Gaussian states near the center of the spectrum. This is known to be a good but not perfect approximation for chaotic many-body systems with local interactions [37,44,220–224], and has been used to analyze ETH [2,10,19,24,28,34,37,39,46,225]. With this assumption, the reduced density matrix is a Wishart matrix, while the infinite-temperature canonical density matrix is an identity matrix. Thus, the question is how fast does a $p$-normalized Wishart matrix concentrate around an identity matrix? One can show that this dependence is at most $D_B^{-1/2}$ [200].

The width of $\min(d_1)$ clouds appears to decrease at least as fast as $\sim D_B^{-1/2}$ as well, as shown in Figure 2.7(A)/(D). This is reasonable as $d_1$ is bounded from below and the average $\min(d_1)$ decreases as $\sim D_B^{-1/2}$.

The width of the $\beta_S$ values which minimize $d_1$ also appears to have $\sim D_B^{-1/2}$ scaling (at most), see Figure 2.7(B)/(E). We have been unable to formulate an analytic argument for this scaling. As the width of the $\beta_S$ cloud decreases, these values concentrate on a line in the $L \to \infty$ limit. Figure 2.7(C)/(F) shows, by plotting the average distance of the $\beta_S$ cloud to the $\beta_C$ line, that the asymptotic shape of the $\beta_S$ cloud coincides with the $\beta_C$ line. From the available data, it is unclear whether this approach is power-law or exponential in $L$. Again, no analytical prediction is currently available for this dependence. These results would imply that the overwhelming majority of eigenstates appear to have a temperature that coincides with the canonical temperature in the large system size limit. However, this behavior does not rule out the existence of outliers, i.e., eigenstates that have a temperature far from the canonical temperature (See Section 2.6 for a discussion). In Ref. [35], an upper-bound scaling of $L^{-1}$ is derived for a closely related quantity, namely, $d_1(\rho^A, \rho_C^A)$ evaluated at $\beta_C$, instead of at its minimum $\beta_S$. Figure 2.7(C)/(F) shows that the actual scaling of $\min(d_1)$ is much faster. In Appendix A.2 we calculate the average value of $d_1(\rho^A, \rho_C^A)$ at $\beta_C$ as a

function of $L$.

### 2.3.2 Using various $p$-distances

Here, we consider the subsystem temperature for various $p$-distances. We stated that the qualitative behavior of $\beta_S$ is the same for all $p$ except $p = \infty$. To illustrate this behavior, we present the scaling behaviors in the limit of increasing $L$, with $L_A$ a fixed small value for three different $p$ values. In Figure 2.8, we show results for the $p = 1$, 2, and 3 distances for the staggered field model. While the exact values of the quantities presented may differ, we observe similar scalings with increasing $L$ for all three distances.

The only exception that we found was the $p = \infty$ distance (using the operator norm), which resulted in a gap in $\beta_S$ around $\beta = 0$, i.e., $\beta_S$ was never close to $\beta_C$ where $\beta_C$ was near zero. We illustrate this result in Figure 2.9, wherein we plot $\beta_S$ for the $p = 1$ distance on the left and $p = \infty$ distance on the right.

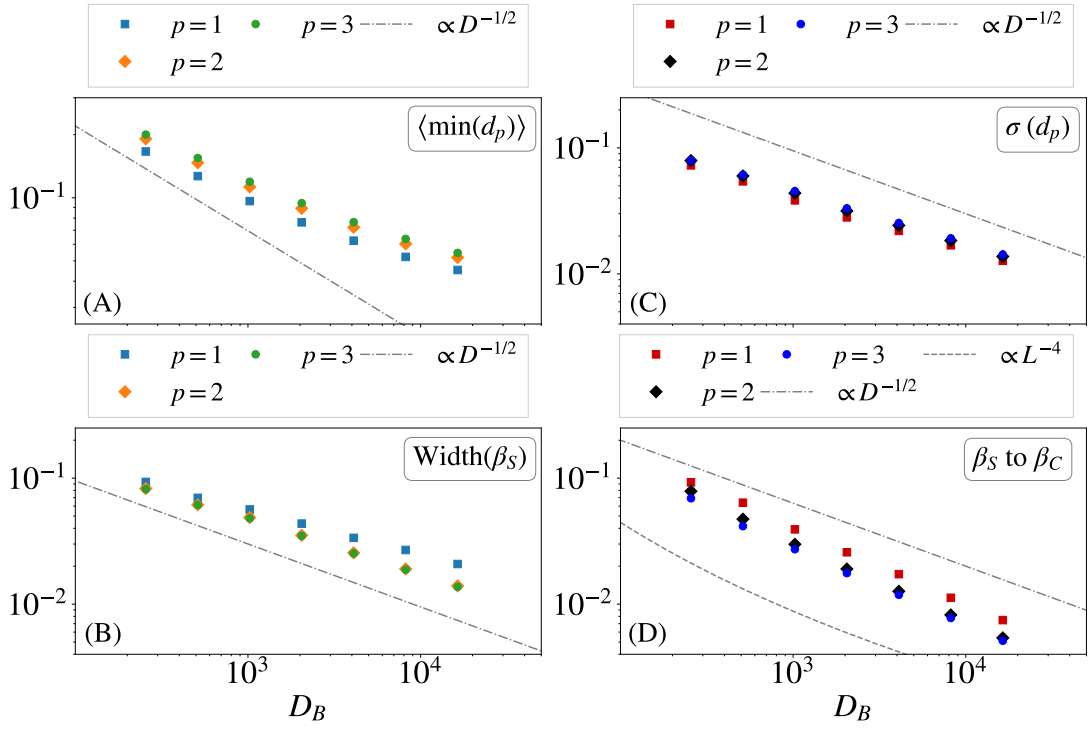


Figure 2.8: Subsystem temperature results using $p = 1, 2$ and 3 distances, for the staggered field model, Eq. (1.15), with $h_x = h_z = 0.5$ and $L_A = 2$. Statistics taken from the central 20% of the spectrum. **(A)** Mean of $\min(d_p(\rho^A, \rho_C^A))$ vs. $D_B$. **(B)** Standard deviation of $\min(d_p(\rho^A, \rho_C^A))$, labeled $\sigma(d_p)$, plotted versus $D_B$. **(C)** Width of $\beta_S$ vs. $D_B$. **(D)** RMS-distance from the linear fit of $\beta_S$, to $\beta_C$ curve vs. $D_B$.

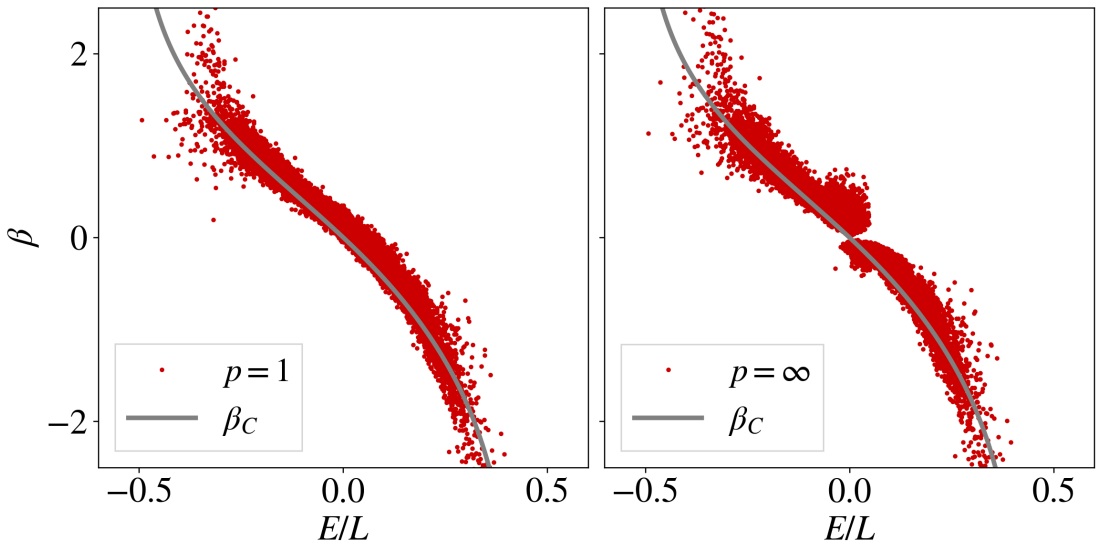


Figure 2.9: Subsystem temperature results: $\beta$ that minimizes $d_p(\rho^A, \rho_C^A)$ versus energy plotted along side the canonical $\beta_C$ curve. Data shown for $p = 1$ (left) and $p = \infty$ (right) distances, for the staggered field model, Eq. (1.15), with $L = 12$, $L_A = 2$, and $h_x = h_z = 0.5$.

### 2.3.3 Zero coupling limit

Here, we discuss the subsystem temperature in the limit of subsystem coupling $H_{AB} \to 0$. We find that for $H_{AB} = 0$, the subsystem temperature reduces to the eigenstate temperature for the subsystem $A$.

A weak or even zero system-bath coupling is often considered the natural setting for discussing quantum thermalization [61, 69]. In the present context, we did not consider it natural to modify $H_{AB}$, as we do not *a priori* have a system-bath separation, and the partition into $A$ and $B$ is arbitrary. However, it would be interesting to explore the effect of varying $H_{AB}$. For the exact limit of $H_{AB} = 0$, the reduced canonical density matrix $\rho_C^A = \mathrm{tr}_B(\rho_C)$ is simply $e^{-\beta H_A}$. The eigenstates of the full system also decompose into tensor products of the eigenstates of the two subsystems

$$|E_n\rangle = |E_j^A\rangle \otimes |E_k^B\rangle\,, \tag{2.22}$$

with eigenvalues $E_n = E_j^A + E_k^B$. Here, $|E^A\rangle$ ($|E^B\rangle$) are eigenstates of $H_A$ ($H_B$) with corresponding eigenvalue $E^A$ ($E^B$). Following this, we can write the reduced

eigenstate density matrix as

$$\begin{aligned}\rho_n^A &= \mathrm{tr}_B(|E_n\rangle\langle E_n|) = \mathrm{tr}_B(|E_j^A\rangle \otimes |E_k^B\rangle \langle E_j^A| \otimes \langle E_k^B|) \\ &= \mathrm{tr}_B(|E_j^A\rangle\langle E_j^A| \otimes |E_k^B\rangle\langle E_k^B|) = |E_j^A\rangle\langle E_j^A| \,\mathrm{tr}\big(|E_k^B\rangle\langle E_k^B|\big) \\ &= |E_j^A\rangle\langle E_j^A|. \end{aligned} \tag{2.23}$$

This allows us to write the distance $d_1(\rho^A, \rho_C^A)$ for $H_{AB} = 0$ as

$$\begin{aligned} d_1(\rho_n^A, \rho_C^A) &= |\rho_n^A - \rho_C^A|_1 = ||\,\mathrm{tr}_B(|E_n\rangle\langle E_n|) - \mathrm{tr}_B(e^{-\beta H})||_1 \\ &= ||\ |E_j^A\rangle\langle E_j^A| - e^{-\beta H_A}\ ||_1. \end{aligned} \tag{2.24}$$

Thus, the subsystem temperature $\beta_S$ for $H_{AB} = 0$, is actually the eigenstate temperature $\beta_E$, of the contributing eigenstate in $H_A$. We now know, via the result obtained in Section 2.2, that this temperature will in fact be $\beta_C$ of the eigenstate of the subsystem $H_A$ (for $p = 1$), as opposed to $\beta_C$ of the total system.

We have determined the result for the exact limit of $H_{AB} = 0$, however one can still ask how the correspondence between $\beta_S$ and $\beta_C$ changes systematically in the $H_{AB} \to 0$ limit. In particular it would be interesting to determine how $\beta_S$ transitions from $\beta_C^A$ (for $H_A$) to $\beta_C$ (for $H$) as a function of $H_{AB}$. Is the transition a smooth function of the interaction, or does it exhibit non-monotonic behavior?

## 2.4 Alternate formulations

In this section, we explore possible alternate formulations of our eigenstate-based temperatures. First, we discuss using the Bures distance instead of the Schatten $p$-distance. We derive an analytical result for the eigenstate temperature utilizing the Bures distance, analogous to that shown in Section 2.2. Following this, we discuss the use of $\exp(-\beta H_A)$ in place of $\mathrm{tr}(\rho_C)$ in the subsystem temperature. We provide numerical results for this alternate formulation of $\beta_S$.

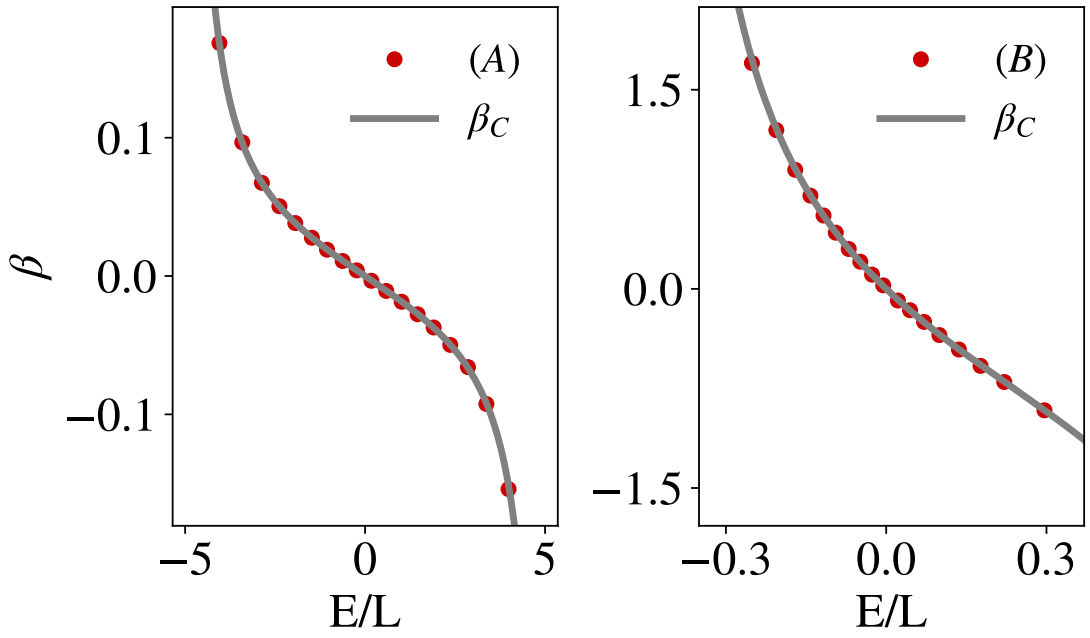


Figure 2.10: Finite window eigenstate temperature $\beta_{\Delta E}$ calculated using Bures distance $d_B(\rho_{MC}, \rho_C)$, for two models: (**A**) Random, real and symmetric matrix, (**B**) Chaotic Ising model, Eq. (1.21), with $h_x = 0.5$, $h_z = 0.75$. In both cases, $L = 9$ ($D = 2^9$) and 20 energy windows are uniformly chosen from the spectrum of the given Hamiltonian.

### 2.4.1 Bures Distance

Instead of the Schatten $p$-distances, one could justifiably use the Bures distance, related to the fidelity [203,204]. We have found that the subsystem temperature $\beta_S$, when calculated using the Bures distance, has the same overall features observed using the Schatten distances.

Additionally, the eigenstate temperature defined with the Bures distance is the same as $\beta_C$, i.e., the same as $\beta_E$ for $p = 1$. We derive this analytically below and also illustrate the result numerically in Figure 2.10.

The fidelity between two density matrices $\rho$ and $\sigma$ is given as

$$F(\rho, \sigma) \;=\; (\mathrm{tr}\,\sqrt{\rho^{1/2}\sigma\rho^{1/2}})^2, \tag{2.25}$$

or sometimes as the square root fidelity (quantity fidelity)

$$F'(\rho, \sigma) \;=\; \sqrt{F(\rho, \sigma)} \;=\; \mathrm{tr}\,\sqrt{\rho^{1/2}\sigma\rho^{1/2}} \tag{2.26}$$

It is a measure of how similar $\rho$ and $\sigma$ are, but it is not a metric on density operators. It is symmetric in the inputs, and is bounded between 0 and 1 [204].

Before delving into maximizing $F$, we note that the square root of a microcanonical density matrix $\rho$, as defined in Eq. (2.6), is $\sqrt{\mathcal{N}}\rho$, as :

$$(\sqrt{\mathcal{N}}\rho)^2 = \frac{\mathcal{N}}{\mathcal{N}^2} \sum_{E_j, E_{j'} \in \Delta E} |E_j\rangle \langle E_j|E_{j'}\rangle \langle E_{j'}| \tag{2.27}$$

$$= \frac{1}{\mathcal{N}} \sum_{E_j \in \Delta E} |E_j\rangle\langle E_j| = \rho \tag{2.28}$$

Now, we want to maximize the fidelity between a microcanonical state $\rho = \rho_{MC}$ and a canonical state $\rho_C = \exp(-\beta H)/\operatorname{tr}(\exp(-\beta H))$.

$$\begin{aligned} F(\rho, \rho_C) &= \operatorname{tr}\Big(\sqrt{\rho^{1/2}\rho_C\rho^{1/2}}\Big)^2 = (\operatorname{tr}\sqrt{\rho\rho_C})^2 \\ &= \Big(\operatorname{tr}\Big(\sqrt{\mathcal{N}}\rho e^{-\beta H/2}\Big)\Big)^2 / \operatorname{tr}\big(e^{-\beta H}\big) \\ &= \frac{1}{\mathcal{N}\operatorname{tr}(e^{-\beta H})} \left(\operatorname{tr}\left(\sum_{E_j \in \Delta E} e^{-\beta E_j/2} |E_j\rangle\langle E_j|\right)\right)^2 \\ &= \frac{1}{\mathcal{N}\operatorname{tr}(e^{-\beta H})} \left(\sum_{E_j, E_{j'} \in \Delta E} e^{-\frac{\beta}{2}(E_j + E_{j'})}\right) \end{aligned} \tag{2.29}$$

Now to find the value of $\beta$ which maximizes $F(\rho, \rho_C)$, we simply differentiate Eq. (2.29) to obtain

$$\begin{aligned} \frac{\partial F}{\partial \beta} &= \frac{\operatorname{tr}\big(He^{-\beta H}\big)}{\mathcal{N}\operatorname{tr}(e^{-\beta H})^2} \sum_{E_j, E_{j'} \in \Delta E} e^{-\frac{\beta}{2}(E_j + E_{j'})} \\ &\quad + \frac{1}{\mathcal{N}\operatorname{tr}(e^{-\beta H})} \sum_{E_j, E_{j'} \in \Delta E} -\frac{(E_j + E_{j'})}{2} e^{-\frac{\beta}{2}(E_j + E_{j'})} \\ &= \frac{1}{\mathcal{N}\operatorname{tr}(e^{-\beta H})^2} \sum_{E_j, E_{j'} \in \Delta E} e^{-\frac{\beta}{2}(E_j + E_{j'})} \times \\ &\qquad \times \left(\operatorname{tr}\big(He^{-\beta H}\big) - \frac{E_j + E_{j'}}{2} \operatorname{tr}\big(e^{-\beta H}\big)\right) \end{aligned} \tag{2.30}$$

We then make the approximation of $E_j \approx E_{j'} \approx E$ for $E_j, E_{j'} \in \Delta E$, which is

accurate for small $\Delta E$, and is exact when $\Delta E$ contains a single eigenstate.

$$\frac{\partial F}{\partial \beta} = \frac{e^{-\beta E}}{\mathrm{tr}(e^{-\beta H})} \left( \frac{\mathrm{tr}\big(H e^{-\beta H}\big)}{\mathrm{tr}(e^{-\beta H})} - E \right) \tag{2.31}$$

Then setting this equal to zero, we find the only roots of the equation are when

$$E = \frac{\mathrm{tr}\big(H e^{-\beta H}\big)}{\mathrm{tr}(e^{-\beta H})}. \tag{2.32}$$

This is the precisely the canonical energy-temperature relation, Eq. (1.1), meaning that the temperature which maximizes the fidelity between a microcanonical state $\rho$ with energy $E$, and a canonical state, is in fact the canonical temperature $\beta_C$.

The Bures distance is defined as

$$d_B(\rho, \sigma)^2 \;=\; 2(1 - \sqrt{F(\rho, \sigma)}), \tag{2.33}$$

with $F(\rho, \sigma)$ defined as Eq. (2.25). The Bures distance is minimized when the fidelity is maximized (i.e., when $F = 1$). Thus the Bures distance is minimized when $\beta = \beta_C$ also.

We numerically demonstrate this result in Figure 2.10. We present results for both the chaotic Ising model used previously, and also for a random real symmetric matrix whose elements are chosen from a normal distribution with mean 0 and variance 1, both clearly illustrating the model independent result $\beta_{\Delta E} = \beta_C$ for the Bures distance $d_B(\rho_{MC}, \rho_C)$.

### 2.4.2 Local Hamiltonian density matrix

In the case of the subsystem temperature $\beta_S$, we compared the reduced eigenstate density matrix $\rho^A$ to the reduced canonical density matrix $\rho_C^A = \mathrm{tr}_B \exp(-\beta H)$. An obvious alternative is to compare with $\exp(-\beta H_A)$, which we will refer to as the local Hamiltonian density matrix. If the interaction $H_{AB}$ is nonzero, the two are not equivalent, as discussed widely in the literature [35, 61, 226–236], e.g., in the context of extracting an effective "Hamiltonian of mean force" for

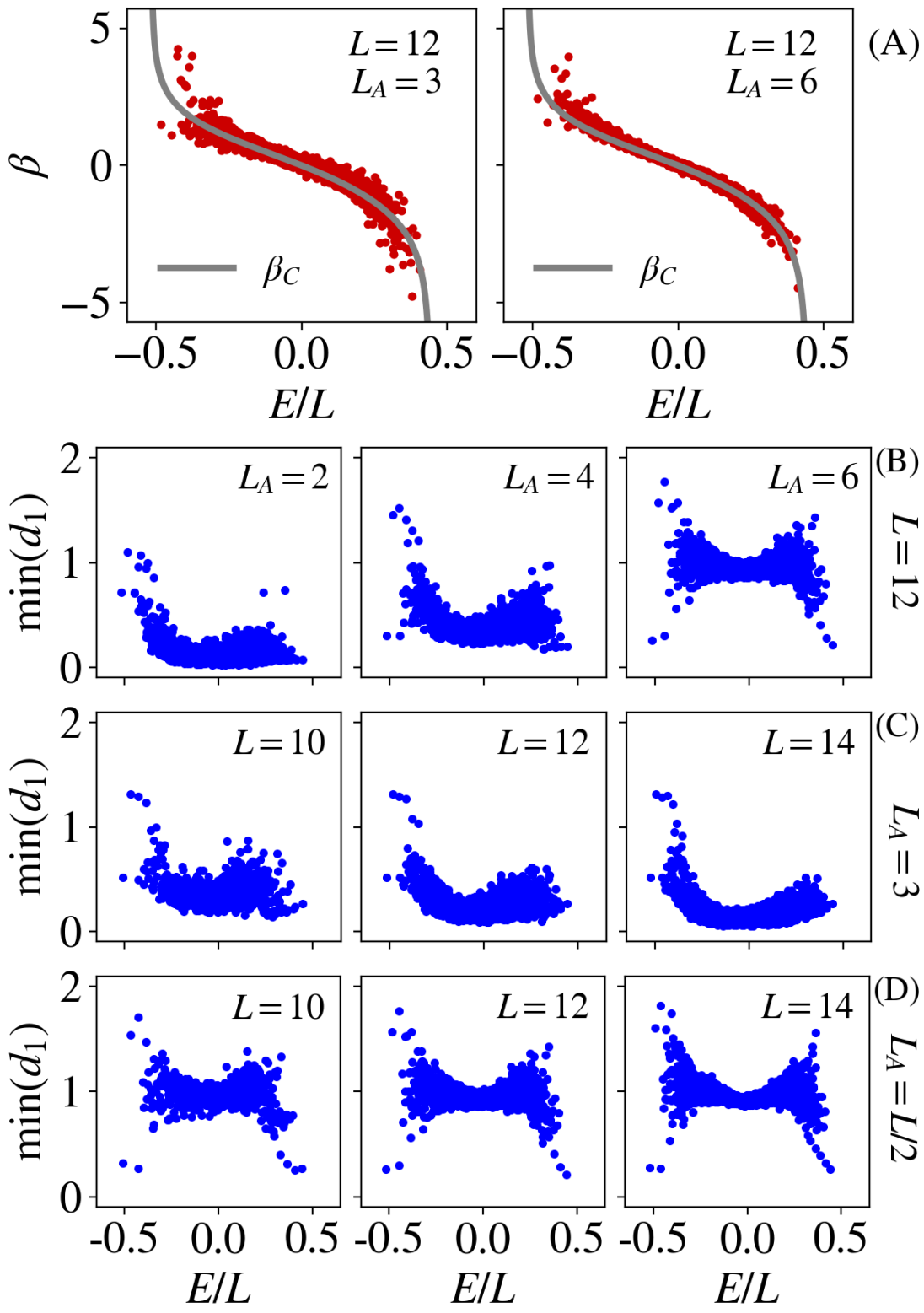


Figure 2.11: Subsystem temperature results with $\rho^A = \exp(-\beta H_A)$, for the staggered field model, Eq. (1.15), with $h_x = h_z = 0.5$, $J = 1$ and $\Delta = 0.95$. **(A)** $\beta$ minimizing $d_1(\rho^A, \rho_C^A)$ ($\beta_S$) versus energy, plotted along side the canonical $\beta_C$ curve, for the given system/subsystem size. **(B)-(D)** $\min(d_1(\rho^A, \rho_C^A))$ plotted versus energy, each row illustrating a different scaling of system/subsystem size.

the subsystem [226, 227, 233–237]. The Hamiltonian of mean force is an effective Hamiltonian $\tilde{H}_A$ that allows one to write the reduced canonical density matrix in the standard Gibbs form $e^{-\beta \tilde{H}_A}$.

Numerically, we have found that using $\exp(-\beta H_A)$ to define $\beta_S$ leads to very similar results to those obtained using $\rho_C^A$, except for eigenstates towards the spectral edges. In Figure 2.11 we illustrate the behavior of $\beta_S$ and $\min(d_p(\rho^A, \rho_C^A))$ with $\rho_C^A = \exp(-\beta H_A)$. We see the general behavior is the same as in Figures 2.5 and 2.6. In Figure 2.12 we also illustrate similar scalings as seen in Figure 2.7.

We can explain the behavior of eigenstates near infinite temperatures ($\beta$ close to zero). By expanding $\mathrm{tr}_B(e^{-\beta H})$ in $\beta$, we obtain sums of the partial trace of powers of the Hamiltonian $H$. To zeroth order in $\beta$, the only contributing term is $\mathrm{tr}_B(H) \propto H_A$, as our Hamiltonians are assumed to be traceless. This result also implies that the Hamiltonian of mean force to zeroth order is the local Hamiltonian $H_A$ [238]. Thus for bulk eigenstates (those near $\beta = 0$), we expect the results using $\mathrm{tr}_B \exp(-\beta H)$ and $e^{-\beta H_A}$ to be similar, even for $H_{AB} \neq 0$.

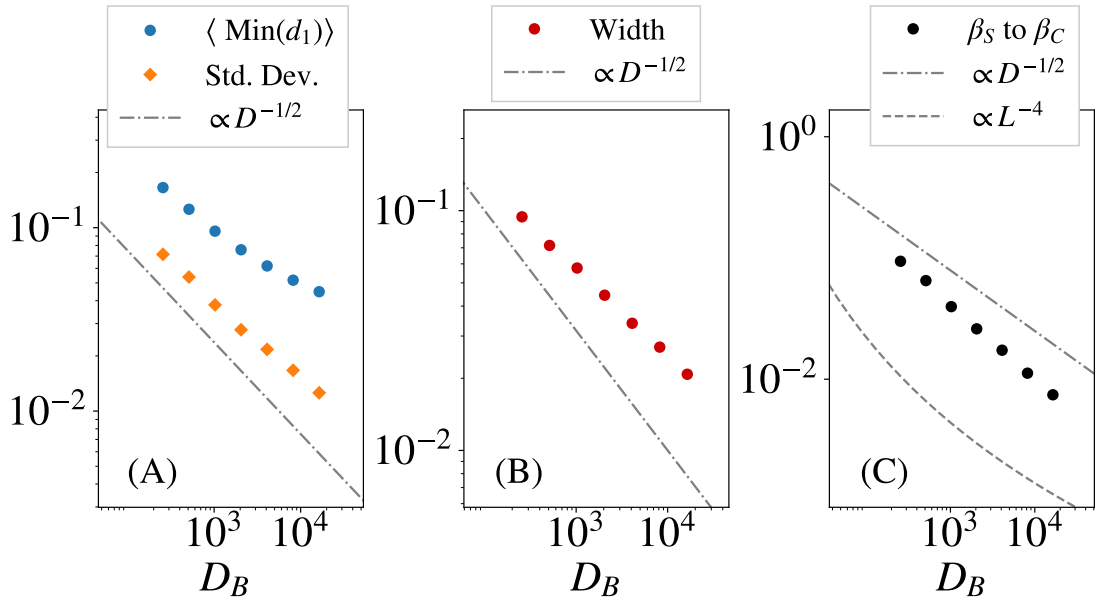


Figure 2.12: Subsystem temperature results with $\rho^A = \exp(-\beta H_A)$, for the staggered field model, Eq. (1.15), with $J = 1$, $\Delta = 0.95$, $h_x = h_z = 0.5$ and $L_A = 2$. Statistics from the central 20% of the spectrum. **(A)** Mean of $\min(d_1(\rho^A, \rho_C^A))$ and its standard deviation, vs. $D_B$ for $p = 1$. **(B)** Width of $\beta_S$ vs. $D_B$ for $p = 1, 2$. **(C)** RMS-distance from the linear fit of $\beta_S$, to $\beta_C$ curve versus $D_B$, for $p = 1, 2$.

## 2.5 Deviation in non-thermalizing systems

Up to this point, we have been solely concerned with chaotic systems expected to thermalize and thus satisfy the ETH (i.e., ergodic systems). The subsystem temperature $\beta_S$, Eq. (2.21), is based on ETH predictions for density matrices restricted to a local subsystem. In this section, we ask what happens to the subsystem temperature in a system that is expected to violate the ETH, i.e., one which does not thermalize (non-ergodic). In addition, we present results for a random matrix in place of a physical Hamiltonian.

### 2.5.1 Results in the integrable limit

To investigate this effect of integrability on $\beta_S$, we shall consider the staggered field model with varying field strength $h = h_z = h_x$. For finite, non-zero $h$, the system should generally be thermalizing. Of course, when $h = 0$, the system is simply the $XXZ$ chain and is known to be exactly solvable via the Bethe ansatz. Thus, if we tune $h$ towards zero from some finite non-zero value, the system should approach a non-thermalizing regime. In the top panel of Figure 2.13, we plot the RMS-distance between $\beta_C$ and $\beta_S$ for such a system as a function of magnetic field strength $h$. As one could expect, when $h \to 0$, the deviation between the temperatures increases due to the system no longer thermalizing.

To illustrate the systems approach to a non-thermalizing regime, we have plotted the mean consecutive level spacing ratio $\langle r \rangle$ versus the field strength $h$ in the bottom panel of Figure 2.13. The mean consecutive level spacing ratio is a prevalent measure of chaos, which we have previously defined in the introduction (Section 1.4). We have marked the predicted mean consecutive level spacing ratio values for chaotic and integrable systems, $\sim 0.5307$ and $\sim 0.386$ respectively [196]. As expected, $\langle r \rangle$ approaches the predicted value for non-ergodic systems as $h \to 0$, coinciding with the increasing deviation between $\beta_S$ and $\beta_C$. An example of the subsystem temperature results obtained for an entirely integrable system, the $XXZ$ chain (Eq.(1.13)), is shown in Figure 2.14. We observe the large spread of $\beta_S$ around $\beta_C$ in $(A)$, and that generally, the reduced eigenstates do not appear

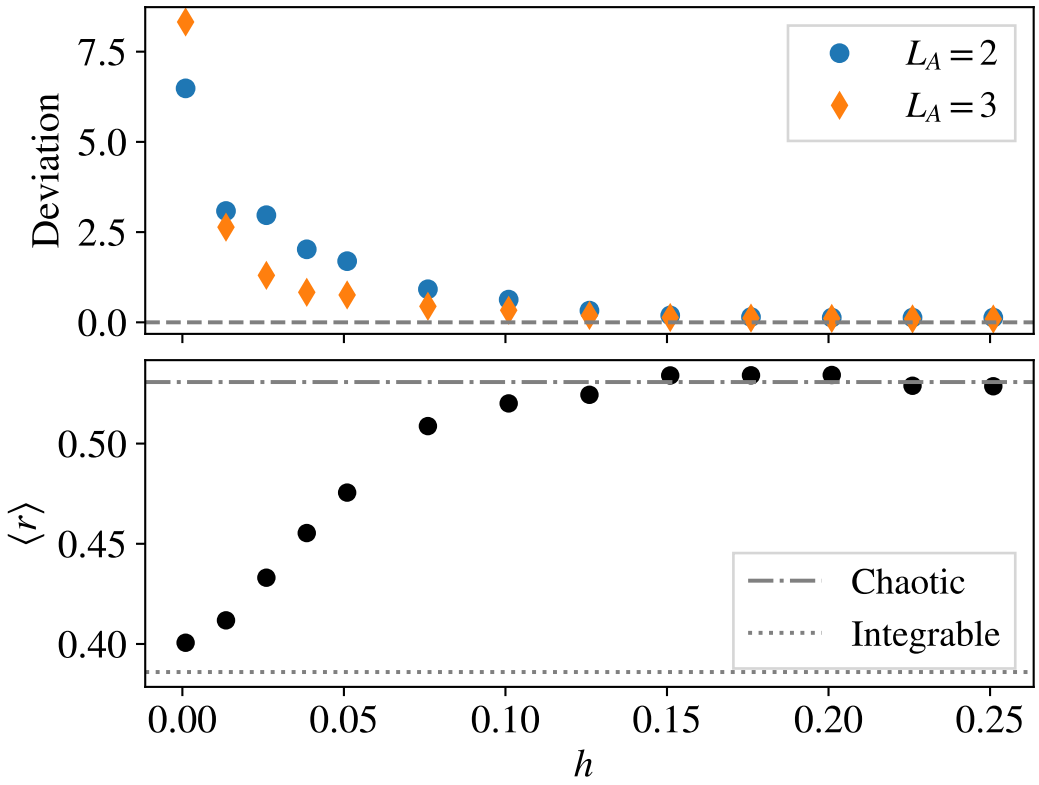


Figure 2.13: Results of subsystem temperature in the integrable limit for the staggered field model, Eq. (1.15), with $L = 12$, $J = 1$, $\Delta = 0.95$, and $h_z = h_x = h$. **Top:** The RMS-distance between $\beta_S$ and $\beta_C$ (Deviation) plotted versus shared field strength $h$. The RMS-distance is calculated for eigenstates in the central 20% of the spectrum. **Bottom:** mean consecutive level spacing ratio value plotted versus shared field strength $h$.

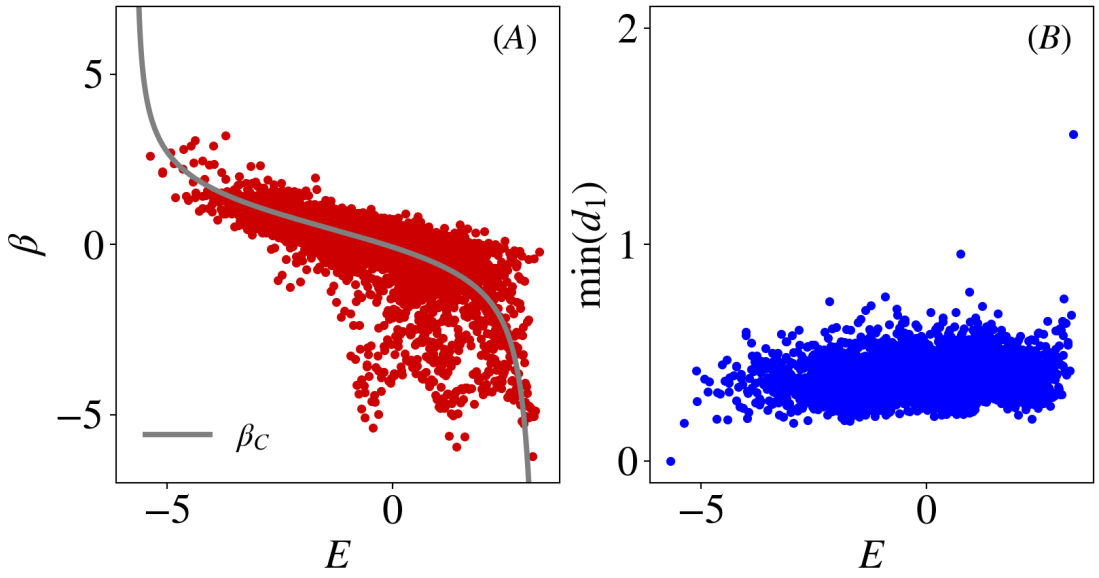


Figure 2.14: Results of subsystem temperature in the $XXZ$ chain, Eq. (1.13), with $L = 14$, $N = 6$, $J = 1$, $\Delta = 0.95$ and $L_A = 4$. **(A)** $\beta$ minimizing $d_1(\rho^A, \rho_C^A)$ ($\beta_S$) versus energy, plotted along side the canonical $\beta_C$ curve. **(B)** $\min(d_1(\rho^A, \rho_C^A))$ versus energy.

thermal, illustrated by the distance between the matrices in $(B)$. In $(A)$, we can observe that $\beta_S$ is closer to $\beta_C$ in the left half of the spectrum compared to the right, perhaps indicating the presence of some underlying structure. It would be intriguing to investigate the behavior of $\beta_S$ and $\min(d_1)$ in this integrable system, following a similar approach as shown in Figure 2.7.

There are two aspects that we should consider regarding this calculation in the integrable system. Firstly, owing to symmetries in the $XXZ$ chain (Section 1.4.1), it is possible for the spectrum to contain degenerate eigenvalues. This implies that different eigenstates can possess the same eigenvalue and, consequently, the same canonical temperature. In such cases, it may be more appropriate to consider a superposition of these eigenstates and compute the canonical temperature based on the resulting state. Secondly, within this integrable system, there exist additional conserved quantities beyond just energy. It is plausible that we would achieve a similar agreement between $\beta_S$ and $\beta_C$ if we were to compare the reduced eigenstates of integrable systems with the reduced density matrix of a generalized Gibbs ensemble [83].

### 2.5.2 Results for a random matrix

We have illustrated the deviation of $\beta_S$ from $\beta_C$ in the integrable limit, a consequence of the ETH being only expected to hold in chaotic quantum systems. Here, we further illustrate the deviation of $\beta_S$ by computing the temperature for a random matrix in place of a physical Hamiltonian. In Figure 2.15, we present the results for a symmetric $D \times D$ matrix with elements drawn randomly from a from a normal distribution with mean 0 and variance 1. The temperature shows no alignment with the canonical temperature for a random matrix. This could be expected, as when treating a random matrix as a Hamiltonian, there is no notion of locality. This absence of locality means the division into two subsystems is artificial and has no physical significance. This implies the partial trace is meaningless in a random matrix; there is no sense of tracing out a subsystem.

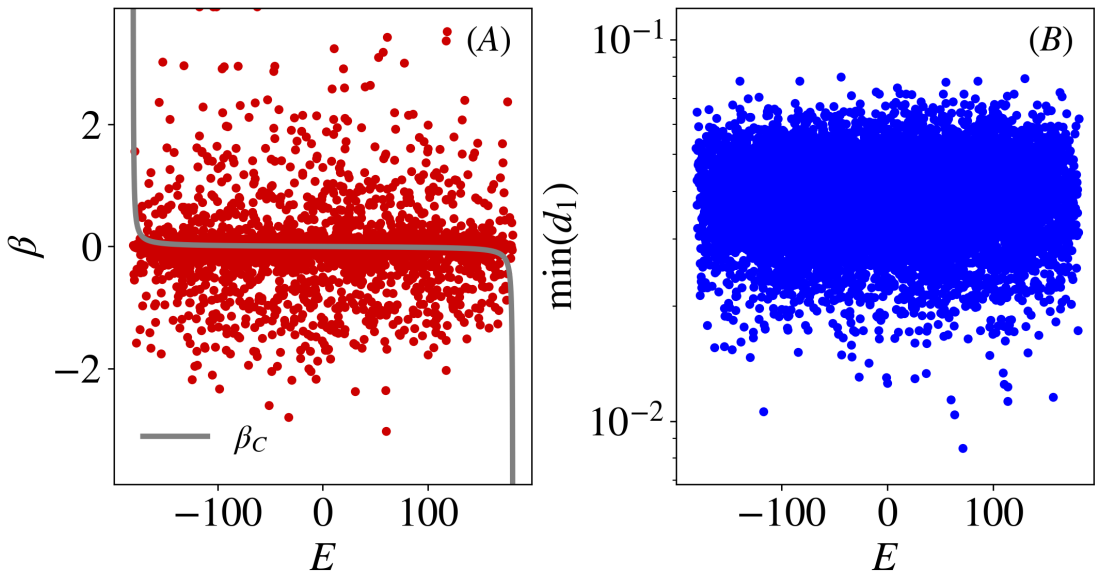


Figure 2.15: Subsystem temperature results for a random symmetric matrix with $D = 2^{13}$. **(A)** $\beta$ minimizing $d_1(\rho^A, \rho_C^A)$ ($\beta_S$) versus energy, plotted along side the canonical $\beta_C$ curve. **(B)** $\min(d_1(\rho^A, \rho_C^A))$ plotted versus energy.

## 2.6 Discussion & Context

Our first eigenstate-based temperature, $\beta_E$, turned out to be determined solely by the eigenvalues. It has interesting (arguably unexpected) dependencies on the distance measure. The relation $\beta_E = \beta_C/p$ is a mathematical result that holds for any system, including non-chaotic (e.g., integrable or localized) systems and even systems without any notion of locality.

In contrast, the second eigenstate-based temperature, $\beta_S$, is independent of the distance measure and reflects the physics of the eigenstates. This contrast highlights that the partial trace operation is a crucial ingredient for the emergence of thermodynamics. We have shown that $\beta_S$ conforms increasingly to $\beta_C$ when the system size increases while keeping $L_A$ (subsystem size) fixed and also while keeping the ratio $L_A/L$ fixed to some value smaller than 1/2. As $\beta_S$ depends on the chaotic (thermalizing) nature of the system and the physical content of the eigenstates, it does not match $\beta_C$ for random matrices and generally shows deviant behavior for non-chaotic systems, as shown in Section 2.5.

By asking how close $\rho^A$ can be to $\rho_C^A$, we have characterized the best temperature (typically different from the canonical temperature at finite sizes) and also the degree to which the system is thermal, e.g., through the value of the minimum

distance $d_1$. The issues addressed in the investigation of $\beta_S$ are closely related to (in some sense the converse of) questions addressed in the ETH/thermalization literature, e.g., in Refs. [11, 35, 52, 239–244]. Our results on size dependence confirms the intuition obtained from Refs. [11, 52, 240, 242] that thermal behavior is best seen in the limit of $L_A/L \to 0$.

The work described in this chapter raises a number of new questions.

(1) The partial trace and minimization operations in the definition of $\beta_S$ render analytical treatments difficult. Thus, it remains an open task to prove analytically that $\beta_S$ should be independent of $p$, or that it should approach $\beta_C$ in the large size limit. The latter is consistent with the spirit of ETH, which is similarly difficult to prove, but is verified in a wide array of numerical studies [7, 8, 10, 12–15, 17–19, 22–28, 31, 33, 34, 36–39, 41–45, 49, 225, 245–250].

(2) The correspondence between $\beta_S$ and $\beta_C$ may break down when approaching non-chaotic regimes, such as near-integrability or many-body localization [29, 195, 251]. There is the possibility of scaling with different power-laws than those seen here, in analogy to the power-law ETH scaling displayed by integrable models [24, 28, 246, 252–254]. In Section 2.5, we did observe the deviation of $\beta_S$ from $\beta_C$ as the system approached integrability, as one might have expected. A deeper investigation into the effects of integrability and localization is required.

(3) The subsystem temperature coinciding with the canonical temperature heavily relies on the eigenstate obeying the ETH. Therefore, it is possible that the subsystem temperature outlined here could be used to detect many-body quantum scars [96, 97]. If the overwhelming majority of eigenstates in a system have a subsystem temperature $\beta_S$ coinciding with the canonical temperature, then it should be considered a thermalizing system. Now, consider an eigenstate from the bulk of the spectrum whose subsystem temperature deviates significantly from the canonical value. This pronounced temperature deviation may indicate the presence of a rare non-thermal eigenstate, namely, a quantum many-body scar. In contrast to the entanglement entropy, often employed to detect scars, we do not need to determine the behavior of the rest of the eigenstates in the bulk of

the spectrum to classify an eigenstate as a scar state, as we know the expected canonical temperature. It is possible the minimum distance between the two reduced density matrices (used to define $\beta_S$) would also be abnormally large for scar states.

# Chapter 3

# Temperature from entropy

In this chapter, we investigate the definition of temperature arising from the standard thermodynamic relation in statistical mechanics (Eq.(1.3));

$$T = \left(\frac{\partial E}{\partial S}\right) = \left(\frac{\partial S}{\partial E}\right)^{-1}, \tag{3.1}$$

where $S(E)$ is the microcanonical entropy. We explore four procedures to compute the microcanonical entropy in finite quantum systems of sizes accessible to exact diagonalization, as discussed in Section 1.1.2, and derive a temperature via Eq. (3.1).

We start in Section 3.1 by recounting the definitions and saddle-point expressions that lead to the four procedures for calculating the microcanonical entropy in finite systems. We also provide details (subsection 3.1.3) of the quantum many-body systems that we use for numerical exploration — we present results for multiple systems with different geometries to ensure that the resulting conclusions are not artifacts of a particular lattice or Hamiltonian. In the following sections, we describe the four procedures for calculating entropy and present the results in each case. First, Section 3.2 describes counting eigenstates in an energy window of finite width. We first illustrate the results of using a constant-width energy window $\Delta E$ (subsection 3.2.1). Then, we describe using an energy-dependent window $\Delta E(E)$ designed to cancel out the explicit $\Delta E$-dependence of the resultant temperature (subsection 3.2.2), following and extending the suggestion of Ref. [54]. In Section

3.3, we instead formulate the entropy in terms of the integrated density of states. We start by outlining the use of a smoothed cumulative density of states $\Omega(E)$ to calculate the density of states $g(E)$. First, we can avoid making an explicit choice of $\Delta E$ — a possibility now that we are no longer counting eigenstates. We explain that this choice leads to finite size deviations between the resulting $\beta$ and $\beta_C$ (subsection 3.3.2). Finally, we can choose to make use of the derived energy-dependent $\Delta E(E)$ designed to account for the deviations (subsection 3.3.3). Section 3.4 provides a concluding discussion and some context. The results in this chapter are presented in [201], with some changes in the discussion and figures.

## 3.1 Preliminaries

In this section, we first recall the standard definition of the microcanonical entropy and highlight the roles of the density of states $g(E)$ and the energy window $\Delta E$ (subsection 3.1.1). We then recall the saddle-point formulation in subsection 3.1.2, often used to show the equivalence of microcanonical and canonical ensembles in the large-size limit [54], and extend beyond the leading order to analyze the effect of $\Delta E$ at finite sizes. Subsection 3.1.3 describes the quantum systems used in subsequent sections to provide numerical examples.

### 3.1.1 Entropy, density of states, and the energy window

In this chapter, we are concerned with computing temperature in an isolated finite quantum system via the standard statistical mechanical relation between entropy and temperature, Eq. (3.1). The microcanonical entropy $S(E)$ of a system at energy $E$ is given by [54, 73–77]

$$S(E) = k_B \ln \Gamma(E). \tag{3.2}$$

Here, $\Gamma(E)$ is the statistical weight, which is the number of microstates at energy $E$. In quantum systems, microstates are to be interpreted as eigenstates. For a quantum system with a discrete spectrum, counting the number of eigenstates is

problematic because, at a particular energy, there is usually zero, one, or perhaps a handful of eigenstates if there are degeneracies. Thus, $S(E)$ would be $= -\infty$ for all energy values except at a countable number of discrete energy values. This issue is usually resolved [54,75,76] by taking $\Gamma(E)$ to be the number of eigenstates in an energy window $\Delta E$ around $E$, rather than the number of eigenstates exactly at energy $E$. Thus we define

$$\begin{aligned} \Gamma(E) &= \int_{E-\Delta E/2}^{E+\Delta E/2} g(E')dE' \\ &= \int_{E-\Delta E/2}^{E+\Delta E/2} \sum_n \delta(E'-E_n)dE' \ , \end{aligned} \tag{3.3}$$

where the sum is understood to include all the eigenvalues of the Hamiltonian that lie in the window, i.e., all $E_n$ satisfying $E_n \in (E - \frac{\Delta E}{2}, E + \frac{\Delta E}{2})$ [1]. It is then common to approximate this integral [54, 94, 255–257] via

$$\Gamma(E) = \Delta E g(E) = \Delta E \sum_n \delta(E - E_n). \tag{3.4}$$

Here $g(E)$ is the *density of states* — the number of many-body eigenstates per unit energy interval. Due to the nature of the delta function, $g(E)$ has units of inverse energy. Thus $\Gamma(E)$ as defined in Eq. (3.4) is dimensionless. Although defined as a sum over delta functions, the density of states can be thought of as a smooth function of energy over energy scales much larger than the typical level spacing. In numerical work, this is often achieved by broadening the delta functions into Gaussians or Lorentzians of finite width [25, 192, 258–264]. Alternatively, we can define $\Omega(E)$ as the number of eigenstates with energy less than $E$, i.e., the integrated density of states. Fitting a smooth function to the staircase form of $\Omega(E)$, one can obtain a smooth density of states as the derivative; $g(E) = \Omega'(E)$.

The entropy now depends on an energy window $\Delta E$, so we are thus faced with choosing an appropriate $\Delta E$. The purpose of introducing a finite energy width was to smooth out the discreteness of the energy spectrum, thus $\Delta E$ should

[1] It is also common to use the window $[E, E + \Delta E)$. We choose to work with the window $[E - \Delta E/2, E + \Delta E/2]$. This choice presumably does not have significant effects.

be large enough to include a large number of eigenstates. On the other hand, we want $\Delta E$ to be sufficiently small so that the density of states (regarded as a smooth function of energy) does not vary appreciably within the window, i.e., $\Delta E$ should be much smaller than the scale of the bandwidth of the system. Other than these general principles, we have the freedom to choose $\Delta E$, and in general, the entropy $S$ will depend on the choice.

As we will explain in the following subsection 3.1.2, the sub-leading contributions to the entropy, which contain $\Delta E$, vanish in the large system size limit. So, for infinite systems, it will generally not matter what $\Delta E$ is, but for finite quantum systems, the choice can drastically affect the entropy, and resultant temperature. The purpose of this chapter is to investigate and clarify the effect of this choice for finite systems whose Hilbert space sizes makes them accessible to full numerical diagonalization.

### 3.1.2 Saddle point expressions

To understand the role of $\Delta E$, it is helpful to express the entropy as an integral over (complex) inverse temperature and perform a saddle-point approximation [54, 72, 74], extending the order beyond what is necessary in the thermodynamic limit, to account for finite sizes. The full saddle point calculation can be found in Appendix B, and is outlined below.

Replacing the delta function in the statistical weight definition Eq. (3.4), with its integral representation

$$\delta(x) = \int_{-\infty}^{\infty} \frac{d\beta}{2\pi} e^{i\beta x}, \tag{3.5}$$

and defining the free energy as $F(\beta) = -\beta^{-1} \ln\left(\sum_n e^{-\beta E_n}\right)$, we can write the entropy, Eq. (3.2), as

$$e^{S/k_B} = \Gamma(E) = i\Delta E \int_{-i\infty}^{i\infty} \frac{d\beta}{2\pi} e^{\beta(E - F(\beta))}. \tag{3.6}$$

The integral over $\beta$ is along the imaginary axis in the complex $\beta$ plane. To apply the saddle-point approximation, we first find the critical point of the exponent

$h(\beta) = \beta(E - F(\beta))$, by setting $h'(\beta) = 0$ and solving for $\beta$. The condition is

$$E - F(\beta) - \beta\frac{\partial F}{\partial \beta} = 0 \ , \tag{3.7}$$

which is equivalent to Eq. (1.1) defining the canonical temperature. Thus the saddle point is at $\beta = \beta_C$, the canonical inverse temperature. The leading order saddle-point approximation is thus

$$\frac{S}{k_B} = \beta_C E - \beta_C F(\beta_C), \tag{3.8}$$

with $\beta_C$ being the solution of Eq. (3.7) (or Eq. (1.1)), which lies on the real axis in the $\beta$ plane. This matches the standard thermodynamic relation, and is consistent with the energy derivative of $S$ being the inverse temperature $\beta_C$.

To examine the effect of $\Delta E$, one needs to extend the calculation to a higher order. One expands $h(\beta)$ as a Taylor series about $\beta_C$ up to second order, as the first order term is zero by definition. Introducing the heat capacity $C = \frac{\partial E}{\partial T} = -T\frac{\partial^2 F}{\partial T^2}$, one obtains [54]

$$e^{S/k_B} \approx \frac{\Delta E}{2\pi} e^{\beta_C(E - F(\beta_C))} \int_{-\infty}^{\infty} dy e^{-k_B T_C^2 C_C y^2/2}. \tag{3.9}$$

Here, $T_C$ and $C_c$ are the values at the saddle point $\beta_C$. Evaluating the Gaussian integral, one obtains

$$\frac{S}{k_B} = \beta_C E - \beta_C F(\beta_C) + \ln \Delta E - \ln \sqrt{2\pi k_B T_C^2 C_C}. \tag{3.10}$$

Here $\beta_C$ is determined by the energy, and hence so are $T_C$ and $C_C$. The two leading terms are both extensive in system size. The first correction term $\ln \Delta E$ is sub-extensive as long as $\Delta E$ is not chosen to grow exponentially or faster with system size. The second correction term grows logarithmically with system size, as the heat capacity is extensive. However, as it appears in the argument of a logarithm, its dependence on $L$ disappears when differentiated with respect to $E$. This means that when differentiating Eq. (3.10) to obtain $\beta$, the contribution

from the last term is does not grow with $L$, not even logarithmically. Thus, at large enough sizes, the leading-order saddle-point approximation suffices, and the choice of energy window $\Delta E$ plays no role.

However, the two correction terms should be considered when calculating the entropy at finite sizes. From Eq. (3.10), we see that choosing $\Delta E$ to be an energy-independent constant (the most obvious choice, explored in subsection 3.2.1) would leave an energy-dependent correction term, causing deviations from the canonical temperature. Thus, we see that the energy dependence of the correction terms could be canceled by an informed choice of energy dependence for the width $\Delta E$, as pointed out in Ref. [54] and explored below in subsection 3.2.2.

### 3.1.3 Systems and numerics

To investigate the effect of different choices for defining the microcanonical entropy in finite systems, we use several spin-1/2 lattice systems consisting of $L$ spins, $N$ of which are up. The spins interact via $XXZ$-like couplings, which have a $U(1)$ symmetry conserving $N$. We check all results and show data for 1D, 2D, and fully-connected geometries, to demonstrate that our results are very general and not particular to any model. In the case of the 1D chain, we also include magnetic fields in the $z$ and $x$ directions; the latter break the $U(1)$ symmetry. The Hilbert space dimension is $D = \binom{L}{N}$ when $N$ is conserved and $D = 2^L$ otherwise. The models, which are detailed in Section 1.4, consist of the staggered field model (Eq. (1.15)), a square lattice (Eq. (1.17)), and a fully connected lattice (Eq. (1.19)).

The system parameters are always chosen such that the level spacing statistics match that expected of chaotic quantum systems. This ensures there are no complications due to proximity to integrability or localization. For the fully-connected model, where interactions are of arbitrary range, the parameters are also chosen so that the density of states has a single peak, avoiding the possibility of non-monotonic behavior in the derivative of the microcanonical entropy. We

have checked our results for all three models, with various parameters satisfying these conditions. Below, we generally select one or two of the models to illustrate the results, but we emphasize that they are broadly invariant across the models; an exception being the energy scales.

*Units*: For numerical work, we use $k_B = 1$. We express energies in units of spin couplings. Thus, if $J$ (or $J_{jk}$) is set to 1, when we plot energies they are actually $E/J$; whereas if the couplings have other values, then the energy is to be thought of as the energy divided by a hypothetical coupling equal to 1. In this way, the units of all energies, temperatures, and entropies in the figures are determined.

## 3.2 Computing the entropy by counting eigenstates

In this section, we compute the entropy via Eq. (3.2) by counting the number of eigenstates in a window of finite width. First, we discuss the obvious choice — using a constant energy-independent width $\Delta E$ (subsection 3.2.1). Second, following the result of the saddle point approximation, we discuss making a judicious choice of energy-dependent $\Delta E(E)$ to cancel correction terms at finite sizes (subsection 3.2.2).

### 3.2.1 Using a constant width window

Eq. (3.10) implies that an energy-independent $\Delta E$ acts as an energy-independent shift of the entropy and hence does not affect the temperature. However, the last term in Eq. (3.10) is energy-dependent, and thus the temperature will differ from the canonical temperature — corresponding to the leading (first two) terms. This deviation should vanish in the large-size limit, but the extent of this deviation for finite sizes is not a priori clear. We show below, using explicit numerical examples, that using an energy-independent width leads to poor agreement between the resulting and canonical temperatures, for the system sizes under investigation

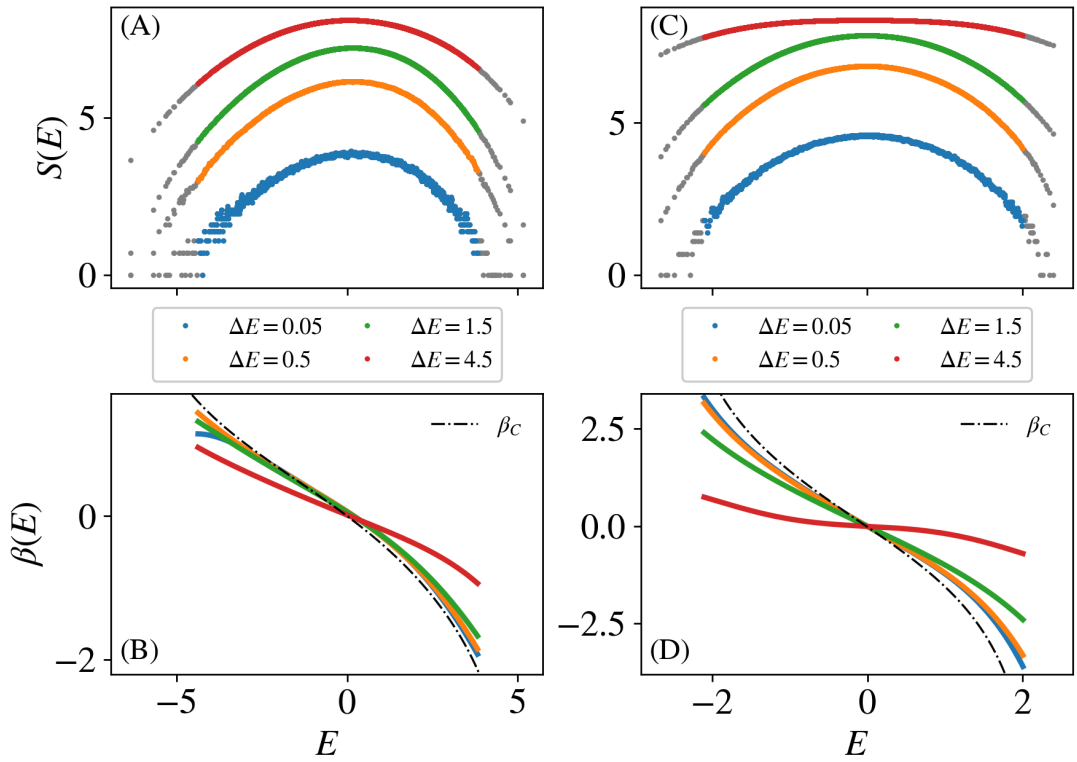


Figure 3.1: Result of using constant energy width: **(A,C)** Microcanonical entropy $S(E)$ calculated with constant (energy-independent) $\Delta E$. Evaluated only at the eigenenergies $E = E_n$. **(B,D)** Resultant inverse temperature $\beta(E)$ obtained as derivative of 6th-order polynomial fitted to $S(E)$ data. 25 eigenstates from both ends of the spectrum (shown in gray in **(A,C)**) were excluded from the fit. **(A,B)** Staggered field model, Eq. (1.15), with $L = 12$, $h_z = h_x = 0.5$ ($J = 1$, $\Delta = 0.95$). **(C,D)** $4 \times 4$ fully connected lattice, Eq. (1.19), with $L = 4 \times 4$, $N = 5$ ($J_{j,k} \in [-.4, .4]$, $\Delta_{jk} \in [-.1, .1]$).

here (sizes accessible to exact diagonalization).

Examples of entropy found by counting the number of eigenvalues within the window $[E - \Delta E/2, E + \Delta E/2]$ are shown in Figure 3.1(A, C) for two open-boundary spin-$\frac{1}{2}$ lattices with $XXZ$-like couplings. Here, and in later figures, we plot one point for each eigenvalue so that there is at least one eigenvalue in each window — the minimum entropy value is $\ln 1 = 0$, and we thus avoid the possibility of obtaining entropy $\ln 0 = -\infty$.

To calculate the temperature from the entropy, we fit a polynomial to the $S(E)$ points and then take the derivative of the polynomial; results are shown in Figure 3.1(B, D).

Increasing $\Delta E$ by a factor approximately increases the number of eigenvalues in each window by that factor, so that the $S(E)$ curve undergoes an approximately

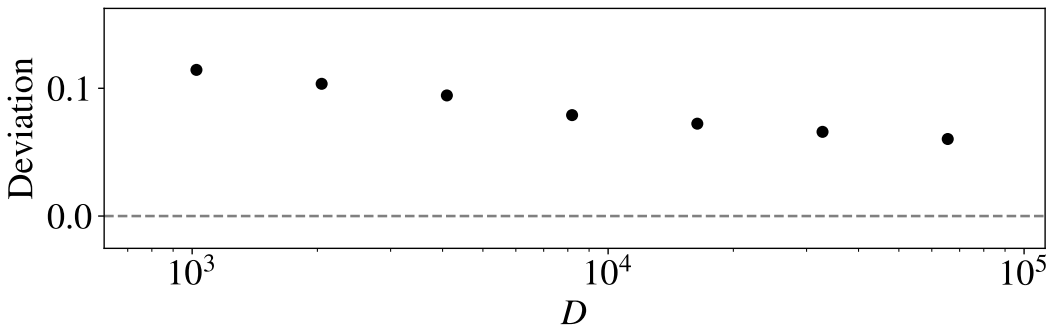


Figure 3.2: Root-mean-square (RMS) distance between $\beta(E)$ and the canonical temperature, versus Hilbert space dimension $D = 2^L$, with $\Delta E = 0.5$. Data for the staggered field model with $L$ spins, Eq. (1.15), $J = 1$, $\Delta = 0.95$, $h_z = h_x = 0.5$.

constant upward shift. This leaves the temperature $[S'(E)]^{-1}$ approximately unchanged. Accordingly, for moderate $\Delta E$, the calculated $\beta(E)$ curves are robust to changes in $\Delta E$. For the largest $\Delta E(= 4.5)$ shown, this argument does not work as the window is significant compared to the variation scale of the density of states $g(E)$, so that $g(E)$ cannot be considered constant within each window. This leads to a markedly different $\beta(E)$ curve for the large $\Delta E$ case. This effect is not captured by the saddle-point analysis or Eq. (3.10).

Even for moderate $\Delta E$, the deviation from the canonical $\beta_C$ curve is considerable. This shows that using a constant energy window width is not an ideal approach to defining entropy for finite quantum systems having Hilbert space dimensions $\sim O(10^4)$ — if we intend for the resultant temperature to match the canonical value. The results of Figure 3.1(B, D) provide a visual presentation of the extent of the discrepancy for such sizes. In Figure 3.2, we show the root-mean-square deviation of the inverse temperatures obtained with a constant $\Delta E$ from the canonical $\beta_C(E)$ values as a function of Hilbert space dimension. (We show data for a spin chain, for which finite size scaling is numerically more convenient than a square lattice.) The deviation decreases with increasing system size, as expected, although it is quite slow with respect to the growth of the Hilbert space dimension.

A remark on the edges of the spectrum is in order. As there are only a few eigenvalues in each window, the entropy values are noticeably discrete, namely $\ln n$, where $n$ is a small integer. For a regime with such discrete behavior,

statistical-mechanical considerations are not meaningful — we expect entropy to be a continuous function of energy. Therefore, we omit the edge points from the polynomial fit to $S(E)$. In Figure 3.1, we have omitted 25 eigenstates from each edge of the spectrum. This is approximately the energy region for which $S(E) \lesssim \ln 10$ for the $\Delta E = 0.5$ case. Later in this chapter, the same criterion will be used to exclude the spectral edges.

### 3.2.2 Using an energy-dependent window

We now describe using an energy-dependent window width $\Delta E \propto \sqrt{T_c^2 C_c}$. First, we explain the rationale behind our choice of $\Delta E(E)$ and then present numerical results.

#### Rationale

In Eq. (3.10), the leading-order terms (first two terms) yield the canonical temperature upon differentiation by energy, but there are two correction terms: $\ln \Delta E$ and $-\ln \sqrt{2\pi k_B T_c C_c}$. In Ref. [54], it is suggested to choose the two terms to be equal, so that the corrections vanish and the canonical temperature is recovered.

We note, however, that the correction terms need not cancel exactly — they will not affect the temperature $[S'(E)]^{-1}$ as long as they sum to an energy-dependent constant. Thus we could choose

$$\Delta E(E) \equiv \alpha^{-1} \sqrt{2\pi k_B T_c^2 C_c}. \tag{3.11}$$

with $\alpha$ being some constant. The window $\Delta E$ is thus energy-dependent because $T_c$ and $C_c$ are energy-dependent. The proposal of Ref. [54] corresponds to $\alpha = 1$.

The energy-dependent $\Delta E$ can also be motivated by the physical idea that the energy window should be determined by the fluctuation of energy in the canonical ensemble, as suggested, e.g., in Refs. [255, 256]. It turns out [74] that the distribution in energy in the canonical ensemble has width $\propto \sqrt{T^2 C}$. Thus, choosing the energy uncertainty as the energy window leads to the same prescription as Eq. (3.11).

So, labeling the number of states in an energy-dependent energy window $\Delta E(E)$ as $\tilde{\Gamma}(E)$, the entropy is obtained as

$$\tilde{S}(E) = k_B \ln\left(\tilde{\Gamma}(E)\right). \tag{3.12}$$

Differentiation gives the corresponding inverse temperature $\tilde{\beta}$. In the following subsection, we will describe the procedure for obtaining $\tilde{S}$ and $\tilde{\beta}$ numerically and discuss the results obtained.

We do not know of a principle guiding the choice of $\alpha$. We will show that, for the sizes of primary interest to us, $\alpha$ needs to be larger than 1. The reason is that for $\alpha = 1$, the energy window $\Delta E(E)$ turns out to be too broad, exceeding the energy scale at which the density of states varies, leading to poor results similar to the large constant $\Delta E$ case in Figure 3.1. This is clear from Eq. (3.11): the right-hand side scales like $\sqrt{L}$ as $C_c$ is extensive, while the variance of the density of states typically scales linearly with $L$. Thus for the system sizes under consideration here, $\sqrt{L}$ cannot be considered negligible compared with $L$. For larger system sizes, the acceptable range of $\alpha$ broadens, compatible with our expectation that the choice of $\Delta E$ should be less important for larger sizes.

**Numerical calculation and results**

In order to obtain $\Delta E(E)$ as defined in Eq. (3.11), we first need to calculate the heat capacity $C_c$ and the canonical temperature. We start by numerically computing the energy $E$ as a function of $\beta$ (or of $T$) via Eq. (1.1), using the eigenvalues of the Hamiltonian $H$, obtained numerically via exact diagonalization. This leaves us with a (numerical approximation to a) smooth injective function $E(T)$. As usual, inverting this numerically produces the canonical temperature $T_c$ as a function of $E$. In addition, estimating the derivative of $E(T)$ provides us with the heat capacity $C = \partial E/\partial T$, which we evaluate at the canonical value $T_c$. Figure 3.3(A) shows an example of $C_c$ as a function of energy, calculated in this way. The function is non-monotonic, going to zero at both zero and infinite temperatures.

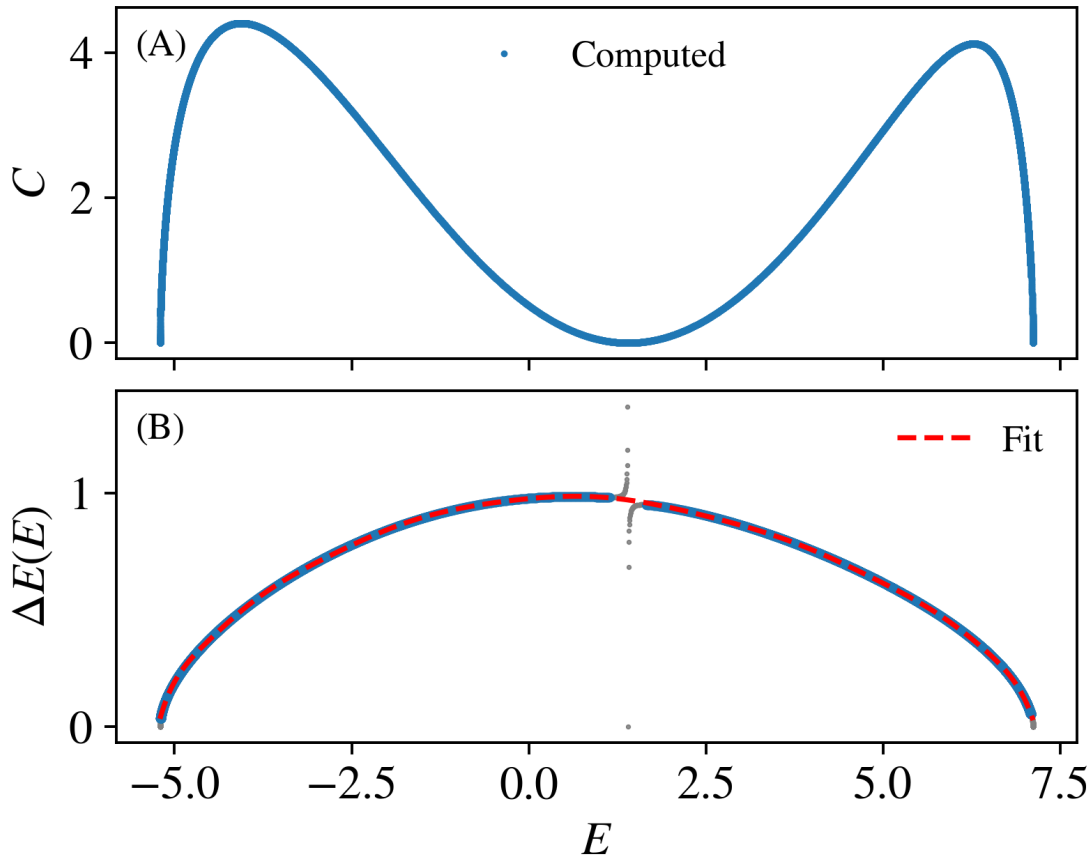


Figure 3.3: **(A):** Specific heat $C = \partial E/\partial T$. **(B):** $\Delta E(E) = \alpha^{-1}\sqrt{2\pi k_B T_S^2 C_S}$, for $\alpha = 5$, numerically computed. Dashed curve: 12-th order polynomial fit to points, excluding gray points around $C \to 0$, used to avoid the spurious divergence. Data for 5×4 square lattice, Eq. (1.17), with $N = 4$.

We can now calculate $\Delta E(E)$ via Eq. (3.11) for all energies. Figure 3.3(B) shows an example of the computed $\Delta E(E)$.

Near the center of the spectrum, $T_c \to \infty$ and $C_c \to 0$, leading to a finite $\Delta E(E) \propto \sqrt{T_c^2 C_c}$. Due to the numerical discreteness of the computed $E$ and $T$ functions, the computed $\Delta E(E)$ acquires a spurious divergence at this point. This effect can be confined to a smaller energy region; by using a finer grid of $T$ (or $E$) values. We avoid the effect by fitting a polynomial, excluding points within the direct vicinity of the discontinuity. An example is shown in Figure 3.3(B). The fitted polynomial is then used as $\Delta E(E)$.

We are now equipped to compute the entropy using an energy-dependent energy window, $\Delta E(E) = \alpha^{-1}\sqrt{2\pi k_B T_c^2 C_c}$. In Figure 3.4(A, C), we show the numerically computed entropy $\tilde{S}$. The data presented is for a chaotic square lattice of spins with $XXZ$-like connections between nearest neighbor spins and for

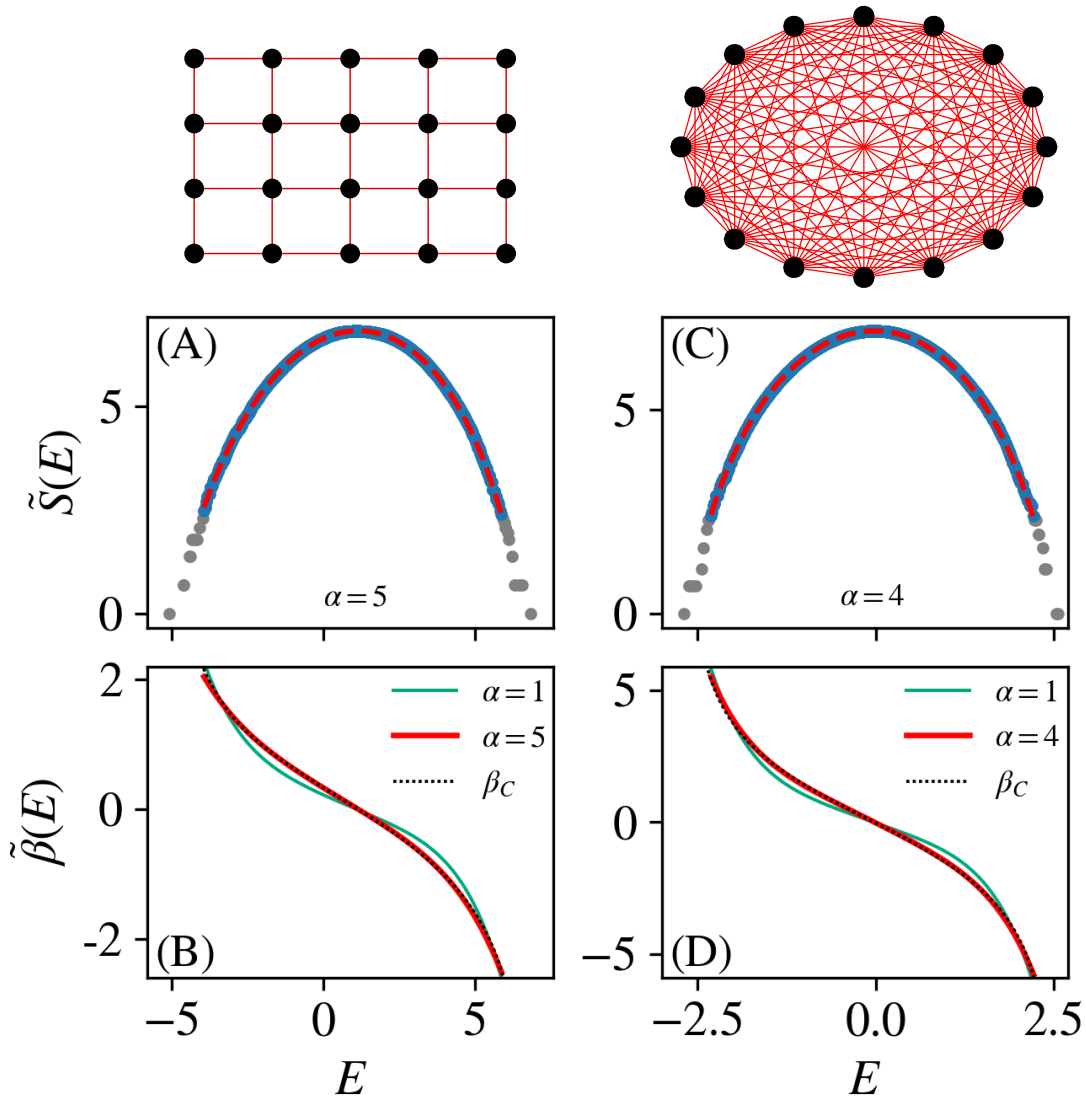


Figure 3.4: Using an energy-dependent window, Eq. (3.11). Left panels **(A, B)** and right panels **(C, D)** show data for two different systems. **(A,C):** Microcanonical entropy calculated with $\Delta E(E) = \alpha^{-1}\sqrt{2\pi k_B T_S^2 C_S}$ along with 6th-order polynomial fit. Fit excludes gray points. **(B,D)** Resultant temperature $\tilde{\beta}(E)$, with two different values of $\alpha$ in each case, compared with canonical temperature $\beta_C(E)$. **(A,B)** Data for 5×4 square lattice, Eq. (1.17), with $N = 4$. **(C,D)** Fully connected lattice, Eq. (1.19), with $L = 16$, $N = 5$.

a fully connected lattice with $XXZ$-like connections between every pair of sites. The geometry of each system is illustrated above the relevant plot. We used $\alpha = 5$ and $\alpha = 4$ in the two cases. Similar results were found for various chaotic 1D chains.

As before, we numerically fit a polynomial to our entropy data, excluding values at the edge of the spectrum, and then take its derivative to obtain a temperature. The resultant inverse temperatures $\tilde{\beta}$ are shown in Figures 3.4 (B,

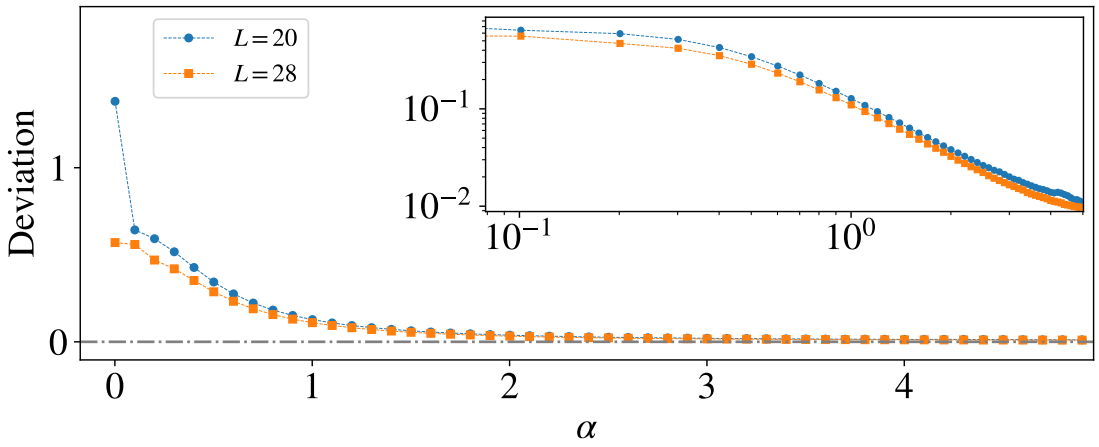


Figure 3.5: Using an energy-dependent window, Eq. (3.11). RMS distance between $\tilde{\beta}(E)$ and $\beta_C(E)$ plotted against $\alpha$ for two square lattices, Eq. (1.17), a $5 \times 4$ lattice with $N = 4$, and a $7 \times 4$ lattice with $N = 5$.

D). For $\alpha \sim 5$, the temperature matches the canonical temperature remarkably well. We also show the result of using $\alpha = 1$; in both cases, the deviation between the temperatures is markedly worse than for $\alpha \sim 5$.

We found that the procedure produces an excellent match between $\tilde{\beta}$ and $\beta_C$ when $\alpha$ is beyond some minimum value, as shown by the vanishing root-mean-square deviation in Figure 3.5. Beyond this minimal $\alpha$, the exact choice is somewhat arbitrary as long as the window is not made ultra-small (by having too large an $\alpha$). Figure 3.5 shows that this minimal value (the value of $\alpha$ at which the deviation can be considered negligible) is smaller for larger systems. This is consistent with the expectation that the exact choice of the window $\Delta E$ is increasingly irrelevant as the system size increases.

To summarize: this numerical analysis shows that counting eigenstates in an energy-dependent window is a very successful strategy for defining entropy in a finite-size system. We observed good agreement between the resultant and canonical temperatures for all systems we checked, including various 1D chaotic spin chains and a handful of 2D lattices, including that presented in Figure 3.4.

## 3.3 Using the integrated density of states

In this section, we formulate the entropy in terms of the cumulative density of states, or integrated density of states, $\Omega(E)$. We describe how to numerically

obtain a smoothed approximation to the density of states, $g(E) = \Omega'(E)$. In this formulation, we no longer count eigenstates in a window of width $\Delta E$. We first approximate the entropy purely in terms of the integrated density of states, circumventing the need to choose a value of $\Delta E$ explicitly. We explain that this will lead to finite size deviations from the canonical temperature. Following this, we utilize the energy-dependent $\Delta E(E)$, derived in Section 3.2.2 to account for finite-size effects, in conjunction with the smoothed approximation to the density of states. We observe that this leads to excellent agreement with the canonical temperature.

### 3.3.1 Formulation

An alternative to counting eigenstates in an explicit energy window is to use the expression for the entropy in terms of the (integrated) density of states:

$$\begin{aligned} S = \; k_B \ln \Gamma(E) &= k_B \ln \big(g(E)\Delta E\big) \\ &= k_B \ln g(E) + k_B \ln \Delta E \\ &= k_B \ln\left(\frac{\partial \Omega(E)}{\partial E}\right) + k_B \ln \Delta E. \end{aligned} \tag{3.13}$$

Here,

$$\Omega(E) = \sum_{n=1}^{D} \Theta(E - E_n), \tag{3.14}$$

is the number of eigenstates $|E_n\rangle$ with energy $E_n$ less than $E$, i.e., the integrated density of states or the cumulative density of states, also known as the cumulative level density [265–276] or the cumulative spectral function [15, 38, 194, 243, 274, 277–283].

From the eigenvalue spectrum of the system Hamiltonian, computed numerically using exact diagonalization, the integrated density of states $\Omega(E)$ can be obtained as a function of $E$. It is a series of steps with constant integer values between eigenvalues and a step to the next integer at every eigenvalue. In order to obtain the derivative of this non-smooth function, we will fit an analytic function to the computed $\Omega(E)$ data, and then simply take its derivative. Fitting an

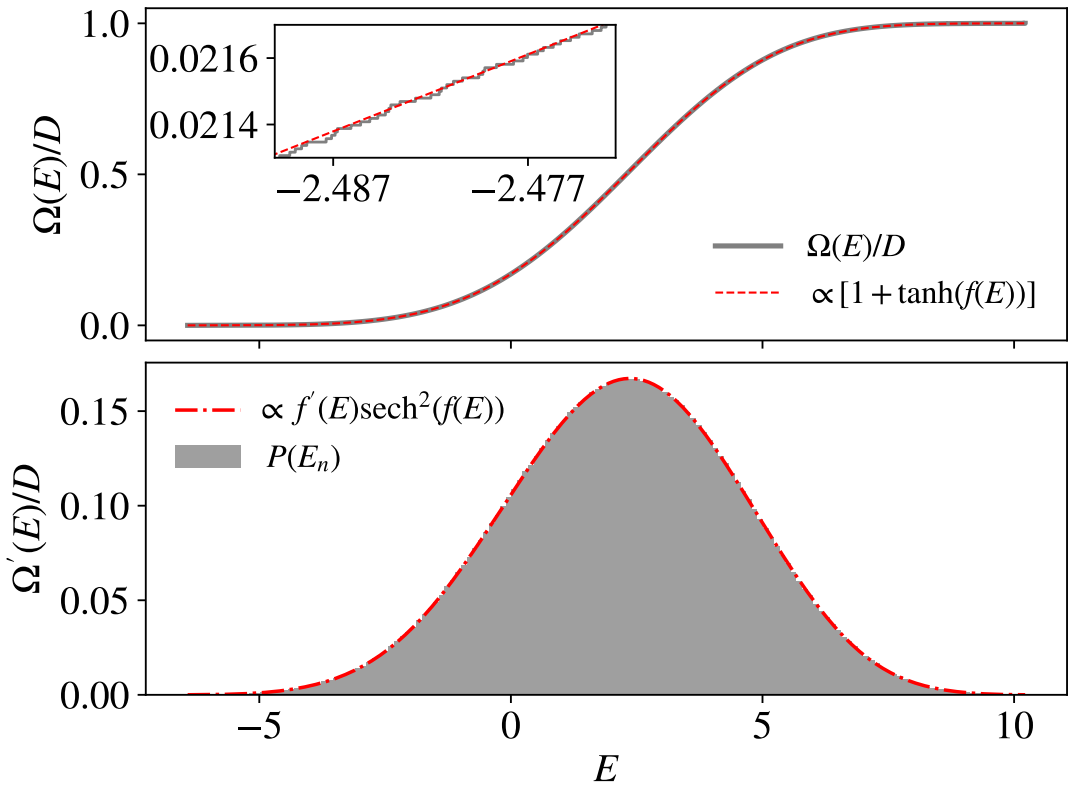


Figure 3.6: **Upper:** Cumulative density of states $\Omega(E)$ (normalized by Hilbert space dimension), fitted by a polynomial $f(E)$ of degree 10. Inset: zoom. **Lower:** $\Omega'(E)/D$ from derivative of fitted function, compared with histogram (distribution) of eigenvalues, $P(E_n)$. Data for $7 \times 4$ square lattice, Eq. (1.17), with $N = 5$.

analytic function to $\Omega(E)$ is common practice in the unfolding procedure utilized for computing level spacing statistics [38, 187, 191–194] as discussed in Section 1.4 of the introduction.

We found that using a function of the form

$$\Omega(E) \;=\; \frac{D}{2}\big[1 + \tanh(f(E))\big] \tag{3.15}$$

works remarkably well to fit the numerical $\Omega(E)$ data, where $f(E)$ is some polynomial in $E$, which is generally of order $\sim 10$ to allow for the data to be fit accurately. We note that Eq. (3.15) is of a similar form to the standard logistic function, used to approximate the Heaviside step function; it is thus not all that surprising that it works well.

If $f(E)$ is a monotonically increasing polynomial, then the form of the function automatically imposes the correct low-energy and high-energy behavior of the smoothed $\Omega(E)$. This functional form was inspired by its use in [281] to unfold a

many-body spectrum. Once the fitting function $f(E)$ is determined, the density of states is obtained as the derivative:

$$g(E) \;=\; \Omega'(E) \;=\; \frac{D}{2}\,\mathrm{sech}^2(f(E))f'(E). \tag{3.16}$$

An example of the numerically calculated $\Omega(E)$ and the fitted function are shown in Figure 3.6 (top) for a square lattice with $XXZ$-like connections. The resulting derivative $\Omega'(E)$ is compared with the normalized histogram of eigenvalues (bottom). In both panels, we normalize the functions by $D$ so that they are plotted between 0 and 1, and the derivative can be directly compared with the normalized eigenvalue distribution $P(E_n)$.

With the density of states $\Omega'(E)$ in hand, we are now equipped to compute the entropy via Eq. (3.13), and the resultant temperature. In the following two subsections we present two ways to do so.

### 3.3.2 Avoiding a choice of window width

The density of states increases exponentially with the system size; hence the first term in Eq. (3.13) is extensive. On the other hand, $\ln \Delta E$ is presumably either constant or, at most, weakly increasing with system size.

Thus, at sufficiently large system sizes the second term can be neglected so that the first term approximates the entropy:

$$S \approx S_\Omega = k_B \ln g(E) = k_B \ln\left(\frac{\partial \Omega(E)}{\partial E}\right). \tag{3.17}$$

One can thus use a continuous approximation for $\Omega(E)$ to define a continuous $S_\Omega(E)$, without choosing an explicit energy window $\Delta E$.

$S_\Omega$ is the logarithm of $g(E) = \Omega'(E)$, and $\beta_\Omega$ is thus the derivative of this. For the analytical approximation to $\Omega'(E)$ above, one obtains

$$\beta_\Omega(E) = \frac{f''(E)}{f'(E)} - 2f'(E) \cdot \tanh(f(E)). \tag{3.18}$$

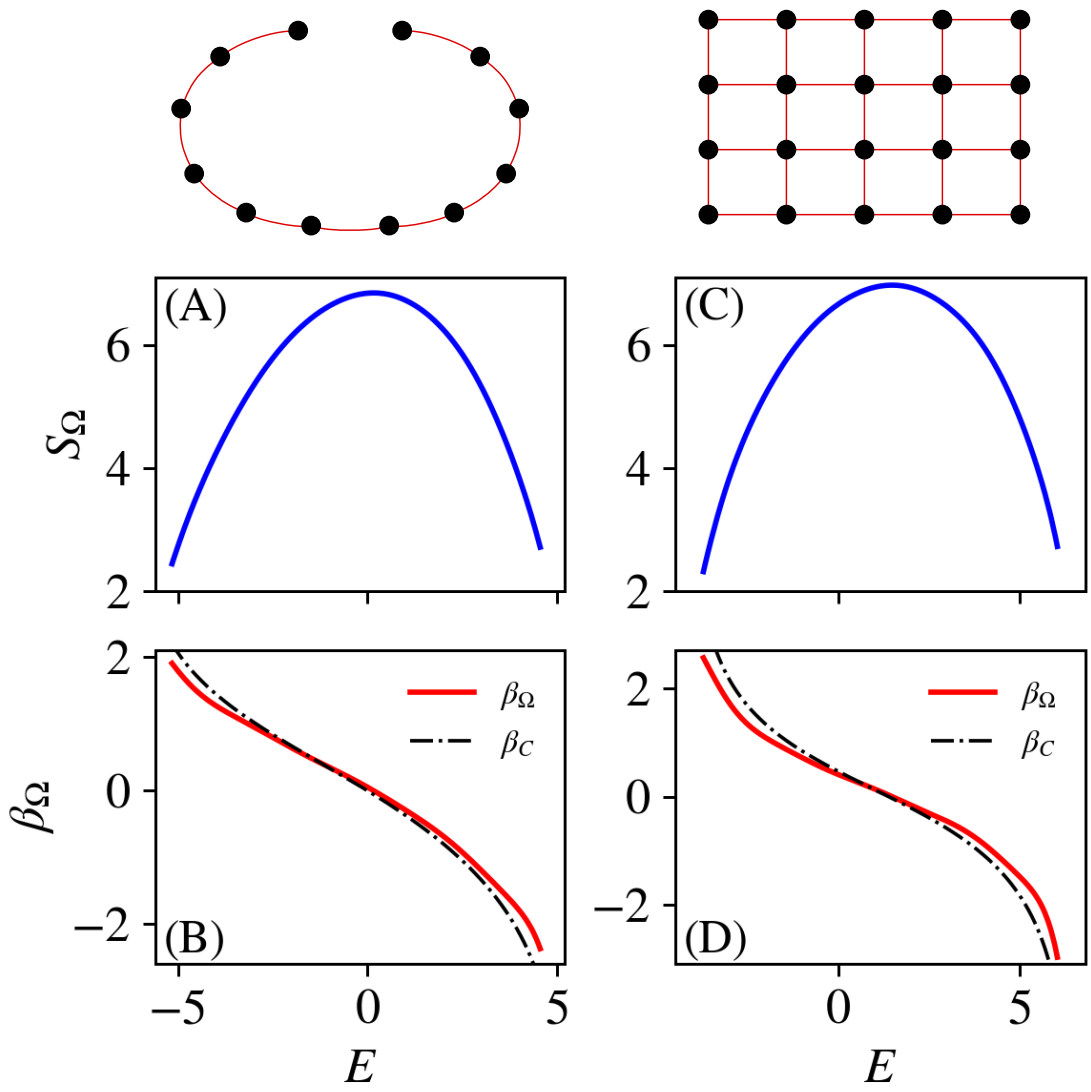


Figure 3.7: Entropy and temperature using a continuous approximation to the cumulative density of states. **(A,C)** $S_\Omega = \ln \Omega'(E)$. **(B,D)** Resultant inverse temperature $\beta_\Omega = \partial_E S_\Omega$ compared with the canonical temperature $\beta_C$. **(A,B)** Staggered field model, Eq. (1.15), with $L = 12$, $J = 1$, $\Delta = 0.95$, $h_z = h_x = 0.5$. **(C,D)** $5 \times 4$ square lattice, Eq. (1.17), with $N = 4$.

Examples of the computed entropy $S_\Omega$ are shown in Figure 3.7(A, C). The presented numerical results are for a 1D spin chain and a square lattice, both with nearest neighbor $XXZ$-like connections and open boundary conditions. The geometry of each system is illustrated above the relevant plot. The resultant inverse temperature $\beta_\Omega$ are shown in panels (B, D). While $\beta_\Omega$ has the correct overall form, the deviations from the canonical curves are clearly visible.

The extent of the deviation is shown quantitatively in Figure 3.8 by plotting the root-mean-square (RMS) distance between the canonical and resultant temperature

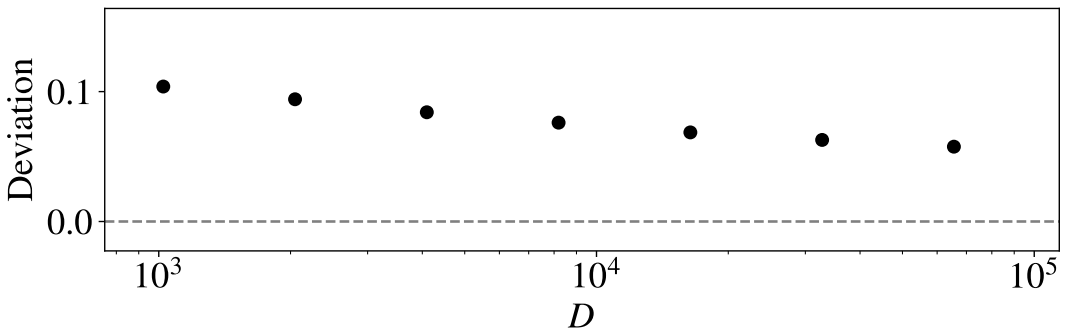


Figure 3.8: RMS distance between $\beta_\Omega(E)$ and $\beta_C(E)$, versus $D = 2^L$, for the staggered field model, Eq. (1.15), $J = 1$, $\Delta = 0.95$, $h_z = h_x = 0.5$, and variable $L$.

versus Hilbert space dimension $D$, for an $L$-site spin chain ($D = 2^L$). The deviation decreases very slowly — it would take exceedingly large system sizes for the two temperatures to be considered 'close'.

We now discuss two ways of understanding the finite-size deviation of the temperature obtained using $S_\Omega$ as defined in Eq. (3.17).

First, using Eq. (3.17) for the entropy means omitting the $\ln \Delta E$ term from the definition, Eq. (3.13), which can be written as

$$S = S_\Omega + k_B \ln \Delta E. \tag{3.19}$$

Since we avoided explicitly choosing a value for $\Delta E$, it is not immediately obvious what the effect of dropping the second term is, but we can analyze different cases:

- If we consider $\Delta E$ energy-independent, then $S_\Omega$ will lead to the same temperature obtained from the microcanonical entropy $S$. However, we know from subsection 3.2.1 that $S$ obtained using an energy-independent $\Delta E$ leads to considerable finite-size deviations in the temperature.

- On the other hand, if we consider $\Delta E$ to be energy-dependent, e.g., if it were designed to cancel the sub-leading deviations from the canonical ensemble as in subsection 3.2.2, then $S'_\Omega(E)$ will differ from $S'(E)$, and we would again get finite-size deviations.

Thus, it appears that $S'_\Omega(E)$ can be expected to deviate from $\beta_C$ in either case.

Second, we note that Eq. (3.17) applies the logarithm to a dimensionful

quantity, which, strictly speaking, is not allowed. For consistency, one needs to multiply the argument of the logarithm in Eq. (3.17) by a quantity with dimensions of energy; let us call this quantity $\epsilon$. Then Eq. (3.17) should really have the form

$$S_\Omega = \ln\left[g(E)\epsilon\right] = \ln\left[\Omega'(E)\epsilon\right]. \tag{3.20}$$

One can then carry out the same saddle point approximation as previously performed in subsection 3.1.2 for the original definition of $S$, leading to

$$\frac{S_\Omega}{k_B} \approx \beta_C E - \beta_C F(\beta_C) + \ln\epsilon - \ln\sqrt{2\pi k_B T_c^2 C_c}. \tag{3.21}$$

We again observe that unless $\epsilon$ is carefully chosen, as we described for $\Delta E$ in subsection 3.2.2, the last term will lead to finite-size deviations. The procedure in this section avoids specifying $\Delta E$ and ignores the need for the quantity $\epsilon$. Thus, one would expect deviations due to the $-\ln\sqrt{T_c^2 C_c}$ term, essentially of the same type as that encountered in subsection 3.2.1 when using an explicit energy-independent value of $\Delta E$.

### 3.3.3 Using an energy-dependent window

Now, rather than neglect $\Delta E$ in Eq. (3.13), we retain the term, i.e., we consider the entropy in terms of the integrated density of states as:

$$S(E) = k_B \ln(g(E)\Delta E) = k_B \ln\left(\frac{\partial\Omega(E)}{\partial E}\Delta E\right). \tag{3.22}$$

We have a smooth approximation to $\Omega'(E)$, and as proposed in subsection 3.2.2, we could choose an energy-dependent $\Delta E(E) \propto \sqrt{T_c^2 C_c}$ to account for the finite size deviations. Here, the constants of proportionality will only result in a shift in entropy, as we are not counting eigenstates in an energy window of width $\Delta E(E)$ around $E$. In that case, we had to choose a constant $\alpha$, such that the window width was not comparable to the bandwidth of the spectrum.

Here, rather than count the number of eigenstates, we are using the derivative

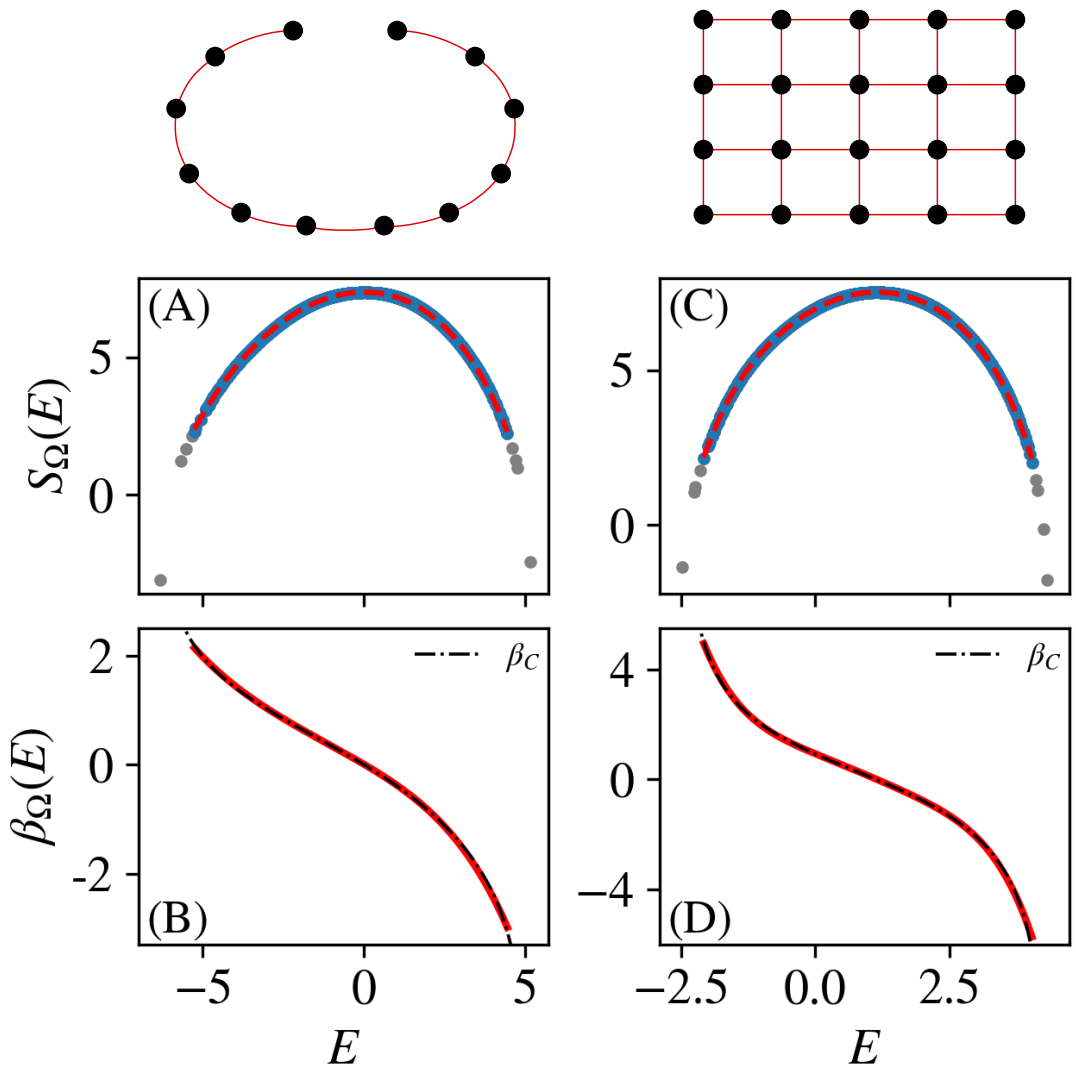


Figure 3.9: Entropy and temperature using a continuous approximation to the cumulative density of states and an energy dependent $\Delta E(E) = \sqrt{T_c^2 C_c}$. **(A,C)** $S_\Omega(E) = \ln(\Omega'(E)\Delta E(E))$. **(B,D)** Resultant inverse temperature $\beta_\Omega(E) = \partial_E S_\Omega(E)$ compared with the canonical temperature $\beta_C$. **(A,B)** Staggered field model, Eq. (1.15), with $L = 12$, $J = 1$, $\Delta = 0.95$, $h_z = h_x = 0.5$. **(C,D)** $5 \times 4$ square lattice, Eq. (1.17), with $N = 4$.

of our smoothed approximation to the integrated density of states to compute $g(E)$. The proportionality constants in this formulation are arbitrary — the entropy can thus be written as:

$$S_\Omega(E) = \ln\left[\Omega'(E)\sqrt{T_c^2 C_c}\right]. \tag{3.23}$$

Here, we once again make use of the smoothed approximation $\Omega'(E) = \frac{D}{2}\operatorname{sech}^2(f(E))f'(E)$ (Eq. (3.16)). Determining the canonical temperature $T_c$ and heat capacity $C_c$ nu-

merically has been previously discussed (subsection 3.2.2). Thus we are equipped to numerically calculate the entropy, Eq. (3.23), and by fitting a polynomial to the resulting data, we can take its derivative to obtain the inverse temperature.

Examples of the computed entropy $S_\Omega(E)$ are shown in Figure 3.9(A,C). The numerical results shown are for a 1D spin chain and a square lattice, both with nearest neighbor $XXZ$-like connections and open boundary conditions. The resultant inverse temperatures $\beta_\Omega(E)$ are shown in panels (B,D). We see that $\beta_\Omega(E)$ aligns very well with the canonical temperature $\beta_c$. We note that a pleasing aspect of this formulation is that it requires no fine-tuning of constants, as they only result in a shift of entropy.

## 3.4 Concluding discussion & context

The equivalence of the microcanonical and canonical ensembles emerges in the infinite-size limit. However, as the discussion of statistical mechanics in isolated systems often relies on finite-size examples obtained through numerical diagonalization, we must understand deviations from ensemble equivalence in systems of such sizes. In finite systems, the definition of the microcanonical entropy involves choices that become relevant when dealing with system sizes accessible to numerical diagonalization. In this chapter, we contribute to this understanding by investigating and comparing various ways of computing the microcanonical entropy and comparing the resultant temperatures (via Eq. (1.3)) to the canonical temperature (Eq. (1.1)).

The microcanonical entropy $S(E)$ is defined as in Eqs. (3.2) and (3.4). Inspired by the discussion of Ref. [54], we explored four ways of calculating $S(E)$ numerically. First, in Section 3.2, we computed the entropy by counting eigenstates in a finite window. We explored the result of using a constant-width energy window (subsection 3.2.1) and using an energy-dependent window with the energy-dependence designed to cancel sub-leading terms (subsection 3.2.2). As an alternative to counting eigenstates, in Section 3.3, we formulated the entropy in terms of the integrated density of states. Within this formulation, we explored

using an approximation that avoids the energy window altogether (subsection 3.3.2). Finally, we used this formulation in combination with the energy-dependent $\Delta E(E)$ designed to account for deviations.

We have demonstrated that counting eigenstates in the energy-dependent window, $\Delta E(E) = \alpha^{-1}\sqrt{2\pi k_B T_c^2 C_c}$, reproduces the canonical temperature particularly well for the sizes under consideration. Utilizing an energy-dependent window was suggested by Ref. [54] with $\alpha = 1$, designed to exactly cancel the sub-leading terms in Eq. (3.10). We have shown (Figure 3.4) that, for the sizes under question, a greater $\alpha$ is required; for $\alpha = 1$, the windows exceed the energy scale of variation of the density of states. A consequence of this result is that, since we have no further criterion for fixing $\alpha$, the microcanonical entropy is only defined up to an arbitrary additive constant. The constant is sub-extensive and is unimportant in the infinite-size limit, and an additive constant does not affect the temperature. Nevertheless, the arbitrariness is unsatisfactory. In fact, a pleasing aspect of the suggestion of Ref. [54] was a reasonable criterion for defining entropy without such an arbitrary constant. For the size ranges under consideration in this work, the $\alpha = 1$ prescription is not usable, so we are forced to accept an arbitrary choice.

However, using the entropy $S_\Omega(E)$ in Section 3.3.3, combining the use of an energy-dependent $\Delta E(E)$ with an approximation to the density of states constructed from the integrated density of states $\Omega$, we observed excellent agreement between the resulting temperature and the canonical temperature. In this case, the constants in $\Delta E(E)$ (Eq. (3.11)) do not affect the resultant temperature, as they shift the entropy — a consequence of no longer counting eigenstates. This method is thus free from any fine-tuning of constants, an aspect that we find quite pleasing.

The other two procedures, counting eigenstates in an energy-independent $\Delta E$ and avoiding a choice of $\Delta E$ altogether ($S \approx S_\Omega$), both lead to very noticeable finite-size deviations. The deviations in the constant-$\Delta E$ case are expected from the sub-leading corrections. For the procedure in Section 3.3 using $S \approx$

$k_B \ln\left(\frac{\partial\Omega(E)}{\partial E}\right)$, we have argued that the deviations are essentially the same type as that in the constant-$\Delta E$ case.

*Numerically*, calculations of microcanonical entropy and temperature have appeared in the recent literature [94, 243, 256, 257]. Refs. [243, 257] have used the $S \approx S_\Omega$ approximation. The resulting temperature presented in Ref. [243] (Figure 4) appears to have similar deviations from the canonical temperature as we have presented and analyzed in Section 3.3. The density of states is approximated in Ref. [243] via a polynomial fit to the cumulative spectral function and in Ref. [257] via the kernel polynomial method [284, 285]. In Ref. [256], the microcanonical entropy has been calculated with $\Delta E$ "determined by the energy uncertainty" — this is presumably equivalent to the energy-dependent window we explored in Section 3.2.2.

*Alternatively,* in finite quantum systems, the entanglement entropy of a subsystem is often discussed as representing the thermal entropy [11, 52, 53, 286, 287]. The reason is that, in a chaotic (thermalizing) quantum system, it is expected that the reduced density matrix of subsystems smaller than half the system should resemble thermal density matrices [11, 35, 51, 53, 57, 66, 200], an expectation inspiring our eigenstate-based temperature in Chapter 2. It is amusing to note that the entanglement entropy is obtained from eigenstates, whereas the entropies and temperatures studied in this chapter are derived from eigenenergies. Ref. [11] describes the finite-size behavior of the deviation of the entanglement entropy from the canonical entropy for a particular spin chain. The behavior of the temperature derived using Eq. (3.1) from the entanglement entropy (interpreted as entropy) would be interesting to examine in future work, building upon our eigenstate-based temperatures in Chapter 2.

It has also been argued that entropy for finite-size systems should be defined as $S \sim \ln \Omega(E)$ [288–293], instead of the more common $S \sim \ln \Omega'(E)$ examined here. This approach avoids the appearance of negative temperatures even in systems with finite Hilbert space dimension, as the function $\Omega(E)$ is non-decreasing. Thus, it is clear that the temperature obtained from the entropy $\ln(\Omega(E))$ will not match

the canonical temperature once $\beta_C < 0$. It may still be interesting to ask how the deviations from ensemble equivalence behave under this alternative definition.

*Regarding the ETH* - In this chapter, we have largely focused on the microcanonical entropy in the context of temperature and ensemble equivalence. However, the microcanonical entropy also appears in the ETH ansatz put forward by Srednicki [4] (Eq. (1.6)), presented as the 'thermodynamic entropy' and is defined in a similar fashion to Eqs. (3.2) and (3.4). It would be interesting to investigate the result of using Eq. (3.23) in its place for finite systems.

# Chapter 4

# Non-Hermitian scattering on a tight-binding lattice

In this chapter, our primary focus is analyzing the scattering dynamics and spectrum of a quantum particle on a tight-binding lattice subject to a non-Hermitian (purely imaginary) local potential. We also consider a $\mathcal{PT}$-symmetric system, constructed by balancing loss and gain in the lattice; we make statements about its spectrum using similar methods as in the purely dissipative model. In addition, we begin to build towards an understanding of a many-body system by presenting results for a system of non-interacting particles.

In the single-particle system, the non-Hermitian Hamiltonian describing a tight-binding lattice under the influence of an imaginary potential, as defined in Eq. (1.4), is given by

$$H \;=\; -J\sum_{j=1}^{L-1}\Big(|j\rangle\langle j+1| + |j+1\rangle\langle j|\Big) \;-\; i\gamma|q\rangle\langle q|, \tag{4.1}$$

where $q \in [1, L]$ is the location of the dissipative impurity. Here $\gamma$ is a positive constant so that the imaginary potential is absorbing. The labels for the bras and kets here are site labels: The particle lives on an $L$-site chain with open boundary conditions. The hopping strength will subsequently be set to $J = 1$, i.e., energies and times are measured in units of $J$ and $1/J$, respectively, and are therefore presented without units. Additionally, the spacing between sites is set to unity so

that lengths and wavenumbers are also dimensionless. In the following sections, we present the results of our investigation.

Starting with the purely dissipative model, in Section 4.1, we present the scattering results and comparisons with the continuum case. Section 4.2 discusses the spectrum and exceptional points. In Section 4.3, we investigate the system at large values of $\gamma$ and draw a comparison between real and imaginary potentials via their bound states. Following this, in Section 4.4, we introduce a $\mathcal{PT}$-symmetric system and prove the existence of exceptional points analytically. Then in Section 4.5, we present some results for a non-interacting system, building towards a many-body system. We show that interactions lead to the absence of a particular exceptional point pattern observed in the non-interacting case. Finally, Section 4.6 presents some discussion and concluding remarks. The material in Sections 4.1-4.3 are published in Ref. [202], with some differences in the details of the presentation.

## 4.1 Scattering at an absorbing potential — reflection, transmission, absorption

In this section, we examine the scattering of a quantum particle by a single dissipative impurity. To compare with the corresponding continuum system, we first work out the results for the continuum system in subsection 4.1.1. We then present numerical results for the lattice problem in subsection 4.1.2 before comparing both cases in subsection 4.1.3.

### 4.1.1 Continuum scattering by an imaginary delta-potential

Complex scattering potentials in the continuum have been considered generally in the literature [174, 175, 294]. We are specifically interested in the case of an imaginary potential of delta-function shape, which is the analog of the single-site potential on a lattice.

In the continuum, the wavefunction $\psi(x)$ satisfies the time-independent Schrödinger

Equation:

$$-\frac{\hbar^2}{2m}\frac{d^2\psi(x)}{dx^2} \; + \; V(x)\psi(x) \; = \; E\psi(x). \tag{4.2}$$

(We will eventually set $\hbar = 1$ but retain it for now.) We take $V(x)$ to be a negative imaginary delta potential: $V(x) \; = \; -i\gamma\delta(x)$.

Solving the scattering problem is a variation of the standard textbook scattering problem with a real delta-function potential [295]. We take the wavefunction $\psi(x)$ to be of the form $Ae^{ikx} + Be^{-ikx}$, although the coefficients are not necessarily the same on both sides of the potential ($x = 0$); hence we write

$$\psi(x) \; = \; \begin{cases} \psi_L(x) \; = \; A_L e^{ikx} + B_L e^{-ikx} \; , & x < 0 \\ \psi_R(x) \; = \; A_R e^{ikx} + B_R e^{-ikx} \; , & x > 0. \end{cases} \tag{4.3}$$

Considering a particle moving from the left side of the potential to the right, we set the coefficients as:

$$\begin{aligned} A_L \; &= \; 1, \; B_L \; = \; r, \\ A_R \; &= \; 0, \; B_R \; = \; t, \end{aligned} \tag{4.4}$$

with $r$ and $t$ the coefficients of the wave that are reflected and transmitted, respectively. We then use the appropriate (dis)continuity conditions at $x = 0$,

$$\psi(0) \; = \; \psi_L(0) \; = \; \psi_R(0) \; , \quad \frac{\hbar^2}{2m}(\psi'_R(0) - \psi'_L(0)) \; = \; -i\gamma\psi(0), \tag{4.5}$$

to solve for the reflection ($r$) and transmission ($t$) amplitudes. Here, the second condition is obtained by integrating the Schrödinger equation around $x = 0$ over an interval $[-\epsilon, \epsilon]$.

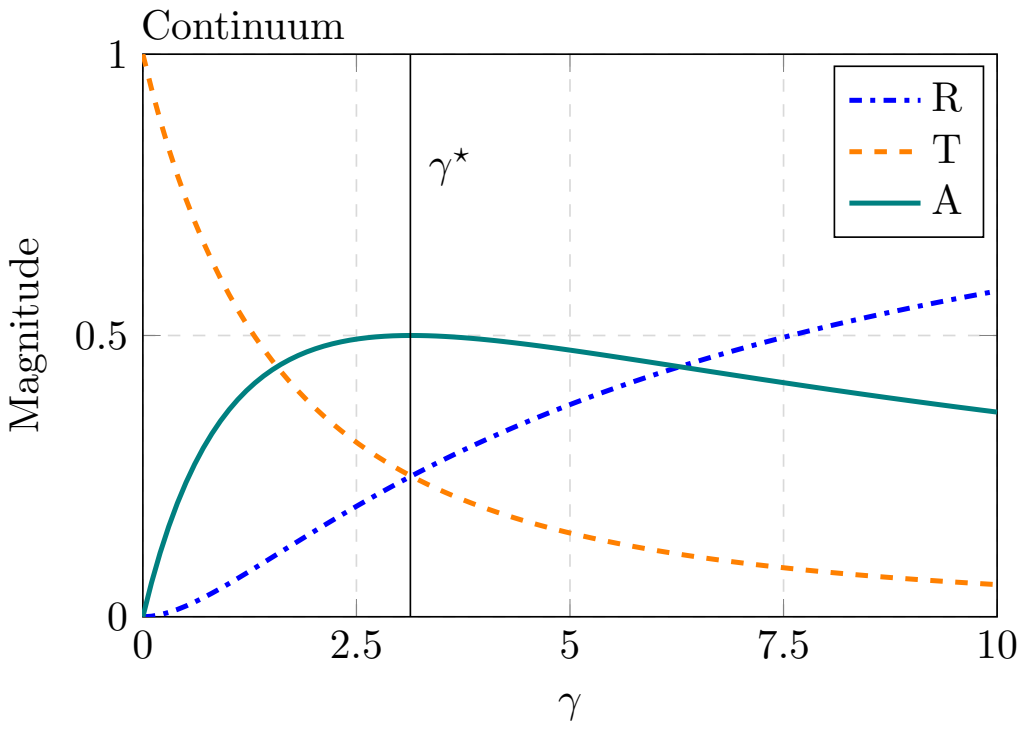


Figure 4.1: Results of continuum scattering: The reflection, transmission, and absorption probabilities ($R$, $T$, $A$), plotted against the strength $\gamma$ of the dissipative delta-potential. Here $k = \pi/2$, $\hbar = 1$, and $m = 0.5$.

This yields the coefficients

$$r = \frac{-1}{1 + \dfrac{k\hbar^2}{m\gamma}} \quad , \quad t = \frac{1}{1 + \dfrac{m\gamma}{k\hbar^2}} \, . \tag{4.6}$$

Using Eq. (4.6), we can obtain the reflection, transmission, and now also absorption probability as functions of the parameter $\gamma$:

$$R = |r|^2, \quad T = |t|^2, \quad A = 1 - R - T \, , \tag{4.7}$$

where we have defined the probability to be absorbed as the probability to not be reflected or transmitted. These coefficients are plotted in Figure 4.1 as a function of $\gamma$.

We see in Figure 4.1 that $R = T$ for a particular value of $\gamma$, and that $A$ is maximized by some value of $\gamma$. Using equations (4.6) and (4.7), we find that these points are both equal to

$$\gamma^\star = \frac{k\hbar^2}{m}. \tag{4.8}$$

These expressions depend on $\hbar$ and the mass $m$. We set $\hbar = 1$. To facilitate comparison with the lattice situation, we choose $m = 1/2$ so that the quadratic dispersion ($\hbar^2 k^2/2m$) on the continuum matches the low-energy part of the cosine dispersion ($-2\cos k$) on the lattice without an impurity. Thus

$$r \;=\; \frac{-\gamma}{\gamma + 2k}\,, \quad t \;=\; \frac{2k}{\gamma + 2k}\,, \quad \gamma^\star = 2k\,. \tag{4.9}$$

### 4.1.2 Lattice

We now turn to the lattice problem. Through numerical time evolution, we will calculate the reflection and transmission fractions, $R$ and $T$, and obtain the absorption fraction using $A = 1 - R - T$.

We initialize our particle as (a discrete version of) a Gaussian wavepacket localized around the site $j_0$ and carrying lattice momentum $k$:

$$|\psi(0)\rangle \;=\; \sum_j \psi_j(0)\,|j\rangle \;=\; \mathcal{N}^{-1} \sum_j e^{\frac{-(j-j_0)^2}{2\sigma^2}}\, e^{ikj}\;|j\rangle \;\;, \tag{4.10}$$

where $\mathcal{N}$ is a normalization constant. A positive $k$ ensures that the wavepacket will propagate rightwards initially. The position $j_0$ is chosen such that the wavepacket starts on the left side of the lattice, and does not initially overlap significantly with either the lattice edges or the impurity. The width $\sigma$ is chosen to be significantly larger than 1 but significantly smaller than $L/2$. The wavepacket is evolved in time using the non-Hermitian Hamiltonian, Eq. (4.1), via:

$$|\psi(t)\rangle \;=\; e^{-iHt}\,|\psi(0)\rangle\,. \tag{4.11}$$

Note that due to the non-Hermiticity of $H$, the eigenspectrum can be complex, and thus the evolution is, in general, non-unitary. If we express the wavefunction at time $t$ in the site basis:

$$|\psi(t)\rangle \;=\; \sum_j \psi_j(t)\,|j\rangle\,, \tag{4.12}$$

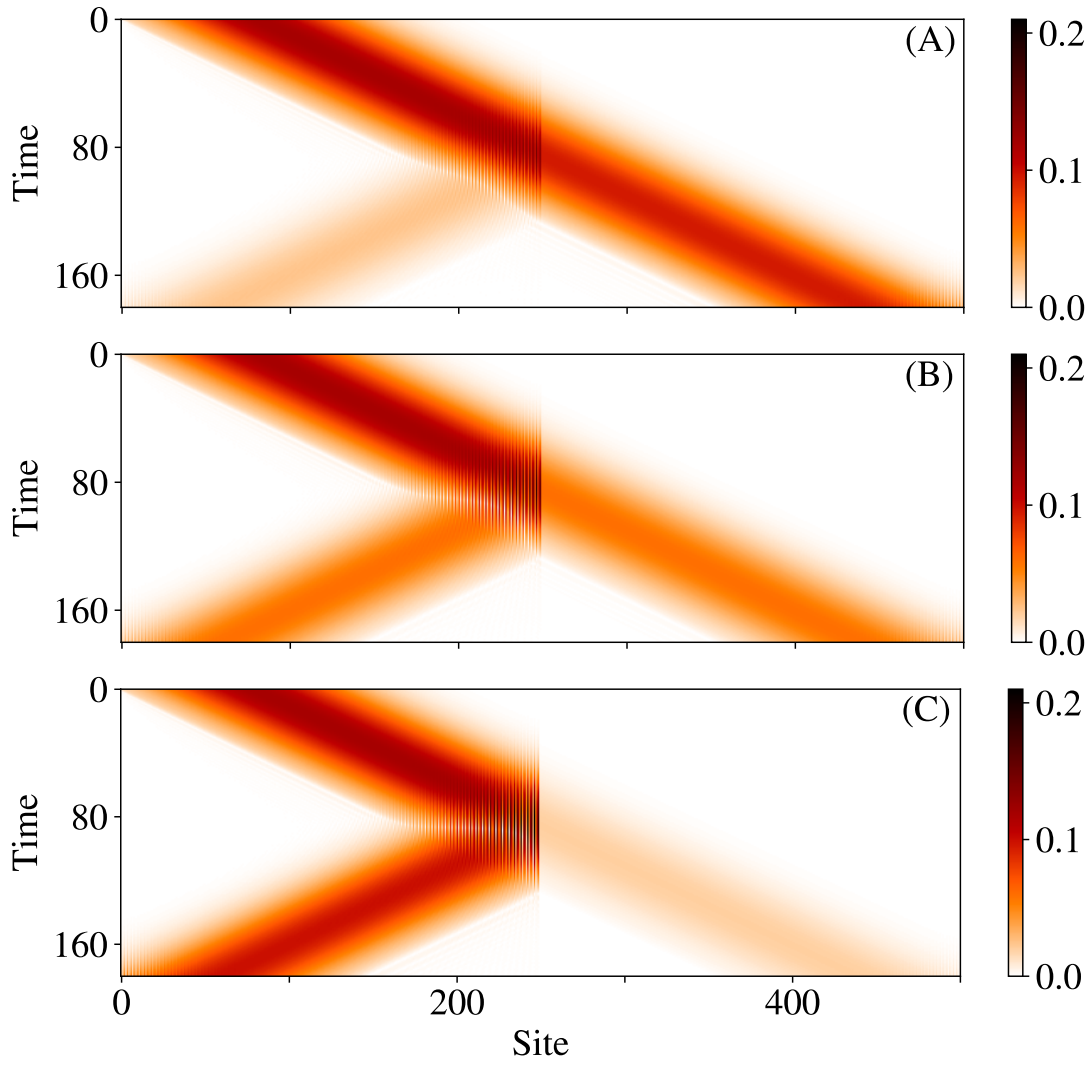


Figure 4.2: Wavepacket evolution illustrated by a density plot of site occupancies $|\psi_j|^2$. Here $L = 500$, $\sigma = 40$, $k = \pi/2$. **(A)**: $\gamma = 0.5$ - Shows less of the wavepacket being reflected than transmitted. **(B)**: $\gamma = 2$ - Shows roughly similar amounts of the wavepacket being reflected/transmitted. **(C)**: $\gamma = 10$ - Shows less of the wavepacket being transmitted than reflected.

then the coefficients $\psi_j(t)$ provide the occupancies, $|\psi_j(t)|^2$.

Figure 4.2 illustrates the numerical time evolution of a wavepacket for three different values of $\gamma$, initially localized near the left end of a 500-site lattice. After the particle is incident on the impurity, we see different portions of the wavepacket being reflected and transmitted.

Choosing a time after the collision has occurred, such that the reflected and transmitted packets are well-separated from the impurity, one can define the coefficients based on the wavefunction coefficients at this time. The reflected fraction is the weight to the left of the impurity, while the transmitted fraction is

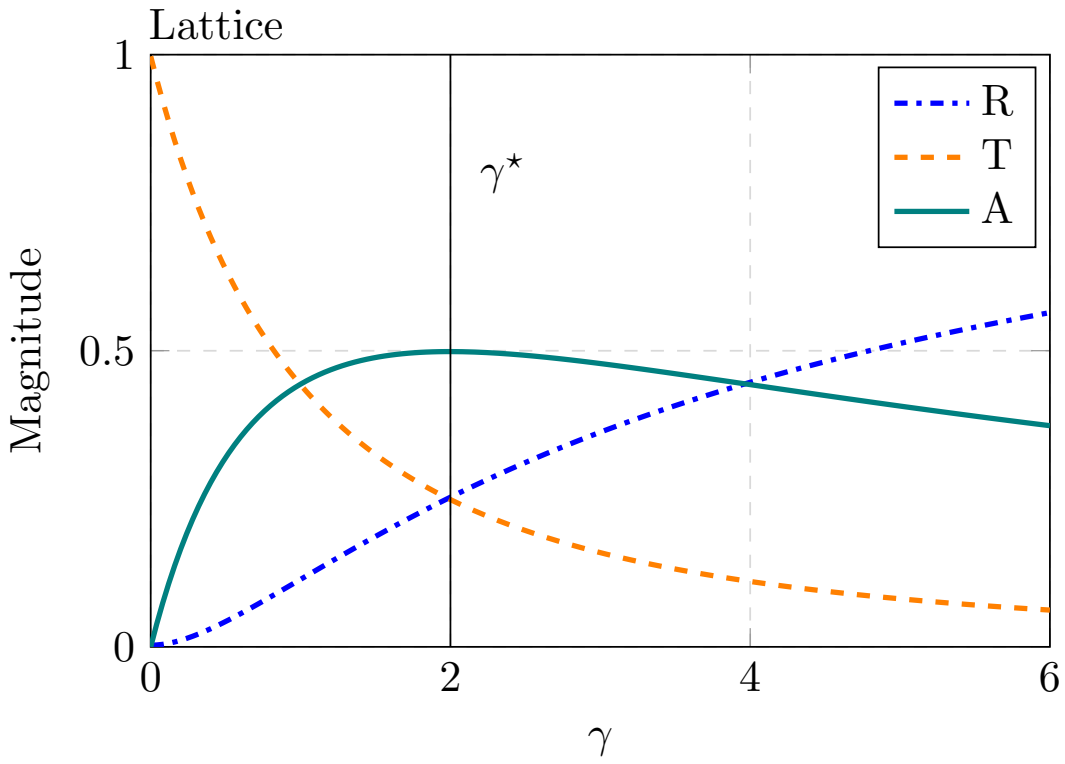


Figure 4.3: Reflection, transmission and absorption probabilities calcuated using wavepacket evolution on the lattice. ($R, T, A$ plotted against $\gamma$.) Here $L = 500$, $\sigma = 40$, $k = \pi/2$.

that to the right. Denoting the impurity site as $q$, the coefficients are given as

$$R = \sum_{j=1}^{q} |\psi_j|^2, \quad T = \sum_{j=q+1}^{L} |\psi_j|^2, \quad A = 1 - R - T \ . \tag{4.13}$$

Figure 4.3 shows the results of calculating the coefficients for a lattice with 500 sites, with the impurity at site 250, for a range of values for $\gamma$. The coefficients are extracted from time evolution with a $\sigma = 40$ wavepacket. The measurement of weights on the left and right parts of the lattice is performed at a time well after the wavepacket has scattered off the impurity but well before either the reflected or the transmitted wavepacket reaches one of the boundaries. For Figure 4.3, this time was $t = 160$. For other values of $k$ (Figure 4.4), the times are different as the speed of the wavepacket depends on $k$. We have checked that the dependence on $\sigma$ is negligible provided $1 \ll \sigma \ll L/2$. For both Figure 4.2 and Figure 4.3, the wavepacket momentum is $k = \pi/2$, for which the dispersion of the wavepacket is least severe.

### 4.1.3 Comparison between continuum and lattice

Comparing Figures 4.1 and 4.3, we see that our lattice results are very similar to the continuum results, except for a rescaling of $\gamma$. In the continuum case, we have found that the main feature, namely the maximum of $A(\gamma)$, or the crossing point of $R(\gamma)$ and $T(\gamma)$, occurs at a value of $\gamma$ that is proportional to the momentum, $\gamma^\star = 2k$. Therefore, one would expect that in the lattice case, $\gamma^\star$ should also depend on the momentum of the scattering particle. More specifically, since the single-particle dispersion changes as $k^2 \to -2\cos k$ in going from the continuum to lattice, one expects from the dependence of $\gamma^\star = 2k$ in the continuum that the dependence might be $\gamma^\star = 2\sin k$ on the lattice.

To extract $\gamma^\star$ for various momenta, we perform the numerical time evolution of the wavepacket scattering for multiple momentum values and identify the maximum of the absorption $A(\gamma)$. The results are shown in Figure 4.4, comparing the continuum and lattice case. Indeed the momentum dependence of the $\gamma^\star$ appears to be $\approx 2\sin k$ on the lattice, with a maximum of $\gamma^\star \approx 2$ for $k = \pi/2$.

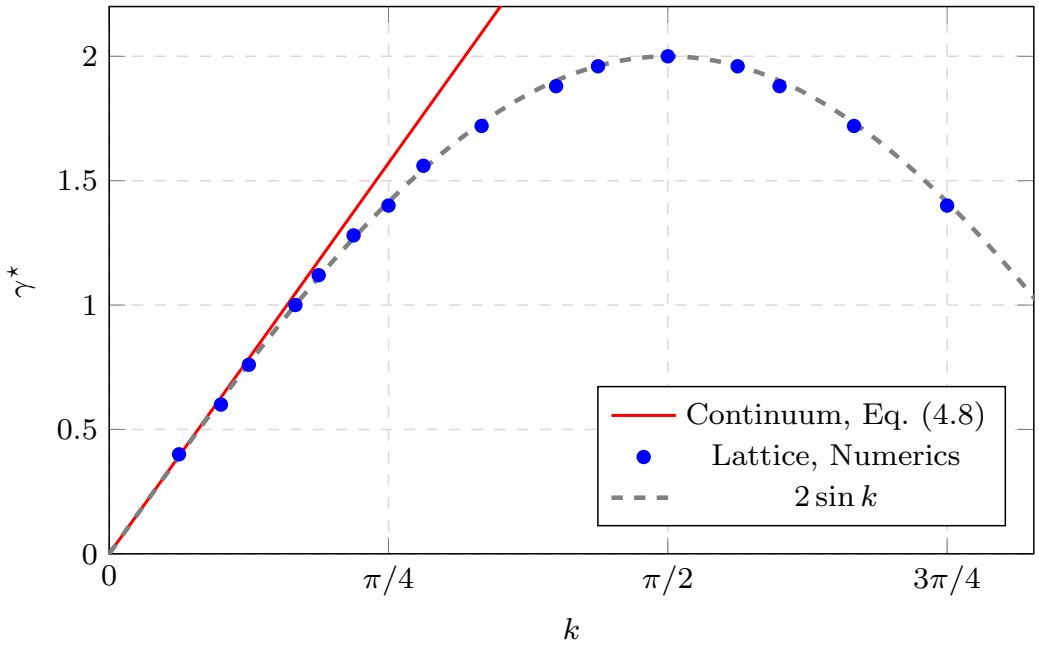


Figure 4.4: Comparing results of the value of $\gamma$ for which absorption is maximized in the continuum ($\gamma^\star = 2k$) and on the lattice (obtained from numerical wavepacket evolution). Lattice results are obtained with $L = 250$ and $\sigma = 15$. For comparison, the function $2\sin k$ is plotted (dashed curve).

## 4.2 Spectrum and exceptional points

In this section, we analyze the spectrum of the single particle non-Hermitian Hamiltonian, Eq. (4.1). It turns out that the value $\gamma \approx 2$ also plays a special role in the spectrum.

Previously we presented data for systems with 500 and 250 sites. In this section, for clarity, we focus on the spectrum of smaller system sizes. As the eigenvalues are complex, there is no particularly natural way to order them. Here, we order the eigenstates based on their real component and then by their imaginary component, from smallest to largest, i.e., $1 - 2i$ comes before $1 + 2i$. Figure 4.5 presents the eigenvalues for a system with 14 sites as a function of $\gamma$. The real and imaginary components are shown separately. We also plot the 14 eigenvalues

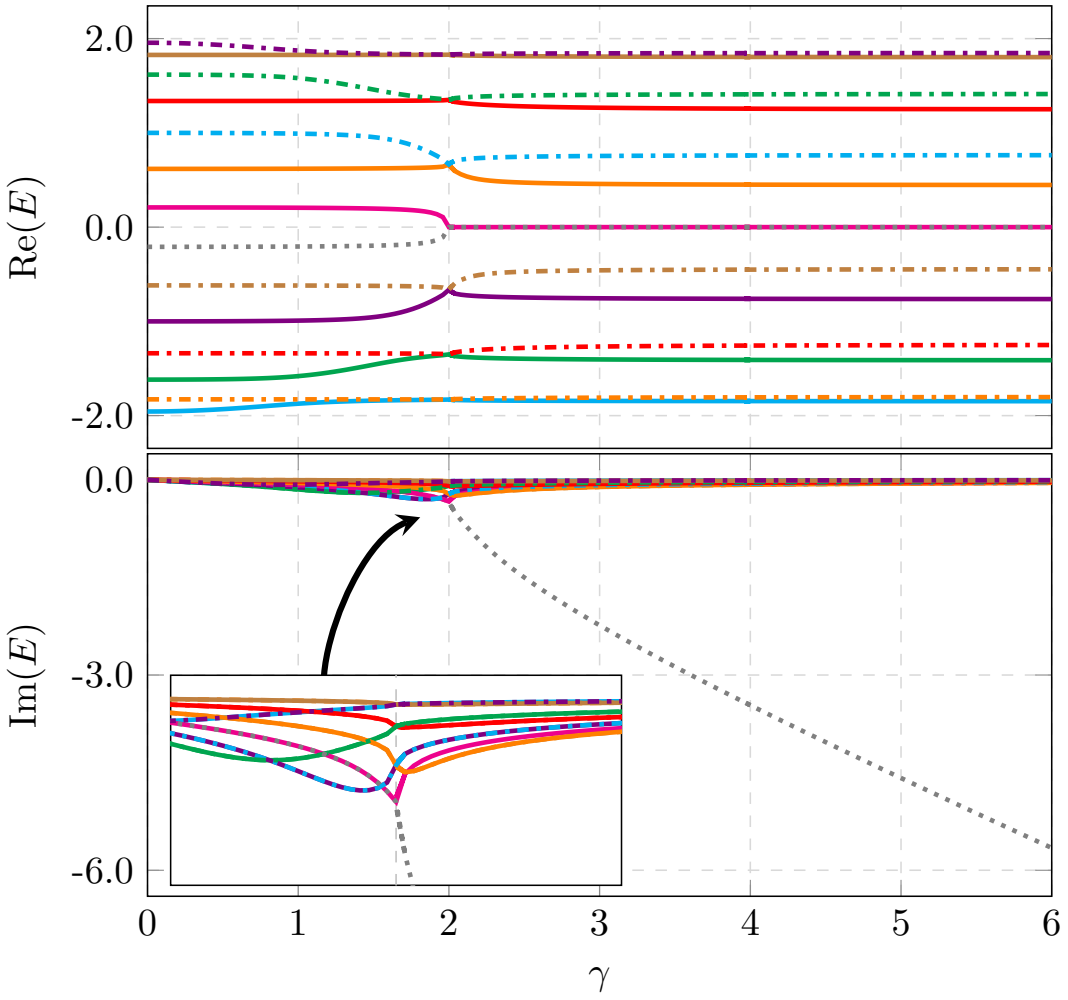


Figure 4.5: Energy spectrum of the Hamiltonian, Eq. (4.1), for $L = 14$, as function of the potential strength $\gamma$. Real and imaginary parts of the eigenvalues are plotted separately.

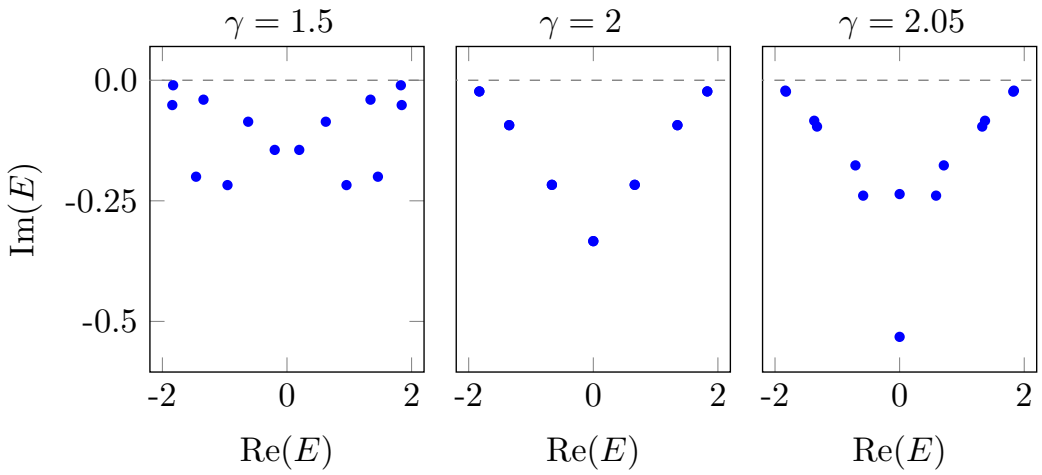


Figure 4.6: Eigenvalues of the Hamiltonian, Eq. (4.1), for $L = 14$, for three values of $\gamma$, below, at, and above the exceptional point. For each value of $\gamma$, the $L$ eigenvalues are plotted in the complex plane. For $\gamma = 2$, only $L/2$ points are visible due to the pairing of the eigenvalues.

in the complex plane, for three different values of $\gamma$, in Figure 4.6. For any value of $\gamma$, the real part of the eigenvalues are generally spaced between $-2$ and $+2$, as one expects from a tight-binding one-dimensional lattice. The most visibly striking feature in the spectrum is that, at $\gamma = 2$, *all* of the eigenvalues coalesce in pairs. We note that the imaginary components are already paired up for $\gamma < 2$, and these pairs proceed to coalesce at $\gamma = 2$, at which point the real components also pair up.

This is not a higher-order exceptional point [296–298], but rather an exceptional point where *all* eigenvalues pair up as second-order exceptional points, not just two eigenvalues. Of course, observing the eigenvalues is not sufficient to say that this is an exceptional point — the eigenvectors also need to coalesce. Indeed, considering the pair of eigenstates whose eigenvalues become equal at $\gamma = 2$, we find numerically that one of the eigenstates becomes equal to $-i$ times the other eigenstate. To illustrate the eigenstate coalescence, we use the (non) orthogonality matrix

$$U_{jk} = \langle E_j | E_k \rangle \tag{4.14}$$

between the eigenstates $|E_j\rangle$. As each eigenstate is simply $-i$ times another at $\gamma = 2$, we would expect the absolute value of the overlap of an eigenstate with at least one other eigenstate to be 1. In Figure 4.7, we illustrate the observed unit

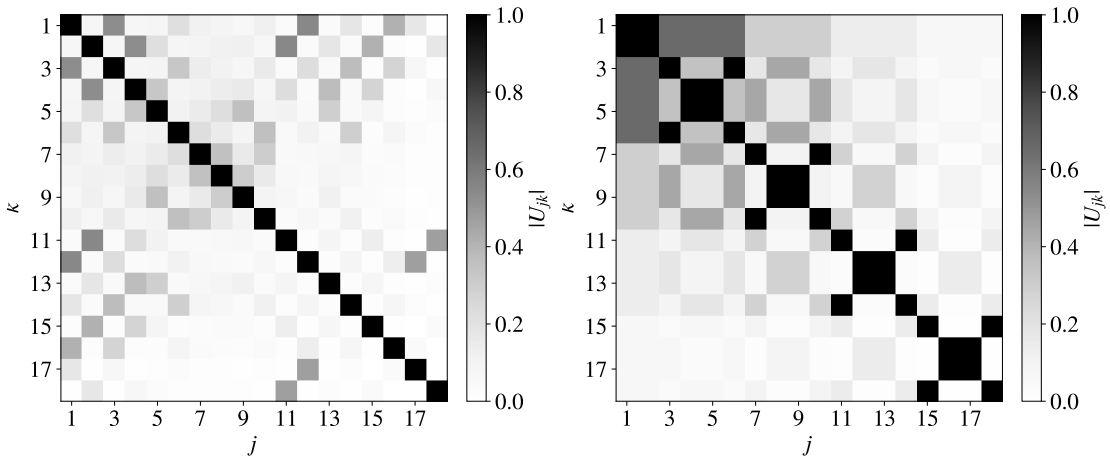


(a) $\gamma = 1.0$ (b) $\gamma = 2.0$

Figure 4.7: The absolute value of non-orthogonality matrix elements, Eq. (4.14), for the eigenstates of the Hamiltonian, Eq. (4.1), for $L = 18$ sites.

overlap between pairs of eigenstates at $\gamma = 2$ (b), in contrast to the $\gamma = 1$ (a) case.

We can show analytically that the eigenvalues always group into degenerate pairs at $\gamma = 2$ for a lattice with an even number of sites and the impurity at one of the center lattice sites. The complete derivation is detailed in Appendix C.1, but we outline the derivation below.

We wish to find the eigenvalues of the Hamiltonian, Eq. (4.1), which is an $L \times L$ matrix with elements:

$$[H_q]_{jk} = -\delta_{j,k+1} - \delta_{j+1,k} - i\gamma\delta_{jq}\delta_{jk}, \tag{4.15}$$

with $1 \leq q \leq L$ a fixed integer. The characteristic polynomial of $H$, up to a minus sign, is the determinant of the matrix

$$[A_q]_{jk} = \delta_{j,k+1} + \delta_{j+1,k} + \lambda\delta_{j,k} + i\gamma\delta_{jq}\delta_{jk}, \tag{4.16}$$

It is straightforward to show that the determinant, $P_n$, of an $n \times n$ tridiagonal matrix $A_{ij} = b_i\delta_{i,j+1} + c_j\delta_{i+1,j} + a_i\delta_{ij}$ satisfies a recurrence relation

$$P_n = a_n P_{n-1} - c_{n-1}b_{n-1}P_{n-2}. \tag{4.17}$$

Thus we can define a recurrence relation for the tridiagonal matrix $H$, Eq. (4.15). A standard method of solving linear recurrence relations is to use the $Z$-transform. Since $P_n$ for Eq. (4.15) is only defined for $n \geq 0$, we use the unilateral $Z$-transform defined as $\mathcal{Z}\{P_n\} = \sum_{n=0}^{\infty} P_n z^{-n}$. Using the $Z$-transform, shifting the summation index, and utilizing the recurrence relation, following some algebra we end up with the characteristic polynomial of the Hamiltonian, Eq. (4.15), with $L$ sites, and an impurity on site $q$ as

$$P_{L,q} = K_{q-1}K_{L-q+1} + (i\gamma K_{q-1} - K_{q-2})K_{L-q} \tag{4.18}$$

for $1 \leq q \leq L$. Here, $K_n$ is a function of $n$ and the parameter $\lambda$. For the specific case of $q = L/2$ (or $L/2+1$) with $L$ even, we find

$$P_{L,L/2} = K_{L/2}^2 - K_{L/2-1}^2 + i\gamma K_{L/2-1}K_{L/2}. \tag{4.19}$$

Thus, when $\gamma = 2$, this can be written as

$$P_{L,L/2} = \left(K_{\frac{L}{2}} + iK_{\frac{L}{2}-1}\right)^2. \tag{4.20}$$

This means that every root of the polynomial is a zero of order at least 2, i.e., the eigenspectrum is doubly degenerate at $\gamma = 2$.

The eigenstate degeneracy is quite easily shown once we know there is an eigenvalue degeneracy. For tridiagonal matrices, such as Eq. (4.15), it is straightforward to argue a coalescence of eigenvalues implies a coalescence of eigenstates, i.e., the eigenstates are linearly dependent. Consider some eigenvalue $E_n$ and corresponding eigenvector $|E_n\rangle = (x_1, x_2, ..., x_L)^T$. Due to the tridiagonal form of the matrix, all the components $x_i$ can be written as a function of $E_n$ and the terms on the diagonals, times the first component $x_1$. If we have two eigenvectors with the same eigenvalue $E_n$, then the functions in the eigenvectors are the same. This implies the eigenvectors only differ in the choice of $x_1$, i.e., they are linearly dependent. Thus, if there is an eigenvalue degeneracy at some point, the eigenvectors are linearly dependent.

We have thus shown, analytically, that for even $L$, and impurity at the center of the lattice, the eigenvalues and eigenvectors of the matrix Eq. (4.15) coalesce at $\gamma = 2$, demonstrating the existence of an exceptional point.

Unlike exceptional points which separate a $\mathcal{PT}$-symmetric phase from a $\mathcal{PT}$-symmetry-broken phase (see Section 4.4), the eigenvalues of our system are complex on both sides of the exceptional point. The imaginary parts typically have a larger magnitude near the exceptional point and generally decrease as one moves away from $\gamma = 2$, with one striking exception. The exception corresponds to one of the two eigenvalues whose real part becomes zero. The imaginary part becomes large and negative as $\gamma$ increases, and eventually becomes $\approx -\gamma$. This eigenvalue corresponds to a bound state localized at the dissipative impurity, which we will analyze in the next section.

The spectral structure discussed here for $L = 14$ is applicable for $L \mod 4 = 2$. With other values of $L$, there are variations, which we detail in Appendix D.1. In particular, for odd values of $L$, there is only a single pair of eigenvalues coalescing ($L \mod 4 = 3$) or none at all ($L \mod 4 = 1$). However, even with an odd number of sites, the localized eigenstate still exists for large values of $\gamma$. In Appendix D.2, we also discuss the dependence on the location of the impurity site.

## 4.3 Large $\gamma$

In this section, we explore the effect of large $\gamma$ on the scattering dynamics and the spectrum. We observed that the absorption decreased towards zero once $\gamma > \gamma^\star$, in both the continuum (Figure 4.1) and the lattice (Figure 4.3) systems. This suggests that the effect of the imaginary potential is similar to that of a real potential, wherein the reflection dominates. In what follows, we draw a comparison between the effects of real and imaginary on-site potentials.

In Section 4.2, we observed a single eigenvalue with a purely imaginary negative component. At large $\gamma$, the eigenvalue approaches $-i\gamma$, for which a plausible explanation would be that the eigenstate is localized at or around the impurity site $q$ and hence its energy is primarily determined by the $-i\gamma \left|q\right\rangle \left\langle q\right|$ term in the

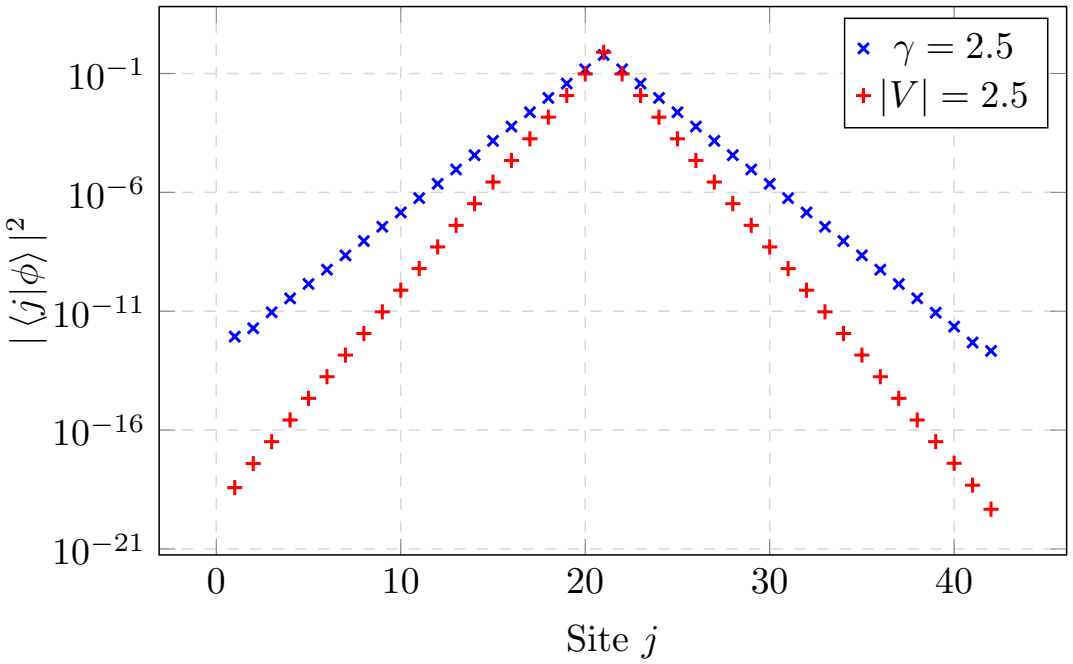


Figure 4.8: Site occupancies of the localized eigenstate, for both a real ($V$) and an imaginary ($-i\gamma$) potential of magnitude 2.5, and $L = 42$ sites. The scale is log-linear.

Hamiltonian, Eq. (4.1). Indeed the corresponding eigenstate is numerically found to be exponentially localized around the impurity site, as illustrated in Figure 4.8.

For comparison, we also consider the effect of a real potential, i.e., the Hermitian Hamiltonian

$$H = -J\sum_{j=1}^{L-1}\Big(|j\rangle\langle j+1| + |j+1\rangle\langle j|\Big) + V|q\rangle\langle q|. \tag{4.21}$$

Here, $V$ is a real parameter that could be either positive or negative. The spectrum, which is real, contains one state which separates from the band and at large $|V|$ approaches $V$. It is known that this Hamiltonian supports a bound state for negative $V$ and an anti-bound state for positive $V$. This eigenstate is exponentially localized around site $q$.

In Figure 4.8, we show the exponential localization of the eigenstate both for the real potential with $|V| = 2.5$ and for the dissipative impurity with $\gamma = 2.5$. At these values, the eigenstate is more strongly localized (has a smaller localization length) for the case of the real potential, i.e., for Eq. (4.21). By approximating the occupancies at site $j$ with an exponential of the form: $\propto e^{(j-q)/\alpha}$, where $q$ is

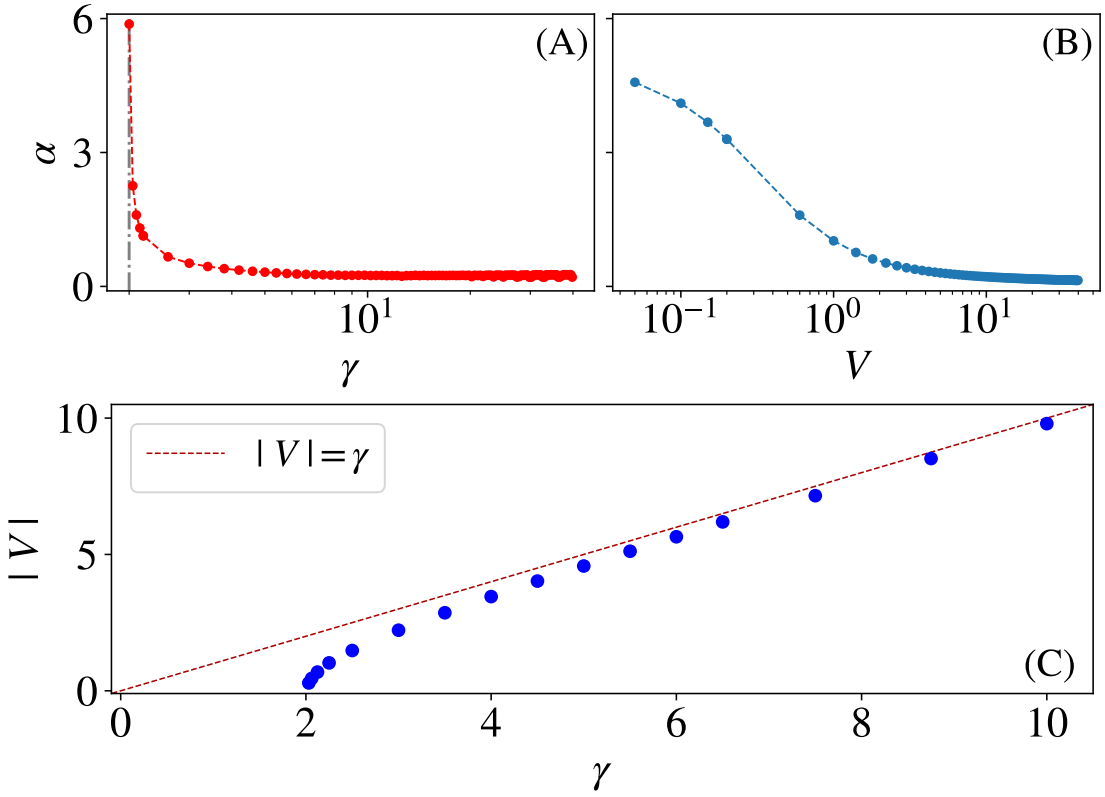


Figure 4.9: **(A,B)** Localization length of the bound state ($\alpha$) plotted as a function of $\gamma$ ($|V|$) for an imaginary (real) potential. **(C)** A correspondence between the parameters of the real and imaginary potentials, using the localization length of the bound states. $L = 42$ in all panels.

the impurity position, we can extract the localization length $\alpha$. In Figure 4.9(A, B), we show the resulting localization lengths $\alpha$ for both an imaginary and real potential as a function of their respective magnitudes. By extracting $\alpha$ for the localized eigenstate for various values of $\gamma$ in the case of our non-Hermitian system, Eq. (4.1), and for various values of $V$ in the case of the system Eq. (4.21), we can assign to each $\gamma > 2$ a value of $V$, for which the same localization length is obtained. Results of this calculation are shown in Figure 4.9(C) for a system with $L = 42$ sites. This quantifies the idea that, at large $\gamma$, an absorbing impurity behaves like a real-valued impurity.

For values of $\gamma < 2$ there is no bound state. For $\gamma$ slightly larger than 2, the localization length corresponds to the bound state of a very weak real potential (very small $|V|$). As $\gamma$ grows, the corresponding $|V|$ increases and asymptotically approaches $|V| = \gamma$. In other words, the effect of an absorbing impurity of large strength $\gamma \gg 2$ is similar to that of a real-valued impurity of the same strength.

One can ask whether there is a similar correspondence in the continuum case — in that case, the absorption is also low for the non-Hermitian model at large $\gamma$, as clear from Eq. (4.9). It is well known that the negative real delta potential has a single bound (localized) state. However, neither the positive-real potential nor the imaginary potential has a bound state.

To see that a bound state is not permitted in the case of a purely imaginary potential, we start by assuming there is a bound state, which has the form

$$\psi(x) \;=\; \begin{cases} \psi_L(x) \;=\; Ae^{(k_1+ik_2)x}\,, & x<0 \\ \psi_R(x) \;=\; Be^{-(k_1+ik_2)x}\,, & x>0 \end{cases} \tag{4.22}$$

for some potential $V(x)=\lambda\delta(x)$, with $\lambda$ a complex number. This form of $\psi(x)$ results in a bound state if $k_1>0$ as

$$|\psi(x)|^2 \;=\; \begin{cases} |\psi_L(x)|^2 \;=\; A^2e^{(k_1+ik_2)x}e^{(k_1-ik_2)x} \;=\; A^2e^{2k_1x}, & x<0 \\ |\psi_R(x)|^2 \;=\; B^2e^{-(k_1+ik_2)x}e^{-(k_1-ik_2)x} \;=\; B^2e^{-2k_1x}, & x>0. \end{cases} \tag{4.23}$$

In the same spirit as solving for the transport coefficients, we use the (dis)continuity conditions at $x=0$,

$$\psi(0) \;=\; \psi_L(0) \;=\; \psi_R(0)\,, \quad \frac{\hbar^2}{2m}(\psi_R'(0)-\psi_L'(0)) \;=\; \lambda\psi(0). \tag{4.24}$$

These conditions give us that $A=B$, and thus

$$\lambda=-\frac{\hbar^2}{m}(k_1+ik_2). \tag{4.25}$$

Since we already assumed $k_1>0$ to have a bound state in the first place, we see that $\lambda$ must have a non-zero real component for a bound state to exist. Thus we have ruled out a bound state in the continuum for a purely imaginary potential. Hence no quantitative correspondence can be made as measured by the localization length, as we have done for the lattice.

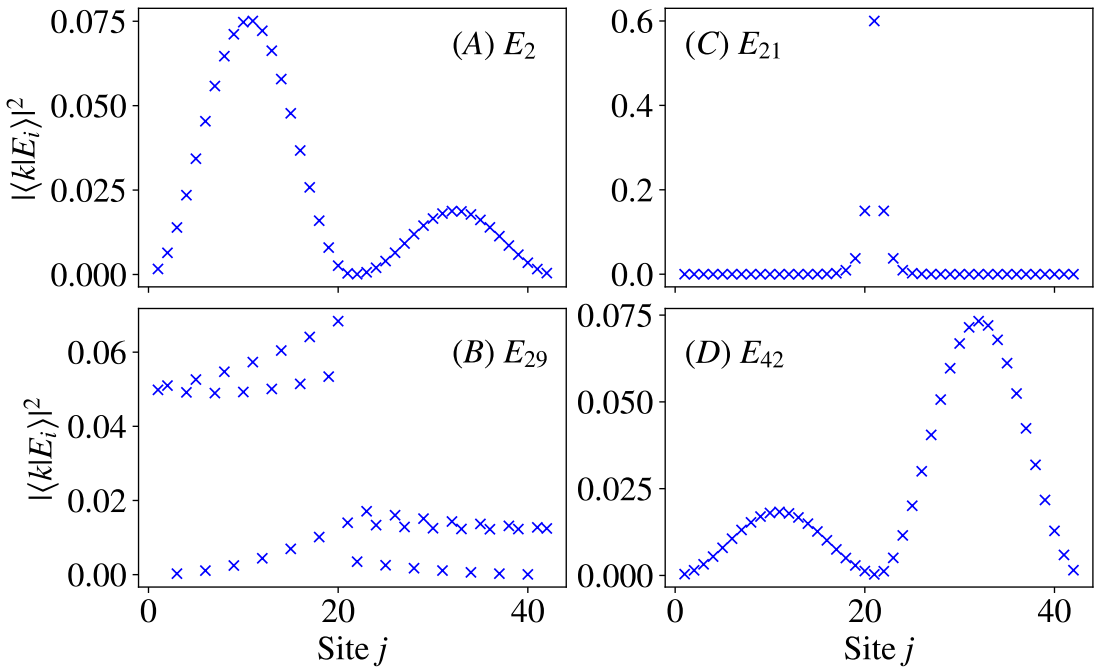


Figure 4.10: Occupancy profiles of a sample of eigenstates, for a system with $L = 42$ and $\gamma = 2.5$. The legend indicates which eigenvalue the eigenstate corresponds to. Panel (B) illustrates the localized eigenstate.

The existence of a strongly localized eigenstate provides a simple 'spectral' interpretation of the suppression of absorption at large $\gamma$ that we have presented in Subsection 4.1.2. For large $\gamma$, the localized eigenstate has near-zero overlap with the incident wavepacket; in the initial state, the wavepacket is far from the impurity site. Thus, the wavepacket is 'shielded' from the potential as its dynamics are confined to the subspace of all the other eigenstates, which have near-zero weight at the impurity site. Therefore, the wavepacket experiences almost zero absorption. Curiously, for the suppression of absorption in the continuum case (Subsection 4.1.1), this spectral interpretation is invalid; there is no localized eigenstate in that case. However, it is clear from the expressions for $r$ and $t$, Eq. (4.6), that in the large $\gamma$ limit $R \to 1$ and $T \to 0$. This then implies that the absorption $A \to 0$ as was observed in the lattice case.

Other than the localized eigenstate, the eigenstates resemble those for a real potential — the eigenstates at the bottom and top of the band have few nodes, while those near the center have many nodes. Figure 4.10 illustrates a selection of the eigenstates of a system with $L = 42$ sites. They are labeled as '$E_i$', i.e., the eigenstate presented is the state corresponding to the $i^{th}$ eigenvalue when ordered

in the described manner.

Note that the eigenvector coefficients $\langle j|E_i\rangle$ are themselves complex; we only show the occupancies $|\langle j|E_i\rangle|^2$ and not the real and imaginary parts separately. (Here $|E_i\rangle$ is the eigenvector in question and $j$ is the site index.)

## 4.4 $\mathcal{PT}$-symmetric model

In this section, we shall examine a $\mathcal{PT}$-symmetric model that is obtained by introducing an additional 'enhancing' potential to the previously studied non-Hermitian model. Using the same analytical argument derived for the purely dissipative potential, we can prove the existence of an exceptional point for this $\mathcal{PT}$-symmetric model.

*$\mathcal{PT}$-symmetry.-* A $\mathcal{PT}$-symmetric system is not symmetric under a parity (spatial) or time reversal (temporal) transformation independently. If the Hamiltonian of the system is invariant under a combined parity-time ($\mathcal{PT}$) transformation, then the system is said to be $\mathcal{PT}$-symmetric. This is equivalent to saying the Hamiltonian commutes with the $\mathcal{PT}$ operator. Non-Hermitian Hamiltonians that preserve $\mathcal{PT}$-symmetry can exhibit purely real spectra in the so-called unbroken $\mathcal{PT}$-symmetric regime. In this regime, the eigenstates of the Hamiltonian are also eigenstates of the $\mathcal{PT}$ operator simultaneously. In contrast, the broken $\mathcal{PT}$-symmetric regime features a complex spectrum, and not all of the eigenstates of the Hamiltonian are simultaneous eigenstates of the $\mathcal{PT}$ operator. Due to this possibility of real eigenvalues in the unbroken phase, $\mathcal{PT}$-symmetry has been suggested as a generalization of the standard postulate that a quantum mechanical Hamiltonian should be Hermitian [299]. Hermiticity ensures real eigenvalues and unitary time evolution under the Schrödinger equation. Similarly, in the unbroken $\mathcal{PT}$-symmetric phase, the eigenvalues of the non-Hermitian Hamiltonian are real, guaranteeing unitary evolution. The subject of $\mathcal{PT}$-symmetric Hamiltonians gained significant interest due to early studies such as [300, 301] and has continued to attract attention in recent years [161–167, 302]. For a comprehensive overview, references such as [299] or [303] can be consulted.


Figure 4.11: The loss/gain sites are placed equidistant from the center of the lattice, as shown here for $L = 12$. We consider setups with the loss site placed before the gain site.

$\mathcal{PT}$-symmetric non-Hermitian Hamiltonians are considered to be effective models of dissipative systems with balanced loss and gain. Thus, a $\mathcal{PT}$-symmetric version of our non-Hermitian tight-binding setup, originally consisting of a single absorbing potential, is achieved by balancing the loss via an 'enhancing' potential. We use the term 'enhance' as the potential does not continually emit into the system; it only amplifies passing wavepackets. To ensure $\mathcal{PT}$-symmetry, the two potentials are placed equidistant from the center of the lattice and have potentials of opposite signs but equal magnitude. Figure 4.11 illustrates an example of the setup. The Hamiltonian describing such a system is given by

$$\begin{aligned} H &= -J\sum_{j=1}^{L-1}\left(|j\rangle\langle j+1| + |j+1\rangle\langle j|\right) \\ &\quad - i\gamma\left(|q\rangle\langle q| - |L-q+1\rangle\langle L-q+1|\right). \end{aligned} \tag{4.26}$$

Generally, $1 \leq q \leq L$, but here we focus on systems with $1 \leq q \leq L/2$, i.e., the absorbing potential is in the left half of the lattice.

This model harbors many exceptional points for various configurations of $q$ and values of $\gamma$ [167]. We focus on the exceptional points appearing for $\gamma = 1$ with both $q = L/2$ and $q = 1$. In the former case, with the two potentials placed side-by-side in the center of the lattice, *all* eigenvalues coalesce into degenerate pairs, similarly to what we observed for our single absorber. In the latter case, with the potentials placed at opposite ends of the open chain, only a single pair of eigenvalues coalesce. These exceptional points have previously been observed numerically [167].

We illustrate examples of the eigenvalue coalescence in Figure 4.12 for a lattice with $L = 10$ for the cases of $q = 1$ and $q = L/2$. The figure illustrates the entirely real spectrum in the unbroken $\mathcal{PT}$-symmetric regime for $\gamma < 1$ for both cases.

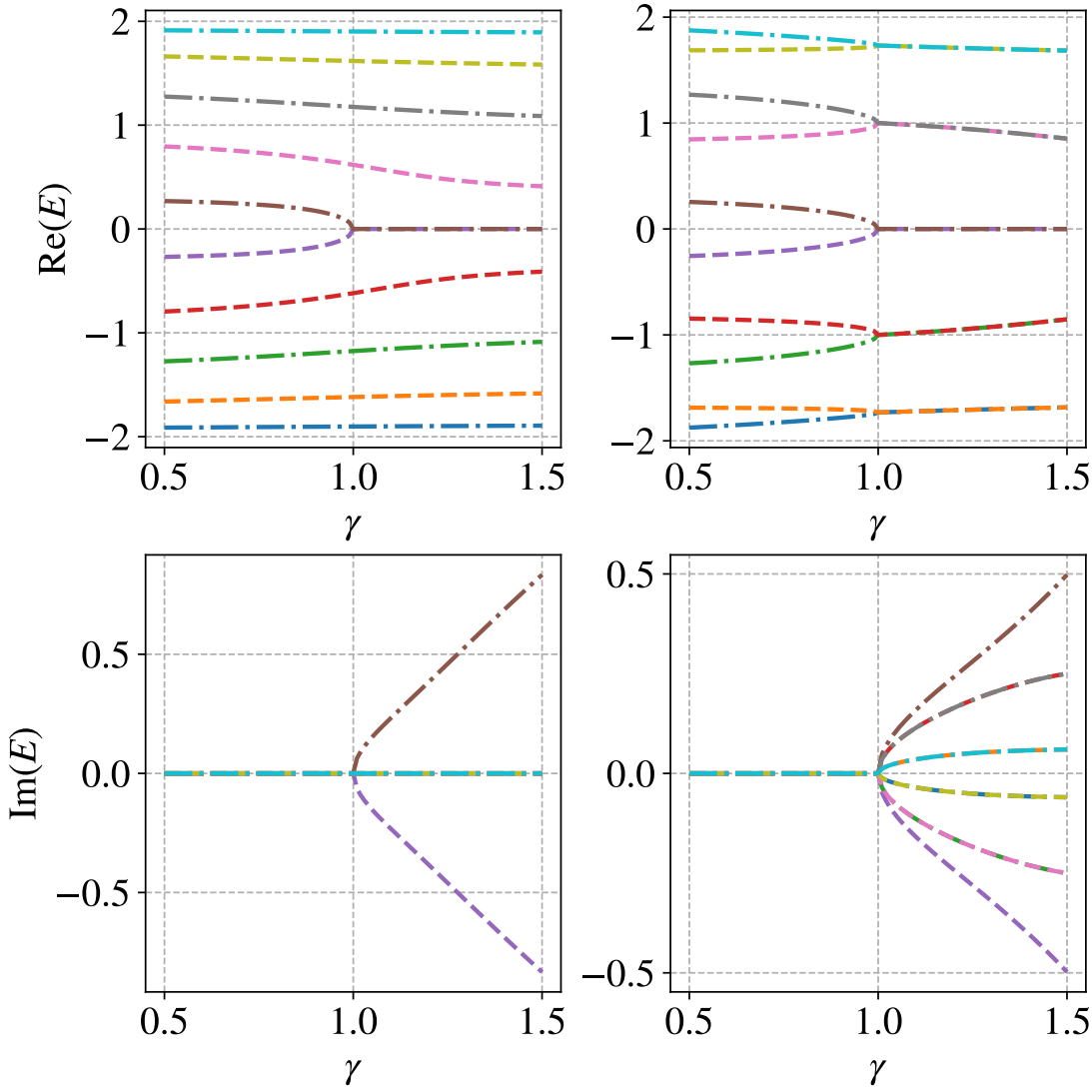


Figure 4.12: Energy spectrum of the $\mathcal{PT}$-symmetric Hamiltonian, Eq. (4.26), for $J = 1$, $L = 10$, with $q = 1$ (left) and $q = L/2$ (right), as a function of the potential strength $\gamma$. Real and imaginary parts of the eigenvalues are plotted separately.

In addition, we can see that the eigenvalues which coalesced at $\gamma = 1$ become complex conjugate pairs after the exceptional point.

By using the same methodology employed in the case of a single dissipative potential in Section 4.2 to demonstrate the existence of many exceptional points, we are able to prove, analytically, the existence of the observed exceptional points in this $\mathcal{PT}$-symmetric model. The analytical proof proves there are exceptional points at $\gamma = 1$ for both cases of the potentials: at the center and opposite ends of the chain. The complete proof is detailed in Appendix C.2. Here, we outline the main results:

(i) For $q = 1$ (impurities at opposite ends of the chain) when $\gamma = \pm 1$, we

can show that the characteristic polynomial of the Hamiltonian, Eq. (4.26), is proportional to that of an open boundary $L-1$ site tight-binding chain. For $(L-1)+1=L$ even, this is known to have a single pair of degenerate eigenvalues. Thus, when $L$ is even, Eq. (4.26) has a single pair of degenerate eigenvalues. A similar result was derived using a Bethe ansatz in Ref. [162].

(ii) For $q = L/2$ (impurities at the center) when $\gamma = \pm 1$, we can show that the characteristic polynomial of the Hamiltonian in Eq. (4.26) is doubly degenerate, i.e., any root of the polynomial is a zero of at least order 2. In addition, the characteristic polynomial at this point, interestingly, is the square of the characteristic polynomial of a chain of length $L/2$.

In both cases, once we have an eigenvalue degeneracy, it is straightforward to prove there is an eigenstate coalescence, precisely the same as in Section 4.2. Thus, we have proved the existence of these exceptional points.

The result (ii), for $q = L/2$, implies the spectrum at $\gamma = \pm 1$ can be interpreted as two decoupled chains of length $L/2$. This can be seen from the characteristic polynomial but can also be illustrated by performing a basis transformation that converts the Hamiltonian $H$ into block form.

To perform the transformation, we start with the basis $\{|m\rangle : m \in [1, L]\}$, which our Hamiltonian $H$ is written in. Then, we can define new basis states

$$|n, \pm\rangle = \frac{1}{\sqrt{2}} \left( |n\rangle \pm i \, |L - n + 1\rangle \right), \tag{4.27}$$

where $n \in [1, L/2]$. We can write then write the original basis states in terms of the new basis states via

$$|n\rangle = \begin{cases} \frac{1}{\sqrt{2}} \left( |n, +\rangle + |n, -\rangle \right) & , \ 1 \leq n \leq L/2 \\ -\frac{i}{\sqrt{2}} \left( |L - n + 1, +\rangle - |L - n + 1, -\rangle \right) & , \ L/2 < n \leq L \end{cases}, \tag{4.28}$$

to obtain the Hamiltonian as

$$\begin{aligned}\tilde{H} = &- J \sum_{n=1}^{L/2-1} \left(|n,+\rangle\langle n+1,+| \;+\; |n,-\rangle\langle n+1,-| \;+\; h.c.\right) \\ &+ i(J-\gamma)|L/2,+\rangle\langle L/2,-| - i(J+\gamma)|L/2,-\rangle\langle L/2,+|. \end{aligned} \tag{4.29}$$

From this we can clearly see the coupling between the two sectors $|.\,,+\rangle$ and $|.\,,-\rangle$ is controlled by $\gamma$. Alternatively, we can define the transformation matrix $S^\dagger$, such that its columns are the new basis vectors $|n,\pm\rangle$. Our Hamiltonian in this new basis is then retrieved by computing $\tilde{H} = SHS^\dagger$. With the basis properly ordered ($|1,+\rangle$, ... $|L/2,+\rangle$, $|L/2,-\rangle$, ... $|1,-\rangle$), we can write the Hamiltonian in the following block form:

$$\tilde{H} = \begin{pmatrix} H_{\text{hop}} & Q_- \\ Q_+ & H_{\text{hop}} \end{pmatrix}. \tag{4.30}$$

Here, $H_{\text{hop}}$ are simply tight-binding Hamiltonians for chains of length $L/2$ while $Q_\pm$ represent the couplings of the form $\mp i(1 \pm \gamma)$. Therefore, we can see that when $\gamma = \pm 1$, $Q_\mp = 0$, resulting in a triangular block matrix. In this case, the spectrum is just the spectrum of two decoupled half-chain hopping Hamiltonians — as the remaining coupling term does not affect the determinant and hence, the characteristic polynomial. An interpretation of this is that the system acts as two half chains that are coupled in both directions. Thus, at $\gamma = \pm 1$, one of the couplings is broken, resulting in unidirectional transport.

## 4.5 Many-body system

In earlier chapters of this thesis, our focus was exclusively on many-body quantum systems. In this chapter, up to this point, we have been solely concerned with single-particle non-Hermitian systems. In this section, we start to bridge this investigation into the realm of many-body systems. We begin to build towards a complete understanding of the many-body system by first considering the case

of many non-interacting quantum particles. Using results derived for the single-particle case, we can make statements about the spectrum of the non-interacting many-body system. We show that these statements break down in the interacting many-body system, as could be expected.

### 4.5.1 Non-interacting system

As we are now considering a system of many particles, we use the spin representation of our Hamiltonian introduced in Eq. (1.24). We focus on the case of a single dissipative potential, resulting in the Hamiltonian

$$H_{MB} = \frac{J}{2}\sum_{j}^{L-1}(S_j^+ S_{j+1}^- + S_j^- S_{j+1}^+) - i\gamma(S_q^z + \frac{1}{2}), \tag{4.31}$$

for a system of $L$ spins (lattice sites), and $N$ spin-up excitations (particles). The model is similar to an $XX$ chain with a purely imaginary magnetic field.

Using numerical exact diagonalization to obtain the complex spectrum of the Hamiltonian, Eq. (4.31), we observe a similar proliferation of exceptional points at $\gamma = 2$, following the same constraint as the single particle case of $L$ even. In Figure 4.13, we illustrate an example of the spectrum for a small many-body system. The real and imaginary components of the eigenvalues are plotted in separate panels as functions of $\gamma$. The coalescence at $\gamma = 2$ can be observed in both the real and imaginary components.

As this is a system of non-interacting (free) fermions, we can construct the many-body eigenvalues and eigenstates using those from the single-particle case. In Section 4.2, we discovered the eigenvalues and eigenstates in the single-particle case are all doubly degenerate for $L$ even, so we can expect the many-body values and states to be degenerate.

For $L$ even and $N$ odd, every many-body eigenvalue coalesces with at least one other value at $\gamma = 2$, akin to the behavior in the single-particle case. However, for $N$ even, there are always unique many-body eigenvalues that do not coalesce, constructed out of unique combinations of $N$ single-particle states. For example,

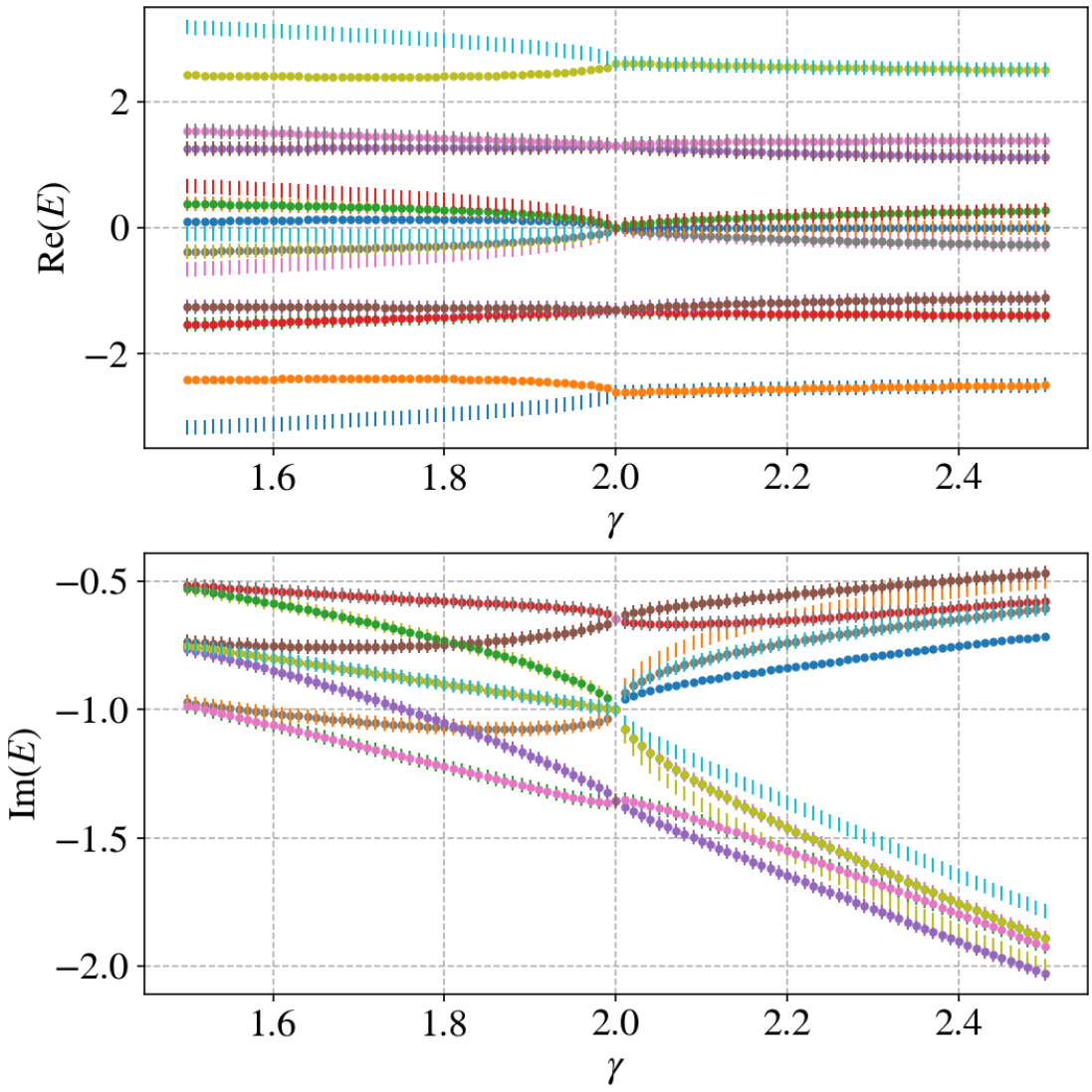


Figure 4.13: Energy spectrum of the Many-Body Hamiltonian Eq. 4.31, for $L = 6$, $N = 3$, and $q = L/2$, as a function of the potential strength $\gamma$. Real and imaginary parts of the eigenvalues are plotted separately.

consider the case of $L = 4$ and $N = 2$. Labeling the single particle states $\phi_n$, the two many-body values consisting of $\phi_1 + \phi_2$ and $\phi_3 + \phi_4$ are unique, as there are no other combinations of the single particle values that make the same many-body value. Similar arguments hold for the eigenstates.

Thus, we conclude that exceptional points occur in the non-interacting many-body system for a single dissipative potential in the center of a lattice with an even number of sites. For an odd number of particles (spins up), every eigenvalue becomes doubly degenerate, while there are eigenvalues that do not become degenerate for an even number of particles (spins up).

### 4.5.2 Effect of interactions

Now we consider the case of many interacting particles. As introduced in the introduction (Section 1.4.1), we allow nearest neighboring particles to interact via $n_j n_{j+1} = (c_j^\dagger c_j)(c_{j+1}^\dagger c_{j+1})$. Mapping this to a spin system, we obtain the interacting non-Hermitian Hamiltonian (Eq. (1.26))

$$H_q = \frac{J}{2}\sum_j^{L-1}(S_j^+ S_{j+1}^- + S_j^- S_{j+1}^+) - i\gamma(S_q^z + \frac{1}{2}) \\ +\Delta\sum_j^{L-1}(S_j^z + 1/2)(S_{j+1}^z + 1/2). \tag{4.32}$$

This is not a system of many free fermions; thus, we can no longer construct the many-body eigenvalues and eigenstates using those from the single-particle case. Numerically, we observed that if the particles are allowed to interact, the proliferation of exceptional points at a single point in parameter space ceases to occur. While one or more eigenvalues can still coalesce, there is no longer a single point where every eigenvalue pairs up with at least one other.

In Figure 4.14, we illustrate the spectrum of both an interacting and non-interacting system for comparison. In the non-interacting case (Left) at $\gamma = 2$, the real and imaginary components merge in groups of at least two eigenvalues. In the interacting case, we see that gaps open in the imaginary part of the spectrum for many of the previously pairing eigenvalues. Additionally, in the real part of the spectrum, the components merge away from the point $\gamma = 2$. Different pairs of eigenvalues merge at different values of $\gamma$, signifying the absence of our previously observed unique exceptional point.

## 4.6 Discussion and context

In this chapter, we have studied the scattering dynamics and the spectrum of a tight-binding single-particle lattice system with a non-Hermitian absorbing impurity at one site, focusing on the case where the impurity is near the center of the lattice. Here, we discuss some similar setups that have been investigated and

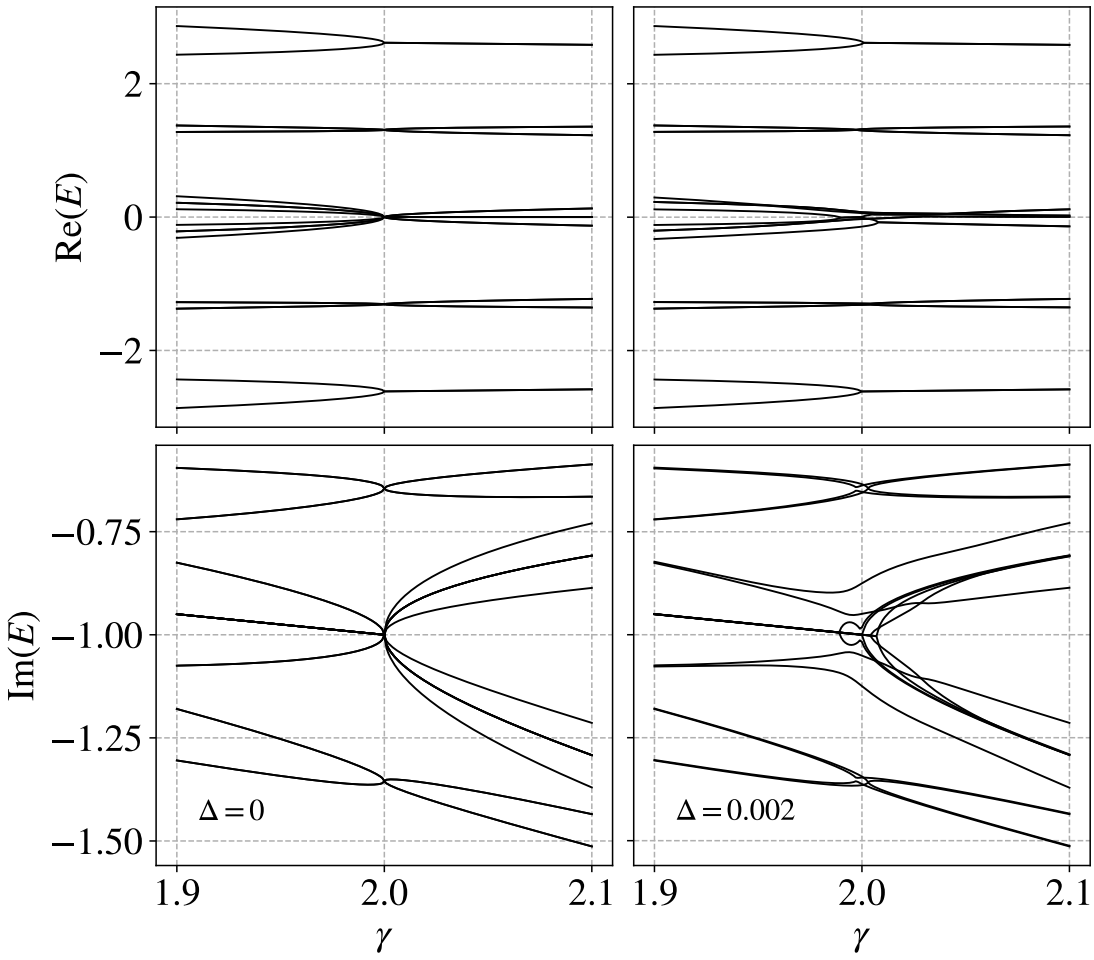


Figure 4.14: The energy spectrum of the interacting many-body Hamiltonian Eq. 4.32, plotted as a function of the potential strength $\gamma$. System consisting of $L = 6$, $N = 3$, and $q = L/2$, with $J = 2$, and $\Delta = 0$ (Left) and $\Delta = 0.002$ (Right). Real and imaginary parts of the eigenvalues are plotted separately.

possible experimental realizations. Following this, we summarize our findings in this chapter.

Setups loosely similar to the one studied here have been explored in a few other recent works. In Ref. [158], scattering off a localized lattice impurity is studied, where the strength and phase of the impurity are oscillating. Scattering was studied using Gaussian wavepackets, as in the present work. For certain parameters, the oscillatory non-Hermitian impurity was reported to allow perfect transmission ('Floquet invisibility'). In Ref. [304], the lattice impurity was placed at the lattice edge and the role of the non-orthogonality of the eigenstates on the non-unitary time evolution was explored. In addition, some related issues have been discussed in the context of $\mathcal{PT}$-symmetric lattice systems, formed by having imaginary potentials on multiple sites [161–167] akin to the $\mathcal{PT}$-symmetric

model introduced in Section 4.4. As already discussed, the spectrum of lattices with two impurities has been studied in Refs. [162, 167], wherein the authors demonstrate the existence of exceptional points using different methodologies to those employed in this thesis. Ref. [161] reported an eigenstate which is localized on the two impurity sites — this may be considered a $\mathcal{PT}$-symmetric version of the localized eigenstate we have studied. Refs. [162, 163] have made comparisons between the non-Hermitian system and corresponding Hermitian system, as we have done. After the appearance of our single absorber investigation as a preprint, our single-particle non-Hermitian Hamiltonian has appeared in Ref. [183] as an effective Hamiltonian. Additionally, a similar investigation into the dynamics of non-interacting quantum particles under the influence of localized losses has since been made using the Linblad formalism [305].

*Experimentally*, lattice systems with localized losses have been studied in several contexts. In the setup of Ref. [306, 307], a Bose-Einstein condensate is realized in a one dimensional optical lattice, with engineered losses on a single site acting as a local dissipative potential. Connecting single-particle results such as ours to many-boson physics in such a setup remains an interesting challenge for future work.

A realization more similar to the single particle tight-binding system considered in this work is that with photonic lattice systems, such as those in Refs. [308, 309]. In this setup, photonic lattices are realized using femtosecond laser writing to inscribe waveguide arrays with appropriate index profiles in fused silica. The physics of photons in such an architecture can be well-described by a tight-binding model, with an additional spatial direction taking the role of time. This setup, or its variants, has been used to demonstrate a number of paradigmatic tight-binding phenomena, including Bloch oscillations [310] and Anderson localization [311, 312]. Both one-dimensional and two-dimensional lattices have been realized, and lossy sites and other types of non-Hermiticity have been explored [109, 309, 313]. It is possible to create localized excitations (wavepackets) and observe their propagation [312, 314]. Thus, studies of scattering off lossy sites should be possible in such a

setup.

Another possible experimental setting for observing scattering off non-Hermitian potentials in a tight-binding lattice might be microwave realizations using coupled dielectric resonators, such as that discussed in [115]. This setup is well approximated by a nearest-neighbor tight-binding Hamiltonian. The resonance frequency of an isolated resonator, and the coupling strength between two resonators (due to the evanescent electromagnetic field), correspond to the on-site energy and the hopping term, respectively. A controllable on-site loss is created by placing an absorbing material on a particular resonator.

In this chapter, by explicit time evolution starting from initial states consisting of momentum-carrying wavepackets, we found the reflection, transmission, and absorption coefficients ($R$, $T$, $A$) as a function of the impurity strength $\gamma$ and of the incident momentum $k$. The absorption was shown to first grow and then decrease as the strength $\gamma$ was increased. It can be argued that this non-monotonic behavior is related to the quantum Zeno effect. The experimentally observed non-monotonic behavior of Ref. [131] can be interpreted in the same light. We have demonstrated and analyzed the effect in a simple lattice setting. We have also compared the lattice results with the scattering of a single particle in a continuum from an absorptive delta-potential, finding good agreement between the two.

We have presented the spectrum of the non-Hermitian system. The system we focus on — an even number of sites, with an impurity at one of the center sites — has an unusual exceptional point structure. At the same value of $\gamma$, *all* the eigenstates of the system coalesce in pairs. This is not a higher-order exceptional point [296–298], but rather it is a collection of many second-order coalescences at the same point in parameter space. We also demonstrated the same unusual collection of many second-order exceptional points in a $\mathcal{PT}$-symmetric non-Hermitian system.

At large $\gamma$, the spectrum contains a single localized eigenstate. This is another way in which a strongly dissipative impurity acts like a real-valued impurity potential. The eigenvalue corresponding to the localized eigenstate has a *purely*

*imaginary* value. This feature is specific to the lattice, as we have demonstrated that there are no bound states in the corresponding continuum problem. Therefore, it would be intriguing to examine the disappearance of the bound state as the lattice system approaches the continuum limit. Such an investigation could provide insights into the potential significance of the bound state in the observed non-monotonic behavior exhibited in the scattering dynamics.

We established various foundational results in understanding a particular many-body non-Hermitian system. We demonstrated the occurrence of many exceptional points at a single parameter point in the non-interacting many-body system by utilizing our new knowledge of the single-particle case. The same phenomenon did not appear to occur in the interacting system. Our work opens up several avenues of research. In this thesis, we have explored scattering dynamics. A detailed study of other types of dynamics remains to be done, not only for tight-binding lattices, but also for continuum particles subjected to localized absorbers. Extending such dynamical considerations to nonlinear cases [178, 307, 315] also deserves further exploration. The spectral part of the present study provides motivation for a more thorough investigation of the spectrum of relatively simple non-Hermitian models. The structure we have found — many pairs of eigenvalues coalescing at a single point — persists in the non-interacting many-body system as can be proven from the single particle case, but is lost in the presence of interactions. This behavior suggests that non-Hermitian spectra may hold more surprises not yet known in the literature.

# Chapter 5

# Summary

In this thesis, we carried out investigations that can generally be placed in the context of many-body quantum physics. We investigated various ways to define a correspondence between energy and temperature in finite isolated quantum systems. The first central idea was inspired by implications of the eigenstate thermalization hypothesis, namely that reduced eigenstate density matrices should resemble thermal states. To provide sufficient context, we introduced the idea of thermalization in isolated quantum systems, in particular, the eigenstate thermalization hypothesis. Following this, we considered a standard definition of temperature in statistical mechanics, relating temperature to entropy, and applied it to isolated quantum systems. Finally, we considered the antithesis of an isolated quantum system, namely an open quantum system. We explored the emerging phenomena from a non-Hermitian lattice system, effectively describing a dissipative open quantum system.

In Chapter 2, we proposed methods of defining temperature based on minimizing the distance between (full or reduced) eigenstate density matrices and the canonical ensemble. These definitions were inspired by the idea that an eigenstate has information regarding thermalization encoded in its structure, an implication of the ETH. We found that for full eigenstate matrices, the corresponding temperature $\beta_E$ was proportional to the canonical temperature (Eq. (1.1)), a standard in the study of thermalization. The constant of proportionality originates in the Schatten $p$-distance utilized. This was a general result, independent of integra-

bility, chaos, or even thermalization; the relation holds even for non-physical Hamiltonians. This temperature definition reduced to depending solely on the eigenvalues of the system.

For reduced eigenstate matrices, independent of distance measure, the corresponding temperature conformed increasingly well to $\beta_C$ when increasing the system size; while holding the subsystem size fixed to some small value less than half the total size. The subsystem temperature heavily relies on the ETH, and as such, it depends on the chaotic (thermalizing) nature of the system and hence the structure of the eigenstates. As could thus be expected, the subsystem temperature does not work well for non-chaotic physical Hamiltonians, or random matrices, in which there is no sense of locality.

In Chapter 3, we considered temperature defined via the standard thermodynamic relation (Eq. (1.3)) between microcanonical entropy and temperature. This investigation is related to the equivalence of microcanonical and canonical ensembles, wherein exact equality is expected in the thermodynamic limit. However, in recent years the emergence of statistical mechanics has been heavily investigated in finite systems of sizes accessible to exact diagonalization. As such, it is essential to understand deviations from ensemble equivalence in systems of such size. We investigated various ways of numerically computing the microcanonical entropy in such systems and compared the resultant temperatures obtained via Eq. (1.3) to the canonical temperature Eq. (1.1).

We investigated four ways of numerically determining the microcanonical entropy $S(E)$, defined as Eq. (3.2). Two of the procedures, counting eigenstates in a constant valued (energy-independent) energy window $\Delta E$ and neglecting a choice of $\Delta E$ entirely via an approximation to the integrated density of states, both result in noticeable finite-size deviations between the resultant temperatures and the canonical temperature. In both cases, we determined that the deviations are expected due to sub-leading corrections in the entropy. However, we demonstrated that counting eigenstates in an energy-dependent window $\Delta E = \alpha^{-1}\sqrt{2\pi k_B T_c^2 C_c}$ results in a temperature that is in excellent agreement with the canonical temper-

ature. Here, $\alpha$ is an arbitrary constant for which we do not have precise criteria for fixing its value. We did note that smaller systems appear to require a larger $\alpha$ for a good agreement between the temperatures. Meanwhile, for larger systems, the required $\alpha$ seems to decrease with system size.

These issues surrounding proportionality constants can be avoided by using this energy-dependent window in conjunction with the formulation of entropy in terms of the integrated density of states instead of counting eigenstates in the window. As explained, the constants in $\Delta E(E)$ (Eq. (3.11)) result in a constant shift in entropy, which has no bearing on the temperature. The resultant temperature obtained using this formulation is in excellent agreement with the canonical temperature, even for the small system sizes under consideration in this thesis. Thus, we have determined a prescription that results in a microcanonical entropy that reproduces the canonical temperature in finite isolated quantum systems — without the necessity of any arbitrary constants.

In Chapter 4, we investigated the intriguing phenomena arising from a simple dissipative non-Hermitian lattice model. By studying the explicit time evolution of a single excitation from an initial state consisting of momentum-carrying wavepackets, we found the reflection, transmission, and absorption coefficients $(R, T, A)$ as a function of the dissipation strength $\gamma$ and momentum $k$. The absorption exhibited non-monotonic dependence on $\gamma$, initially growing to a maximum rate before decaying to zero at large $\gamma$. This behavior can be interpreted as a realization of the quantum Zeno effect in a simple lattice setting. We were able to match these lattice results with the scattering of a single particle in a continuum in the presence of an imaginary delta potential. Furthermore, at large $\gamma$ the system behaves similarly to a system with a real potential $V$, including the emergence of a localized eigenstate, which allowed us to directly compare values of $\gamma$ and $V$.

We presented a detailed study of the spectrum of the single-particle system. In particular system configurations, we identified many exceptional points occurring at a single point in parameter space. We analytically proved this peculiar

proliferation of exceptional points. Using the same analytical methodology, we demonstrated a similar proliferation of exceptional points in a $\mathcal{PT}$-symmetric non-Hermitian system, constructed by balancing dissipative and enhancing potentials symmetrically in the lattice. Using these new results for the single-particle system, we proved that there is a similar proliferation of many exceptional points in the non-interacting many-particle system. This proliferation appears to cease in the presence of interactions.

# Appendix A

# Eigenstate temperature correspondence - Additional data

In this appendix, we provide additional numerical results for the eigenstate based temperatures investigated in Chapter 2:

- In Appendix A.1 we present further numerical data for the subsystem temperature, in particular, the result of varying the subsystem size in the staggered field model.
- In Appendix A.2, we compute the distance between $\rho^A$ and $\rho_C^A$ at the canonical temperature $\beta_C$.

## A.1 Subsystem temperature - Various subsystem sizes

Here, we present the result of using different subsystem sizes when computing the subsystem temperature $\beta_S$, in various models.

In Figure A.1 we show the explicit scaling of various quantities with subsystem size. We see in (A) that the average minimum of $d_1$ increases as $L_A$ increases, i.e., the two matrices become less alike. In (B) the standard deviation of the minima increases but then decreases again as $L_A$ approaches $L/2$. In (C) we see the width of $\beta_S$ decreased as $L_A$ increased, and similarly in (D) the distance between $\beta_C$

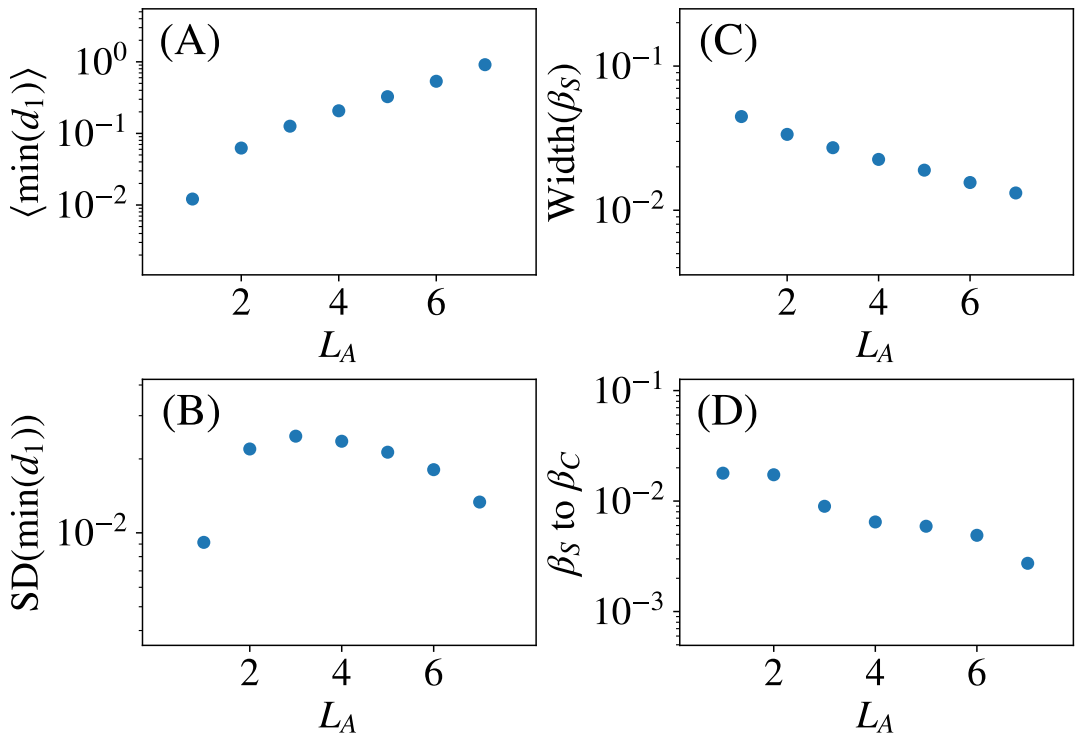


Figure A.1: Subsystem temperature scaling with subsystem size results. Staggered field model with $h_x = h_z = 0.5$, $J = 1$, $\Delta = 0.95$ and $L = 14$. **(A)** Mean value of $\min(d_1(\rho^A, \rho_C^A))$, **(B)** Standard deviation of $\min(d_1(\rho^A, \rho_C^A))$, **(C)** Width of $\beta_S$ data **(D)** RMS-distance between $\beta_C$ and linear fit to $\beta_S$, versus $L_A$. All quantities are calculated in the central 20% of the spectrum.

and $\beta_S$ decreased as $L_A$ increased.

In Figure A.2 we show the resultant minimum distance $\min(d_1(\rho^A, \rho_C^A))$ when using different subsystem sizes for various system sizes. This again illustrates the decrease in average minimum distance as $L$ increases, but also shows that the average minimum distance increases with increasing $L_A$.

In Section 2.3, we restricted our results to subsystems with $L_A < L/2$. In Figure A.3 we present an example of the result of using a subsystem with $L_A > L/2$. The minimum distance $\min(d_p(\rho^A, \rho_C^A))$ continues the trend previously described of increasing as $L_A$ increases, and the variance of the values also decreases. However, the $\beta_S$ values appeared to cease to align with the $\beta_C$ curve, although the variance did continue to decrease. An example of the resultant $\beta_C$ for a subsystem greater than half the total system can be seen in Figure A.3. One can also see that the distance between the matrices is close to the maximum value.

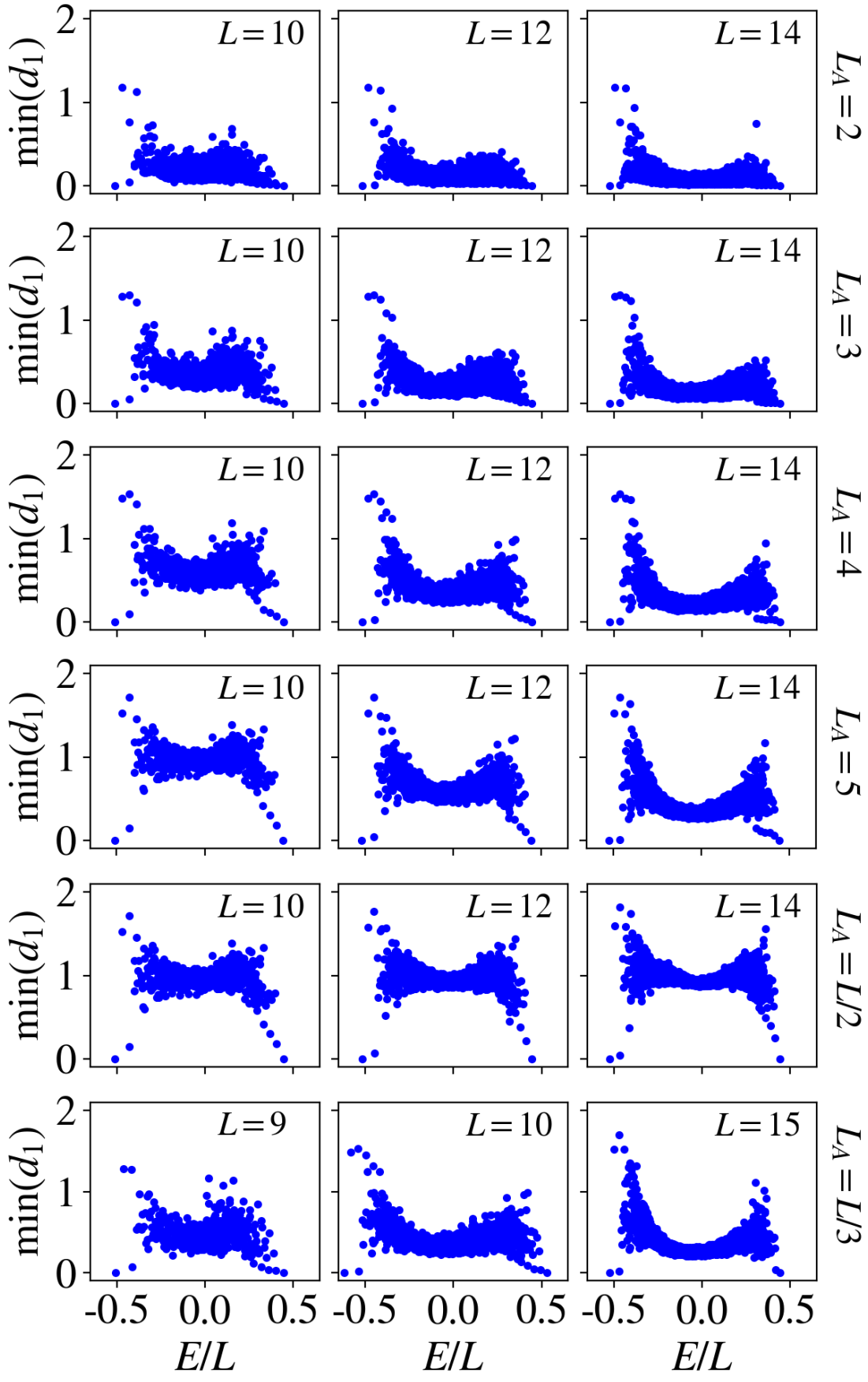


Figure A.2: Subsystem temperature results for the staggered field model with $h_x = h_z = 0.5$, $J = 1$ and $\Delta = 0.95$, Eq. (1.15). $\min(d_1(\rho^A, \rho^A_C))$ plotted versus energy, each row illustrating a different scaling of system/subsystem size.

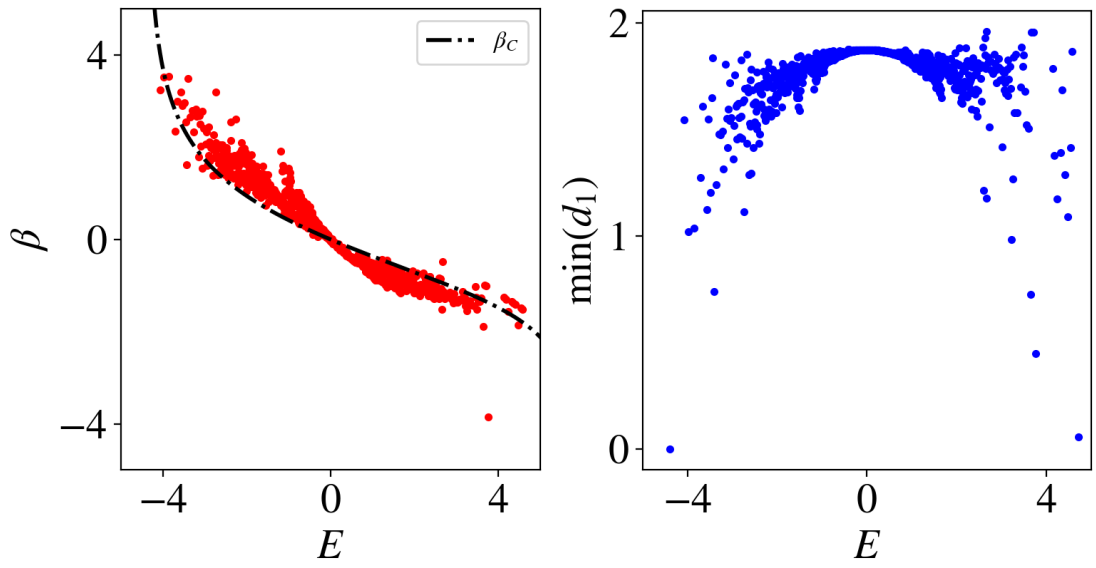


Figure A.3: Subsystem temperature results for chaotic Ising model with $L = 10$ and $L_A = 7$, $h_x = 0.75$ and $h_z = 0.5$. **Left:** $\beta_S$ vs. $E$ with canonical $\beta_C$ curve shown. **Right:** $\min(d_1(\rho^A, \rho_C^A))$ versus energy.

## A.2 Distance at canonical temperature

In the main text, we minimized the distance between the reduced density matrix $\rho^A = \mathrm{tr}_B\,|E_n\rangle\langle E_n|$, and the reduced canonical matrix $\rho_C^A = \mathrm{tr}_B \exp(-\beta H)$, as a function of $\beta$, to obtain the subsystem temperature $\beta_S$. One could instead ask how close the two matrices are at the canonical temperature $\beta_C$. In Figure A.4,

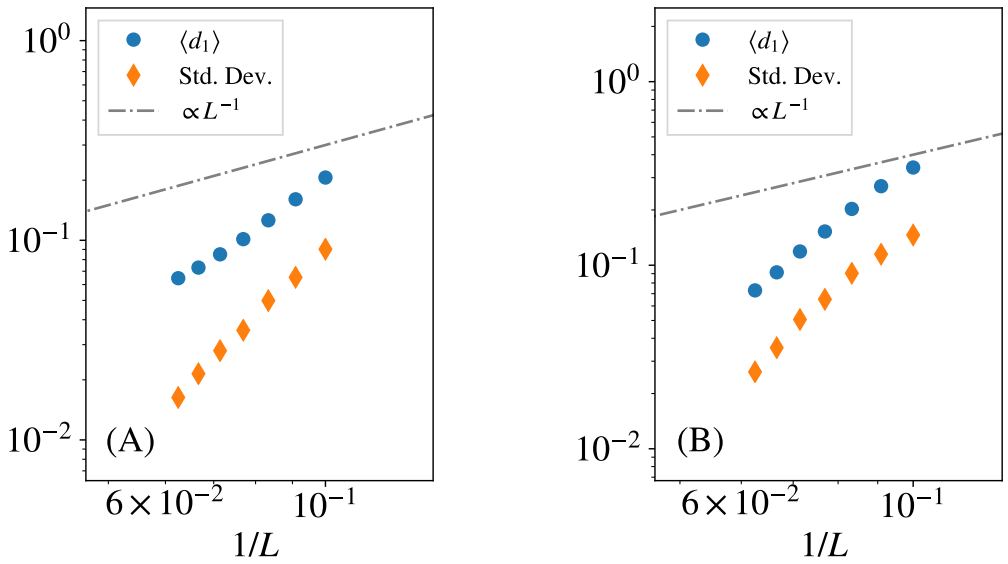


Figure A.4: Distance $d_1$ at canonical temperature $\beta_C$, averaged over the central 20% of the spectrum, versus inverse system size $L$. We also show the mean standard deviation of the minima. With $L_A = 2$ for (**A**) the staggered field model, Eq. (1.15), with $h_z = h_x = 0.5$, and (**B**) the chaotic Ising model, Eq. (1.21), with $h_z = 0.5$ and $h_x = 0.75$.

we plot the resulting trace distance ($p = 1$) between the two matrices for two chaotic spin chains. Alongside the data, we plot a line proportional to the inverse system size $1/L$ — clearly illustrating that the distance between the matrices at $\beta_C$ decreases faster than $1/L$, for these particular systems at least.

# Appendix B

# Saddle point calculation

In this appendix, we provide the full saddle point calculation that is used to derive the energy-dependent window width $\Delta E(E)$ utilized in Chapter 3. The same calculation is performed in Ref. [54] although with less details than presented here, and similar ones can be found Section 7.2 of Ref. [74], Section 6.8 of Ref. [72], and Chapter 3 of Ref. [75].

We wish to calculate the microcanonical entropy

$$S(E) \;=\; k_B \ln(\Gamma(E)), \tag{B.1}$$

as defined in Eq. (3.2) of Chapter 3. Here,

$$\Gamma(E) \;=\; \Delta E g(E) \;=\; \Delta E \sum_n \delta(E - E_n) \tag{B.2}$$

is the statistical weight, which counts the number of eigenstates with energy $E$ in a window of width $\Delta E$ around $E$, and

$$g(E) \;=\; \sum_n \delta(E - E_n), \tag{B.3}$$

is the density of states. Rearranging Eq. B.1 as

$$e^{S/k_B} \;=\; \Gamma(E) \;=\; \Delta E \sum_n \delta(E - E_n), \tag{B.4}$$

we then replace the delta function with its integral representation

$$\delta(x) = \int_{-\infty}^{\infty} \frac{dp}{2\pi} e^{ipx} \tag{B.5}$$

and introduce the Helmholtz free energy $F(\beta) = -\beta^{-1} \ln\left(\sum_n e^{-\beta E_n}\right)$, to obtain

$$e^{S/k_B} \;=\; i\Delta E \int_{-i\infty}^{i\infty} \frac{d\beta}{2\pi} e^{\beta(E - F(\beta))}. \tag{B.6}$$

The integral over $\beta$ is along the imaginary axis in the complex $\beta$-plane. The integral in Eq. (B.6) needs to be evaluated, which can be done via a saddle point approximation. To apply the saddle point approximation, we first need to find the critical point of the exponent $h(\beta) = \beta(E - F(\beta))$, by setting $h'(\beta) = 0$ and solving for $\beta$.

$$\begin{aligned}
\frac{\partial h(\beta)}{\partial \beta} &= E - F(\beta) + \beta(\frac{\partial E}{\partial \beta} - \frac{\partial F(\beta)}{\partial \beta}) = E - F(\beta) - \beta \frac{\partial F(\beta)}{\partial \beta}, \\
\frac{\partial F(\beta)}{\partial \beta} &= \beta^{-2} \ln(Z) - \beta^{-1} \frac{\partial Z}{\partial \beta}, \\
\implies h'(\beta) &= E - \frac{\partial Z}{\partial \beta} = E - \frac{\sum_n E_n e^{-\beta E_n}}{\sum_n e^{-\beta E_n}}.
\end{aligned} \tag{B.7}$$

This means the condition for the critical point is

$$E = \frac{\sum_n E_n e^{-\beta E_n}}{\sum_n e^{-\beta E_n}}, \tag{B.8}$$

which is precisely Eq. (1.1) defining the canonical temperature. Thus the saddle point is at $\beta = \beta_C$, the canonical inverse temperature.

Now to perform the saddle point approximation to second order, so as to examine the effect of $\Delta E$ in finite sized systems, we must expand $h(\beta)$ as a Taylor series about $\beta_C$, up to second order, as the first is zero by definition. First, we obtain the derivatives

$$\begin{aligned}
\frac{\partial^2 h(\beta)}{\partial \beta^2} &= \frac{\partial h'(\beta)}{\partial \beta} = \frac{\partial}{\partial \beta}(E - F(\beta) - \beta \frac{\partial F(\beta)}{\partial \beta}), \\
\frac{\partial^2 h(\beta)}{\partial \beta^2} &= -2\frac{\partial F(\beta)}{\partial \beta} - \beta \frac{\partial^2 F(\beta)}{\partial \beta^2}.
\end{aligned} \tag{B.9}$$

Then, replacing $\beta$ derivatives with $T$ derivatives, we observe

$$\frac{\partial^2 h(\beta)}{\partial \beta^2} = -2(-\frac{1}{\beta^2 k_B}\frac{\partial F(\beta)}{\partial T}) - \beta(\frac{2}{\beta^3 k_B}\frac{\partial F(\beta)}{\partial \beta} + \frac{1}{\beta^4 k_B^2}\frac{\partial^2 F(\beta)}{\partial T^2}),$$
$$\frac{\partial^2 h(\beta)}{\partial \beta^2} = -\frac{1}{\beta^3 k_B^2}\frac{\partial^2 F(\beta)}{\partial T^2} = -k_B T^2(T\frac{\partial^2 F(\beta)}{\partial T^2}) \tag{B.10}$$

Introducing the heat capacity $C = \frac{\partial E}{\partial T} = -T\frac{\partial^2 F}{\partial T^2}$, we finally have

$$h''(\beta) = \frac{\partial^2 f(\beta)}{\partial \beta^2} = -k_B T^2 C. \tag{B.11}$$

We are now equipped to perform the saddle point approximation. Expanding in (B.6), we can write

$$e^{S/k_B} \approx i\Delta E \int_{-i\infty}^{i\infty} \frac{d\beta}{2\pi} e^{h(\beta_C)+h''(\beta_C)(\beta-\beta_C)^2/2}, \tag{B.12}$$

then pulling out the constant $h(\beta_C)$ term, and substituting for $h''(\beta_C)$, we obtain

$$e^{S/k_B} \approx i\Delta E \cdot e^{\beta_C(E-F(\beta_C))} \int_{-i\infty}^{i\infty} \frac{d\beta}{2\pi} e^{k_B T_C^2 C_C(\beta-\beta_C)^2/2}. \tag{B.13}$$

Substituting $ix = \beta - \beta_C$, we end up with the Gaussian integral

$$e^{S/k_B} \approx \frac{\Delta E}{2\pi} \cdot e^{\beta_S(E-F(\beta_C))} \int_{-\infty}^{\infty} dx\ e^{-(k_B T_C^2 C_C/2)x^2}, \tag{B.14}$$

which evaluated equals

$$e^{S/k_B} \approx \frac{\Delta E}{\sqrt{2\pi k_B T_C^2 C_C}} e^{\beta_C(E-F(\beta_C))}. \tag{B.15}$$

Then simply taking the logarithm to calculate the entropy, we obtain

$$\frac{S}{k_B} = \beta_C E - \beta_C F(\beta_C)) + \ln\left(\frac{\Delta E}{\sqrt{2\pi k_B T_C^2 C_C}}\right). \tag{B.16}$$

# Appendix C

# Analytical derivation of exceptional points

In this appendix, we provide the full analytical derivations of the exceptional points that were observed numerically in Chapter 4.

- In Appendix C.1 we provide the full analytical derivation of the exceptional points in the single dissipative potential system.
- In Appendix C.2 we provide the full analytical derivation of the exceptional points in the $\mathcal{PT}$-symmetric system.

## C.1 Analytical expressions for the spectrum of a purely dissipative system

In the main text, we have shown numerically that the eigenvalues of the purely dissipative system (Eq. (1.25)) coalesce in pairs at $\gamma = 2$, for even $L$, when the impurity site $q$ is one of the central sites, i.e., when $q = L/2$ or $q = (L/2)+1$. In this Appendix, we analyze the eigenvalues analytically. We express the characteristic polynomial (whose roots are the eigenvalues) in a form that allows us to predict: first, that all the eigenvalues pair up when $q$ is one of the central sites, and second, that there are multiple exceptional points because each eigenstate pair is linearly dependent. The characteristic polynomial is treated in Section C.1.1, and the case

of $q = L/2$ (or $q = L/2 + 1$) is considered in Section C.1.2.

### C.1.1 General location, $q$

We want to find the eigenvalues of the $L \times L$ matrix

$$[H_q]_{jk} = -\delta_{j,k+1} - \delta_{j+1,k} - i\gamma\delta_{jq}\delta_{jk}\,. \tag{C.1}$$

Here, $1 \leq q \leq L$. The characteristic polynomial of this matrix up to a minus sign is the determinant of the tridiagonal matrix

$$\begin{pmatrix} \lambda & 1 & 0 & \dots & \dots & \dots & \dots & \dots \\ 1 & \lambda & 1 & \dots & \dots & \dots & \dots & \dots \\ \vdots & \vdots & \ddots & \ddots & \ddots & \dots & \dots & \dots \\ \vdots & \vdots & \vdots & 1 & \lambda + i\gamma & 1 & \dots & \dots \\ \vdots & \vdots & \vdots & \vdots & \ddots & \ddots & \ddots & \dots \\ \vdots & \vdots & \vdots & \vdots & \vdots & 1 & \lambda & 1 \\ \vdots & \vdots & \vdots & \vdots & \vdots & \vdots & 1 & \lambda \end{pmatrix}. \tag{C.2}$$

The determinants of tridiagonal matrices satisfy a recurrence relation. If $P_n$ is the determinant of the $n \times n$ matrix with elements

$$A_{ij} = b_i\delta_{i,j+1} + c_j\delta_{i+1,j} + a_i\delta_{ij}, \tag{C.3}$$

then ,

$$P_n = a_n P_{n-1} - c_{n-1}b_{n-1}P_{n-2}\,. \tag{C.4}$$

This recurrence relation can be verified by determinant expansion and appears in numerous sources, e.g., is mentioned in Section 8.5 of Ref. [145]. The characteristic

polynomial of $H$ (C.1), i.e., the determinant of the matrix (C.2), therefore satisfies

$$\begin{aligned} P_n &= \lambda P_{n-1} - P_{n-2}, \quad \text{if } n \neq q \\ P_q &= (\lambda + i\gamma) P_{q-1} - P_{q-2}, \quad \text{if } q > 1 \\ P_0 &= 1 \\ P_1 &= \lambda + i\gamma\delta_{q1}. \end{aligned} \tag{C.5}$$

A standard method of solving such linear recurrence relations is to use the $Z$-transform. Ignoring the second line in Eq. (C.5), i.e., ignoring the impurity, we can get an expression for $P_n$ in terms of $P_0$, $P_1$ and $\lambda$. Since $P_n$ is only defined for $n \geq 0$, we use the unilateral $Z$-transform defined as

$$\mathcal{Z}\{P_n\} = \sum_{n=0}^{\infty} P_n z^{-n}. \tag{C.6}$$

Now, letting $F(z) = \mathcal{Z}\{P_n\}$ and expanding the sum, we can write

$$F(z) = P_0 + P_1 z^{-1} + \sum_{n=2}^{\infty} P_n z^{-n}, \tag{C.7}$$

$$z^2 F(z) - z^2 P_0 - z P_1 = \sum_{n=2}^{\infty} P_n z^{2-n}. \tag{C.8}$$

Then, shifting the summation index and utilizing the recurrence relation we obtain

$$z^2 F(z) - z^2 P_0 - z P_1 = \lambda(z F(z) - z P_0) - F(z). \tag{C.9}$$

We then start by solving for $F(z)$,

$$F(z) = \frac{P_0 z^2}{z^2 - \lambda z + 1} + \frac{(P_1 - \lambda P_0) z}{z^2 - \lambda z + 1}, \tag{C.10}$$

which we can then decompose into partial fractions as,

$$F(z) = P_0 \left( \frac{A(\lambda) z}{z - x_+} + \frac{B(\lambda) z}{z - x_-} \right) + (P_1 - \lambda P_0) \left( \frac{C(\lambda) z}{z - x_+} + \frac{D(\lambda) z}{z - x_-} \right), \tag{C.11}$$

with $x_\pm(\lambda) = \frac{1}{2}\left[\lambda \pm \sqrt{\lambda^2 - 4}\right]$. We can then obtain the functions by comparing

equations (C.10) and (C.11). We can now take the inverse $Z$-transform, which is easily done here as the function is of the form $z/(z-\alpha)$. Performing the inverse transform, followed by some rearranging, this yields

$$P_n = \frac{P_0}{\sqrt{\lambda^2-4}}\left[(x_+)^{n+1} - (x_-)^{n+1}\right] \; + \; \frac{P_1 - \lambda P_0}{\sqrt{\lambda^2-4}}\left[(x_+)^n - (x_-)^n\right]. \tag{C.12}$$

Now, defining:

$$K_n(\lambda) := \begin{cases} \dfrac{1}{\sqrt{\lambda^2-4}}\left[(x_+)^{n+1} - (x_-)^{n+1}\right] & \text{for } n \geq 0 \\ 0 & \text{for } n < 0 \end{cases} \tag{C.13}$$

we can rewrite Eq. (C.12) as

$$P_n = P_0 K_n + (P_1 - \lambda P_0) K_{n-1}. \tag{C.14}$$

Since we have derived this ignoring the impurity, Eqs. (C.12) and (C.14) are valid either for $q = 1$, in which case $P_1 = \lambda + i\gamma$, or for values of $n$ less than $q$.

For $q = 1$, we have $P_0 = 1$ and $P_1 = \lambda + i\gamma$ so that $P_n = K_n + i\gamma K_{n-1}$, and therefore:

$$P_L = K_L + i\gamma K_{L-1} \quad \text{for } q = 1. \tag{C.15}$$

We now turn to $q > 1$. For $n < q$, Eqs. (C.12) and (C.14) are valid directly with $P_0 = 1$ and $P_1 = \lambda$, i.e., with $P_1 - \lambda P_0 = 0$, so that

$$P_n = K_n \quad \text{for } q > 1 \text{ and } n < q. \tag{C.16}$$

We have expressions for $P_n$ up to $n = q - 1$, but we want $P_L$ and $L \geq q$. To go beyond $q$, we define a new sequence of functions $Q_n(\lambda)$, satisfying the same recurrence relation as $P_n$ (C.5), except with new initial conditions: $Q_0 = P_{q-1}$

and $Q_1 = P_q = (\lambda + i\gamma)P_{q-1} - P_{q-2}$. Thus we need to solve

$$\begin{aligned} Q_n &= \lambda Q_{q-1} - Q_{q-2}, \quad Q_0 = K_{q-1}, \\ Q_1 &= (\lambda + i\gamma)K_{q-1} - K_{q-2}. \end{aligned} \tag{C.17}$$

Now we have already solved the same recurrence relation for $P_n$, using the $Z$ transform. The solution is $Q_n = Q_0 K_n + (Q_1 - \lambda Q_0)K_{n-1}$. Therefore

$$Q_n = K_{q-1}K_n + (i\gamma K_{q-1} - K_{q-2})K_{n-1}\,. \tag{C.18}$$

Noting that $Q_n(\lambda) = P_{n+q-1}(\lambda)$, the determinant of the full matrix can be found as $P_L(\lambda) = Q_{L-q+1}(\lambda)$. Thus

$$P_L(\lambda) = K_{q-1}K_{L-q+1} + (i\gamma K_{q-1} - K_{q-2})K_{L-q}\,. \tag{C.19}$$

We now introduce a slight change of notation: We refer to this polynomial as $P_{L,q}$. In other words, the characteristic polynomial of the Hamiltonian matrix of a lattice of size $L$ and having the impurity at position $q$ will be called $P_{L,q}$. Note that Eq. (C.19) reduces to Eq. (C.15) for $q = 1$; thus

$$P_{L,q} = K_{q-1}K_{L-q+1} + (i\gamma K_{q-1} - K_{q-2})K_{L-q} \tag{C.20}$$

for all positions of the impurity, $1 \leq q \leq L$.

By binomial-expanding $(x_\pm)^{n+1}$, one can show that

$$P_{L,q}(-\lambda^*) = (-1)^L P_{L,q}(\lambda)^*\ . \tag{C.21}$$

This shows that the zeros of $P_{L,q}$ (eigenvalues of $H$) are symmetric by reflection through the imaginary axis in the complex plane, since if $\lambda = a + ib$ is a zero then $-\lambda^* = -a + ib$ is also a zero. This symmetry is obvious from the spectra shown in Figure 4.6.

### C.1.2 Impurity at center

We now turn to the case we have focused on in this paper: when $L$ is even and $q = L/2$ or $q = L/2 + 1$. In this case,

$$\begin{aligned} P_{L,\frac{L}{2}} &= K_{\frac{L}{2}-1}K_{\frac{L}{2}+1} + (i\gamma K_{\frac{L}{2}-1} - K_{\frac{L}{2}-2})K_{\frac{L}{2}} \\ &= K_{\frac{L}{2}-1}(\lambda K_{\frac{L}{2}} - K_{\frac{L}{2}-1}) + (i\gamma K_{\frac{L}{2}-1} - K_{\frac{L}{2}-2})K_{\frac{L}{2}} \\ &= -(K_{\frac{L}{2}-1})^2 + K_{\frac{L}{2}}\left(\lambda K_{\frac{L}{2}-1} - K_{\frac{L}{2}-2}\right) + i\gamma K_{\frac{L}{2}-1}K_{\frac{L}{2}} \\ &= (K_{\frac{L}{2}})^2 - (K_{\frac{L}{2}-1})^2 + i\gamma K_{\frac{L}{2}-1}K_{\frac{L}{2}}\,. \end{aligned}$$

Now precisely when $\gamma = 2$, this can be written as

$$P_{L,L/2} = \left(K_{\frac{L}{2}} + iK_{\frac{L}{2}-1}\right)^2\,. \tag{C.22}$$

This means that every root of the polynomial is a zero of order at least 2, i.e., the eigenspectrum is doubly degenerate at $\gamma = 2$. We have thus analytically derived the most prominent feature of the spectrum presented in the main text.

### C.1.3 Eigenstate degeneracy

We now argue that, for a tridiagonal system such as ours, a coalescence of eigenvalues implies a coalescence of eigenstates, i.e., that the eigenstates corresponding to equal eigenvalues are always linearly dependent. Consider some eigenvalue $\lambda$ and corresponding eigenvector $X = (x_1, x_2, \ldots, x_L)^T$ of $-H$, Eq. (C.1), for convenience. Using the eigenvalue equation $-H \cdot X = \lambda X$, we can then determine

the coefficients $x_i$ via:

$$\begin{aligned} x_2 &= \lambda x_1 \\ x_3 &= (\lambda^2 - 1)x_1 \\ &\vdots \\ x_q &= \lambda x_{q-1} - x_{q-2} \\ x_{q+1} &= x_q(\lambda - i\gamma) - x_{q-1} \\ x_{q+2} &= \lambda x_{q+1} - x_q \\ &\vdots \end{aligned} \tag{C.23}$$

It is clear to see that every component of the vector can be written as a function of $\lambda$, and $\gamma$, times the first component $x_1$. So an eigenvector $X$ only has one free component $x_1$.

If we had two eigenvectors, $X$ and $Y$, which corresponded to the same eigenvalue $\lambda$, i.e., we had a degeneracy, then it is now a trivial exercise to show that the two eigenvectors are not linearly independent. Consider the equation:

$$a \cdot X \; + \; b \cdot Y \; = \; 0. \tag{C.24}$$

Starting with the coefficients

$$a \cdot x_1 + b \cdot y_1 = 0 \implies a = -b \cdot y_1/x_1 \tag{C.25}$$

$$a \cdot x_2 + b \cdot y_2 = 0 \implies -b \cdot f(\lambda) \cdot (y_1/x_1) \cdot x_1 + b \cdot f(\lambda) \cdot y_1 = 0 \tag{C.26}$$

$$\implies -b \cdot f(\lambda) + b \cdot f(\lambda) = 0 \tag{C.27}$$

This implies there is a nontrivial solution to Eq. (C.24), and the eigenvectors are linearly dependent. Thus, if any two eigenvectors have the same eigenvalue $\lambda$, the functions in the eigenvectors are the same — hence, the eigenvectors only differ in the choice of $x_1$, i.e., they are linearly dependent. Thus, if there is an eigenvalue degeneracy at some point, the eigenvectors are linearly dependent, and hence, we have an exceptional point.

## C.2 Analytical expressions for $\mathcal{PT}$-symmetric spectrum

We utilize the same analytical method presented in C.1 to analyze the eigenspectrum of the $\mathcal{PT}$-symmetric Hamiltonian, Eq. (4.26). First, we consider the case with the impurities at the center of the lattice, followed by the case of the impurities at opposite ends of the lattice. In both cases, due to the tridiagonal nature of the matrices, once we have proved a degeneracy, the existence of an exceptional point follows trivially as in Section C.1.2.

### C.2.1 Impurities at center of the lattice

It was observed numerically that all of the eigenvalues coalesce in pairs at $\gamma = 1$, for even $L$, when the absorbing site $q$ is one of the central sites, i.e., when $q = L/2$, and the enhancing site is $L/2 + 1$. We can, again, express the characteristic polynomial (whose roots are the eigenvalues) in a form that allows us to predict that at least one pair of eigenvalues coalesce when $q$ is a central site.

We want to find the eigenvalues of the $L \times L$ matrix

$$[H_q]_{jk} = -\delta_{j,k+1} - \delta_{j+1,k} - i\gamma\delta_{j,k}(\delta_{j,q} - \delta_{j,q+1})\,. \tag{C.28}$$

Here, $1 \leq q \leq L$, and the matrix is only $\mathcal{PT}$-symmetric when $q = L/2$. Because of this we will restrict ourselves to the case where $L/2$. The characteristic polynomial of this matrix up to a minus sign is the determinant of the tridiagonal matrix

$$[A]_{jk} = \delta_{j,k+1} + \delta_{j+1,k} + \delta_{j,k}(\lambda + i\gamma(\delta_{j,q} - \delta_{j,q+1})) \tag{C.29}$$

Now, the determinants of tridiagonal matrices satisfy a recurrence relation. If $P_n$ is the determinant of the $n \times n$ matrix with elements

$$A_{ij} = b_i\delta_{i,j+1} + c_j\delta_{i+1,j} + a_i\delta_{ij}, \tag{C.30}$$

then

$$P_n = a_n P_{n-1} - c_{n-1} b_{n-1} P_{n-2}\,. \tag{C.31}$$

The characteristic polynomial of $H$ (C.1), i.e., the determinant of the matrix (C.29), therefore satisfies

$$\begin{aligned} P_n &= \lambda P_{n-1} - P_{n-2}, \quad \text{if } n \neq q, q+1 \\ P_q &= (\lambda + i\gamma) P_{q-1} - P_{q-2}, \\ P_{q+1} &= (\lambda - i\gamma) P_q - P_{q-1} \\ P_0 &= 1, \quad P_1 = \lambda. \end{aligned} \tag{C.32}$$

What follows is the very same as in Appendix C.1. Using the $Z$ transform, ignoring the impurities, we can get an expression for $P_n$ in terms of $P_0$, $P_1$ and $\lambda$, namely Eq. (C.14) in Appendix C.1. Again, this was derived ignoring the impurities, so it is valid for values of $n$ less than $q$. They are valid directly with $P_0 = 1$ and $P_1 = \lambda$, i.e., with $P_1 - \lambda P_0 = 0$, so that

$$P_n = K_n \quad \text{for } n < q. \tag{C.33}$$

We have expressions for $P_n$ up to $n = q - 1$, but we want $P_L$ and $L \geq q$. To go beyond $q$, we define a new sequence of functions $Q_n(\lambda)$, satisfying the same recurrence relation as $P_n$ (C.32), except with new initial conditions: $Q_0 = P_q = (\lambda + i\gamma) P_{q-1} - P_{q-2}$ and $Q_1 = P_{q+1} = (\lambda - i\gamma) P_q - P_{q-1}$. Thus we need to solve

$$\begin{aligned} Q_n &= \lambda Q_{n-1} - Q_{n-2}, \\ Q_0 &= (\lambda + i\gamma) K_{q-1} - K_{q-2}, \\ Q_1 &= (\lambda - i\gamma) P_q - K_{q-1}. \end{aligned} \tag{C.34}$$

Now we have already solved the same recurrence relation for $P_n$, using the $Z$

transform. The solution is $Q_n = Q_0 K_n + (Q_1 - \lambda Q_0) K_{n-1}$. Therefore

$$\begin{aligned} Q_n &= P_q K_n + ((\lambda - i\gamma) P_q - K_{q-1} - \lambda P_q) K_{n-1} \\ &= P_q K_n - (i\gamma P_q + K_{q-1}) K_{n-1}. \end{aligned} \tag{C.35}$$

Comparing (C.34) with (C.32), we can see that $Q_n(\lambda) = P_{n+q}(\lambda)$. Then the determinant of the full $L \times L$ matrix can be found as $P_L(\lambda) = Q_{L-q}(\lambda)$. Remembering that $q = L/2$, so $L - q = L/2 = q$, we therefore obtain

$$\begin{aligned} P_L = Q_q &= P_q K_q - (i\gamma P_q + K_{q-1}) K_{q-1} \\ &= P_q \left(K_q - i\gamma K_{q-1}\right) - K_{q-1}^2 \\ &= \left((\lambda + i\gamma) K_{q-1} - K_{q-2}\right) \left(K_q - i\gamma K_{q-1}\right) - K_{q-1}^2 . \end{aligned} \tag{C.36}$$

Then, using that $K_{q-2} = \lambda K_{q-1} - K_q$,

$$\begin{aligned} P_L &= \left((\lambda + i\gamma) K_{q-1} - \lambda K_{q-1} + K_q\right) \left(K_q - i\gamma K_{q-1}\right) - K_{q-1}^2 \\ &= \left(K_q + i\gamma K_{q-1}\right) \left(K_q - i\gamma K_{q-1}\right) - K_{q-1}^2 \\ &= K_q^2 + (\gamma^2 - 1) K_{q-1}. \end{aligned} \tag{C.37}$$

Now we can clearly see that when $\gamma = \pm 1$, $P_L = K_q^2$. So for $q = L/2$, and $\gamma = 1$, we can see that any root of the polynomial is a zero of at least order 2. Therefore we have shown the spectrum is doubly degenerate at this point. We also note that the characteristic polynomial of this system with $L$ sites is the square of the polynomial of a chain of length $L/2$.

### C.2.2 Impurities at ends of the lattice

Here, we instead consider the case with the potentials at opposite ends of the lattice. Thus, we now want to find the eigenvalues of the $L \times L$ matrix

$$[H_1]_{jk} = -\delta_{j,k+1} - \delta_{j+1,k} - i\gamma \delta_{j,k} (\delta_{j,1} - \delta_{j,L}) . \tag{C.38}$$

Here, $1 \leq q \leq L/2$. The characteristic polynomial of this matrix up to a minus sign is the determinant of the tridiagonal matrix

$$[A]_{jk} = \delta_{j,k+1} + \delta_{j+1,k} + \delta_{j,k}(\lambda + i\gamma(\delta_{j,1} - \delta_{j,L})). \tag{C.39}$$

The characteristic polynomial of $H$ (C.38), i.e., the determinant of the matrix (C.39), therefore satisfies

$$P_L = (\lambda + i\gamma)\, P_{L-1} - P_{L-2}, \tag{C.40}$$

where $P_{L-1}$ and $P_{L-2}$ satisfy the recurrence relation

$$\begin{aligned} P_n &= \lambda P_{n-1} - P_{n-2}, \\ P_0 &= 1, \quad P_1 = \lambda - i\gamma. \end{aligned} \tag{C.41}$$

We have already solved a recurrence relation of this kind; referring to the solution (C.14) and now replacing $P_0$ and $P_1$ as in (C.40), we obtain

$$P_n = K_n - i\gamma K_{n-1}. \tag{C.42}$$

Therefore,

$$P_L = (\lambda + i\gamma)\,(K_{L-1} - i\gamma K_{L-2}) - K_{L-2} + i\gamma K_{L-3}, \tag{C.43}$$

and using $K_{L-3} = \lambda K_{L-2} - K_{L-1}$, we obtain

$$\begin{aligned} P_L &= (\lambda + i\gamma)\,(K_{L-1} - i\gamma K_{L-2}) - K_{L-2} + i\gamma(\lambda K_{L-2} - K_{L-1}) \\ P_L &= \lambda K_{L-1} + (\gamma^2 - 1)K_{L-2}. \end{aligned} \tag{C.44}$$

Thus, at $\gamma = \pm 1$, we are left with

$$P_L = \lambda K_{L-1}. \tag{C.45}$$

We see that $P_L$ has a root when $\lambda = 0$ and when $K_{L-1} = 0$. $K_{L-1}$ is the characteristic polynomial of an $L-1$ site hopping model, which for open boundary conditions has a zero when $(L-1)+1 = L$ is even. Thus, when $L$ is even, $P_L$ has a degeneracy of order two.

# Appendix D

# Non-Hermitian scattering - Additional data

In this appendix we provide additional data for the purely dissipative non-Hermitian investigation in Chapter 4:

- In Appendix D.1 we illustrate the affect of the number of lattice sites on the proliferation of exceptional points.
- In Appendix D.2 we explore the effect of moving the impurity's location on the exceptional points.

## D.1 Size dependence of the spectrum

In Figure 4.5, we saw a coalescence of every pair of eigenvalues at $\gamma = 2$. This was for a system with $L = 14$ sites and the impurity at site $q = 7$. We now outline the $L$-dependence of the spectrum. The pattern is different for odd $L$. For even $L$, there is a difference between $L$ values satisfying $L = 4n + 2$ and those satisfying $L = 4n$, where $n$ is a non-negative integer.

The case of $L = 14$, presented in the main text, belongs to the $L = 4n + 2$ sequence (6, 10, 14, 18, ...). In Figure D.1, we show the case of $L = 30$, showing the same pattern: all eigenvalues pair up in multiple exceptional points exactly at $\gamma = 2$. There are an odd number of pairs, and the real components of the

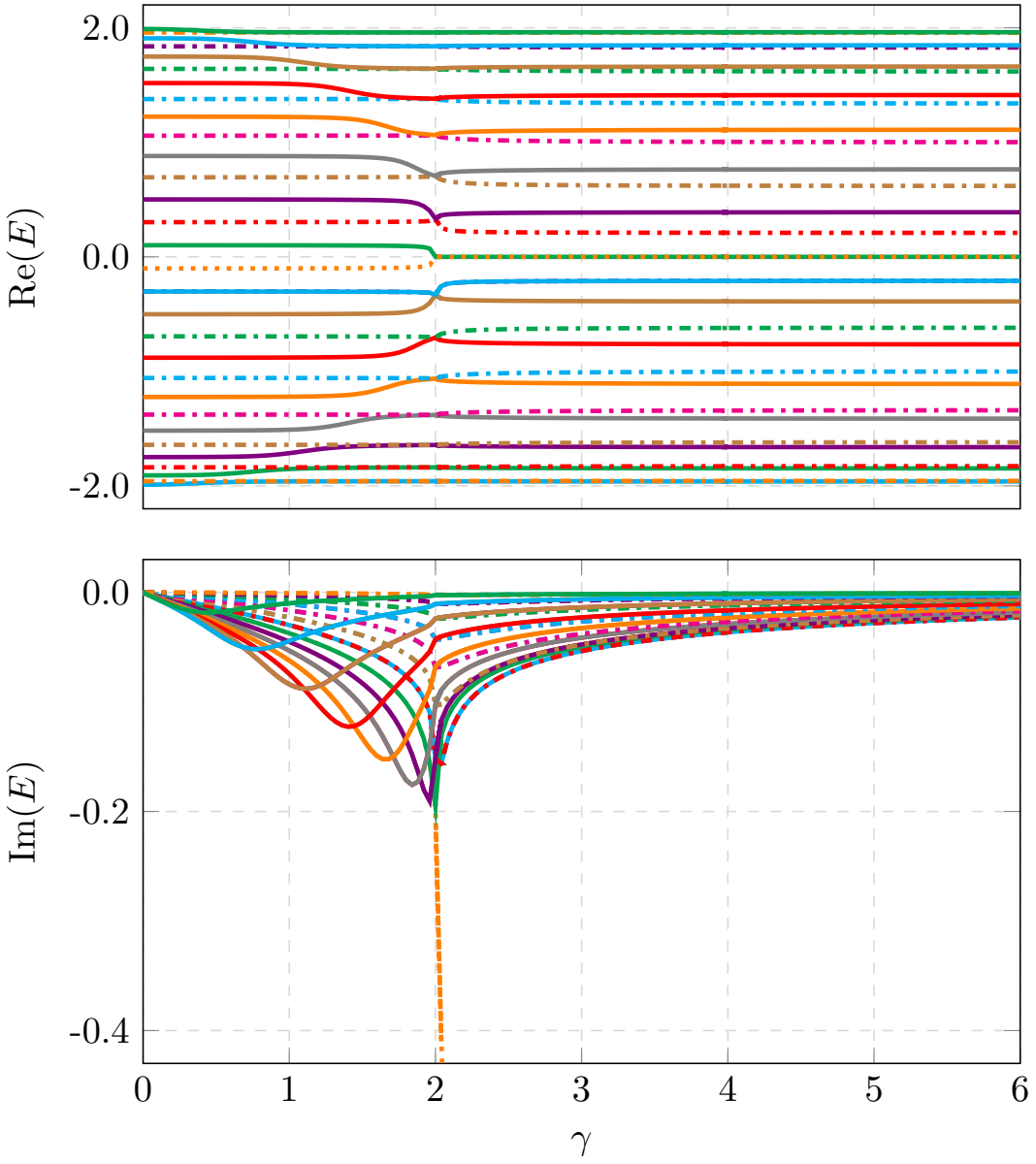


Figure D.1: Energy spectrum of a system with $L = 30$. As this value is in the $L = 4n + 2$ sequence, the features are the same as those described in the main text for $L = 14$.

eigenvalues centered around zero become zero after the coalescence, i.e., for $\gamma > 2$. One of these two eigenvalues corresponds to the localized eigenstate and has an imaginary part growing with $\gamma$.

The situation is very similar for even values of $L$ satisfying $L = 4n$, with one additional structure. As proved in Appendix C.1 for even $L$, at exactly $\gamma = 2$, all eigenvalues pair up; this is true for both $L = 4n + 2$ and $L = 4n$. In addition, for $L = 4n$, at a value slightly above $\gamma = 2$, the two eigenvalues with real values nearest to zero coalesce in an additional exceptional point, as seen in Figure D.2

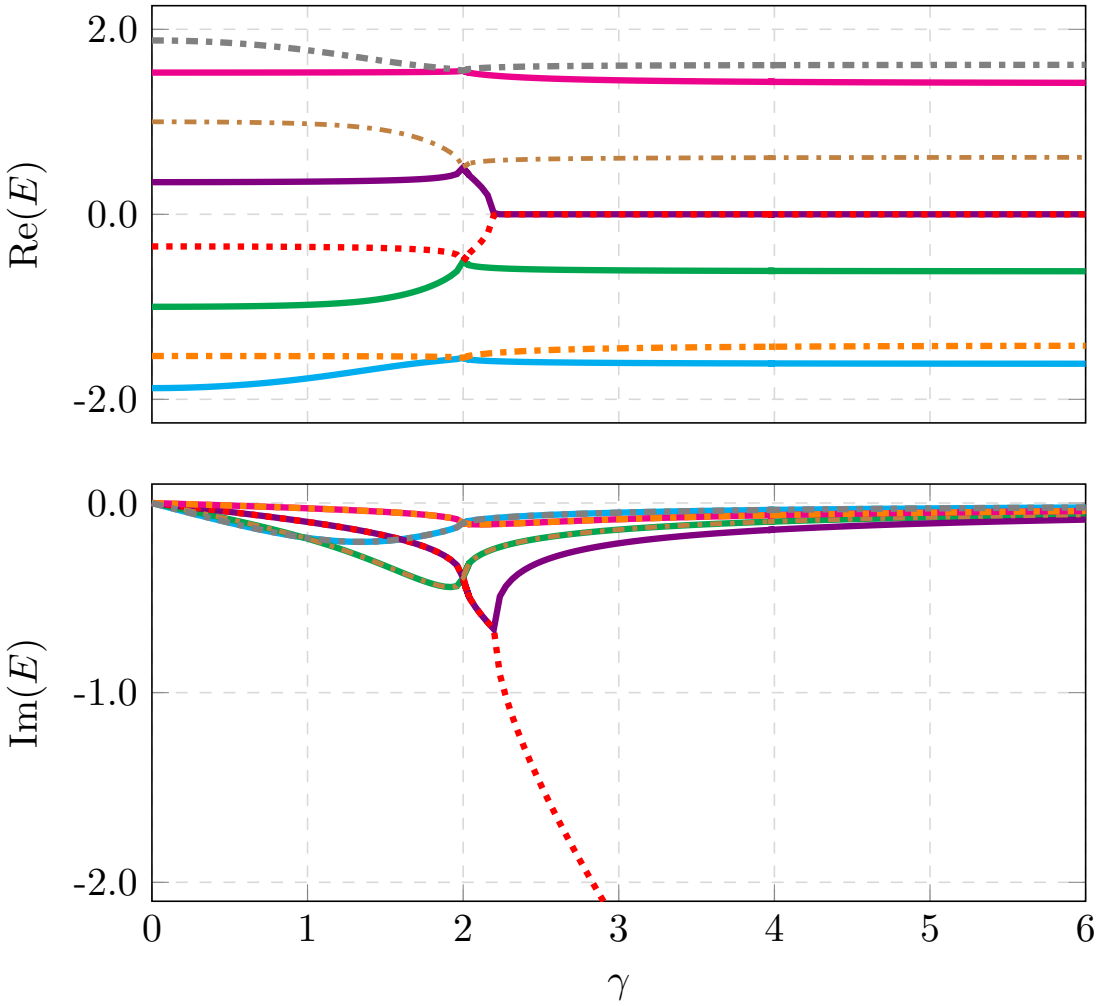


Figure D.2: Energy spectrum of a system with $L = 8$. For values of $L$ in the sequence $L = 4n$, there is an extra exceptional point slightly above $\gamma = 2$. The localized eigenstate appears beyond this new exceptional point.

for $L = 8$. It is at this point, $\gamma = \gamma_1 > 2$, that the localized state appears, and the imaginary part of the corresponding eigenvalue separates off and starts to increase unboundedly in the negative direction. With increasing $L$ in the sequence $L = 4n$, the location of the new exceptional point, $\gamma_1$, approaches 2.

We now turn to odd $L$, with the impurity placed on the central site, $q = (L + 1)/2$. For $L = 4n + 3$, there is only a single exceptional point that occurs at a value $\gamma > 2$. An example is shown in Figure D.3, for $L = 7$. As the system size tends to infinity, the location of the point tends to $\gamma \to 2$. There is always a single eigenvalue with a zero real component — the two other eigenvalues with real parts closest to zero both merge with this eigenvalue at the exceptional point.

Finally, for $L = 4n + 1$, there appear to be no exceptional points; nevertheless, at large $\gamma$, the eigenvalues pair up gradually. An example is shown in Figure

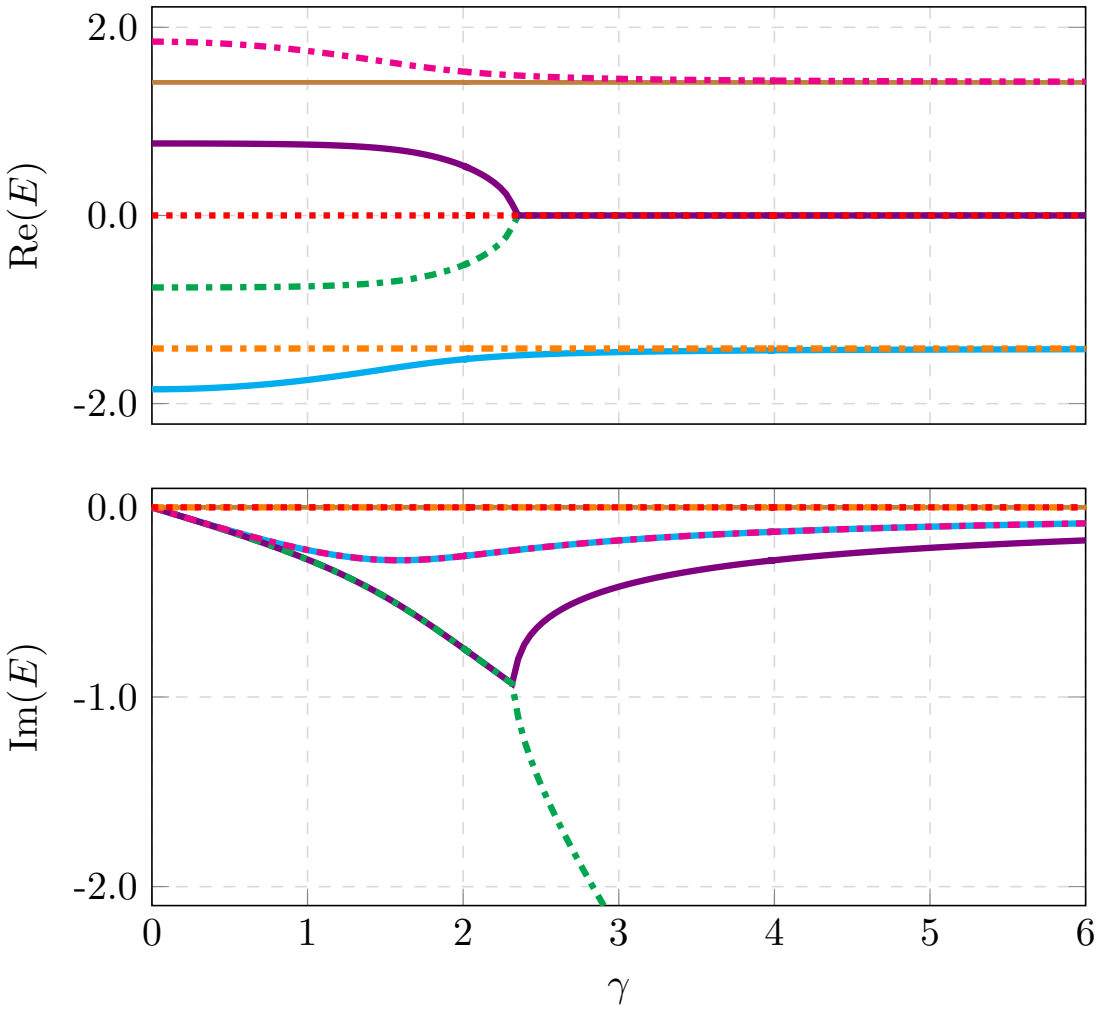


Figure D.3: Energy spectrum for $L = 7$. The impurity is on the central site, $q = 4$.

D.4 for $L = 9$. A single eigenvalue remains unpaired with zero real component. Although this does not merge with any other eigenvalue, around $\gamma \approx 2$, the imaginary component of this eigenvalue starts increasing unboundedly with $\gamma$, indicating that the corresponding eigenstate becomes localized.

In summary, although there are differences in detail between the four cases, there is always a bound state at large $\gamma$, and around $\gamma = 2$, there is always some reorganization of the spectrum. With increasing $L$, the location of these features converges toward $\gamma = 2$.

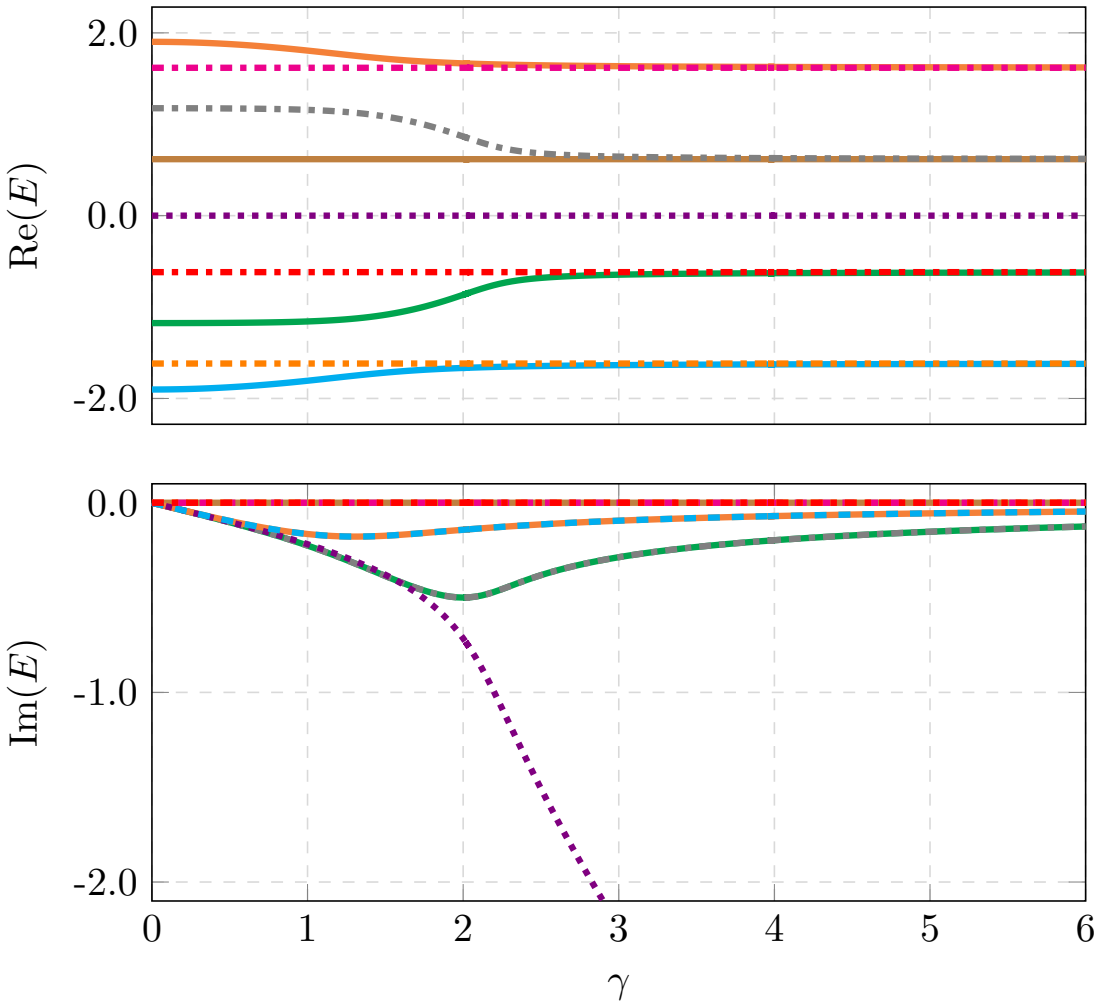


Figure D.4: Energy spectrum for $L = 9$. The impurity is on the central site, $q = 5$.

## D.2 Effect of impurity location

In Appendix D.1, we illustrated the dependence on the lattice size $L$, focusing on the case where the impurity is located at the center of the lattice, $q = L/2$ or $q = (L+1)/2$. In this Appendix, we briefly discuss the dependence of the location $q$ of the impurity, focusing on the case $L = 4n + 2$.

When the impurity is not on one of the central sites, the eigenvalues do not all coalesce as pairs at $\gamma = 2$. As the impurity is moved from the edge site towards the center ($q = 1$, $q = 2$,...), there is a single exceptional point at a value of $\gamma$ smaller than 2 for odd $q$ and greater than 2 for even $q$. This behavior is illustrated in Figure D.5. We note that the behavior of the spectrum for an impurity at $L - q + 1$ is the same as that for $q$, hence why we only present the $q \in [1, 5]$ data for the $L = 10$ system in Figure D.5. At this exceptional point, the two

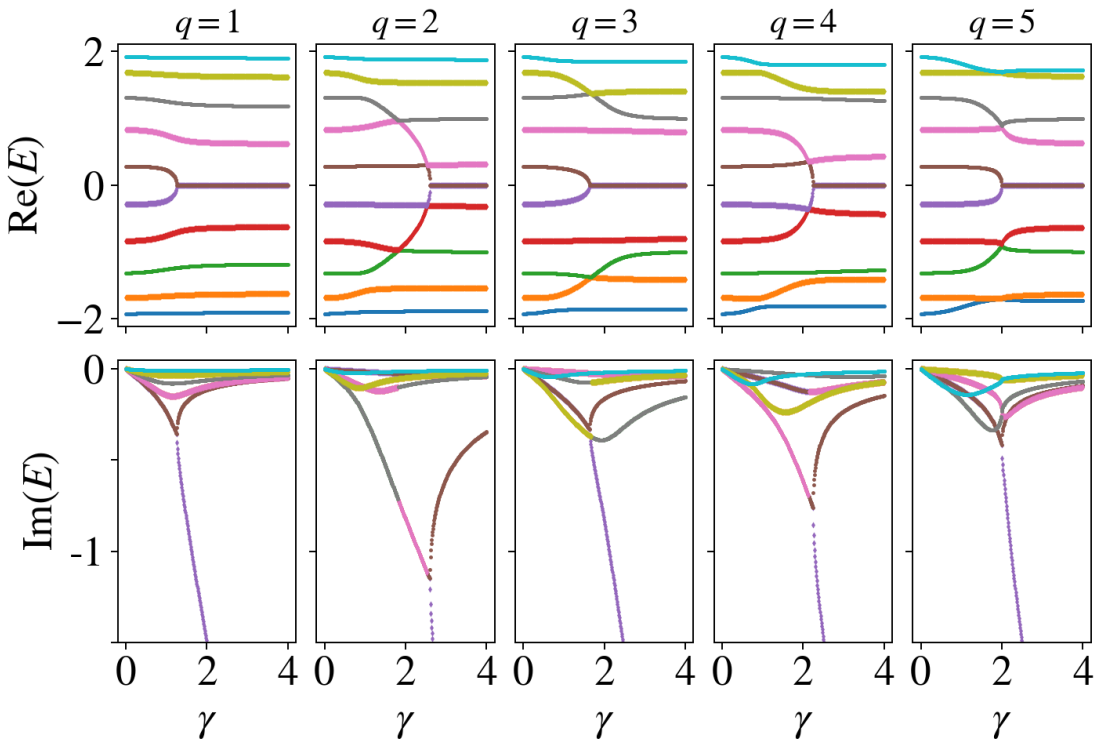


Figure D.5: Energy spectrum for $L = 10$ for various impurity locations.

eigenvalues with real parts closest to zero coalesce. As in the case of a centrally located impurity, when $\gamma$ is raised further beyond this value, the real parts of these two eigenvalues are locked at zero, and the imaginary part of one of this pair starts to increase in magnitude. This indicates an eigenstate localized at the impurity. (E.g., for $q = 1$, this state is localized at the edge of the lattice.)

# Bibliography


[1] J. M. Deutsch. Quantum statistical mechanics in a closed system. *Phys. Rev. A*, 43:2046–2049, Feb 1991.

[2] Mark Srednicki. Chaos and quantum thermalization. *Phys. Rev. E*, 50:888–901, Aug 1994.

[3] Mark Srednicki. Thermal fluctuations in quantized chaotic systems. *Journal of Physics A: Mathematical and General*, 29(4):L75–L79, feb 1996.

[4] Mark Srednicki. The approach to thermal equilibrium in quantized chaotic systems. *Journal of Physics A: Mathematical and General*, 32(7):1163–1175, Jan 1999.

[5] Peter Reimann. Eigenstate thermalization: Deutsch's approach and beyond. *New Journal of Physics*, 17(5):055025, 2015.

[6] Joshua M Deutsch. Eigenstate thermalization hypothesis. *Reports on Progress in Physics*, 81(8):082001, jul 2018.

[7] Takashi Mori, Tatsuhiko N Ikeda, Eriko Kaminishi, and Masahito Ueda. Thermalization and prethermalization in isolated quantum systems: a theoretical overview. *Journal of Physics B: Atomic, Molecular and Optical Physics*, 51(11):112001, 2018.

[8] Marcos Rigol, Vanja Dunjko, and Maxim Olshanii. Thermalization and its mechanism for generic isolated quantum systems. *Nature*, 452(7189):854–858, April 2008.

[9] Marcos Rigol and Mark Srednicki. Alternatives to eigenstate thermalization. *Phys. Rev. Lett.*, 108:110601, Mar 2012.

[10] Luca D'Alessio, Yariv Kafri, Anatoli Polkovnikov, and Marcos Rigol. From quantum chaos and eigenstate thermalization to statistical mechanics and thermodynamics. *Advances in Physics*, 65(3):239–362, 2016.

[11] James R. Garrison and Tarun Grover. Does a single eigenstate encode the full Hamiltonian? *Phys. Rev. X*, 8:021026, Apr 2018.

[12] Marcos Rigol. Quantum quenches and thermalization in one-dimensional fermionic systems. *Phys. Rev. A*, 80:053607, Nov 2009.

[13] Marcos Rigol. Breakdown of thermalization in finite one-dimensional systems. *Phys. Rev. Lett.*, 103:100403, Sep 2009.

[14] Giulio Biroli, Corinna Kollath, and Andreas M. Läuchli. Effect of rare fluctuations on the thermalization of isolated quantum systems. *Phys. Rev. Lett.*, 105:250401, Dec 2010.

[15] Lea F. Santos and Marcos Rigol. Onset of quantum chaos in one-dimensional bosonic and fermionic systems and its relation to thermalization. *Phys. Rev. E*, 81:036206, Mar 2010.

[16] Lea F. Santos and Marcos Rigol. Localization and the effects of symmetries in the thermalization properties of one-dimensional quantum systems. *Phys. Rev. E*, 82:031130, Sep 2010.

[17] Marcos Rigol and Lea F. Santos. Quantum chaos and thermalization in gapped systems. *Phys. Rev. A*, 82:011604, Jul 2010.

[18] Guillaume Roux. Finite-size effects in global quantum quenches: Examples from free bosons in an harmonic trap and the one-dimensional Bose-Hubbard model. *Phys. Rev. A*, 81:053604, May 2010.

[19] Clemens Neuenhahn and Florian Marquardt. Thermalization of interacting fermions and delocalization in Fock space. *Phys. Rev. E*, 85:060101, Jun 2012.

[20] Lea F. Santos, Anatoli Polkovnikov, and Marcos Rigol. Weak and strong typicality in quantum systems. *Phys. Rev. E*, 86:010102, Jul 2012.

[21] S. Genway, A. F. Ho, and D. K. K. Lee. Thermalization of local observables in small Hubbard lattices. *Phys. Rev. A*, 86:023609, Aug 2012.

[22] R. Steinigeweg, J. Herbrych, and P. Prelovšek. Eigenstate thermalization within isolated spin-chain systems. *Phys. Rev. E*, 87:012118, Jan 2013.

[23] Hyungwon Kim, Tatsuhiko N. Ikeda, and David A. Huse. Testing whether all eigenstates obey the eigenstate thermalization hypothesis. *Phys. Rev. E*, 90:052105, Nov 2014.

[24] W. Beugeling, R. Moessner, and Masudul Haque. Finite-size scaling of eigenstate thermalization. *Phys. Rev. E*, 89:042112, Apr 2014.

[25] S. Sorg, L. Vidmar, L. Pollet, and F. Heidrich-Meisner. Relaxation and thermalization in the one-dimensional Bose-Hubbard model: A case study for the interaction quantum quench from the atomic limit. *Phys. Rev. A*, 90:033606, Sep 2014.

[26] R. Steinigeweg, A. Khodja, H. Niemeyer, C. Gogolin, and J. Gemmer. Pushing the limits of the eigenstate thermalization hypothesis towards mesoscopic quantum systems. *Phys. Rev. Lett.*, 112:130403, Apr 2014.

[27] Keith R. Fratus and Mark Srednicki. Eigenstate thermalization in systems with spontaneously broken symmetry. *Phys. Rev. E*, 92:040103, Oct 2015.

[28] Wouter Beugeling, Roderich Moessner, and Masudul Haque. Off-diagonal matrix elements of local operators in many-body quantum systems. *Phys. Rev. E*, 91:012144, Jan 2015.

[29] Rahul Nandkishore and David A. Huse. Many-body localization and thermalization in quantum statistical mechanics. *Annual Review of Condensed Matter Physics*, 6(1):15–38, 2015.

[30] Sonika Johri, Rahul Nandkishore, and R. N. Bhatt. Many-body localization in imperfectly isolated quantum systems. *Phys. Rev. Lett.*, 114:117401, Mar 2015.

[31] Rubem Mondaini, Keith R. Fratus, Mark Srednicki, and Marcos Rigol. Eigenstate thermalization in the two-dimensional transverse field ising model. *Phys. Rev. E*, 93:032104, Mar 2016.

[32] A. Chandran, Marc D. Schulz, and F. J. Burnell. The eigenstate thermalization hypothesis in constrained hilbert spaces: A case study in non-abelian anyon chains. *Phys. Rev. B*, 94:235122, Dec 2016.

[33] David J. Luitz and Yevgeny Bar Lev. Anomalous thermalization in ergodic systems. *Phys. Rev. Lett.*, 117:170404, Oct 2016.

[34] Rubem Mondaini and Marcos Rigol. Eigenstate thermalization in the two-dimensional transverse field Ising model. II. off-diagonal matrix elements of observables. *Phys. Rev. E*, 96:012157, Jul 2017.

[35] Anatoly Dymarsky, Nima Lashkari, and Hong Liu. Subsystem eigenstate thermalization hypothesis. *Phys. Rev. E*, 97:012140, Jan 2018.

[36] Toru Yoshizawa, Eiki Iyoda, and Takahiro Sagawa. Numerical large deviation analysis of the eigenstate thermalization hypothesis. *Phys. Rev. Lett.*, 120:200604, May 2018.

[37] Ivan M. Khaymovich, Masudul Haque, and Paul A. McClarty. Eigenstate thermalization, random matrix theory, and Behemoths. *Phys. Rev. Lett.*, 122:070601, Feb 2019.

[38] David Jansen, Jan Stolpp, Lev Vidmar, and Fabian Heidrich-Meisner. Eigenstate thermalization and quantum chaos in the Holstein polaron model. *Phys. Rev. B*, 99:155130, Apr 2019.

[39] Marcin Mierzejewski and Lev Vidmar. Quantitative impact of integrals of motion on the eigenstate thermalization hypothesis. *Phys. Rev. Lett.*, 124:040603, Jan 2020.

[40] Marlon Brenes, Silvia Pappalardi, John Goold, and Alessandro Silva. Multipartite entanglement structure in the eigenstate thermalization hypothesis. *Phys. Rev. Lett.*, 124:040605, Jan 2020.

[41] Tyler LeBlond and Marcos Rigol. Eigenstate thermalization for observables that break Hamiltonian symmetries and its counterpart in interacting integrable systems. *Phys. Rev. E*, 102:062113, Dec 2020.

[42] Marlon Brenes, Tyler LeBlond, John Goold, and Marcos Rigol. Eigenstate thermalization in a locally perturbed integrable system. *Phys. Rev. Lett.*, 125:070605, Aug 2020.

[43] Jae Dong Noh. Eigenstate thermalization hypothesis and eigenstate-to-eigenstate fluctuations. *Phys. Rev. E*, 103:012129, Jan 2021.

[44] Shoki Sugimoto, Ryusuke Hamazaki, and Masahito Ueda. Test of the eigenstate thermalization hypothesis based on local random matrix theory. *Phys. Rev. Lett.*, 126:120602, Mar 2021.

[45] Christoph Schönle, David Jansen, Fabian Heidrich-Meisner, and Lev Vidmar. Eigenstate thermalization hypothesis through the lens of autocorrelation functions. *Phys. Rev. B*, 103:235137, Jun 2021.

[46] Goran Nakerst and Masudul Haque. Eigenstate thermalization scaling in approaching the classical limit. *Phys. Rev. E*, 103:042109, Apr 2021.

[47] Jiaozi Wang, Mats H. Lamann, Jonas Richter, Robin Steinigeweg, Anatoly Dymarsky, and Jochen Gemmer. Eigenstate thermalization hypothesis and

its deviations from random-matrix theory beyond the thermalization time. *Phys. Rev. Lett.*, 128:180601, May 2022.

[48] Shoki Sugimoto, Ryusuke Hamazaki, and Masahito Ueda. Eigenstate thermalization in long-range interacting systems. *Phys. Rev. Lett.*, 129:030602, Jul 2022.

[49] Ehsan Khatami, Guido Pupillo, Mark Srednicki, and Marcos Rigol. Fluctuation-dissipation theorem in an isolated system of quantum dipolar bosons after a quench. *Phys. Rev. Lett.*, 111:050403, Jul 2013.

[50] Fabian H L Essler and Maurizio Fagotti. Quench dynamics and relaxation in isolated integrable quantum spin chains. *Journal of Statistical Mechanics: Theory and Experiment*, 2016(6):064002, jun 2016.

[51] Adam M. Kaufman, M. Eric Tai, Alexander Lukin, Matthew Rispoli, Robert Schittko, Philipp M. Preiss, and Markus Greiner. Quantum thermalization through entanglement in an isolated many-body system. *Science*, 353(6301):794–800, 2016.

[52] Tsung-Cheng Lu and Tarun Grover. Renyi entropy of chaotic eigenstates. *Phys. Rev. E*, 99:032111, Mar 2019.

[53] Kazuhiro Seki and Seiji Yunoki. Emergence of a thermal equilibrium in a subsystem of a pure ground state by quantum entanglement. *Phys. Rev. Research*, 2:043087, Oct 2020.

[54] V. Gurarie. The equivalence between the canonical and microcanonical ensembles when applied to large systems. *American Journal of Physics*, 75(8):747–751, 2007.

[55] Hal Tasaki. On the local equivalence between the Canonical and the Microcanonical ensembles for quantum spin systems. *Journal of Statistical Physics*, 172(4):905–926, Aug 2018.

[56] M. Cramer, C. M. Dawson, J. Eisert, and T. J. Osborne. Exact relaxation in a class of nonequilibrium quantum lattice systems. *Phys. Rev. Lett.*, 100:030602, Jan 2008.

[57] Noah Linden, Sandu Popescu, Anthony J. Short, and Andreas Winter. Quantum mechanical evolution towards thermal equilibrium. *Phys. Rev. E*, 79:061103, Jun 2009.

[58] A. R. Usha Devi and A. K. Rajagopal. Dynamical evolution of quantum oscillators toward equilibrium. *Phys. Rev. E*, 80:011136, Jul 2009.

[59] Anthony J Short. Equilibration of quantum systems and subsystems. *New Journal of Physics*, 13(5):053009, may 2011.

[60] Christian Gogolin, Markus P. Müller, and Jens Eisert. Absence of thermalization in nonintegrable systems. *Phys. Rev. Lett.*, 106:040401, Jan 2011.

[61] Arnau Riera, Christian Gogolin, and Jens Eisert. Thermalization in nature and on a quantum computer. *Phys. Rev. Lett.*, 108:080402, Feb 2012.

[62] Fernando G. S. L. Brandão, Piotr Ćwikliński, Michał Horodecki, Paweł Horodecki, Jarosław K. Korbicz, and Marek Mozrzymas. Convergence to equilibrium under a random Hamiltonian. *Phys. Rev. E*, 86:031101, Sep 2012.

[63] Giacomo De Palma, Alessio Serafini, Vittorio Giovannetti, and Marcus Cramer. Necessity of eigenstate thermalization. *Phys. Rev. Lett.*, 115:220401, Nov 2015.

[64] J. Eisert, M. Friesdorf, and C. Gogolin. Quantum many-body systems out of equilibrium. *Nature Physics*, 11(2):124–130, Feb 2015.

[65] Terry Farrelly, Fernando G. S. L. Brandão, and Marcus Cramer. Thermalization and return to equilibrium on finite quantum lattice systems. *Phys. Rev. Lett.*, 118:140601, Apr 2017.

[66] Markus P. Müller, Emily Adlam, Lluís Masanes, and Nathan Wiebe. Thermalization and canonical typicality in translation-invariant quantum lattice systems. *Communications in Mathematical Physics*, 340(2):499–561, Dec 2015.

[67] Anatoly Dymarsky. Mechanism of macroscopic equilibration of isolated quantum systems. *Phys. Rev. B*, 99:224302, Jun 2019.

[68] Hal Tasaki. From quantum dynamics to the Canonical distribution: General picture and a rigorous example. *Phys. Rev. Lett.*, 80:1373–1376, Feb 1998.

[69] Sheldon Goldstein, Joel L. Lebowitz, Roderich Tumulka, and Nino Zanghì. Canonical typicality. *Phys. Rev. Lett.*, 96:050403, Feb 2006.

[70] Sandu Popescu, Anthony J. Short, and Andreas Winter. Entanglement and the foundations of statistical mechanics. *Nature Physics*, 2(11):754–758, Nov 2006.

[71] Peter Reimann. Typicality for generalized microcanonical ensembles. *Phys. Rev. Lett.*, 99:160404, Oct 2007.

[72] F. Reif. *Fundamentals of statistical and thermal physics*. New York, McGraw-Hill, 1965.

[73] L. E. Reichl. *A Modern Course in Statistical Physics*. John Wiley & Sons, 1998.

[74] Kerson Huang. *Statistical Mechanics*. John Wiley & Sons, 1987.

[75] R. K. Pathria. *Statistical Mechanics*. Butterworth-Heinemann, Oxford, 1996.

[76] L. D. Landau and E. M. Lifshitz. *Statistical Physics*. Pergamon, Oxford, 1969.

[77] Mehran Kardar. *Statistical Physics of Particles*. Cambridge University Press, 2007.

[78] S. Trotzky, Y.-A. Chen, A. Flesch, I. P. McCulloch, U. Schollwöck, J. Eisert, and I. Bloch. Probing the relaxation towards equilibrium in an isolated strongly correlated one-dimensional Bose gas. *Nature Physics*, 8(4):325–330, Apr 2012.

[79] Govinda Clos, Diego Porras, Ulrich Warring, and Tobias Schaetz. Time-resolved observation of thermalization in an isolated quantum system. *Phys. Rev. Lett.*, 117:170401, Oct 2016.

[80] J. Smith, A. Lee, P. Richerme, B. Neyenhuis, P. W. Hess, P. Hauke, M. Heyl, D. A. Huse, and C. Monroe. Many-body localization in a quantum simulator with programmable random disorder. *Nature Physics*, 12(10):907–911, Oct 2016.

[81] C. Neill, P. Roushan, M. Fang, Y. Chen, M. Kolodrubetz, Z. Chen, A. Megrant, R. Barends, B. Campbell, B. Chiaro, A. Dunsworth, E. Jeffrey, J. Kelly, J. Mutus, P. J. J. O'Malley, C. Quintana, D. Sank, A. Vainsencher, J. Wenner, T. C. White, A. Polkovnikov, and J. M. Martinis. Ergodic dynamics and thermalization in an isolated quantum system. *Nature Physics*, 12(11):1037–1041, Nov 2016.

[82] Marcos Rigol, Vanja Dunjko, Vladimir Yurovsky, and Maxim Olshanii. Relaxation in a completely integrable many-body quantum system: An ab initio study of the dynamics of the highly excited states of 1d lattice hard-core bosons. *Phys. Rev. Lett.*, 98:050405, Feb 2007.

[83] Lev Vidmar and Marcos Rigol. Generalized gibbs ensemble in integrable lattice models. *Journal of Statistical Mechanics: Theory and Experiment*, 2016(6):064007, jun 2016.

[84] Amy C. Cassidy, Charles W. Clark, and Marcos Rigol. Generalized thermalization in an integrable lattice system. *Phys. Rev. Lett.*, 106:140405, Apr 2011.

[85] Patrycja Łydżba, Marcin Mierzejewski, Marcos Rigol, and Lev Vidmar. Generalized thermalization in quantum-chaotic quadratic Hamiltonians, 2022.

[86] Simone Ziraldo, Alessandro Silva, and Giuseppe E. Santoro. Relaxation dynamics of disordered spin chains: Localization and the existence of a stationary state. *Phys. Rev. Lett.*, 109:247205, Dec 2012.

[87] Arijeet Pal and David A. Huse. Many-body localization phase transition. *Phys. Rev. B*, 82:174411, Nov 2010.

[88] P. W. Anderson. Absence of diffusion in certain random lattices. *Phys. Rev.*, 109:1492–1505, Mar 1958.

[89] Jan Šuntajs, Janez Bonča, Toma ž Prosen, and Lev Vidmar. Quantum chaos challenges many-body localization. *Phys. Rev. E*, 102:062144, Dec 2020.

[90] D.A. Abanin, J.H. Bardarson, G. De Tomasi, S. Gopalakrishnan, V. Khemani, S.A. Parameswaran, F. Pollmann, A.C. Potter, M. Serbyn, and R. Vasseur. Distinguishing localization from chaos: Challenges in finite-size systems. *Annals of Physics*, 427:168415, 2021.

[91] J. Berges, Sz. Borsányi, and C. Wetterich. Prethermalization. *Phys. Rev. Lett.*, 93:142002, Sep 2004.

[92] Krishnanand Mallayya, Marcos Rigol, and Wojciech De Roeck. Prethermalization and thermalization in isolated quantum systems. *Phys. Rev. X*, 9:021027, May 2019.

[93] Tyler LeBlond, Dries Sels, Anatoli Polkovnikov, and Marcos Rigol. Universality in the onset of quantum chaos in many-body systems. *Phys. Rev. B*, 104:L201117, Nov 2021.

[94] Angelo Russomanno, Michele Fava, and Markus Heyl. Quantum chaos and ensemble inequivalence of quantum long-range Ising chains. *Phys. Rev. B*, 104:094309, Sep 2021.

[95] Joe Dunlop, Oliver Cohen, and Anthony J. Short. Eigenstate thermalization on average. *Phys. Rev. E*, 104:024135, Aug 2021.

[96] C. J. Turner, A. A. Michailidis, D. A. Abanin, M. Serbyn, and Z. Papić. Weak ergodicity breaking from quantum many-body scars. *Nature Physics*, 14(7):745–749, Jul 2018.

[97] Maksym Serbyn, Dmitry A. Abanin, and Zlatko Papić. Quantum many-body scars and weak breaking of ergodicity. *Nature Physics*, 17(6):675–685, Jun 2021.

[98] I. Rotter. A non-Hermitian Hamilton operator and the physics of open quantum systems. *Journal of Physics A: Mathematical and Theoretical*, 42(15):153001, mar 2009.

[99] H. Cao and J. Wiersig. Dielectric microcavities: Model systems for wave chaos and non-Hermitian physics. *Rev. Mod. Phys.*, 87:61–111, Jan 2015.

[100] S.K. Özdemir, S. Rotter, F. Nori, and L. Yang. Parity-time symmetry and exceptional points in photonics. *Nature Materials*, 18(8):783–798, 2019.

[101] R. El-Ganainy, M. Khajavikhan, D.N. Christodoulides, and S.K. Özdemir. The dawn of non-Hermitian optics. *Communications Physics*, 2(1):37, 2019.

[102] M. Liertzer, Li Ge, A. Cerjan, A. D. Stone, H. E. Türeci, and S. Rotter. Pump-induced exceptional points in lasers. *Phys. Rev. Lett.*, 108:173901, Apr 2012.

[103] M. Brandstetter, M. Liertzer, C. Deutsch, P. Klang, J. Schöberl, H.E. Türeci, G. Strasser, K. Unterrainer, and S. Rotter. Reversing the pump dependence of a laser at an exceptional point. *Nature Comm.*, 5:4034, 2014.

[104] B. Peng, Ş.K. Özdemir, M. Liertzer, W. Chen, J. Kramer, H. Yılmaz, J. Wiersig, S. Rotter, and L. Yang. Chiral modes and directional lasing at exceptional points. *Proceedings of the National Academy of Sciences*, 113(25):6845–6850, 2016.

[105] P. Miao, Z. Zhang, J. Sun, W. Walasik, S. Longhi, N.M. Litchinitser, and L. Feng. Orbital angular momentum microlaser. *Science*, 353(6298):464–467, 2016.

[106] A. Guo, G. J. Salamo, D. Duchesne, R. Morandotti, M. Volatier-Ravat, V. Aimez, G. A. Siviloglou, and D. N. Christodoulides. Observation of $\mathcal{PT}$-symmetry breaking in complex optical potentials. *Phys. Rev. Lett.*, 103:093902, Aug 2009.

[107] C. E. Rüter, K. G. Makris, R. El-Ganainy, D. N. Christodoulides, M. Segev, and D. Kip. Observation of parity–time symmetry in optics. *Nature Physics*, 6, Nov 2010.

[108] B. Alfassi, O. Peleg, N. Moiseyev, and M. Segev. Diverging rabi oscillations in subwavelength photonic lattices. *Phys. Rev. Lett.*, 106:073901, Feb 2011.

[109] J.M. Zeuner, M.C. Rechtsman, Y. Plotnik, Y. Lumer, S. Nolte, M.S. Rudner, M. Segev, and A. Szameit. Observation of a topological transition in the bulk of a non-Hermitian system. *Phys. Rev. Lett.*, 115:040402, Jul 2015.

[110] A. Cerjan, S. Huang, M. Wang, Kevin P. Chen, Y. Chong, and M.C. Rechtsman. Experimental realization of a weyl exceptional ring. *Nature Photonics*, 13(9):623–628, Jun 2019.

[111] E. Persson, I. Rotter, H.-J. Stöckmann, and M. Barth. Observation of resonance trapping in an open microwave cavity. *Phys. Rev. Lett.*, 85:2478–2481, Sep 2000.

[112] C. Dembowski, H.-D. Gräf, H. L. Harney, A. Heine, W. D. Heiss, H. Rehfeld, and A. Richter. Experimental observation of the topological structure of exceptional points. *Phys. Rev. Lett.*, 86:787–790, Jan 2001.

[113] C. Dembowski, B. Dietz, H.-D. Gräf, H. L. Harney, A. Heine, W. D. Heiss, and A. Richter. Observation of a chiral state in a microwave cavity. *Phys. Rev. Lett.*, 90:034101, Jan 2003.

[114] J. Doppler, A.A. Mailybaev, J. Böhm, U. Kuhl, A. Girschik, F. Libisch, T.J. Milburn, P. Rabl, N. Moiseyev, and S. Rotter. Dynamically encircling an exceptional point for asymmetric mode switching. *Nature*, 537(7618):76, 2016.

[115] C. Poli, M. Bellec, U. Kuhl, F. Mortessagne, and H. Schomerus. Selective enhancement of topologically induced interface states in a dielectric resonator chain. *Nature Comm.*, 6:6710, 2015.

[116] W. Chen, S.K. Özdemir, G. Zhao, J. Wiersig, and L. Yang. Exceptional points enhance sensing in an optical microcavity. *Nature*, 548:192, Aug 2017.

[117] Chang-Hwan Yi, Julius Kullig, and Jan Wiersig. Pair of exceptional points in a microdisk cavity under an extremely weak deformation. *Phys. Rev. Lett.*, 120:093902, Feb 2018.

[118] H. Xu, D. Mason, L. Jiang, and J.G.E. Harris. Topological energy transfer in an optomechanical system with exceptional points. *Nature*, 537:80, Jul 2016.

[119] B. Zhen, C. W. Hsu, Y. Igarashi, L. Lu, I. Kaminer, A. Pick, S.-L. Chua, J.D. Joannopoulos, and M. Soljacic. Spawning rings of exceptional points out of dirac cones. *Nature*, 525:354–358, Sep 2015.

[120] H. Zhou, C. Peng, Y. Yoon, C.W. Hsu, K.A. Nelson, L. Fu, J.D. Joannopoulos, M. Soljačić, and B. Zhen. Observation of bulk fermi arc and polarization half charge from paired exceptional points. *Science*, 359(6379):1009–1012, 2018.

[121] X. Zhu, H. Ramezani, C. Shi, J. Zhu, and X. Zhang. $\mathcal{PT}$-symmetric acoustics. *The Journal of the Acoustical Society of America*, 137(4):2403–2403, 2015.

[122] R. Fleury, D. Sounas, and A. Alu. An invisible acoustic sensor based on parity-time symmetry. *Nature communications*, 6:5905, 2015.

[123] C. Shi, M. Dubois, Y. Chen, L. Cheng, H. Ramezani, Y. Wang, and X. Zhang. Accessing the exceptional points of parity-time symmetric acoustics. *Nature communications*, 7:11110, 2016.

[124] K. Ding, G. Ma, M. Xiao, Z.Q. Zhang, and C.T. Chan. Emergence, coalescence, and topological properties of multiple exceptional points and their experimental realization. *Phys. Rev. X*, 6(2):021007, 2016.

[125] Y. Choi, S. Kang, S. Lim, W. Kim, J.-R. Kim, J.-H. Lee, and K. An. Quasieigenstate coalescence in an atom-cavity quantum composite. *Phys. Rev. Lett.*, 104:153601, Apr 2010.

[126] T. Gao, E. Estrecho, K.Y. Bliokh, T.C.H. Liew, M.D. Fraser, S. Brodbeck, M. Kamp, C. Schneider, S. Höfling, Y. Yamamoto, Y.S. Nori, F. Kivshar, A. Truscott, R. Dall, and E.A. Ostrovskaya. Observation of non-Hermitian degeneracies in a chaotic exciton-polariton billiard. *Nature*, 526(7574):554, 2015.

[127] T. Gao, G. Li, E. Estrecho, T. C. H. Liew, D. Comber-Todd, A. Nalitov, M. Steger, K. West, L. Pfeiffer, D. W. Snoke, A. V. Kavokin, A. G. Truscott, and E. A. Ostrovskaya. Chiral modes at exceptional points in exciton-polariton quantum fluids. *Phys. Rev. Lett.*, 120:065301, Feb 2018.

[128] H. Cartarius, J. Main, and G. Wunner. Exceptional points in atomic spectra. *Phys. Rev. Lett.*, 99:173003, Oct 2007.

[129] Z. Lin, H. Ramezani, T. Eichelkraut, T. Kottos, H. Cao, and D.N. Christodoulides. Unidirectional invisibility induced by $\mathcal{PT}$-symmetric periodic structures. *Phys. Rev. Lett.*, 106:213901, May 2011.

[130] A. Regensburger, C. Bersch, M.-A. Miri, G. Onishchukov, D. N. Christodoulides, and U. Peschel. Parity-time synthetic photonic lattices. *Nature*, 488(7410):167–171, Aug 2012.

[131] G. Barontini, R. Labouvie, F. Stubenrauch, A. Vogler, V. Guarrera, and H. Ott. Controlling the dynamics of an open many-body quantum system with localized dissipation. *Phys. Rev. Lett.*, 110:035302, Jan 2013.

[132] Y.-K. Lu, P. Peng, Q.-T. Cao, D. Xu, J. Wiersig, Q. Gong, and Y.-F. Xiao. Spontaneous t-symmetry breaking and exceptional points in cavity quantum electrodynamics systems. *Science Bulletin*, 63(17):1096–1100, 2018.

[133] J. Li, A.K. Harter, J. Liu, L. de Melo, Y.N. Joglekar, and L. Luo. Observation of parity-time symmetry breaking transitions in a dissipative floquet system of ultracold atoms. *Nature communications*, 10(1):855, 2019.

[134] Ryusuke Hamazaki, Kohei Kawabata, and Masahito Ueda. Non-Hermitian many-body localization. *Phys. Rev. Lett.*, 123:090603, Aug 2019.

[135] Kohei Kawabata and Shinsei Ryu. Nonunitary scaling theory of non-Hermitian localization. *Phys. Rev. Lett.*, 126:166801, Apr 2021.

[136] Flore K. Kunst, Elisabet Edvardsson, Jan Carl Budich, and Emil J. Bergholtz. Biorthogonal bulk-boundary correspondence in non-Hermitian systems. *Phys. Rev. Lett.*, 121:026808, Jul 2018.

[137] N. Hatano and D.R. Nelson. Localization transitions in non-Hermitian quantum mechanics. *Phys. Rev. Lett.*, 77:570–573, Jul 1996.

[138] Emil J. Bergholtz, Jan Carl Budich, and Flore K. Kunst. Exceptional topology of non-Hermitian systems. *Rev. Mod. Phys.*, 93:015005, Feb 2021.

[139] Lucas Sá, Pedro Ribeiro, and Toma ž Prosen. Complex spacing ratios: A signature of dissipative quantum chaos. *Phys. Rev. X*, 10:021019, Apr 2020.

[140] T. Kato. *Perturbation Theory for Linear Operators*. Springer-Verlag Berlin Heidelberg, 1995.

[141] W.D. Heiss. Exceptional points of non-Hermitian operators. *Journal of Physics A: Mathematical and General*, 37(6):2455–2464, Jan 2004.

[142] M.V. Berry. Physics of non-Hermitian degeneracies. *Czechoslovak Journal of Physics*, 54(10):1039–1047, Oct 2004.

[143] M. Müller and I. Rotter. Exceptional points in open quantum systems. *Journal of Physics A: Mathematical and Theoretical*, 41(24):244018, 2008.

[144] W.D. Heiss. The physics of exceptional points. *Journal of Physics A: Mathematical and Theoretical*, 45(44):444016, Oct 2012.

[145] G.H. Golub and C.F. Van Loan. *Matrix Computations*. Johns Hopkins Studies in the Mathematical Sciences. Johns Hopkins University Press, 1996.

[146] D.S. Watkins. *Fundamentals of Matrix Computations*. Pure and Applied Mathematics: A Wiley Series of Texts, Monographs and Tracts. Wiley, 2004.

[147] W.D. Heiss and H.L. Harney. The chirality of exceptional points. *The European Physical Journal D - Atomic, Molecular, Optical and Plasma Physics*, 17(2):149–151, Nov 2001.

[148] S. Liu, J. Wiersig, W. Sun, Y. Fan, L. Ge, J. Yang, S. Xiao, Q. Song, and H. Cao. Transporting the optical chirality through the dynamical barriers in optical microcavities. *Laser & Photonics Reviews*, 12(10):1800027, 2018.

[149] J. Wiersig. Enhancing the sensitivity of frequency and energy splitting detection by using exceptional points: Application to microcavity sensors for single-particle detection. *Phys. Rev. Lett.*, 112:203901, May 2014.

[150] J. Wiersig. Sensors operating at exceptional points: General theory. *Phys. Rev. A*, 93:033809, Mar 2016.

[151] H. Hodaei, A.U. Hassan, S. Wittek, H. Garcia-Gracia, R. El-Ganainy, D.N. Christodoulides, and M. Khajavikhan. Enhanced sensitivity at higher-order exceptional points. *Nature*, 548(7666):187, 2017.

[152] I.Ya. Goldsheid and B.A. Khoruzhenko. Distribution of eigenvalues in non-Hermitian anderson models. *Phys. Rev. Lett.*, 80:2897–2900, Mar 1998.

[153] J. Heinrichs. Eigenvalues in the non-Hermitian anderson model. *Phys. Rev. B*, 63:165108, Apr 2001.

[154] Giovanni Barontini and Vera Guarrera. Localization by dissipative disorder: Deterministic approach to position measurements. *Phys. Rev. A*, 91:032114, Mar 2015.

[155] S. Longhi. Topological phase transition in non-Hermitian quasicrystals. *Phys. Rev. Lett.*, 122:237601, Jun 2019.

[156] S. Longhi. Metal-insulator phase transition in a non-Hermitian aubry-andré-harper model. *Phys. Rev. B*, 100:125157, Sep 2019.

[157] S. Longhi. Invisibility in non-Hermitian tight-binding lattices. *Phys. Rev. A*, 82:032111, Sep 2010.

[158] S. Longhi. Non-Hermitian Floquet invisibility. *EPL (Europhysics Letters)*, 117(1):10005, Jan 2017.

[159] D. Leykam, S. Flach, and Y.D. Chong. Flat bands in lattices with non-Hermitian coupling. *Phys. Rev. B*, 96:064305, Aug 2017.

[160] S. Longhi. Bloch oscillations in complex crystals with $\mathcal{PT}$ symmetry. *Phys. Rev. Lett.*, 103:123601, Sep 2009.

[161] O. Bendix, R. Fleischmann, T. Kottos, and B. Shapiro. Exponentially fragile $\mathcal{PT}$ symmetry in lattices with localized eigenmodes. *Phys. Rev. Lett.*, 103:030402, Jul 2009.

[162] L. Jin and Z. Song. Solutions of $\mathcal{PT}$-symmetric tight-binding chain and its equivalent Hermitian counterpart. *Phys. Rev. A*, 80:052107, Nov 2009.

[163] L. Jin and Z. Song. Physics counterpart of the $\mathcal{PT}$ non-Hermitian tight-binding chain. *Phys. Rev. A*, 81:032109, Mar 2010.

[164] Y. N. Joglekar, D. Scott, M. Babbey, and A. Saxena. Robust and fragile $\mathcal{PT}$-symmetric phases in a tight-binding chain. *Phys. Rev. A*, 82:030103, Sep 2010.

[165] L. Jin and Z. Song. Parity-time symmetry under magnetic flux. *Phys. Rev. A*, 93:062110, Jun 2016.

[166] B. Zhu, R. Lü, and S. Chen. $\mathcal{PT}$-symmetry breaking for the scattering problem in a one-dimensional non-Hermitian lattice model. *Phys. Rev. A*, 93:032129, Mar 2016.

[167] Adrian Ortega, Thomas Stegmann, Luis Benet, and Hernán Larralde. Spectral and transport properties of a -symmetric tight-binding chain with gain and loss. *Journal of Physics A: Mathematical and Theoretical*, 53(44):445308, oct 2020.

[168] T. Ozawa, H. M. Price, A. Amo, N. Goldman, M. Hafezi, L. Lu, M.C. Rechtsman, D. Schuster, J. Simon, O. Zilberberg, and I. Carusotto. Topological photonics. *Rev. Mod. Phys.*, 91:015006, Mar 2019.

[169] V. M. Martinez Alvarez, J. E. Barrios Vargas, M. Berdakin, and L. E. F. Foa Torres. Topological states of non-Hermitian systems. *The European Physical Journal Special Topics*, 227(12):1295–1308, Dec 2018.

[170] Luis E F Foa Torres. Perspective on topological states of non-Hermitian lattices. *Journal of Physics: Materials*, 3(1):014002, nov 2019.

[171] P. A. McClarty and J. G. Rau. Non-Hermitian topology of spontaneous magnon decay. *Phys. Rev. B*, 100:100405, Sep 2019.

[172] David J. Luitz and Francesco Piazza. Exceptional points and the topology of quantum many-body spectra. *Phys. Rev. Research*, 1:033051, Oct 2019.

[173] G.R. Allcock. The time of arrival in quantum mechanics I. formal considerations. *Annals of Physics*, 53(2):253 – 285, 1969.

[174] G.R. Allcock. The time of arrival in quantum mechanics II. the individual measurement. *Annals of Physics*, 53(2):286 – 310, 1969.

[175] G.R. Allcock. The time of arrival in quantum mechanics III: The measurement ensemble. *Annals of Physics*, 53(2):311 – 348, 1969.

[176] B. Misra and E.C.G. Sudarshan. The zeno's paradox in quantum theory. *Journal of Mathematical Physics*, 18(4):756–763, 1977.

[177] P. Facchi and S. Pascazio. Quantum zeno dynamics: mathematical and physical aspects. *Journal of Physics A: Mathematical and Theoretical*, 41(49):493001, oct 2008.

[178] D. A. Zezyulin, V. V. Konotop, G. Barontini, and H. Ott. Macroscopic zeno effect and stationary flows in nonlinear waveguides with localized dissipation. *Phys. Rev. Lett.*, 109:020405, Jul 2012.

[179] P. L. Krapivsky, J. M. Luck, and K. Mallick. Survival of classical and quantum particles in the presence of traps. *Journal of Statistical Physics*, 154(6):1430–1460, Mar 2014.

[180] S. Dhar, S. Dasgupta, A. Dhar, and D. Sen. Detection of a quantum particle on a lattice under repeated projective measurements. *Phys. Rev. A*, 91:062115, Jun 2015.

[181] S. Dhar, S. Dasgupta, and A. Dhar. Quantum time of arrival distribution in a simple lattice model. *Journal of Physics A: Mathematical and Theoretical*, 48(11):115304, feb 2015.

[182] W. Kozlowski, S. F. Caballero-Benitez, and I. B. Mekhov. Non-Hermitian dynamics in the quantum zeno limit. *Phys. Rev. A*, 94:012123, Jul 2016.

[183] H. Fröml, A. Chiocchetta, C. Kollath, and S. Diehl. Fluctuation-induced quantum zeno effect. *Phys. Rev. Lett.*, 122:040402, Feb 2019.

[184] H. Bethe. Zur theorie der metalle. *Zeitschrift für Physik*, 71(3):205–226, Mar 1931.

[185] J. Hubbard. Electron correlations in narrow energy bands. *Proceedings of the Royal Society of London. Series A. Mathematical and Physical Sciences*, 276:238 – 257, 1963.

[186] Paolo P Mazza, Jean-Marie Stéphan, Elena Canovi, Vincenzo Alba, Michael Brockmann, and Masudul Haque. Overlap distributions for quantum quenches in the anisotropic heisenberg chain. *Journal of Statistical Mechanics: Theory and Experiment*, 2016(1):013104, jan 2016.

[187] Fritz Haake. *Quantum signatures of chaos*. Springer Berlin, 1991.

[188] M. V. Berry and M. Tabor. Level clustering in the regular spectrum. *Proceedings of the Royal Society of London. Series A, Mathematical and Physical Sciences*, 356(1686):375–394, 1977.

[189] Madan Lal Mehta. *Random Matrices*, volume 142 of *Pure and Applied Mathematics*. Elsevier, 2004.

[190] Giacomo Livan, Marcel Novaes, and Pierpaolo Vivo. *Introduction to Random Matrices*, volume 26 of *SpringerBriefs in Mathematical Physics*. Springer, 2018.

[191] Thomas Guhr, Axel Müller–Groeling, and Hans A. Weidenmüller. Random-matrix theories in quantum physics: common concepts. *Physics Reports*, 299(4):189–425, 1998.

[192] J. M. G. Gómez, R. A. Molina, A. Relaño, and J. Retamosa. Misleading signatures of quantum chaos. *Phys. Rev. E*, 66:036209, Sep 2002.

[193] Ashraf A. Abul-Magd and Adel Y. Abul-Magd. Unfolding of the spectrum for chaotic and mixed systems. *Physica A: Statistical Mechanics and its Applications*, 396:185–194, 2014.

[194] Sherif M. Abuelenin. On the spectral unfolding of chaotic and mixed systems. *Physica A: Statistical Mechanics and its Applications*, 492:564–570, 2018.

[195] Vadim Oganesyan and David A. Huse. Localization of interacting fermions at high temperature. *Phys. Rev. B*, 75:155111, Apr 2007.

[196] Y. Y. Atas, E. Bogomolny, O. Giraud, and G. Roux. Distribution of the ratio of consecutive level spacings in random matrix ensembles. *Phys. Rev. Lett.*, 110:084101, Feb 2013.

[197] Yunxiang Liao, Amit Vikram, and Victor Galitski. Many-body level statistics of single-particle quantum chaos. *Phys. Rev. Lett.*, 125:250601, Dec 2020.

[198] Mohit Pandey, Pieter W. Claeys, David K. Campbell, Anatoli Polkovnikov, and Dries Sels. Adiabatic eigenstate deformations as a sensitive probe for quantum chaos. *Phys. Rev. X*, 10:041017, Oct 2020.

[199] W Beugeling, A Andreanov, and Masudul Haque. Global characteristics of all eigenstates of local many-body Hamiltonians: participation ratio and entanglement entropy. *Journal of Statistical Mechanics: Theory and Experiment*, 2015(2):P02002, feb 2015.

[200] Phillip C. Burke, Goran Nakerst, and Masudul Haque. Assigning temperatures to eigenstates. *Phys. Rev. E*, 107:024102, Feb 2023.

[201] Phillip C. Burke and Masudul Haque. Entropy and temperature in finite isolated quantum systems. *Phys. Rev. E*, 107:034125, Mar 2023.

[202] Phillip C. Burke, Jan Wiersig, and Masudul Haque. Non-Hermitian scattering on a tight-binding lattice. *Phys. Rev. A*, 102:012212, Jul 2020.

[203] S. Barnett. *Quantum Information*. OUP Oxford, 2009.

[204] M.A. Nielsen and I.L. Chuang. *Quantum Computation and Quantum Information*. Cambridge University Press, 2010.

[205] R von Baltz. Distance between quantum states and the motion of wave packets. *European Journal of Physics*, 11(4):215–220, jul 1990.

[206] Ludwig Knöll and Arkadiusz Orłowski. Distance between density operators: Applications to the Jaynes-Cummings model. *Phys. Rev. A*, 51:1622–1630, Feb 1995.

[207] V. Bužek and M. Hillery. Quantum copying: Beyond the no-cloning theorem. *Phys. Rev. A*, 54:1844–1852, Sep 1996.

[208] V V Dodonov, O V Man'ko, V I Man'ko, and A Wünsche. Energy-sensitive and "classical-like" distances between quantum states. *Phys. Scr.*, 59(2):81–89, feb 1999.

[209] V. V. Dodonov, O. V. Man'ko, V. I. Man'ko, and A. Wünsche. Hilbert-Schmidt distance and non-classicality of states in quantum optics. *Journal of Modern Optics*, 47(4):633–654, 2000.

[210] A. Wünsche, V.V. Dodonov, O.V. Man'ko, and V.I. Man'ko. Nonclassicality of states in quantum optics. *Fortschritte der Physik*, 49(10-11):1117–1122, 2001.

[211] V.V. Dodonov and M.B. Renó. Classicality and anticlassicality measures of pure and mixed quantum states. *Physics Letters A*, 308(4):249–255, 2003.

[212] Paulina Marian, Tudor A. Marian, and Horia Scutaru. Distinguishability and nonclassicality of one-mode Gaussian states. *Phys. Rev. A*, 69:022104, Feb 2004.

[213] Marco G. Genoni and Matteo G. A. Paris. Quantifying non-Gaussianity for quantum information. *Phys. Rev. A*, 82:052341, Nov 2010.

[214] W Roga, D Spehner, and F Illuminati. Geometric measures of quantum correlations: Characterization, quantification, and comparison by distances and operations. *J. Phys. A: Math. Theor.*, 49(23):235301, may 2016.

[215] Karol Bartkiewicz, Vojt ěch Trávníček, and Karel Lemr. Measuring distances in Hilbert space by many-particle interference. *Phys. Rev. A*, 99:032336, Mar 2019.

[216] Patrick J. Coles, M. Cerezo, and Lukasz Cincio. Strong bound between trace distance and Hilbert-Schmidt distance for low-rank states. *Phys. Rev. A*, 100:022103, Aug 2019.

[217] V. Trávníček, Karol Bartkiewicz, Antonín Černoch, and Karel Lemr. Experimental measurement of the Hilbert-Schmidt distance between two-Qubit states as a means for reducing the complexity of machine learning. *Phys. Rev. Lett.*, 123:260501, Dec 2019.

[218] Santosh Kumar. Wishart and random density matrices: Analytical results for the mean-square Hilbert-Schmidt distance. *Phys. Rev. A*, 102:012405, Jul 2020.

[219] Jiyong Park, Jaehak Lee, Kyunghyun Baek, and Hyunchul Nha. Quantifying non-Gaussianity of a quantum state by the negative entropy of quadrature distributions. *Phys. Rev. A*, 104:032415, Sep 2021.

[220] Wouter Beugeling, Arnd Bäcker, Roderich Moessner, and Masudul Haque. Statistical properties of eigenstate amplitudes in complex quantum systems. *Phys. Rev. E*, 98:022204, Aug 2018.

[221] Arnd Bäcker, Masudul Haque, and Ivan M. Khaymovich. Multifractal dimensions for random matrices, chaotic quantum maps, and many-body systems. *Phys. Rev. E*, 100:032117, Sep 2019.

[222] Giuseppe De Tomasi, Ivan M. Khaymovich, Frank Pollmann, and Simone Warzel. Rare thermal bubbles at the many-body localization transition from the Fock space point of view. *Phys. Rev. B*, 104:024202, Jul 2021.

[223] Miha Srdinšek, Tomaž Prosen, and Spyros Sotiriadis. Signatures of chaos in nonintegrable models of quantum field theories. *Phys. Rev. Lett.*, 126:121602, Mar 2021.

[224] Lukas Pausch, Edoardo G. Carnio, Alberto Rodríguez, and Andreas Buchleitner. Chaos and ergodicity across the energy spectrum of interacting bosons. *Phys. Rev. Lett.*, 126:150601, Apr 2021.

[225] G. P. Brandino, A. De Luca, R. M. Konik, and G. Mussardo. Quench dynamics in randomly generated extended quantum models. *Phys. Rev. B*, 85:214435, Jun 2012.

[226] Stefanie Hilt, Benedikt Thomas, and Eric Lutz. Hamiltonian of mean force for damped quantum systems. *Phys. Rev. E*, 84:031110, Sep 2011.

[227] Chris Jarzynski. Nonequilibrium work theorem for a system strongly coupled to a thermal environment. *Journal of Statistical Mechanics: Theory and Experiment*, 2004(09):P09005, sep 2004.

[228] H. Dong, S. Yang, X. F. Liu, and C. P. Sun. Quantum thermalization with couplings. *Phys. Rev. A*, 76:044104, Oct 2007.

[229] Maxim F. Gelin and Michael Thoss. Thermodynamics of a subensemble of a canonical ensemble. *Phys. Rev. E*, 79:051121, May 2009.

[230] D. Z. Xu, Sheng-Wen Li, X. F. Liu, and C. P. Sun. Noncanonical statistics of a finite quantum system with non-negligible system-bath coupling. *Phys. Rev. E*, 90:062125, Dec 2014.

[231] David Newman, Florian Mintert, and Ahsan Nazir. Performance of a quantum heat engine at strong reservoir coupling. *Phys. Rev. E*, 95:032139, Mar 2017.

[232] M. Perarnau-Llobet, H. Wilming, A. Riera, R. Gallego, and J. Eisert. Strong coupling corrections in quantum thermodynamics. *Phys. Rev. Lett.*, 120:120602, Mar 2018.

[233] Michele Campisi, Peter Talkner, and Peter Hänggi. Fluctuation theorem for arbitrary open quantum systems. *Phys. Rev. Lett.*, 102:210401, May 2009.

[234] Udo Seifert. First and second law of thermodynamics at strong coupling. *Phys. Rev. Lett.*, 116:020601, Jan 2016.

[235] Philipp Strasberg, Gernot Schaller, Neill Lambert, and Tobias Brandes. Nonequilibrium thermodynamics in the strong coupling and non-markovian regime based on a reaction coordinate mapping. *New Journal of Physics*, 18(7):073007, Jul 2016.

[236] T G Philbin and J Anders. Thermal energies of classical and quantum damped oscillators coupled to reservoirs. *Journal of Physics A: Mathematical and Theoretical*, 49(21):215303, apr 2016.

[237] John G. Kirkwood. Statistical mechanics of fluid mixtures. *The Journal of Chemical Physics*, 3(5):300–313, 1935.

[238] Tyler Chen and Yu-Chen Cheng. Numerical computation of the equilibrium-reduced density matrix for strongly coupled open quantum systems. *The Journal of Chemical Physics*, 157(6):064106, 2022.

[239] Markus P. Müller, David Gross, and Jens Eisert. Concentration of measure for quantum states with a fixed expectation value. *Communications in Mathematical Physics*, 303(3):785–824, May 2011.

[240] Hsin-Hua Lai and Kun Yang. Entanglement entropy scaling laws and eigenstate typicality in free fermion systems. *Phys. Rev. B*, 91:081110, Feb 2015.

[241] Chushun Tian, Kun Yang, Ping Fang, Hai-Jun Zhou, and Jiao Wang. Hidden thermal structure in Fock space. *Phys. Rev. E*, 98:060103, Dec 2018.

[242] Chaitanya Murthy and Mark Srednicki. Structure of chaotic eigenstates and their entanglement entropy. *Phys. Rev. E*, 100:022131, Aug 2019.

[243] Mahdi Kourehpaz, Stefan Donsa, Fabian Lackner, Joachim Burgdörfer, and Iva Březinová. Tuning canonical typicality by quantum chaos. *arXiv*, Mar 2021.

[244] Christoph Fleckenstein and Marin Bukov. Thermalization and prethermalization in periodically kicked quantum spin chains. *Phys. Rev. B*, 103:144307, Apr 2021.

[245] Tyler LeBlond, Krishnanand Mallayya, Lev Vidmar, and Marcos Rigol. Entanglement and matrix elements of observables in interacting integrable systems. *Phys. Rev. E*, 100:062134, Dec 2019.

[246] Masudul Haque and P. A. McClarty. Eigenstate thermalization scaling in Majorana clusters: From chaotic to integrable Sachdev-Ye-Kitaev models. *Phys. Rev. B*, 100:115122, Sep 2019.

[247] Marlon Brenes, John Goold, and Marcos Rigol. Low-frequency behavior of off-diagonal matrix elements in the integrable XXZ chain and in a locally perturbed quantum-chaotic XXZ chain. *Phys. Rev. B*, 102:075127, Aug 2020.

[248] Jonas Richter, Anatoly Dymarsky, Robin Steinigeweg, and Jochen Gemmer. Eigenstate thermalization hypothesis beyond standard indicators: Emergence of random-matrix behavior at small frequencies. *Phys. Rev. E*, 102:042127, Oct 2020.

[249] Felix Fritzsch and Tomaž Prosen. Eigenstate thermalization in dual-unitary quantum circuits: Asymptotics of spectral functions. *Phys. Rev. E*, 103:062133, Jun 2021.

[250] Qing Li, Jin-Lou Ma, and Lei Tan. Eigenstate thermalization and quantum chaos in the Jaynes-Cummings Hubbard model. *Physica Scripta*, 96(12):125709, sep 2021.

[251] Fabien Alet and Nicolas Laflorencie. Many-body localization: An introduction and selected topics. *Comptes Rendus Physique*, 19(6):498–525, 2018.

[252] Simone Ziraldo and Giuseppe E. Santoro. Relaxation and thermalization after a quantum quench: Why localization is important. *Phys. Rev. B*, 87:064201, Feb 2013.

[253] Vincenzo Alba. Eigenstate thermalization hypothesis and integrability in quantum spin chains. *Phys. Rev. B*, 91:155123, Apr 2015.

[254] Sourav Nandy, Arnab Sen, Arnab Das, and Abhishek Dhar. Eigenstate Gibbs ensemble in integrable quantum systems. *Phys. Rev. B*, 94:245131, Dec 2016.

[255] Anatoli Polkovnikov. Microscopic diagonal entropy and its connection to basic thermodynamic relations. *Annals of Physics*, 326(2):486–499, 2011.

[256] Lea F. Santos, Anatoli Polkovnikov, and Marcos Rigol. Entropy of isolated quantum systems after a quench. *Phys. Rev. Lett.*, 107:040601, Jul 2011.

[257] Mark T. Mitchison, Archak Purkayastha, Marlon Brenes, Alessandro Silva, and John Goold. Taking the temperature of a pure quantum state. *Phys. Rev. A*, 105:L030201, Mar 2022.

[258] Henrik Bruus and Jean-Christian Angl'es d'Auriac. Energy level statistics of the two-dimensional Hubbard model at low filling. *Phys. Rev. B*, 55:9142–9159, Apr 1997.

[259] C.-C. Joseph Wang, R. A. Duine, and A. H. MacDonald. Quantum vortex dynamics in two-dimensional neutral superfluids. *Phys. Rev. A*, 81:013609, Jan 2010.

[260] Yulia E. Shchadilova, Pedro Ribeiro, and Masudul Haque. Quantum quenches and work distributions in ultralow-density systems. *Phys. Rev. Lett.*, 112:070601, Feb 2014.

[261] C. Steinke, D. Mourad, M. Rösner, M. Lorke, C. Gies, F. Jahnke, G. Czycholl, and T. O. Wehling. Noninvasive control of excitons in two-dimensional materials. *Phys. Rev. B*, 96:045431, Jul 2017.

[262] J. H. Pixley, Yang-Zhi Chou, Pallab Goswami, David A. Huse, Rahul Nandkishore, Leo Radzihovsky, and S. Das Sarma. Single-particle excitations in disordered weyl fluids. *Phys. Rev. B*, 95:235101, Jun 2017.

[263] Tianyu Liu and Hai-Zhou Lu. Analytic solution to pseudo-landau levels in strongly bent graphene nanoribbons. *Phys. Rev. Research*, 4:023137, May 2022.

[264] Feng Xiong, Carsten Honerkamp, Dante M. Kennes, and Tanay Nag. Understanding the three-dimensional quantum hall effect in generic multi-weyl semimetals. *Phys. Rev. B*, 106:045424, Jul 2022.

[265] H.-D. Gräf, H. L. Harney, H. Lengeler, C. H. Lewenkopf, C. Rangacharyulu, A. Richter, P. Schardt, and H. A. Weidenmüller. Distribution of eigenmodes in a superconducting stadium billiard with chaotic dynamics. *Phys. Rev. Lett.*, 69:1296–1299, Aug 1992.

[266] A. Relaño, J. Dukelsky, J. M. G. Gómez, and J. Retamosa. Stringent numerical test of the Poisson distribution for finite quantum integrable Hamiltonians. *Phys. Rev. E*, 70:026208, Aug 2004.

[267] Anh-Thu Le, Toru Morishita, X.-M. Tong, and C. D. Lin. Signature of chaos in high-lying doubly excited states of the helium atom. *Phys. Rev. A*, 72:032511, Sep 2005.

[268] M. S. Santhanam and Jayendra N. Bandyopadhyay. Spectral fluctuations and $1/f$ noise in the order-chaos transition regime. *Phys. Rev. Lett.*, 95:114101, Sep 2005.

[269] Declan Mulhall. Using the $\delta_3$ statistic to test for missed levels in mixed sequence neutron resonance data. *Phys. Rev. C*, 80:034612, Sep 2009.

[270] Jiao Wang and Jiangbin Gong. Generating a fractal butterfly floquet spectrum in a class of driven su(2) systems. *Phys. Rev. E*, 81:026204, Feb 2010.

[271] Alberto Enciso, Federico Finkel, and Artemio González-López. Level density of spin chains of haldane-shastry type. *Phys. Rev. E*, 82:051117, Nov 2010.

[272] Sudhir Ranjan Jain and Rhine Samajdar. Nodal portraits of quantum billiards: Domains, lines, and statistics. *Rev. Mod. Phys.*, 89:045005, Dec 2017.

[273] W. E. Ormand and B. A. Brown. Microscopic calculations of nuclear level densities with the lanczos method. *Phys. Rev. C*, 102:014315, Jul 2020.

[274] Ángel L. Corps, Rafael A. Molina, and Armando Relaño. Thouless energy challenges thermalization on the ergodic side of the many-body localization transition. *Phys. Rev. B*, 102:014201, Jul 2020.

[275] A. G. Magner, A. I. Sanzhur, S. N. Fedotkin, A. I. Levon, and S. Shlomo. Semiclassical shell-structure micro-macroscopic approach for the level density. *Phys. Rev. C*, 104:044319, Oct 2021.

[276] Ángel L. Corps and Armando Relaño. Long-range level correlations in quantum systems with finite hilbert space dimension. *Phys. Rev. E*, 103:012208, Jan 2021.

[277] Stefano Ciliberti and Tomás S. Grigera. Localization threshold of instantaneous normal modes from level-spacing statistics. *Phys. Rev. E*, 70:061502, Dec 2004.

[278] André Gusso, M. G. E. da Luz, and Luis G. C. Rego. Quantum chaos in nanoelectromechanical systems. *Phys. Rev. B*, 73:035436, Jan 2006.

[279] Matthew D. Frye, Masato Morita, Christophe L. Vaillant, Dermot G. Green, and Jeremy M. Hutson. Approach to chaos in ultracold atomic and molecular physics: Statistics of near-threshold bound states for Li+CaH and Li+CaF. *Phys. Rev. A*, 93:052713, May 2016.

[280] C. P. Dettmann, O. Georgiou, and G. Knight. Spectral statistics of random geometric graphs. *EPL (Europhysics Letters)*, 118(1):18003, apr 2017.

[281] Soumyadeep Chaudhuri, Victor I. Giraldo-Rivera, Anosh Joseph, R. Loganayagam, and Junggi Yoon. Abelian tensor models on the lattice. *Phys. Rev. D*, 97:086007, Apr 2018.

[282] Jonas Wilhelm, Lukas Holicki, Dominik Smith, Björn Wellegehausen, and Lorenz von Smekal. Continuum goldstone spectrum of two-color qcd at finite density with staggered quarks. *Phys. Rev. D*, 100:114507, Dec 2019.

[283] Patrycja Łydżba and Tomasz Sowiński. Signatures of quantum chaos in low-energy mixtures of few fermions. *Phys. Rev. A*, 106:013301, Jul 2022.

[284] Alexander Weiße, Gerhard Wellein, Andreas Alvermann, and Holger Fehske. The kernel polynomial method. *Rev. Mod. Phys.*, 78:275–306, Mar 2006.

[285] Yilun Yang, Sofyan Iblisdir, J. Ignacio Cirac, and Mari Carmen Bañuls. Probing thermalization through spectral analysis with matrix product operators. *Phys. Rev. Lett.*, 124:100602, Mar 2020.

[286] J M Deutsch. Thermodynamic entropy of a many-body energy eigenstate. *New Journal of Physics*, 12(7):075021, Jul 2010.

[287] J. M. Deutsch, Haibin Li, and Auditya Sharma. Microscopic origin of thermodynamic entropy in isolated systems. *Phys. Rev. E*, 87:042135, Apr 2013.

[288] Eric M. Pearson, Timur Halicioglu, and William A. Tiller. Laplace-transform technique for deriving thermodynamic equations from the classical microcanonical ensemble. *Phys. Rev. A*, 32:3030–3039, Nov 1985.

[289] Peter Talkner, Peter Hänggi, and Manuel Morillo. Microcanonical quantum fluctuation theorems. *Phys. Rev. E*, 77:051131, May 2008.

[290] Jörn Dunkel and Stefan Hilbert. Consistent thermostatistics forbids negative absolute temperatures. *Nature Physics*, 10(1):67–72, Jan 2014.

[291] Stefan Hilbert, Peter Hänggi, and Jörn Dunkel. Thermodynamic laws in isolated systems. *Phys. Rev. E*, 90:062116, Dec 2014.

[292] Michele Campisi. Construction of microcanonical entropy on thermodynamic pillars. *Phys. Rev. E*, 91:052147, May 2015.

[293] Peter Hänggi, Stefan Hilbert, and Jörn Dunkel. Meaning of temperature in different thermostatistical ensembles. *Phil. Trans. R. Soc. A*, 374:20150039, Mar 2016.

[294] J.G. Muga, J.P. Palao, B. Navarro, and I.L. Egusquiza. Complex absorbing potentials. *Physics Reports*, 395(6):357 – 426, 2004.

[295] D.J. Griffiths. *Introduction to Quantum Mechanics*. Cambridge University Press, 2017.

[296] E.-M. Graefe, U. Günther, H.J. Korsch, and A.E. Niederle. A non-Hermitian symmetric Bose-Hubbard model: eigenvalue rings from unfolding higher-order exceptional points. *Journal of Physics A: Mathematical and Theoretical*, 41(25):255206, 2008.

[297] W.D. Heiss. Chirality of wavefunctions for three coalescing levels. *Journal of Physics A: Mathematical and Theoretical*, 41(24):244010, 2008.

[298] G. Demange and E.-M. Graefe. Signatures of three coalescing eigenfunctions. *Journal of Physics A: Mathematical and Theoretical*, 45(2):025303, 2011.

[299] Carl M. Bender. *$\mathcal{PT}$ Symmetry in Quantum and classical physics*. World Scientific Publishing, 2018.

[300] Carl M. Bender and Stefan Boettcher. Real spectra in non-Hermitian Hamiltonians having $\mathcal{PT}$ symmetry. *Phys. Rev. Lett.*, 80:5243–5246, Jun 1998.

[301] Carl M. Bender. Introduction to $\mathcal{PT}$-symmetric quantum theory. *Contemporary Physics*, 46(4):277–292, 2005.

[302] Ramy El-Ganainy, Konstantinos G. Makris, Mercedeh Khajavikhan, Ziad H. Musslimani, Stefan Rotter, and Demetrios N. Christodoulides. Non-Hermitian physics and $\mathcal{PT}$ symmetry. *Nature Physics*, 14(1):11–19, Jan 2018.

[303] A Fring. An introduction to pt-symmetric quantum mechanics-time-dependent systems. *Journal of Physics: Conference Series*, 2448(1):012002, feb 2023.

[304] J. Wiersig. Role of nonorthogonality of energy eigenstates in quantum systems with localized losses. *Phys. Rev. A*, 98:052105, Nov 2018.

[305] Vincenzo Alba and Federico Carollo. Noninteracting fermionic systems with localized losses: Exact results in the hydrodynamic limit. *Phys. Rev. B*, 105:054303, Feb 2022.

[306] R. Labouvie, B. Santra, S. Heun, S. Wimberger, and H. Ott. Negative differential conductivity in an interacting quantum gas. *Phys. Rev. Lett.*, 115:050601, Jul 2015.

[307] R. Labouvie, B. Santra, S. Heun, and H. Ott. Bistability in a driven-dissipative superfluid. *Phys. Rev. Lett.*, 116:235302, Jun 2016.

[308] M. Heinrich, M. Miri, S. Stüzer, R. El-Ganainy, S. Nolte, A. Szameit, and D. N. Christodoulides. Supersymmetric mode converters. *Nature Communications*, 5:3698, Apr 2014.

[309] S. Eichelkraut, T.and Weimann, M. Kremer, M. Ornigotti, and A. Szameit. *Passive $\mathcal{PT}$-Symmetry in Laser-Written Optical Waveguide Structures*, pages 123–153. Springer Singapore, Singapore, 2018.

[310] R. Morandotti, U. Peschel, J. S. Aitchison, H. S. Eisenberg, and Y. Silberberg. Experimental observation of linear and nonlinear optical Bloch oscillations. *Phys. Rev. Lett.*, 83:4756–4759, Dec 1999.

[311] T. Schwartz, G. Bartal, S. Fishman, and M. Segev. Transport and anderson localization in disordered two-dimensional photonic lattices. *Nature*, 446(7131):52–55, 2007.

[312] D. Guzman-Silva, M. Heinrich, T. Biesenthal, Y.V. Kartashov, and A. Szameit. Experimental study of the interplay between dynamic localization and Anderson localization. *Opt. Lett.*, 45(2):415–418, Jan 2020.

[313] A. Szameit, M. C. Rechtsman, O. Bahat-Treidel, and M. Segev. $\mathcal{PT}$-symmetry in honeycomb photonic lattices. *Phys. Rev. A*, 84:021806, Aug 2011.

[314] M. Heinrich, M.-A. Miri, S. Stützer, S. Nolte, D.N. Christodoulides, and A. Szameit. Observation of supersymmetric scattering in photonic lattices. *Opt. Lett.*, 39(21):6130–6133, 2014.

[315] V. A. Brazhnyi, V. V. Konotop, V. M. Pérez-García, and H. Ott. Dissipation-induced coherent structures in Bose-Einstein condensates. *Phys. Rev. Lett.*, 102:144101, Apr 2009.